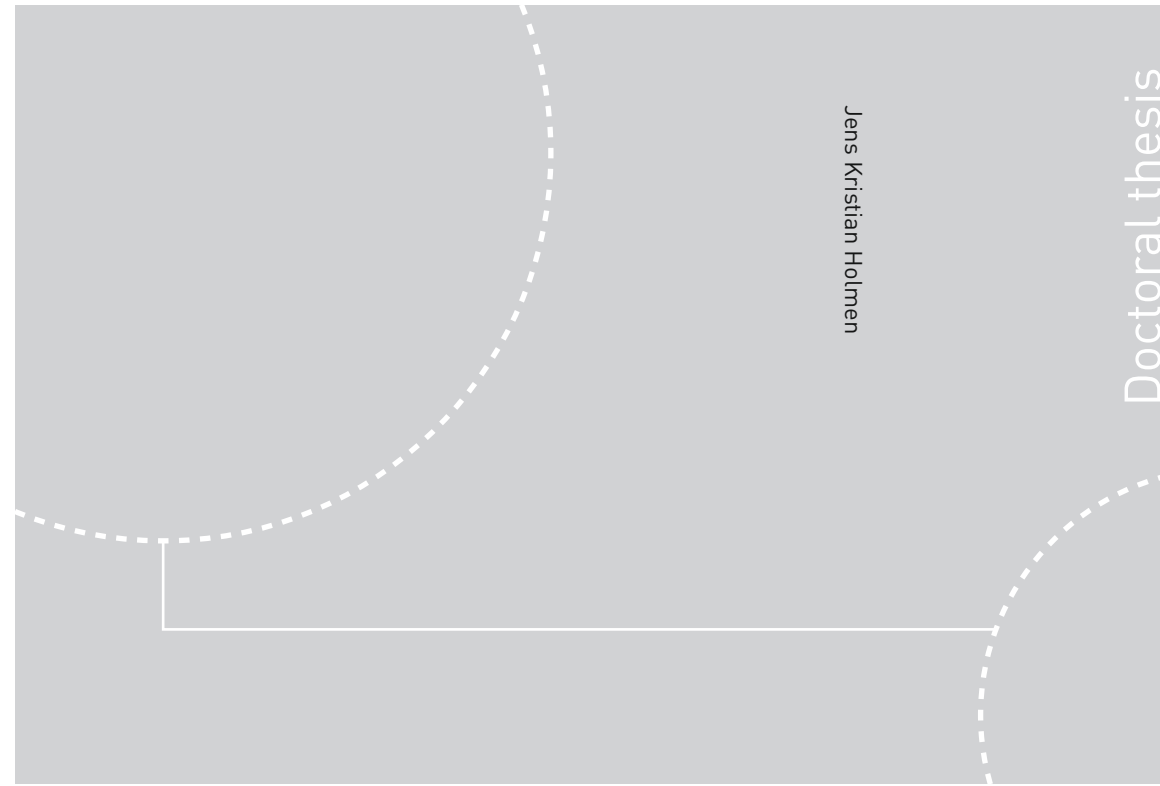


ISBN 978-82-326-1818-7 (printed ver.)
ISBN 978-82-326-1819-4 (electronic ver.)
ISSN 1503-8181



NTNU
Norwegian University of
Science and Technology
Doctoral theses at NTNU, 2016:240
Faculty of Engineering Sciences and Technology
Department of Structural Engineering
Ph.D. theses
Doctoral Degree
Thesis for the Degree of
Science and Technology

Doctoral theses at NTNU, 2016:240

Jens Kristian Holmen

Modeling and Simulation of Ballistic Impact

Jens Kristian Holmen

Modeling and Simulation of Ballistic Impact

Thesis for the Degree of Philosophiae Doctor

Trondheim, September 2016

Norwegian University of Science and Technology
Faculty of Engineering Science and Technology
Department of Structural Engineering



Norwegian University of
Science and Technology

NTNU
Norwegian University of Science and Technology

Thesis for the Degree of Philosophiae Doctor

Faculty of Engineering Science and Technology
Department of Structural Engineering

© Jens Kristian Holmen

ISBN 978-82-326-1818-7 (printed ver.)
ISBN 978-82-326-1819-4 (electronic ver.)
ISSN 1503-8181

Doctoral theses at NTNU, 2016:240

Printed by NTNU Grafisk senter

Preface

This thesis is submitted in partial fulfillment of the requirements for the degree of Philosophiae Doctor in Structural Engineering at the Norwegian University of Science and Technology. Professor Tore Børvik and Professor Odd Sture Hopperstad supervised the work. The thesis consists of five journal articles that are accepted in, or submitted to, international peer-reviewed journals and one conference contribution presented at an international conference. They are referred to as Parts 1-6 in the thesis. A synopsis binds the individual contributions together. The first author has been responsible for the experimental work, numerical work and the preparation of all the manuscripts, with a few exceptions in Part 2: the nano-structural modeling was done by Adjunct Professor Ole Runar Myhr, and the welding simulations were conducted by Dr. Hallvard Gustav Fjær.

Jens Kristian Holmen
Trondheim, Norway
June 2, 2016

Abstract

Numerical simulations are increasingly becoming an important tool to obtain efficient designs of protective structures, and the existing literature shows that many phenomena can be accurately described by standard methods and models. This thesis, specifically, focuses on novel methods of modeling and simulating ballistic impact. Experiments are needed to validate such simulations, so numerous tests were conducted to investigate how projectile nose-shape, plate layering, target strength, ductility, and work hardening affect the penetration and perforation behavior of various structural configurations. Aluminum plates, steel plates, sand, and sand in combination with aluminum profiles were considered. These tests provide new information about the behavior of materials subjected to ballistic impact, and are valuable input for the evaluation of the numerical simulations. The novel node-splitting method, used to introduce fracture into a numerical model, and a newly implemented discrete particle method were particularly important in this work.

The thesis consists of six individual parts. They are contextualized and linked together by a synopsis which includes a state-of-the-art of numerical modeling of ballistic impact and the objectives and scope of the thesis, along with summaries of the different parts, an overall conclusion and suggestions for further work. Part 1 considers low-velocity impact of layered thin steel plates. Two impactor nose shapes were used: blunt and ogival. The experimental setup is explained in detail and it was found that the resistance to perforation is highest for the blunt-nosed impactor. It was further seen that a monolithic configuration dissipates more energy than a layered configuration of the same thickness. The numerical model was able to predict the correct failure mechanisms and the trends from the experiments; however, a one-to-one relation between simulations and experiments was not obtained. In Part 2, microstructural modeling was used to determine the constitutive behavior of the base material and the heat affected zone (HAZ) of welded Al-Mg-Si aluminum alloy extrusions. Finite element simulations were conducted of impacts by 7.62 mm armor piercing bullets. The experimental validation showed that the purely numerical procedure to estimate the perforation capacity was accurate. Part 3 investigated the influence of target fragmentation on the capacity of plates subjected to ballistic impact. This was done by firing blunt and ogival-nosed projectiles at 20 mm thick plates made of four different tempers of aluminum alloy AA6070. It was shown that strength is not the only important parameter for the perforation resistance; ductility must be factored into the design as well. Node splitting, where new

element faces are created at failure, was applied and evaluated in the numerical part. It was found to give as good, or better, results than conventional element erosion. In Part 4, node splitting was used to simulate ballistic impact on layered and surface-hardened steel plates. 7.62 mm armor piercing bullets struck 12 mm thick plate configurations (1x12 mm, 2x6 mm or 3x4 mm). Plate layering was found to be disadvantageous, especially for the surface-hardened plates. Numerical simulations adequately reproduced the experimental behavior. Part 5 and Part 6 looked at penetration and perforation of sand at both high and low impact velocities. A discrete particle method (DPM) where each individual sand grain is treated as a particle was used in the numerical parts of these studies. The DPM gave promising qualitative and quantitative results, and if we also consider results from other studies it becomes clear that the DPM has the potential to be used in a wide range of applications.

Acknowledgment

This work would have been impossible to complete without the exceptional working environment at SIMLab. I wish to acknowledge all my colleagues who made, and continue to make, this a great place to work (even loud Galicians). Special thanks go to Joakim Johnsen for being my closest collaborator for almost nine years, to Vegard Aune for encouraging me to start at SIMLab, and to Lars Edvard Dæhli for providing general theoretical support and for enduring 18 months as my office roommate.

Experimental testing has been the foundation for all the studies presented in this work. So I have to highlight the significant efforts of Mr. Tore Wisth, Mr. Trond Auestad and Mr. Tore André Kristensen. Without them I would never have finished my work on time. I am grateful to Professor Jan Ketil Solberg, Dr. Hallvard Gustav Fjær from the Institute for Energy Technology (IFE) and Adjunct Professor Ole Runar Myhr from Hydro Aluminium for making important contributions as co-authors. I also owe thanks to Dr. Egil Fagerholt for his help with the digital image correlation analyses; Mr. Trygve Schanche for conducting Vickers hardness testing of steel; and Associate Professor Ida Westermann for Vickers hardness testing of aluminum, providing excellent high-resolution images of selected materials, and especially for providing emergency metallurgical support whenever needed. I must also acknowledge Professor Magnus Langseth for technical and non-technical input and for making the daily life at SIMLab anything but boring.

The aid from the master's students who enthusiastically dedicated their final semester at NTNU to work on subjects relevant to my work is appreciated. Their help in the laboratory and insightful questions, comments, and curiosity undoubtedly made this a better thesis.

The financial support for this work came from the Norwegian Defence Estates Agency, the Structural Impact Laboratory (SIMLab) and from the Faculty of Engineering Science and Technology at the Norwegian University of Science and Technology. All the help is greatly acknowledged.

I wish to thank Dr. Lars Olovsson for interesting insight and vital help with the finite element simulations in IMPETUS Afea Solver. His impressive knowledge about simulation techniques and his positive attitude towards problem solving cannot be overstated.

I am genuinely thankful to Professor Tore Børvik and Professor Odd Sture Hopperstad for their attention and supervision. Professor Børvik was my main academic supervisor, but he also provided important moral support when progress was slow. His hands-on and enthusiastic guidance combined with his knowledge of this field was invaluable to me as a student. Professor Børvik was perfectly complemented by co-supervisor Professor Hopperstad whose creativity and attention to detail was truly inspiring. He gives great answers to often not so great questions. I could not have asked for a better team of supervisors.

Finally, I thank you Rachel for your love, support, encouragement, and extreme patience with me during good and bad times. I am also sincerely grateful to the rest of my family and to my friends for their never-ending support and for reminding me that there is more to life than working.

Contents

Synopsis:

1. Introduction	1
2. Objectives and scope.....	4
3. Summary	6
Part 1	6
Part 2	7
Part 3	8
Part 4	10
Part 5	11
Part 6	12
Other contributions	13
4. Concluding remarks	13
5. Further work	15
6. References	16

Articles:

Part 1:

Holmen, J.K., Hopperstad, O.S., Børvik, T., 2015. Low-velocity impact on multi-layered dual-phase steel plates. International Journal of Impact Engineering 78, 161–177.

Part 2:

Holmen, J.K., Børvik, T., Myhr, O.R., Fjær, H.G., Hopperstad, O.S., 2015. Perforation of welded aluminum components: Microstructure-based modeling and experimental validation. International Journal of Impact Engineering 84, 96–107.

Part 3:

Holmen, J.K., Johnsen, J., Hopperstad, O.S., Børvik, T., 2016. Influence of fragmentation on the capacity of aluminum alloy plates subjected to ballistic impact. European Journal of Mechanics A/Solids 55, 221–233.

Part 4:

Holmen, J.K., Solberg, J.K., Hopperstad, O.S., Børvik, T., 2016. Ballistic perforation of layered and surface-hardened steel plates. 1st International Conference on Impact Loading of Structures and Materials, Turin, Italy.

Part 5:

Holmen, J.K., Børvik, T., Hopperstad, O.S., 2016. Experiments and simulations of empty and sand-filled aluminum alloy panels subjected to ballistic impact. Submitted for possible journal publication.

Part 6:

Holmen, J.K., Olovsson, L., Børvik, T., 2016. Discrete modeling of low velocity penetration in sand. Submitted for possible journal publication.

Synopsis

1. Introduction

A protective structure's purpose is to protect lives or economic interests in extreme load situations. Such loads can result from deliberate attacks or they can be inflicted by accidents; meaning that protective structures are not only relevant for the military, but also for civil applications. Examples are the offshore industry that focuses on securing workers and equipment against dropped objects and accidental explosions, and the automotive industry that is concerned about the safety of the occupants of cars in the event of a collision. Another rather common case is bird strike on airplanes that can cause considerable damage unless the fuselage, wings and engines are designed to withstand the impact. Other more typical civil engineering applications can be bridges that are impacted by ships, or impact between adjacent structures during earthquakes. In fact, the integrity of much of the world's important infrastructure, and not to mention the safety of human beings, is dependent on well-designed protective structures.

Conducting research on dynamic impact was for a long time considered to be experimental in nature (Zukas, 1990), and military research institutions led the development of the field. The general public's increasing interest in transient dynamics have made the problem solving techniques that, in the past, were mainly employed to military structures relevant for civilian applications as well. Further, the tremendous growth in computational resources has created a drive towards solving such problems with full three-dimensional numerical analyses.

There is an academic tradition for the study of the penetration and perforation of metals. Comprehensive reviews exist that sum up much of the research prior to 1996. Backman and Goldsmith (1978) focused on analytical and empirical methods in terminal ballistics; they also provided an overview of experimental observations. Jonas and Zukas (1978) reviewed analytical and numerical methods for high-velocity impact, and they even presented some three-dimensional simulations. A decade later Anderson and Bodner (1988) summarized the state of analytical and numerical modeling at that time. The last thorough review of penetration and perforation mechanics was published by Corbett et al. (1996) which covered recent experimental data, and analytical and numerical modeling. These studies all look at analytical and empirical approaches together with rather simple two-dimensional numerical models. While they are less flexible than the full three-dimensional analyses that prevail

today, they give valuable insight into the penetration event as long as the models' limitations are acknowledged. Numerical examples of relatively simple models are given in Rosenberg and Dekel (2009, 2010) and Johnsen et al. (2013), while examples of analytical modeling, more specifically the cavity expansion theory, can be found in Forrestal et al. (1987, 1990, 1992), Rosenberg and Forrestal (1988), and Forrestal and Warren (2009).

The bulk of contemporary penetration and perforation simulations employ the constitutive equation presented by Johnson and Cook (1983) or some modified version of it (e.g., Børvik et al., 2001a). Most often this constitutive relation is combined with a version of the fracture criterion by the same authors (Johnson and Cook, 1985). The reasons for the extreme dissemination of Johnson-Cook type models are several. First, they predict the global behavior of metals subjected to impact both qualitatively and quantitatively rather well. Strain rate and temperature effects are incorporated into the material and fracture behavior, and the fracture strain is dependent upon the stress triaxiality ratio. Second, they are phenomenological and relatively straightforward to both calibrate and implement; still, a complete calibration requires several tension (or compression) tests at various strain rates and temperatures. Third, since they are so frequently used, material data is easily available in the literature facilitating even more use of the models. Recent literature where the Johnson-Cook model was used in ballistic impact studies include Børvik et al. (1999, 2001b, 2005), Gupta et al. (2007, 2008), Arias et al. (2008), Iqbal et al. (2010a, 2010b), Flores-Johnson et al. (2011) and Erice et al. (2012).

Another frequently used failure criterion was presented by Cockcroft and Latham (1968). It requires only one uniaxial tension test for calibration and according to Dey et al. (2006) it gives similar results to the five-parameter Johnson-Cook criterion. The Cockcroft-Latham criterion was used in Børvik et al. (2009, 2011a) and Holmen et al. (2013). It depends upon the stress triaxiality ratio and also on the third stress invariant, but the latter cannot be directly calibrated in the original version of the Cockcroft-Latham criterion. The dependency of ductile failure on the third deviatoric stress invariant, or Lode parameter, has been highlighted in the literature (Bai and Wierzbicki, 2004; Gruben et al., 2012). The Bai-Wierzbicki criterion (Bai and Wierzbicki, 2004) implicitly accounts for the Lode parameter and it was successfully applied in ballistic impact problems by Manes et al. (2013, 2014) and Gilioli et al. (2015). The modified Mohr-Coulomb criterion (Bai and Wierzbicki, 2010) explicitly accounts for the Lode parameter and was used to simulate ballistic impact by Gilioli et al. (2015). The third deviatoric stress invariant has also been accounted for in recent extensions of the Johnson-

Cook model where the objective was to predict fracture patterns and the differing strains at failure between pure shear and tension tests more realistically (Chocron et al., 2011; Erice and Gálvez, 2014; Erice et al., 2014). Some researchers advocate the use of even simpler criteria like the constant failure strain criterion, although it has been found to be incapable of predicting failure in a realistic manner (Teng and Wierzbicki, 2006).

As shown in most of the literature that was referenced above, ductile perforation mechanisms can be accurately predicted by conventional element erosion. In most element erosion algorithms, the stress tensor is set to zero if the failure criterion is fulfilled in an integration point, which effectively removes the element from the analysis. However, several target configurations involving metals exhibit quasi-ductile perforation mechanisms like fragmentation. Fragmentation might occur because the material is not sufficiently ductile to prevent it or because the projectile/target combination promotes fragmentation. This can be numerically predicted by using statistics to introduce heterogeneity into simulation models that feature element erosion (Rakvåg et al., 2014). But there is also increased interest in other methods where failure is not as mesh sensitive as conventional element erosion. For brittle materials it is possible to convert elements to particles at failure, or to simply run a smooth particle hydrodynamics simulation where severe deformations are less detrimental to the analysis (Johnson et al., 1996, 2015; Bresciani et al., 2016). An appealing and rather well-known method of introducing failure into a numerical model is node splitting (Xu and Needleman, 1994; Camacho and Ortiz, 1996; Komori, 2001). It has just recently become available for three-dimensional analyses in commercial codes (Ruggiero et al., 2014; Olovsson et al., 2015; Holmen et al., 2016a) and is a promising substitute or supplement to conventional methods. It would be beneficial to be able to predict purely ductile and quasi-ductile perforation mechanisms with the same model. This is important because if a numerical model fails to predict the correct perforation mechanism it can predict perforation capacities that are severely wrong.

The behavior of granular materials subjected to impact loads has historically been predicted by empirical and analytical methods. However, in recent years the use of numerical modeling to study intricate issues in penetration of granular media has increased. This is especially useful for phenomena that are too complex for empirical or analytical models to capture. Continuum and discrete numerical methods prevail today (Omidvar et al., 2014; Iskander et al., 2015), and they both have advantages and weaknesses. Continuum models require constitutive equations of the bulk sand, and numerical issues might arise in mesh

discretization and with element erosion. Per now, they are not capable of capturing sand ejecta or particle breakage (Cundall, 2001; Deshpande et al., 2009). Discrete methods where each grain of sand is modeled by a particle require few material inputs, and the bulk behavior is a consequence of the individual behavior of each particle. Here the physics of the problem is qualitatively better captured, and from a penetration point of view the sand ejecta and heterogeneity of the sand are readily introduced into the model. Cundall and Strack (1979) pioneered discrete modeling of granular material and several simulation models have been formulated over the years (Oñate and Rojek, 2004; Oñate et al., 2015). The future of simulating penetration of granular media seems to be discrete. A complete three-dimensional discrete particle method (DPM) was proposed by Olovsson et al. (2010) and has been used in combined blast and sand impact on various structures (Børvik et al., 2011b; Wadley et al., 2013; Holloman et al., 2015a, 2015b). Børvik et al. (2015) used the model in deep penetration of sand and it further remains to evaluate the method in other cases of penetration and perforation coupled with finite elements.

2. Objectives and scope

The wide variety of possible projectile shapes, striking velocities and target materials means that extensive experimental testing is needed to fully understand the structural impact problem. But it is an almost impossible task to base all types of design solely on tests, so reliable numerical methods play an increasingly important role in developing the understanding of protective solutions. In the introduction we identified several aspects in modeling that have yet to be completely solved. One of these is fragmentation of both quasi-ductile and brittle solids. This is a difficult subject and has been the topic of numerous studies on various materials. For metals we want to investigate how target fragmentation affects the capacity of a protective plate. This is not a straightforward numerical task since both an accurate failure criterion and an appropriate method of introducing failure into the finite element mesh need to be present in the simulation. Another topic of great interest is impact and penetration of granular media. Accurate and computationally efficient methods of simulating such materials are not plentiful in the literature. It is an active research area, but it is dominated by physicist and geotechnicians who do not have the interaction between soil and deformable structures as their main interest.

Penetration, perforation, fragmentation, and blast loading are related and often take place in the same event even though the phenomena can involve vastly different energy-dissipating

and failure modes. Of these, blast loading is not covered in this thesis since it entails a different solution strategy compared to the others. Blast loading is in general a global problem, which in the case of deformable structures requires a sound description of the applied load and a simulation model of the entire structure (Aune et al., 2016a, 2016b). Penetration, perforation and fragmentation are mainly local phenomena that are dependent upon the material and the geometry in immediate proximity to the impact event.

Accurate numerical models that describe how materials deform under a given load before they fail are essential in order to obtain safe and predictable designs. Both the mathematical foundation and the numerical implementation into the computer code need to be correct for this to be successful. Evaluation and validation of the methods are crucial for the trustworthiness of numerical simulation results. The focus of this PhD project has been to use rather new and untested numerical approaches to model and simulate the complex behavior of protective structures subjected to ballistic impact. Three numerical methods have been studied: (1) node splitting has been considered as an alternative to conventional element erosion in finite element simulations of plate perforation; (2) microstructural modeling was applied to determine the ballistic capacity of welded aluminum components in a completely numerically way, that is without using experimental tests to calibrate the finite element models; and (3) a discrete particle method in combination with the finite element method has been used to represent sand in penetration and perforation problems. Experimental programs were designed partly to evaluate and validate the numerical methods and partly to shed light upon previously unsolved research questions. The effects of layering at high impact velocities are relatively well-known (Dey et al., 2007, 2011; Teng et al., 2007), but further studies regarding layering of thin plates struck at low velocities were conducted in this thesis. Further, the effect of target fragmentation on the capacity of plates, the ballistic resistance of sand subjected to low and high-velocity impact, and the interaction between sand particles and deformable structures were investigated in this thesis.

To obtain more efficient designs in a cost-effective way, we wish to further study how numerical codes can be utilized to predict the capacity of complex structures subject to impact loading. And although the primary motivation behind the thesis is the design of protective structures, no structural designs are presented in the work. The emphasis of the individual contributions has been to obtain sufficient experimental data to evaluate and validate numerical models that can be used in the future to design protective structures.

In conclusion, the main objective of this thesis is to critically evaluate novel numerical techniques and their potential for predicting the behavior of complex structures subjected to ballistic impact. More specifically we investigated if node splitting is better than element erosion, if we can use nano-scale material models to simulate welded aluminum alloy structures, and if the discrete particle method is an appropriate tool for simulating sand subjected to impact loading.

3. Summary

The works in this PhD thesis have been presented at international conferences, submitted for possible publication or published in international peer-reviewed journals. The conference paper and five full-length journal articles are summarized below.

Part 1

Low-velocity impact on multi-layered dual-phase steel plates

The first part of the thesis is an experimental and numerical study on the perforation of thin steel plates. Both monolithic and layered configurations were considered. The main objectives of the study were to: (1) investigate the effect of nose shape on the perforation capacity of thin plates, (2) determine how the perforation capacity of laminated plates compare to monolithic plates, and (3) evaluate the numerical predictions provided by finite element simulations.

Studies of high and medium velocity impact are readily available in the literature, but relatively few systematic studies exist on the effects of projectile shape and layering of thin plates. This study was undertaken to determine how thin plates behave compared to thick plates in the event of impacts.

All the impact tests were conducted in an Instron CEAST 9350 dropped-object-rig. Impactor nose shape was varied between blunt and ogival. We used 0.8 mm thick monolithic plates, as well as double, triple and quadruple-layered configurations in the main study. Monolithic and double-layered 1.8 mm thick plates were tested for comparison. The impact velocity was measured optically in each test, while a load cell continuously measured the force. We did enough tests to determine the ballistic limit velocity for each configuration. In general, the plates' capacity was higher when they were struck by blunt-nosed impactors than when they were struck by ogival-nosed impactors. The perforation mechanisms were vastly different for the two nose shapes. For the blunt nose, significant global deformation preceded failure by

thinning and plug ejection around the circumference of the impactor. For the ogival nose, initial perforation took place almost instantaneously, before petaling dominated the rest of the perforation process. Monolithic plate configurations seem to dissipate more energy than layered plates of the same total thickness, particularly for the ogival-nosed impactor.

To identify the parameters that were needed in the constitutive relation we conducted tension tests and corresponding inverse modeling using LS-DYNA coupled with LS-OPT. A modified version of the well-known Johnson-Cook constitutive relation was used in combination with the one-parameter Cockcroft-Latham failure criterion. Rather simple 3D finite elements models of the impact-test setups were made in the IMPETUS Afea Solver. Conventional element erosion was used in all the simulations. We were able to predict the experimental trends and the failure modes, but we did not obtain a one-to-one correlation to the experiments.

The main shortcomings in the numerical part of this study are the representations of the boundary conditions and the failure initiation. Seeing that the process is relatively slow and that the global behavior is vital to the result of the simulation, the entire geometry must be modeled. On the other hand, the point of failure, that happens in a very small area, is equally important to the simulation result; meaning that a trade-off between computational efficiency and accuracy had to be made. It is clear from this work that the simulation models we used to predict perforation in thin metal plates is reasonably accurate considering the complexity of the problem.

Part 2

Perforation of welded aluminum components: Microstructure-based modeling and experimental validation

A purely numerical approach for determining the ballistic capacity of welded aluminum components was presented in this study. Only the chemical composition, the aging heat treatment, and the welding procedure was used to predict the material behavior of the aluminum alloy as a function of the distance from the weld center. Finite element simulations were conducted and compared to experimental data. Varying the alloying elements and subsequent heat treatment can dramatically change the mechanical properties of aluminum. Thus, to obtain optimal materials for a chosen component it is beneficial to numerically simulate as much as possible before producing expensive prototypes. The first objective of

this paper was to see how welding affects the ballistic properties of aluminum alloy extrusions of different thicknesses. The second objective was to demonstrate a purely numerical method to predict the same ballistic properties.

An experimental program was undertaken before we started on the purely numerical procedure. We used extruded 10 mm, 20 mm and 30 mm thick profiles made of aluminum alloy AA6082-T6. Profiles were welded together with automatic MIG welding and the temperature-time histories were measured by thermocouples. Vickers hardness measurements were conducted across the welds of all the extrusions while tension tests were done of the 10 mm and 30 mm extrusions. We then fired 7.62 mm armor piercing (AP) bullets at the base material and the heat affected zone (HAZ) of all the extrusions. The base material exhibited the highest ballistic limit velocity for all the thicknesses and the HAZ exhibited the lowest ballistic limit velocity. The difference was never more than 10 %.

The numerical procedure consisted of three steps: (1) a thermal solver predicted the thermal field from the welding, (2) a nano-scale material model used the chemical composition and temperature history from aging and welding to calculate the flow-stress curves, and (3) a finite element solver used the flow-stress curves to simulate either the ballistic tests or the tension test. No experimental data whatsoever was used to calibrate the numerical models. Only the 10 mm thick extrusion was considered in the numerical procedure. The final results were in excellent agreement with the experimental results when we compare the ballistic limit velocities, the discrepancy between experiments and simulations was below 10 % in all cases.

In all the tests the dominating failure mechanism was ductile-hole growth. This means that a pinhole could be used in the plate to avoid the need for a failure criterion which could not be calibrated from the proposed method. Although fracture was disregarded, the paper shows that we can predict the ballistic behavior of AA6xxx aluminum alloys subjected to complex thermal histories without conducting a single experiment.

Part 3

Influence of fragmentation on the capacity of aluminum alloy plates subjected to ballistic impact

In this third part of the thesis ogival and blunt-nosed projectiles were fired at 20 mm thick plates made of four different tempers of aluminum alloy AA6070. Finite element simulations were conducted of all the tests, and a novel node-splitting technique was demonstrated. The

main experimental objective of this work was to investigate the role of strength, work hardening, and ductility on the ballistic properties of 20 mm thick plates. This was done by having four different tempers of the same alloy, all with different material behaviors but similar microstructure. In the numerical part of the study the node-splitting technique was compared to conventional element erosion for configurations that fragment and configurations that do not fragment.

Ogival and blunt-nosed projectiles were launched from a gas-gun at moderate velocities (200-300 m/s). Ballistic limit velocities were crudely estimated based on the Recht-Ipson equation. We see that the capacity of the various tempers is not a function of strength only; ductility is an equally important factor for the ballistic resistance of the aluminum plates. Even though one of the tempers had yield stress of 350 MPa, its ballistic limit velocity was lower than the ballistic limit velocity of a temper with a yield stress of 50 MPa.

Finite element models were made with both the blunt-nosed and the ogival-nosed projectiles. Four different methods of introducing failure in the model were used: (1) element erosion where all the components of the stress tensor are set to zero when 16 out of 64 integration points reach full damage; (2) an element erosion algorithm where the shear strength in an integration point vanishes at full damage, but the element can still take compressive stresses; (3) a strain based node-splitting technique where new element surfaces are created perpendicularly to the direction of the maximum principal strain; and (4) a stress based node-splitting technique where new element surfaces are created perpendicularly to the direction of the maximum principal stress. We found that all the failure methods predict similar results when the material is weak and ductile, but there are significant differences when the target material is strong and less ductile, that is when we observe fragmentation in the experiment. Here the node-splitting algorithms quantitatively outperform the element erosion algorithm and the qualitative results are also significantly better.

The experimental part of the study taught us that strength is not the only important material parameter for perforation resistance in all cases. What we can conclude from the numerical part of the study is that node splitting is a promising alternative to element erosion.

Part 4

Ballistic perforation of layered and surface-hardened steel plates

Part 4 deals with similar topics as Part 1 and Part 3. But instead of looking at low-velocity impacts on layered plates, the topic is now high-velocity impacts on layered plates, and due to fragmentation in the target plates we decided to use node splitting to introduce failure into the numerical model. The main objectives of the study were to investigate how the capacity of monolithic plates compares to that of layered plates of equal total thickness and to investigate how the capacity of the plates is affected by increasing the surface hardness.

In this study we used hot-rolled NVE 36 steel plates of thickness 12 mm, 6 mm and 4 mm in either a monolithic configuration (12 mm) or laminated configurations (2×6 mm and 3×4 mm). The plates all have a nominal yield stress of 355 MPa. Some of the plates were tested in the as-received (AR) condition; others were surface hardened (SH) in a carbon-rich environment at elevated temperatures to vary the hardness over the target thickness (also known as case hardening). Tension tests and hardness tests were conducted to identify the parameters needed in the constitutive model. 7.62 mm armor piercing (AP) bullets were fired at the target plates at velocities between 465 m/s and 915 m/s to determine the ballistic limit velocities. The results show that the ballistic limit velocity increased by between 20 % and 30 % for the SH plates compared to the AR plates. Further, lamination will hardly change the capacity for AR plates, but it will reduce the capacity for SH plates. The reason for this seemed to be that the thinner AR plates developed some global deformation that dissipated additional energy which counteracted the drop in dissipation due to layering. This did not happen for the SH plates.

Surface hardening significantly increased the capacity of the plates, but the intended hardness gradient was not always achieved; showing that this type of surface hardening might not be a viable strategy for large-scale protective structures. Lamination reduced the capacity of the AR plates less than the SH plates because of a change in the failure mechanism. Still, it does not appear that structures consisting of layered plates have the same capacity as monolithic plates for this bullet shape. Last, finite element simulations were able to predict the failure modes and the ballistic limit velocities with satisfactory accuracy. All the results were conservative, and within 10 % of the experimentally determined value.

Part 5

Experiments and simulations of empty and sand-filled aluminum alloy panels subjected to ballistic impact

A discrete particle method (DPM) can in combination with the finite element method be used to predict the interaction between structures and granular media during ballistic impact. By applying a DPM to model granular materials, issues such as mesh distortion, element deletion and continuum constitutive equations can be avoided. It also makes intuitive sense to model such media with discrete particles since they imitate the physical nature of sand. This study presents experiments and numerical simulations on the perforation of empty and sand-filled aluminum panels struck by small-arms bullets. The main goal has been to apply and evaluate the coupling of DPM and FEM in a complex penetration problem.

In the experimental part of the study, AA6005-T6 aluminum panels originally intended as bridge decks were struck with 7.62 mm AP bullets. The panels were loosely clamped to the ballistic rig in all tests and the impact point was chosen so that the bullet had to perforate the oblique web of the panel in every test. Impact velocities between 400 m/s and 900 m/s were considered in the study. Precautions were taken in the preparation for the tests of the sand-filled panels; they were all gently tapped with a rubber hammer before testing to make sure that the sand was compacted. As expected, the ballistic limit velocity increased markedly when sand was filled in the panels. The empty panel had a ballistic limit velocity of 450.1 m/s while the sand-filled panels had a minimum ballistic limit velocity of 646.0 m/s which is an increase of 43.5 %. However, the scatter in the tests with sand was rather high. Subsequent testing was done to confirm that this was not due to inconsistencies in the experimental setup.

Simulations were conducted where the aluminum panel was represented by finite elements and the sand by discrete particles. Material parameters for the aluminum were taken from the literature while the parameters for the DPM were based on a simple calibration test. The experimentally determined ballistic limit velocity from the empty panels was predicted within 4.2 % by the simulations. The simulations with sand predicted the ballistic velocity within 11 % of the experimentally determined value. Both underestimated the capacity, meaning that the results were conservative. By considering different pitch angles and impact points the scatter in the experimental results was captured.

The results from this study indicate that applying this combination of discrete particles and finite elements can be helpful in engineering design processes and serve as a useful tool for research applications.

Part 6

Discrete modeling of low-velocity penetration in sand

In this part, the discrete particle method (DPM) was evaluated and used in numerical simulations of low-velocity penetration in sand. The same dropped-object-rig as used in Part 1 was used to obtain experimental force-penetration depth data. Low-velocity penetration might not be directly relevant for protective structures subjected to impacts by bullets. But toward the end of any penetration event the velocity of the penetrator is low, so we need models that can capture the physics of low-velocity penetration accurately.

Hemispherical, blunt and ogival-nosed penetrators were used in the study. Every test included a mass of approximately 5.0 kg. Sand with a median grain size of 0.95 mm was poured into an aluminum container and placed in the dropped-object-rig. Five experiments with a striking velocity of about 2.5 m/s were done for each nose shape. Five additional experiments were done at a striking velocity of about 5.0 m/s with the hemispherical-nosed impactor. The striking velocity was optically measured in each test and a calibrated load-cell measured the resisting force from the sand during each experiment. These values were numerically integrated to obtain the force-penetration depth curves. The experiments revealed that the shape of the force-penetration depth curve changed dramatically with changing impactor geometry; however, the ultimate penetration depth was almost the same for tests with the same striking velocity.

The impactor and aluminum tube were represented by rigid finite elements in the numerical simulations. 3,200,000 discrete particles were used to model the sand, ensuring that the particle size was close to the median grain size in the experiments. The behavior of the sand during penetration was generally captured by the simulations, but the force was underestimated which meant that the ultimate penetration depths were slightly overestimated. If we consider the numerical results presented in this study along with past ones, the DPM shows great versatility and it can be used in a range of applications: low and high velocity penetration and perforation, blast loading, drilling, pile driving and mine blasts of buried charges.

Other contributions

Contributions related to, but not included in, this thesis

The following studies have been conducted parallel to the work with the thesis, but have for various reasons not been included. They are referenced below.

Holmen, J.K., Johnsen, J., Jupp, S., Hopperstad, O.S., Børvik, T., 2013. Effects of heat treatment on the ballistic properties of AA6070 aluminium alloy. International Journal of Impact Engineering 57, 119–133.

Johnsen, J., Holmen, J.K., Myhr, O.R., Hopperstad, O.S., Børvik, T., 2013. A nano-scale material model applied in finite element analysis of aluminium plates under impact loading. Computational Materials Science 79, 724–735.

Holmen, J.K., Børvik, T., Myhr, O.R., Hopperstad, O.S., 2015. Perforation of welded aluminum extrusions: Numerical prediction and experimental validation. Presented at the 11th International Conference on the Mechanical and Physical Behavior of Materials under Dynamic Loading, DYMAT 2015, Lugano, Switzerland.

Holmen, J.K., Dæhli, L.E.B., Hopperstad, O.S., Børvik, T., 2016. Prediction of ductile failure using a phenomenological model calibrated from micromechanical simulations. Presented at the 21st European Conference on Fracture, ECF 21, Catania, Italy.

4. Concluding remarks

The work in this thesis was mainly experimental and numerical. Little emphasis was put on empirical and analytical modeling. Experiments were designed to serve as a basis of comparison to numerical simulations while still providing useful data to advance the field. The numerical contribution was to use and evaluate rather novel methods to solve the penetration problem.

For metal plates it is clear that the effect of the nose shape is different across the velocity regimes. For impacts on thin plates at low striking velocities ($v_0 \leq 10$ m/s) the perforation capacity was in this thesis found to be highest for the blunt-nosed projectile. In the case of higher striking velocities (200 m/s $\leq v_0 \leq 300$ m/s) the perforation capacity is, according to the literature, highest for the ogival-nosed projectile. The reason for this is that the perforation

mechanism changes when the plate thickness and impact velocity change. A blunt-nosed projectile at low velocity gives significant global deformation in the thin plates which dissipates a considerable amount of energy before the final fracture happens. At high velocities and in thicker plates, the deformation localizes in a thin zone around the circumference of the impactor without any global deformation, dissipating less energy. An ogival-nosed impactor perforates a thin plate immediately after impact almost regardless of impact velocity, inducing less global deformation which in turn dissipates less energy. In the thick plates the ogival-nosed projectile pushes the material in the radial direction (if the material is sufficiently ductile). This requires plastic deformation that dissipates more energy than the intense band of shear in the blunt-nosed impact.

The work in this thesis indicates that layering of plates is not necessarily an advantageous strategy if the goal is to increase the ballistic capacity of a structure. This was seen for ogival and blunt-nosed impactors at low impact velocities and for the 7.62 mm armor piercing bullets at high impact velocities. It was also observed (for high velocities) that if the plates are ductile enough to get some global deformation during penetration, this will counteract the unbeneficial drop in energy dissipation due to layering. However, the literature (e.g. Dey et al., 2007) shows that the ballistic capacity can actually increase with an increasing amount of layers at high impact velocities for blunt-nosed projectiles. Therefore, care must be taken when designing layered protective structures.

This thesis showed that strength is not necessarily the only important parameter for the capacity of plates subjected to impact. The capacity is severely reduced if the target plate suffers from fragmentation; and the amount of fragmentation is a function of the material behavior of the plate, the plate thickness and the velocity and size of the projectile. It seems that fragmentation is more likely to happen if the projectile is large compared to the thickness of the plate. This is not straightforward to capture with standard methods in numerical simulations, but node splitting produced promising results and the perforation mechanisms from the experiments were reproduced with good accuracy.

Applying the discrete particle method (DPM) in numerical simulations of granular media subjected to impact looks promising and experimental results can be reproduced at both low and high impact velocities. Further, the formulation makes the coupling of finite elements and discrete particles relatively straightforward and the complex interactions between the structure and the granular material can be modeled.

Lastly, microstructural modeling seems to be a promising strategy in the preliminary design phase of not only protective structures, but all structures. This thesis shows that by applying purely numerical methods, the response of a welded aluminum extrusion subjected to ballistic impact can be predicted with reasonable accuracy. The experimental part of the study revealed that the heat affected zone that results from welding aluminum does not reduce the ballistic limit velocity by more than 10 %.

5. Further work

While working with this thesis several topics of further work were identified. The topics are either needed to advance the subject, or they are interesting studies to illuminate rather mature fields.

Node splitting should be investigated further. This thesis presents some introductory simulations and comparisons to element erosion with rather coarse meshes and simple models. In the future, more refined meshes or even unstructured meshes should be used. In the latter case we might be able to describe the crack propagation even better. It transpires that the node-splitting algorithm is sensitive to numerical noise when the crack direction is defined to be perpendicular to the major principal stress. If we could implement a method where this was remedied it would be a major advantage in predicting correct crack path. Combining node splitting with element erosion could also give very useful models; we can for instance imagine coupling of an energy-based fracture criterion with element erosion and a stress-based fracture criterion with node splitting.

The emphasis of this thesis has been impact, penetration, and perforation problems. These are often local phenomena and the main problem to solve is how the material behaves. Although, in real life situations, and especially in protective design, projectile impact will not be the only load subjected to the structure. Explosions are likely to accompany the projectiles, or maybe even be the cause of fragments that strike the structure. A systematic study of the interaction between blast loading and projectile impact on different structural solutions would be of great value. So would an investigation into the potential of existing numerical codes to simulate such complex problems. This would highlight shortcomings in simulations tools and also provide valuable input to how to optimize protective structures to resist all types of loading.

As computer power has increased tremendously in the last decades there is a growing desire to limit the use of experiments due to cost and achievability. Full scale testing of structures

subjected to extreme loads is hard to perform, sometimes impossible. An ultimate goal is to be able to design a complete protective structure with no experimental data, meaning that the constitutive relation and fracture criterion must be numerically determined with reasonable confidence. Aluminum alloys are most likely the materials for which this can happen first. Relatively comprehensive studies have recently been conducted with this in mind (Johnsen et al., 2013; Holmen et al., 2015). A natural continuation of the work is to utilize micromechanical simulations, or so-called unit-cell models, to calibrate a failure criterion. This was attempted in Holmen et al. (2016b), but further work is needed.

The effects of anisotropy are often neglected in ballistic studies, and modeling and simulation of anisotropic material behavior is more challenging than assuming isotropy. The case of anisotropic fracture should especially be studied. For example, the material orientation from which the failure criterion is based could affect the prediction of fragmentation.

Further experimental and numerical studies regarding the fragmentation of plates and its influence on the perforation capacity should be conducted. It would be interesting to conduct a systematic experimental and numerical study where the transition from target fragmentation to projectile fragmentation is studied. This would be a natural continuation of much of the research conducted at SIMLab in the last years, including this thesis. Experimental facilities and numerical techniques like node splitting need to be joined with expertise in constitutive and fracture modeling to solve this complex problem.

6. References

- Anderson, Jr., C.E., Bodner, S.R., 1988. Ballistic impact: The status of analytical and numerical modeling. *International Journal of Impact Engineering* 7, 9–35.
- Arias, A., Rodríguez-Martínez, J.A., Rusinek, A., 2008. Numerical simulations of impact behavior of thin steel plates subjected to cylindrical, conical and hemispherical non-deformable projectiles. *Engineering Fracture Mechanics* 75, 1635–1656.
- Aune, V., Fagerholt, E., Hauge, K.O., Langseth, M., Børvik, T., 2016a. Experimental study on the response of thin aluminium and steel plates subjected to airblast loading. *International Journal of Impact Engineering* 90, 106–121.
- Aune, V., Valsamos, G., Casadei, F., Larcher, M., Langseth, M., Børvik, T., 2016b. Numerical study on the structural response of blast-loaded thin aluminium and steel plates. *International Journal of Impact Engineering*. Article in press.

- Backman, M.E., Goldsmith, W., 1978. The mechanics of penetration of projectiles into targets. *International Journal of Engineering Science* 16, 1–99.
- Bai, Y., Wierzbicki, T., 2004. A new model of metal plasticity and fracture with pressure and Lode dependence. *International Journal of Plasticity* 24, 1071–1096.
- Bai, Y., Wierzbicki, T., 2010. Application of extended Mohr-Coulomb criterion to ductile fracture. *International Journal of Fracture* 161, 1–20.
- Bresciani, L.M., Manes, A., Romano, T.A., Iavarone, P., Giglio, M., 2016. Numerical modelling to reproduce fragmentation of a tungsten heavy alloy projectile impacting a ceramic tile: Adaptive solid mesh to the SPH technique and the cohesive law. *International Journal of Impact Engineering* 87, 3–13.
- Børvik, T., Langseth, M., Hopperstad, O.S., Malo, K.A., 1999. Ballistic penetration of steel plates. *International Journal of Impact Engineering* 22, 855–886.
- Børvik, T., Hopperstad, O.S., Berstad, T., Langseth, M., 2001a. A computational model of viscoplasticity and ductile damage for impact and penetration. *European Journal of Mechanics A/Solids* 20, 685–712.
- Børvik, T., Hopperstad, O.S., Berstad, T., Langseth, M., 2001b. Numerical simulation of plugging failure in ballistic penetration. *International Journal of Solids and Structures* 38, 6241–6264.
- Børvik, T., Clausen, A.H., Eriksson, M., Berstad, T., Hopperstad, O.S., Langseth, M., 2005. Experimental and numerical study on the perforation of AA6005-T6 panels. *International Journal of Impact Engineering* 32, 35–64.
- Børvik, T., Dey, S., Clausen, A.H., 2009. Perforation resistance of five different high-strength steel plates subjected to small-arms projectiles. *International Journal of Impact Engineering* 36, 948–964.
- Børvik, T., Olovsson, L., Dey, S., Langseth, M., 2011a. Normal and oblique impact of small arms bullets on AA6082-T4 aluminium protective plates. *International Journal of Impact Engineering* 38, 577–589.
- Børvik, T., Olovsson, L., Hanssen, A.G., Dharmasena, K.P., Hansson, E., Wadley, H.N.G., 2011b. A discrete particle approach to simulate the combined effect of blast and sand impact loading of steel plates. *Journal of the Mechanics and Physics of Solids* 59, 940–958.
- Børvik, T., Dey, S., Olovsson, L., 2015. Penetration of granular materials by small-arms bullets. *International Journal of Impact Engineering* 75, 123–139.
- Camacho, G.T., Ortiz, M., 1996. Computational modeling of impact damage in brittle materials. *International Journal of Solids and Structures* 33, 2899–2938.
- Chocron, S., Erice, B., Anderson, C.E., 2011. A new plasticity and failure model for ballistic application. *International Journal of Impact Engineering* 38, 755–764.

- Cockcroft, M.G., Latham, D.J., 1968. Ductility and workability of metals. *Journal of the Institute of Metals* 96, 33–39.
- Corbett, G.G., Reid, S.R., Johnson, W., 1996. Impact loading of plates and shells by free-flying projectiles: A review. *International Journal of Impact Engineering* 18, 141–230.
- Cundall, P.A., Strack, O.D.L., 1979. A discrete numerical model for granular assemblies. *Géotechnique* 1, 47–65.
- Cundall, P.A., 2001. A discontinuous future for numerical modelling in geomechanics?, in: *Proceedings of the Institution of Civil Engineers – Geotechnical Engineering* 149, pp. 41–47.
- Deshpande, V.S., McMeeking, R.M., Wadley, H.N.G., Evans, A.G., 2009. Constitutive model for predicting dynamic interactions between soil ejecta and structural panels. *Journal of the Mechanics and Physics of Solids* 57, 1139–1164.
- Dey, S., Børvik, T., Hopperstad, O.S., Langseth, M., 2006. On the influence of fracture criterion in projectile impact of steel plates. *Computational Materials Science* 38, 176–191.
- Dey, S., Børvik, T., Teng, X., Wierzbicki, T., Hopperstad, O.S., 2007. On the ballistic resistance of double-layered steel plates: An experimental and numerical investigation. *International Journal of Solids and Structures* 44, 6701–6723.
- Dey, S., Børvik, T., Hopperstad, O.S., 2011. Computer-aided design of protective structures: Numerical simulations and experimental validation. *Applied Mechanics and Materials* 82, 686–691.
- Erice, B., Gálvez, F., Cendón, D.A., Sánchez-Gálvez, V., 2012. Flow and fracture behaviour of FV535 steel at different triaxialities, strain rates and temperatures. *Engineering Fracture Mechanics* 79, 1–17.
- Erice, B., Gálvez, F., 2014. A coupled elastoplastic-damage constitutive model with Lode angle dependent failure criterion. *International Journal of Solids and Structures* 51, 93–110.
- Erice, B., Pérez-Martín, M.J., Gálvez, F., 2014. An experimental and numerical study of ductile failure under quasi-static and impact loadings of Inconel 718 nickel-base superalloy. *International Journal of Impact Engineering* 69, 11–24.
- Flores-Johnson, E.A., Saleh, M., Edwards, L., 2011. Ballistic performance of multi-layered metallic plates impacted by a 7.62-mm APM2 projectile. *International Journal of Impact Engineering* 38, 1022–1032.
- Forrestal, M.J., Rosenberg, Z., Luk, V.K., Bless, S.J., 1987. Perforation of aluminum plates with conical-nosed rods. *Journal of Applied Mechanics* 54, 230–232.
- Forrestal, M.J., Luk, V.K., Brar, N.S., 1990. Perforation of aluminum armor plates with conical-nose projectiles. *Mechanics of Materials* 10, 97 – 105.

- Forrestal, M.J., Luk, V.K., Rosenberg, Z., Brar., N.S., 1992. Penetration of 7075-T651 aluminum targets with ogival-nose projectiles. *International Journal of Solids and Structures* 29, 1729–1736.
- Forrestal, M.J., Warren, T.L., 2009. Perforation equations for conical and ogival nose rigid projectiles into aluminum target plates. *International Journal of Impact Engineering* 36, 220–225.
- Gilioli, A., Manes, A., Giglio, M., Wierzbicki, T., 2015. Predicting ballistic impact failure of aluminium 6061-T6 with the rate-independent Bao-Wierzbicki fracture model. *International Journal of Impact Engineering* 76, 207–220.
- Gruben, G., Hopperstad, O.S., Børvik, T., 2012. Evaluation of uncoupled ductile fracture criteria for the dual-phase steel Docol 600DL. *International Journal of Mechanical Sciences* 62, 133–146.
- Gupta, N.K., Iqbal, M.A., Sekhon, G.S., 2007. Effect of projectile nose shape, impact velocity and target thickness on deformation behavior of aluminum plates. *International Journal of Solids and Structures* 44, 3411–3439.
- Gupta, N.K., Iqbal, M.A., Sekhon, G.S., 2008. Effect of projectile nose shape, impact velocity and target thickness on the deformation behavior of layered plates. *International Journal of Impact Engineering* 35, 37–60.
- Holloman, R.L., Deshpande, V.S., Wadley, H.N.G., 2015a. Impulse transfer during sand impact with a solid block. *International Journal of Impact Engineering* 76, 98–117.
- Holloman, R.L., Deshpande, V.S., Wadley, H.N.G., 2015b. Impulse transfer during sand impact with a cellular structure. *International Journal of Impact Engineering* 82, 36–58.
- Holmen, J.K., Johnsen, J., Jupp, S., Hopperstad, O.S., Børvik, T., 2013. Effects of heat treatment on the ballistic properties of AA6070 aluminium alloy. *International Journal of Impact Engineering* 57, 119–133.
- Holmen, J.K., Børvik, T., Myhr, O.R., Fjær, H.G., Hopperstad, O.S., 2015. Perforation of welded aluminum components: Microstructure-based modeling and experimental validation. *International Journal of Impact Engineering* 84, 96–107.
- Holmen, J.K., Johnsen, J., Hopperstad, O.S., Børvik, T., 2016a. Influence of fragmentation on the capacity of aluminum alloy plates subjected to ballistic impact. *European Journal of Mechanics A/Solids* 55, 221–233.
- Holmen, J.K., Dæhli, L.E.B., Hopperstad, O.S., Børvik, T., 2016b. Prediction of ductile failure using a phenomenological model calibrated from micromechanical simulations. *Procedia Structural Integrity* 2, 2543–2549.

- Iqbal, M.A., Gupta, G., Diwakar, A., Gupta, N.K., 2010a. Effect of projectile nose shape on the ballistic resistance of ductile targets. European Journal of Mechanics A/Solids 29, 683–694.
- Iqbal, M.A., Chakrabarti, A., Beniwal, S., Gupta, N.K., 2010b. 3D numerical simulations of sharp nosed projectile impact on ductile targets. International Journal of Impact Engineering 37, 185–195.
- Iskander, M., Bless, S.J., Omidvar, M., 2015. Rapid Penetration into Granular Media, Elsevier Inc., Amsterdam, Netherlands.
- Johnsen, J., Holmen, J.K., Myhr, O.R., Hopperstad, O.S., Børvik, T., 2013. A nano-scale material model applied in finite element analysis of aluminium plates under impact loading. Computational Materials Science 79, 724–735.
- Johnson, G.R., Cook, W.H., 1983. A constitutive model and data for metals subjected to large strains high strain rates and high temperatures, in: Proceedings of the 7th International Symposium on Ballistics, The Hague, pp. 541–547.
- Johnson, G.R., Cook, W.H., 1985. Fracture characteristics of three metals subjected to various strains, strain rates, temperatures and pressures. Engineering Fracture Mechanics 21, 31–48.
- Johnson, G.R., Stryk, R.A., Beissel, S.R., 1996. SPH for high velocity impact computations. Computer Methods in Applied Mechanics and Engineering 139, 347–373.
- Johnson, G.R., Beissel, S.R., Gerlach, C.A., 2015. A 3D combined particle-element method for intense impulsive loading computations involving severe distortions. International Journal of Impact Engineering 84, 171–180.
- Jonas, G.H., Zukas, J.A., 1978. Mechanics of penetration: Analysis and experiment. International Journal of Engineering Science 16, 879–903.
- Komori, K., 2001. Simulation of shearing by node separation method. Computers & Structures 79, 197–207.
- Manes, A., Lumassi, D., Giudici, L., Giglio, M., 2013. An experimental-numerical investigation on aluminium tubes subjected to ballistic impact with soft core 7.62 ball projectiles. Thin-Walled Structures 73, 68–80.
- Manes, A., Serpellini, F., Pagani, M., Saponara, M., Giglio, M., 2014. Perforation and penetration of aluminium target plates by armour piercing bullets. International Journal of Impact Engineering 69, 39–54.
- Olovsson, L., Hanssen, A.G., Børvik, T., Langseth, M., 2010. A particle-based approach to close-range blast loading. European Journal of Mechanics A/Solids 29, 1–6.
- Olovsson, L., Limido, J., Lacome, J.-L., Hanssen, A.G., Petit, J., 2015. Modeling fragmentation with new higher order finite element technology and node splitting. EJP Web of Conferences 94, 1–6.

- Omidvar, M., Iskander, M., Bless, S.J., 2014. Response of granular media to rapid penetration. *International Journal of Impact Engineering* 66, 60–82.
- Oñate, E., Rojek, J., 2004. Combination of discrete element and finite element methods for dynamic analysis of geomechanics problems. *Computer Methods in Applied Mechanics and Engineering* 193, 3087–3128.
- Oñate, E., Zárate, F., Miquel, J., Santasusana, M., Celigueta, M.A., Arrufat, F., Gandikota, R., Valiullin, K., Ring, L., 2015. A local constitutive model for the discrete element method. Application to geomaterials and concrete. *Computational Particle Mechanics* 2, 139–160.
- Rakvåg, K.G., Børvik, T., Hopperstad, O.S., 2014. A numerical study on the deformation and fracture modes of steel projectiles during Taylor bar impact tests. *International Journal of Solids and Structures* 51, 808–821.
- Rosenberg, Z., Forrestal, M.J., 1988. Perforation of aluminum plates with conical-nosed rods – additional data and discussion. *Journal of Applied Mechanics* 55, 236–238.
- Rosenberg, Z., Dekel, E., 2009. On the deep penetration and plate perforation by rigid projectiles. *International Journal of Solids and Structures* 46, 4169–4180.
- Rosenberg, Z., Dekel, E., 2010. Revisiting the perforation of ductile plates by sharp-nosed rigid projectiles. *International Journal of Solids and Structures* 47, 3022–3033.
- Ruggiero, A., Iannitti, G., Testa, G., Limido, J., Lacome, J.L., Olovsson, L., Ferraro, M., Bonora, N., 2014. High strain rate fracture behavior of fused silica. *Journal of Physics: Conference series* 500, 1–4.
- Teng, X., Wierzbicki, T., 2006. Evaluation of six fracture models in high velocity perforation. *Engineering Fracture Mechanics* 73, 1653–1678.
- Teng, X., Dey, S., Børvik, T., Wierzbicki, T., 2007. Protection performance of double-layered metal shields against projectile impact. *Journal of Mechanics of Materials and Structures* 2, 1309–1330.
- Wadley, H.N.G., Børvik, T., Olovsson, L., Wetzel, J.J., Dharmasena, K.P., Hopperstad, O.S., Deshpande, V.S., Hutchinson, J.W., 2013. Deformation and fracture of impulsively loaded sandwich panels. *Journal of the Mechanics and Physics of Solids* 61, 674–699.
- Xu, X.-P., Needleman, A., 1994. Numerical simulations of fast crack growth in brittle solids. *Journal of the Mechanics and Physics of Solids* 42, 1397–1434.
- Zukas, J.A., 1990. *High Velocity Impact Dynamics*, 1st edition, John Wiley & Sons, Inc.

Part 1

Jens Kristian Holmen, Odd Sture Hopperstad, Tore Børvik

Low-velocity impact on multi-layered dual-phase steel plates

International Journal of Impact Engineering 78 (2015) 161–177.



Low-velocity impact on multi-layered dual-phase steel plates



Jens Kristian Holmen*, Odd Sture Hopperstad, Tore Børvik

Structural Impact Laboratory (SIMLab), Centre for Research-based Innovation (CRI), Department of Structural Engineering, Norwegian University of Science and Technology, NO-7491 Trondheim, Norway

ARTICLE INFO

Article history:
Received 12 September 2014
Received in revised form
15 December 2014
Accepted 17 December 2014
Available online 8 January 2015

Keywords:
Perforation
Experimental validation
3D-DIC
Finite element analysis
IMPETUS Afea Solver

ABSTRACT

In this paper an experimental program investigating the behavior of monolithic and multi-layered configurations of 0.8 mm and 1.8 mm medium-strength steel plates is presented. We have considered impacts by blunt-ended and ogival-ended impactors in the low-velocity regime ($\leq 16 \text{ m/s}$). Experimental outputs include measurements of force and velocity, and deformation fields. Force and velocity readings were provided by a strain-gauge instrumented striker, while digital image correlation was used to obtain the displacement field from the rear side of the bottom plate. For the 0.8 mm plates a near linear relationship between the number of layers and the ballistic limit velocity was found. The plates' resistance against perforation was found to be higher for the blunt-ended impactor than for the ogival-ended impactor. This can be explained by the failure mechanisms. The monolithic plates have a higher capacity than layered plates with the same total thickness: this is particularly clear for plates struck by the ogival-ended impactor. The experiments provide ample data to validate the subsequent 3D numerical simulations. The analysis model is double-symmetric in simulations using the ogival-ended impactor, while only a 10° slice of the plate and impactor is needed in simulations using the blunt-ended impactor. A thermelastic–thermoviscoplastic constitutive relation combined with the Cockcroft–Latham criterion for failure is implemented in IMPETUS Afea Solver, and used in all simulations. The simulations predict the failure modes fairly well, and the numerical results are within the range seen in previous publications. Sensitivity studies regarding friction, mesh refinement, thermal formulation and strain-rate dependence are conducted and discussed.

© 2015 Elsevier Ltd. All rights reserved.

1. Introduction

Numerous factors influence the penetration and perforation processes in structural impact events, and for each of these factors there are several approaches to investigating the different effects. Impact loading of plates has for a long time been of interest, and the mechanisms of penetration and perforation of different layer configurations due to impact from various projectile shapes are well documented, especially for relatively thick targets, see e.g. Refs. [1–4]. More recently, Kpenyigba et al. [5] used 30 g projectiles and 100 mm spanned thin steel plates to perform an experimental, analytical and numerical study on the influence of projectile shape in impact events. It was found that the capacity of plates subjected to impact by hemispherical-ended penetrators is larger than that of plates struck by ogival-ended penetrators and blunt-ended penetrators. A similar numerical study was performed using 52.5 g

penetrators by Iqbal et al. [6] where the results indicate a positive correlation between increased target span and ballistic limit. The study indicated that a plate can resist impacts by blunt-ended penetrators better than impacts by ogival-ended penetrators. For the smallest span, however, the opposite was found, showing that a plate's capacity is highly dependent on its configuration. Monolithic targets were found to be stronger than layered targets in contact and layered targets with spacing.

The effect of projectile shape, impact velocity and target configuration on the perforation behavior of thin aluminum plates was studied by Gupta et al. [7]. They found that the plates resisted impacts by hemispherical projectiles better than they resisted impacts from blunt and ogival-shaped projectiles. The double-layered plates performed equally well as the monolithic plates, but a further increase in layers impaired the total capacity. The same authors published another paper where the results from numerical simulations were shown to be sensitive to the mesh refinement [8]. The ballistic properties of blunt and hemispherical projectiles were also studied. Similar to Ref. [7] the plates' capacity against hemispherical projectile impact was found to be the highest.

* Corresponding author. Tel.: +47 73 59 52 02.
E-mail address: jens.k.holmen@ntnu.no (J.K. Holmen).

Table 1

Nominal chemical composition of Docol 600DL steel in wt-% [17].

C	Si	Mn	P	S	Al _{tot}	Fe
0.10	0.40	1.50	0.010	0.002	0.040	Balance

Work conducted by Woodward and Cimpoeru [9] on the high-velocity perforation processes in monolithic and layered aluminum plates revealed that the ballistic limit of plates struck by conical-shaped projectiles is higher than that of plates struck by flat-ended projectiles. This was found to be independent of the target configuration. The transition from ejection of a target plug for a thick plate to dishing and stretching dominated energy absorption for thinner plates was discussed.

Dey et al. [10] conducted a large experimental and numerical study on the ballistic perforation resistance of monolithic and double-layered Weldox 700E steel plates. Blunt-ended and ogival-ended projectiles were considered. They found that for blunt-ended projectiles a double-layered configuration of 2 × 6 mm performed much better than a monolithic 12 mm configuration. The opposite was found for ogival-ended projectiles, where the monolithic plates performed slightly better than the double-layered configuration. However, the overall protection level increased for layered targets, since the plates' initial perforation capacity using ogival-ended projectiles was considerably higher than the capacity for blunt-ended projectile impact.

Ben-Dor et al. [11] published a review paper in 2012 that gave an overview of some of the most important work regarding layering of target plates in impact engineering. They stated that layering of plates commonly leads to a degradation of ballistic properties and that increasing the velocity reduces the effect of layering. Conclusions from the study highlight the complexity of the problem and that more research is needed to improve our understanding of how target configuration affects the penetration and perforation behavior of protective structures. Further studies concerning low and medium velocity impact are available in the literature (e.g. Refs. [12–16]), however, relatively few systematic studies of the effect of projectile shape and layering of thin plates exist. In general, the large number of parameters involved in the penetration and perforation process of layered plates makes it hard to draw definitive conclusions. Varying the span, projectile shape, projectile weight, impact velocity, target material, angle of incidence etc., will inevitably affect the result. It is thus important to establish reliable and validated numerical models in order to study this problem in a systematic way.

In this study, the response of monolithic and multi-layered steel plates subjected to projectile impact in the low-velocity regime is investigated. Configurations consisting of up to four target plates are considered. No adhesives are applied prior to testing, but the plates are in physical contact at the beginning of each test. A dropped-objects-rig is used to strike the targets using blunt-ended and ogival-ended cylindrical impactors. To assess the accuracy of subsequent finite element simulations and to get a better physical understanding of the impact process, digital image correlation (DIC) is used in most of the experiments. Ballistic limit velocities are reported for all configurations.

2. Target and impactor materials

Thin plates made of the medium-strength, high-hardening steel Docol 600DL were chosen for this study. The nominal chemical composition of the material can be found in Table 1. The steel has been heat treated to obtain a dual-phase structure of ductile ferrite and strong martensite where the content of martensite determines the strength of the material. All the plates were produced and delivered by Swedish Steel Ltd. (SSAB). Nominal mechanical properties for the direction transverse to the rolling direction are provided: the yield strength is reported to be between 280 MPa and 360 MPa, while the tensile strength is reported to be between 600 MPa and 700 MPa [17]. Plates of thicknesses 0.8 mm and 1.8 mm are used in the experimental program described in Section 3. In this study, the tensile testing and subsequent material characterization are only performed for the 0.8 mm thick plates.

Tensile tests were conducted at angles 0°, 45° and 90° with respect to the rolling direction of the plate using both an extensometer and DIC functionality [18]. Standard dog-bone specimens with a 70 mm gauge area were used, see Ref. [19] for the geometry. To ensure repeatability, three specimens were tested in each direction. All tests were carried out with a cross-head velocity of 2.0 mm/min which corresponds to an approximate initial strain rate of $5 \times 10^{-4} \text{ s}^{-1}$. Fig. 1a shows that the material is nearly isotropic with respect to flow stress, but with slight variations in elongation at failure, which is further highlighted in Fig. 2a where the strain at incipient fracture based on DIC measurements is shown as a function of test orientation. As seen, some variation of fracture strain is observed, especially in the 45° direction. Grytten et al. [20] showed that plastic anisotropy is practically insignificant for low-velocity perforation problems. Thus, the limited plastic anisotropy found from the material tests in this study can be

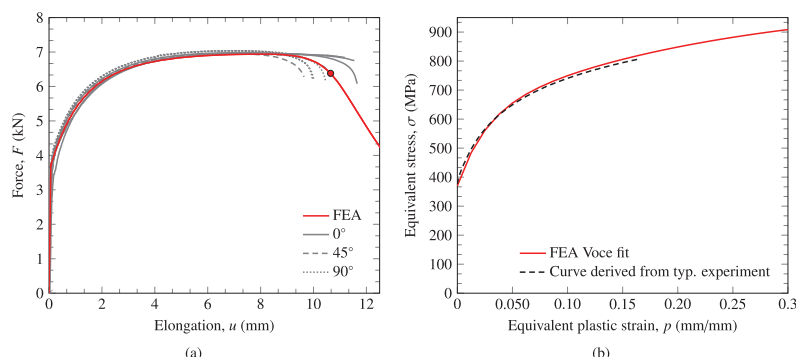


Fig. 1. (a) Force-elongation curves from DIC-measurements with 40 initial gauge-length and the corresponding finite element solution. The circle denotes the assumed point of fracture in the calculation of W_{cr} . (b) Equivalent stress-equivalent plastic strain curves for the representative uniaxial tensile test (until necking), and the optimized extended Voce hardening rule with parameters shown in Table 5.

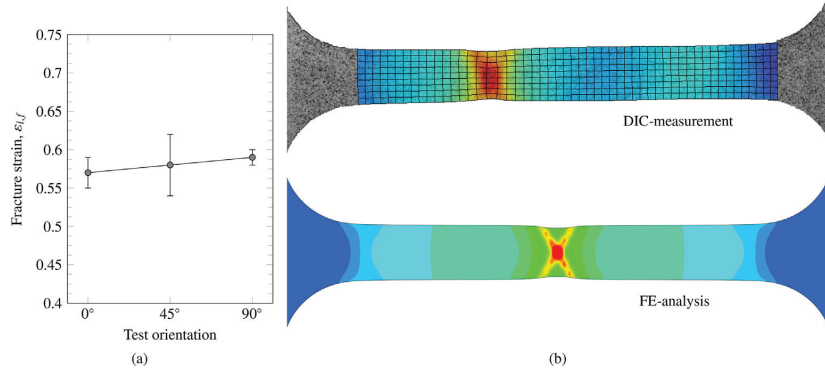


Fig. 2. (a) The logarithmic surface strain at incipient fracture ε_{lf} taken from DIC measurements for the three different directions. (b) Comparison of the surface strain in a DIC measurement and a corresponding finite element model of a tensile test at incipient fracture. The fringes are in the range from 0 (blue) to 0.5 (red). (For interpretation of the references to color in this figure legend, the reader is referred to the web version of this article.)

ignored and we can safely adopt an isotropic yield function in the material modeling described in Section 5.

The impactors were made of hardened steel with a nominal yield stress $\sigma_0 = 1900$ MPa, fracture strain of about 2.15%, and a Young's modulus $E = 204,000$ MPa [21].

3. Experimental work

3.1. Test set-up

Two impactor shapes were considered in this study: a blunt-ended impactor, and an ogival-ended impactor with a caliber radius head (CRH) of 3 - see Ref. [22] for an explanation. Their respective geometries are shown in Fig. 3. They were machined from the same generic projectiles which have been used in several previous research programs on ballistic impact (see e.g. Refs. [21,23]). All of the experiments reported in this paper were done in an Instron CEAST 9350 dropped-objects-rig with a maximum kinetic energy of 1800 J [24]. We used the standard instrumented striker and striker-holder and these have a combined mass of 5.735 kg. By including the impactors and 4 kg additional weights we achieved a total mass of approximately 10 kg (9.82 kg

and 9.78 kg for the blunt-ended and ogival-ended impactors respectively). For all practical purposes this means that a constant mass was applied regardless of the impactor shape (the difference is only 0.4%). The dropped-objects-rig permits velocities ranging from 0 m/s to 15.5 m/s for masses of approximately 10 kg [24].

Fig. 4 shows how the square target plates of dimensions 400 mm \times 400 mm \times 0.8 mm were clamped in a circular frame with an inner diameter (span) of 300 mm, ensuring fixed boundary conditions. Clamping was obtained by using 12 equidistant M12 bolts to confine the target plates between two circular frames and to fix this to the dropped-objects-rig. The instrumented striker

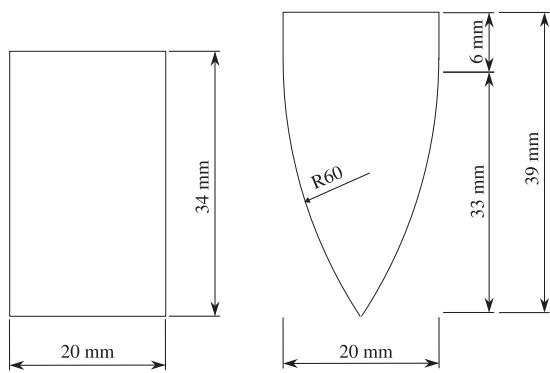


Fig. 3. Geometry of the impactors. The ogival-ended impactor has a caliber radius head (CRH) of 3.

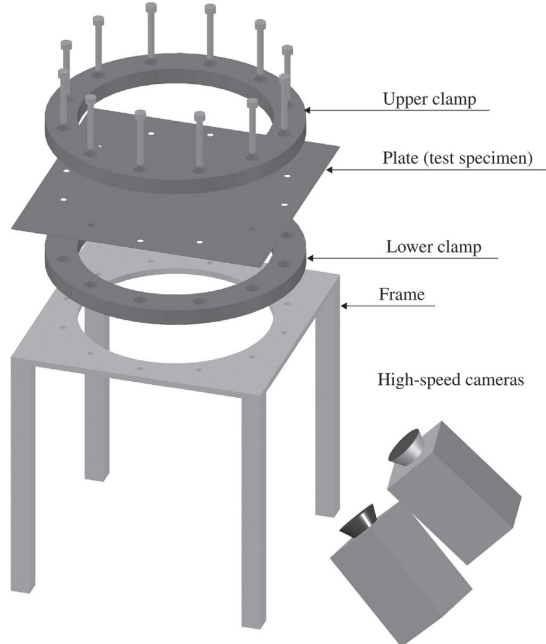


Fig. 4. Illustration of the test set-up and camera placement.

Table 2

Number of impact experiments conducted in this study as a function of impactor shape, plate thickness and layer configuration.

Plate thickness	Blunt-ended				Ogival-ended			
	1 plate	2 plates	3 plate	4 plates	1 plate	2 plates	3 plate	4 plates
0.8 mm	4	4	5	4	4	4	4	4
1.8 mm	4	1	—	—	6	1	—	—

measured the force at discrete points in time during the experiments. In all tests a load cell with a strain-gauge instrumented tup for interchangeable inserts (in our case blunt-ended and ogival-ended inserts) with a capacity of 90 kN was used. The sensor is placed 150 mm from the tip of the striker. Data was extracted from the sensor every 5×10^{-4} ms. Considering that the experiments last between 15 ms and 25 ms we got from 30,000 to 50,000 data points per experiment.

Table 2 provides an overview of the experiments conducted on the different configurations. The main part of the experimental program involved impact testing of the 0.8 mm plates. A total of 33 successful tests were performed on the various plate-impactor configurations with this plate thickness. We considered finding the ballistic limit velocity for all the configurations as the primary task of the experimental program, so a minimum of four individual tests were conducted on each configuration.

A smaller study was done on thicker plates to compare the ballistic limits from the laminated plates to monolithic plates of approximately the same thickness. 1.8 mm thick Docol 600DL plates were delivered by SSAB and we employed the same experimental procedure for these plates as for the 0.8 mm plates. In total, 12 such impact tests were performed. The mechanical behavior of the 1.8 mm thick plates was characterized by Gruben [25] and they were found to be somewhat weaker than the 0.8 mm plates investigated in the rest of this study (the ductility is hardly

affected). This is probably due to differences in the cold rolling process and is further commented on in Section 4.

3.2. Data processing

The load cell in the dropped-objects-rig provides enough information to calculate accelerations, and subsequently the velocity and energy for each experiment. The striker velocity just before impact was measured optically by the rig, and this velocity is denoted the initial velocity, v_i . Any bias in the force measurements from the load cell was accounted for by subtracting the average of the first 100 data points from each force measurement in the experiment. We find the incremental velocity-change by numerically integrating the acceleration. Finding the current velocity is done by subtracting the incremental velocity-change from the previous velocity,

$$v_{n+1} = v_n - \left(\frac{F_{n+1} + F_n}{2m_p} - g \right) \Delta t \quad (1)$$

where v_{n+1} is the current velocity, v_n is the previous velocity, F_{n+1} is the current force, F_n is the previous force, m_p is the impacting mass, g is the gravitational acceleration, and Δt is the sampling time (typically 5×10^{-4} ms).

3.3. Digital image correlation

We used the 3D digital image correlation (DIC) software *Ecorr* [18] developed at SIMLab to measure the out-of-plane displacement field of the bottom plate as shown in [Figs. 5 and 6](#). From these values we may obtain the strain fields present at the surface of the bottom plate in the experiments [18,19,26]. The software uses images from two synchronized cameras, placed as indicated in [Fig. 4](#), to compare the relative displacement of a specimen at a deformed stage to an undeformed reference stage. Two Phantom v1610 high-

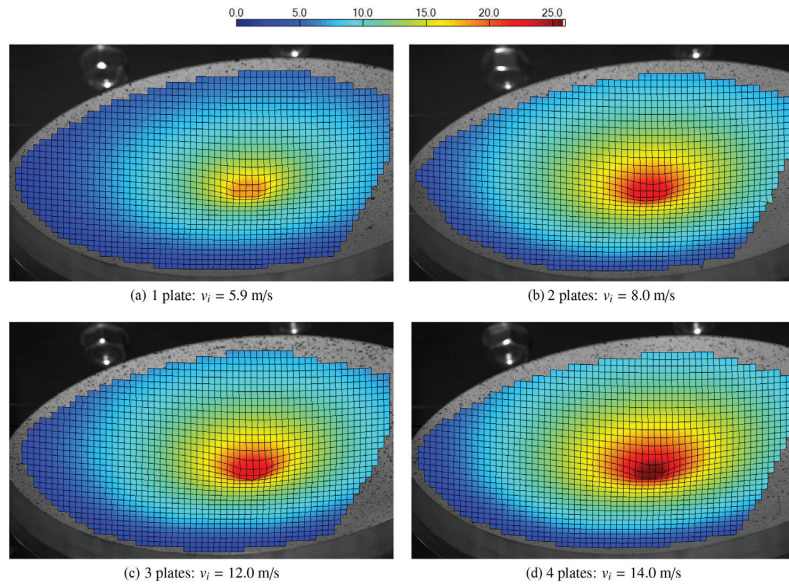


Fig. 5. Deformation profiles based on DIC-measurements just before perforation from tests with the blunt-ended impactor: (a) 1 plate, (b) 2 plates, (c) 3 plates, and (d) 4 plates. Fringe values are given in mm.

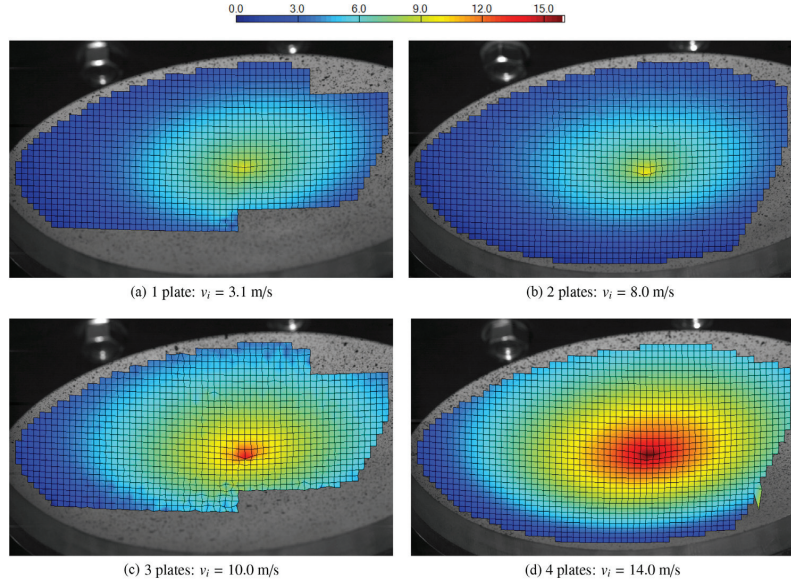


Fig. 6. Deformation profiles based on DIC-measurements just before perforation from tests with the ogival-ended impactor: (a) 1 plate, (b) 2 plates, (c) 3 plates, and (d) 4 plates. Fringe values are given in mm.

speed cameras with a resolution of 1280×800 pixels and a frame rate of 16,000 frames per second were used in this study. Before each test the back side of the bottom plate was spray-painted with a black and white speckle pattern. This substantially improved the results from the DIC analyses due to the increased grey-scale contrast.

4. Experimental results

4.1. Ballistic limit velocities

From the measured initial and residual velocities of each impact test we can determine the ballistic limit velocities and the ballistic

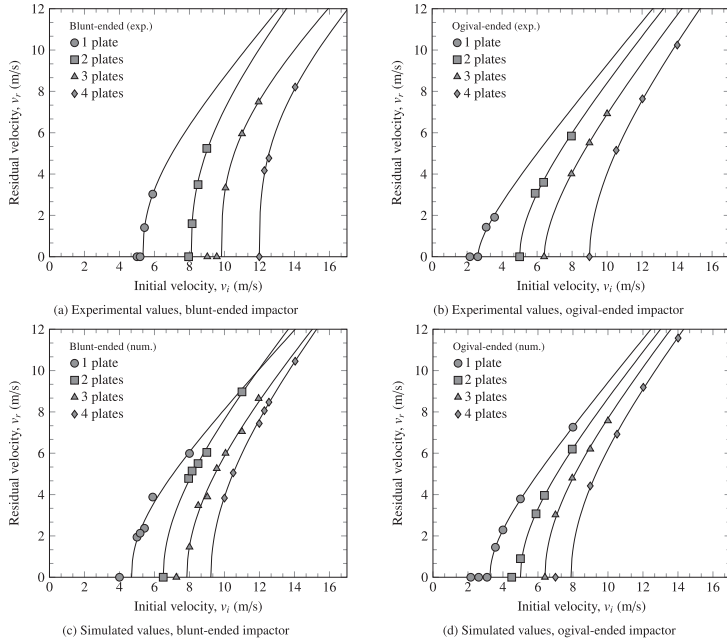


Fig. 7. Ballistic curves from experimental tests with (a) the blunt-ended impactor and (b) the ogival-ended impactor; and ballistic curves from finite element simulations with (c) the blunt-ended impactor (d) the ogival-ended impactor.

Table 3

Ballistic limit velocities, v_{bl} , and the parameters, a and p , of the Lambert equation for the various plate configurations involving 0.8 mm Docol 600DL plates.

Impactor shape	No. of layers	Experimental data			Numerical simulations			Deviation Δv_{bl} (m/s)
		v_{bl} (m/s)	a	p	v_{bl} (m/s)	a	p	
Blunt-ended	1	5.3	0.96	2.43	4.7	0.89	2.24	-0.6
	2	8.1	1.00	2.57	6.5	0.99	2.04	-1.6
	3	9.8	0.83	2.98	7.9	0.93	2.04	-1.9
	4	12.0	0.82	2.91	9.2	0.97	2.05	-2.8
Ogival-ended	1	2.6	1.00	1.63	3.3	1.00	1.97	0.7
	2	5.0	1.00	1.88	5.0	1.00	2.00	0.0
	3	6.4	1.00	1.70	6.4	1.00	2.00	0.0
	4	9.0	1.00	1.88	7.9	1.00	2.02	-1.1

curves for the clamped Docol 600DL steel plates. Impacts with higher initial velocities than the ballistic limit velocity will perforate the target, while impacts with lower initial velocities will be stopped by the plate. Fig. 7a and b shows the ballistic curves for each layer configuration and impactor shape (tabulated data in Table 3). The data points shown are test results directly plotted into the diagram. The solid lines follow a generalized version of the Recht-Ipson model [27], namely the Lambert equation [1], given as

$$v_r = a(v_i^p - v_{bl}^p)^{1/p} \quad (2)$$

where v_{bl} is the ballistic limit velocity; $a \leq 1$ and p are empirical constants. The curves in Fig. 7a and b are the least-squared-error optimizations of Eq. (2) to the experimental results. All the ballistic limit velocities reported were found by performing this type of optimization. Fig. 8a shows the ballistic limit velocities with respect to impactor shape and total plate thickness. An almost linear increase in the ballistic limit velocity is observed with increasing total plate thickness for both impactor-shapes. It is readily seen that the plates have higher capacity against the blunt-ended impactor than they do against the ogival-ended impactor for the impact conditions investigated in this study, also for the single plate configuration. This is contradictory to what is normally obtained for thicker plates at higher impact velocities, see e.g. Refs. [4,10]. Figs. 5 and 6 indicate that this is most likely due to substantially larger global bending in the tests with the blunt-ended impactor which is induced by delayed shear localization and subsequent perforation when the initial velocity is as low as it is in this study.

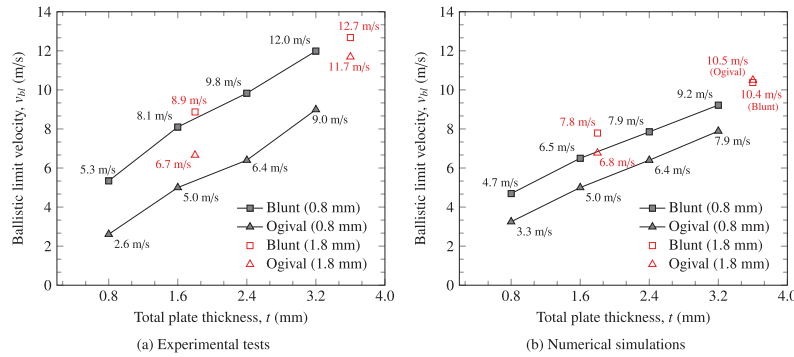


Fig. 8. Ballistic limit velocities from all plate-impactor combinations as a function of the total plate thickness found from (a) the experimental tests and (b) the numerical simulations.

Table 4

Ballistic limit velocities, v_{bl} , and the parameters, a and p , of the Lambert equation for the various plate configurations involving 1.8 mm Docol 600DL plates.

Impactor shape	No. of layers	Experimental data			Numerical simulations			Deviation Δv_{bl} (m/s)
		v_{bl} (m/s)	a	p	v_{bl} (m/s)	a	p	
Blunt-ended	1	8.9	1.00	2.37	7.8	1.00	2.27	-1.2
	2	12.7	1.00	2.00	10.5	1.00	2.00	-2.2
Ogival-ended	1	6.7	1.00	2.05	6.8	1.00	1.93	0.1
	2	11.7	1.00	2.00	10.5	1.00	2.00	-1.2

Fig. 8a also shows the ballistic limits from the experiments conducted on the 1.8 mm plates. These values are tabulated in Table 4. In the case of the monolithic plates, multiple experiments were performed with each impactor shape (again see Table 2) so the previously described procedure could be used to determine the ballistic limit. However, the ballistic limit from the double-layered 1.8 mm thick plates were based on a single experiment conducted with each impactor-shape. By solving Eq. (2) with respect to v_{bl} and assuming $a = 1$ and $p = 2$, we found estimates of the ballistic limits for this configuration. These results give a clear indication that the ballistic limit velocity drops for impacts by ogival-ended impactors when the target is layered compared to monolithic targets. This distinct drop was not seen for blunt-ended impactors.

4.2. Deformation modes

Fig. 9 shows timelapses of typical impact tests and Fig. 10 shows pictures of cross sections taken from tests with four layers. In plates struck by the blunt-ended impactor several energy absorbing modes contributed during perforation. First, a transient phase took place before the supports were activated. Second, global bending and membrane stretching were evident from the relatively large deformations out of the plane for all configurations. In this phase the supports were fully activated [28]. Third, plugs were ejected as a result of shearing and local thinning around the circumference of the impactor. In Fig. 5 we see increased maximum deflection due to global bending and increased plastic deformation around the tip of the impactor as the number of plates is increased, and the highest perforation resistance correlates with the largest global deformation.

Comparing the timelapse provided in Fig. 9a to that in Fig. 9b reveals different deformation modes for different impactor shapes. The differences between layered configurations struck with the

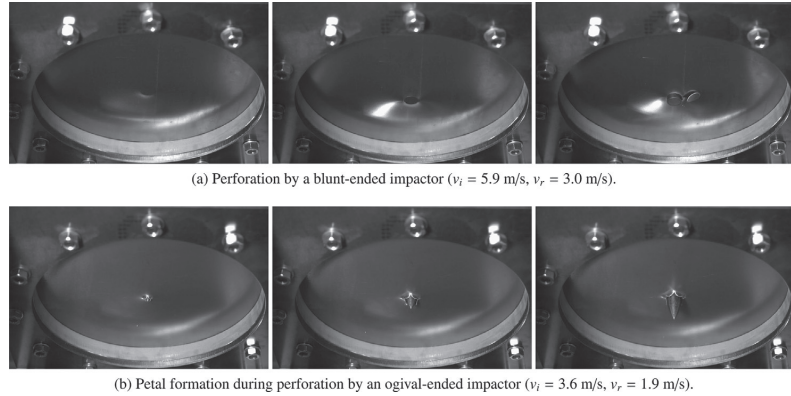


Fig. 9. Timelapses showing perforation of a single 0.8 mm plate by (a) the blunt-ended impactor and (b) the ogival-ended impactor.

ogival-ended impactor are not as pronounced as for the blunt-ended impactor. Every plate showed unmistakable petaling which is frequently observed for thin plates impacted by conical-ended or ogival-ended projectiles at low impact velocities [2]. High radial and circumferential tensile stresses are usually responsible for the formation of a star-shaped crack near the tip of the impactor before the thicker part of the impactor creates the distinct petals [3]. In Fig. 10b we see individual petal patterns in each plate and that the petals seem to be slightly skewed relative to the adjacent plate's petals. There are four petals in each plate in every experiment with the 0.8 mm thick plates.

The DIC field maps in Figs. 5 and 6 show out-of-plane deformation of typical configurations just prior to perforation while Fig. 11a shows the out-of-plane deformation of the same configurations as a function of the radial coordinate. These plots clearly display how the deflection increases with total thickness. They also show that the maximum deflection for the blunt-ended impactor is significantly larger than the corresponding maximum deflections for the ogival-ended impactor. The ogival-ended impactor induces limited global deformation (dishing), but distinct petaling as mentioned above. Additional studies regarding petaling can be

found in previous work by Wierzbicki [29], and Lee and Wierzbicki [30,31].

4.3. Energy considerations

We can directly assess the effectiveness of the protective properties of the plates by comparing the energy spent on perforating the given configuration. Fig. 12 shows the absorbed energy (work) per unit thickness for the experiments conducted in this study. These curves are found by assuming that the difference between the kinetic energy prior to perforation (K_i) and after perforation (K_r) represents the total energy absorption by the plate (W). We now get the expression

$$W = \Delta K = K_i - K_r = \frac{1}{2} m_p (v_i^2 - v_r^2) \quad (3)$$

where m_p is the impacting mass, v_i is the initial velocity, and v_r is the residual velocity. Note that we omit the mass of the ejected plug since it in practice is negligible compared to the impacting mass. It has been stated that the energy required to perforate a given

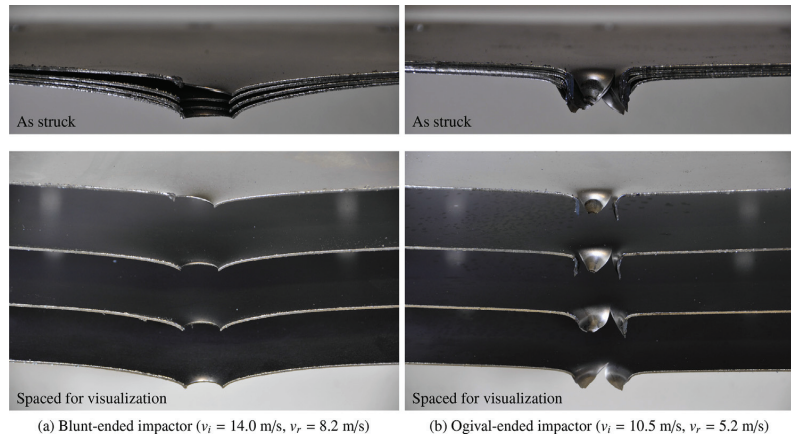


Fig. 10. Post perforation pictures of 0.8 mm quadruple-layered plates: (a) shows plates struck by the blunt-ended impactor while (b) shows plates struck by the ogival-ended impactor. The bottom pictures show the plates with spacing to better illustrate the failure process.

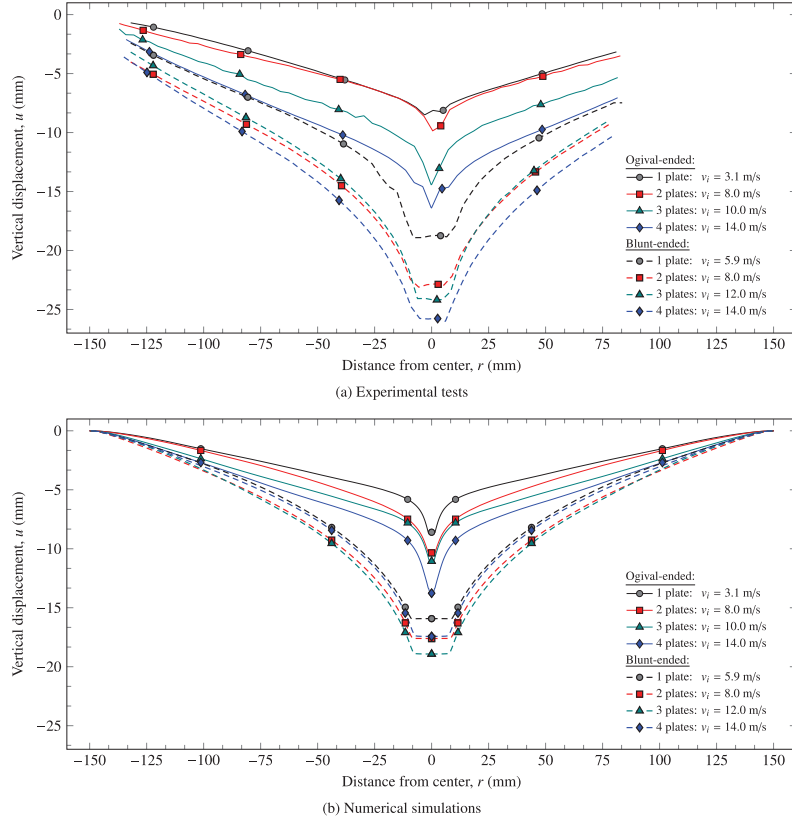


Fig. 11. Deflection profiles extracted just before failure for a selection of experiments: (a) DIC-based from experiments, (b) from the finite element simulations.

configuration is nearly constant for a given projectile, regardless of initial velocity [32]. However, this is not necessarily true for thin plates where the ballistic limit curve does not adhere to the original Recht-Ipson equation (Eq. (2) with $a = 1$ and $p = 2$). The current

series of experiments showed that a near linear relationship between ballistic limit velocity and the number of plates is evident for both impactor-shapes. The same trend is seen for the energy absorption, where the work per unit thickness increases with increasing numbers of layers, especially for the ogival-ended impactor (Fig. 12). This is consistent with the increased global deformation seen in configurations with multiple layers. Iqbal et al. [6] performed a purely numerical study on AA1100-H12 aluminum plates finding that for thin plates ($H/D \ll 1$) ogival-ended projectile impact is more detrimental to the plate than blunt-ended projectile impact (except for very small target spans). Thus, our experimental results coincide with that study.

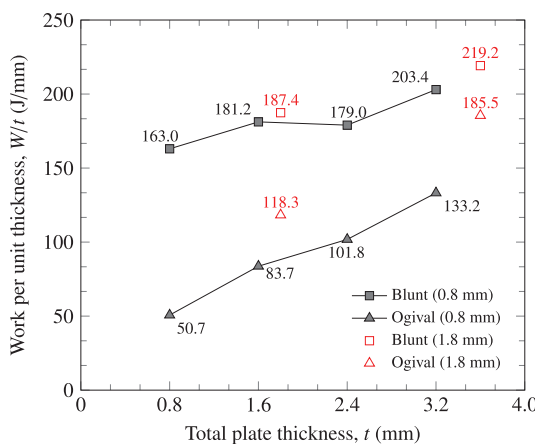


Fig. 12. Average work per unit thickness (W/t) for the different plate-projectile configurations.

4.4. Perforation process

We can analyze the perforation process further by inspecting the force-time plots given in Fig. 13 and Fig. 14. For the tests with the blunt-ended impactor we see in Fig. 13 an initial bending phase, identified as the part of the curve with a steady force increase, before the membrane stretching of the target develops and the force level increases rapidly. This is seen for all plate configurations. When target plate failure occurs we observe an abrupt drop in the force level for each failed plate; this is clearly visible for the single and the double-layered configurations. For the triple-layered and quadruple-layered plates the drop is less clear, but still visible. The force-time curves for the tests with the ogival-ended impactor in

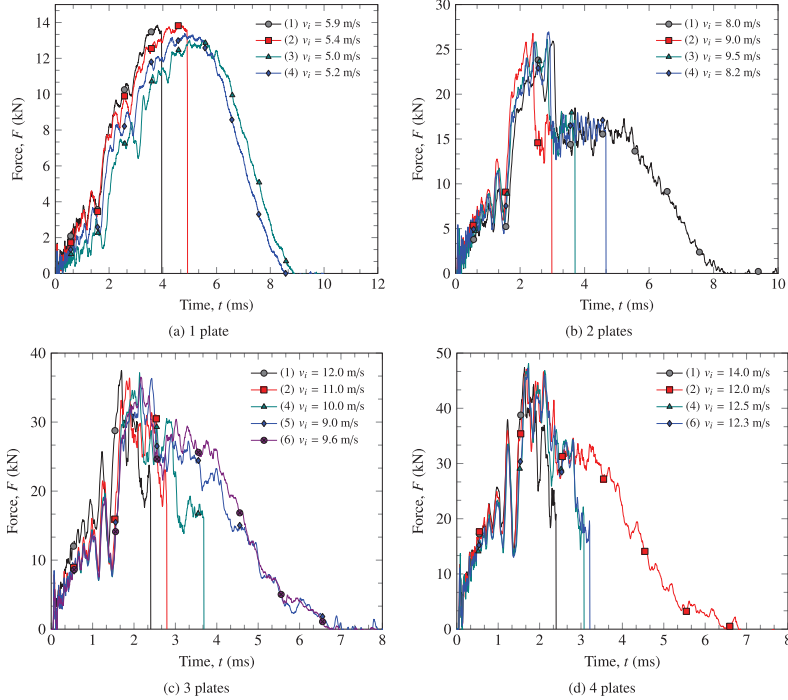


Fig. 13. Force-time curves for experiments carried out with the blunt-ended impactor: (a), (b), (c) and (d) show curves for 1, 2, 3 and 4 plates respectively.

Fig. 14 exhibit a steeper climb (relatively) to the maximum force level, and a less dramatic failure process since the initial plate perforation comes almost instantly after impact and petaling is a gradual process. Comparing **Figs. 13 and 14** reveals major differences in the maximum force level and the duration of the respective impacts for the blunt-ended and ogival-ended impactors. The force-time curves from the tests with the blunt-ended impactor rise quickly to a high force, whereas the force-time curves for the ogival-ended impactor in general display lower forces and a delayed time of complete perforation. Note that the maximum force in each configuration is almost constant and rather insensitive to the initial velocity. This is because the maximum force is determined by a mode change from global bending and membrane stretching to localized indentation/perforation of the target.

Fig. 15 displays some typical velocity–time curves where we see that the point of full perforation is more distinct in the tests with the blunt-ended impactor, identified by the acute angle change just when the residual velocity reaches a constant value.

4.5. Comparison to thicker plates

In **Fig. 8a** the ballistic limit velocities determined from experiments on the 1.8 mm thick plates are compared to the ballistic limits of 0.8 mm plates. The results indicate that the capacity of a monolithic plate exceeds the capacity of layered plates of the same thickness for the ogival-ended impactor. In the case of the blunt-ended impactor the effect of layering is negligible. As previously mentioned the 1.8 mm plates are weaker than (but just as ductile as) the 0.8 mm plates due to cold-rolling conditions, meaning that in reality the monolithic plates are even stronger than what

appears in **Fig. 8a**. Comparing these results to the findings by Dey et al. [10] shows that the velocity regime and failure mode seriously affect the perforation resistance of metal plates, and that these need to be carefully considered in each case. Dey et al. studied high-strength steel plates struck by 0.198 kg projectiles (of the same shape as the impactors considered in this study) with ballistic velocities well above 100 m/s. In high-speed impact problems global effects are less pronounced and the failure modes can deviate significantly from what we see in low-velocity impact. This manifests itself in a more localized failure process at high impact velocities.

5. Target material characterization

5.1. Constitutive modeling

Simulation of impact events such as the ones investigated in this paper requires a material model that accounts for large plastic strains, high strain rates, and temperature softening during plastic flow. Borvik et al. [33] proposed a thermoelastic–thermovisco-plastic constitutive model based on the well-known Johnson–Cook flow stress model. This constitutive relation applied with an extended Voce hardening rule is used in this paper. A brief review of the model is provided in the following.

We assume isotropic material behavior, small elastic strains and no kinematic hardening. However, the plastic strains and rotations can be finite. Thus we can use the J_2 flow theory for pressure insensitive materials. We adopt a hypoelastic formulation for the large deformations and decompose the rate-of-deformation tensor \mathbf{D} additively as

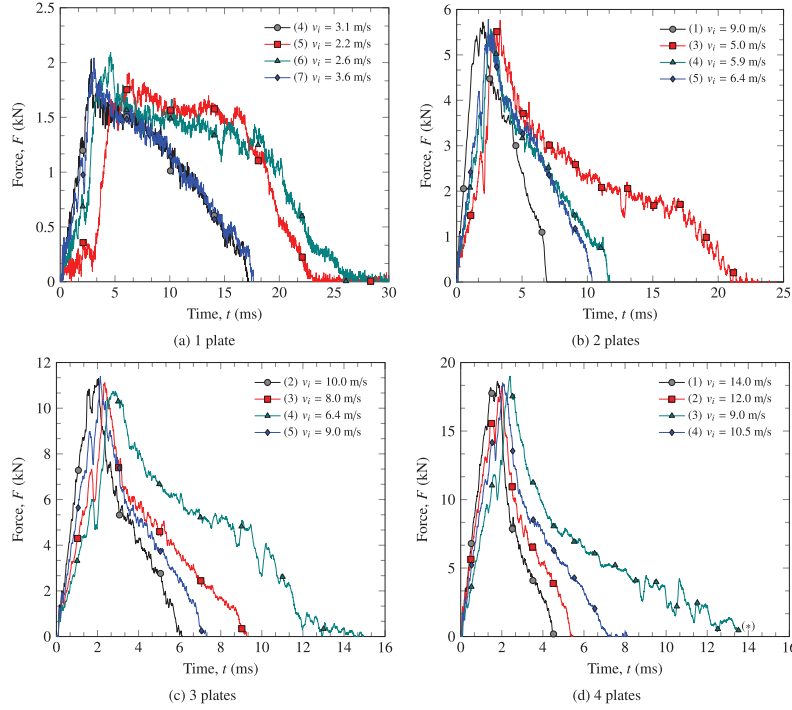


Fig. 14. Force-time curves for experiments carried out with the ogival-ended impactor: (a), (b), (c) and (d) show curves for 1, 2, 3 and 4 plates respectively. (*) This test did not perforate the plate, however, not enough data was acquired to plot the entire curve.

$$\mathbf{D} = \mathbf{D}^e + \mathbf{D}^t + \mathbf{D}^p \quad (4)$$

where \mathbf{D}^e , \mathbf{D}^t and \mathbf{D}^p are the elastic, thermal and plastic parts, respectively. The elastic and thermal parts are defined by

$$\mathbf{D}^e = \frac{1+\nu}{E} \boldsymbol{\sigma}^{\nabla G} - \frac{\nu}{E} \text{tr}(\boldsymbol{\sigma}^{\nabla G}) \mathbf{I}, \quad (5)$$

and

$$\mathbf{D}^t = \alpha \dot{T} \mathbf{I}, \quad (6)$$

where ν and E are elastic constants, $\boldsymbol{\sigma}^{\nabla G}$ is the Green-Naghdi rate of the Cauchy stress tensor $\boldsymbol{\sigma}$, \mathbf{I} is the second order identity tensor, \dot{T} is the rate of change of the temperature due to adiabatic heating while α is the thermal expansion coefficient of the material.

The yield function is defined in the form

$$f(\boldsymbol{\sigma}, p, T) = \sigma_{eq}(\boldsymbol{\sigma}) - \sigma_y(p, T) \quad (7)$$

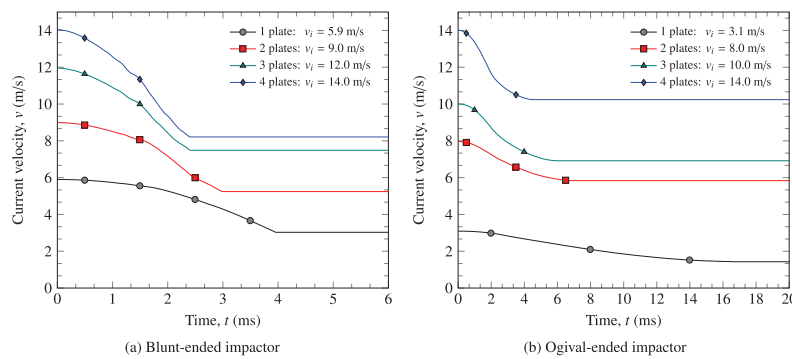


Fig. 15. Typical experimental velocity–time curves for (a) tests with the blunt-ended impactor and (b) tests with the ogival-ended impactor.

where p is the equivalent plastic strain, and T is the temperature. According to the J_2 flow theory the equivalent stress is given by

$$\sigma_{eq} = \sqrt{\frac{3}{2}\boldsymbol{\sigma}' : \boldsymbol{\sigma}'}, \quad (8)$$

where $\boldsymbol{\sigma}'$ is the stress deviator calculated as

$$\boldsymbol{\sigma}' = \boldsymbol{\sigma} - \frac{1}{3}\text{tr}(\boldsymbol{\sigma})\mathbf{I}. \quad (9)$$

The yield stress is defined as

$$\sigma_y(p, T) = \left[\sigma_0 + \sum_{i=1}^2 Q_i (1 - \exp(-C_i p)) \right] [1 - T^{*m}], \quad (10)$$

where the homologous temperature is given as $T^* = (T - T_0)/(T_m - T_0)$, and m is a model parameter controlling the thermal softening. Here T_m is the melting temperature of the material and T_0 is the ambient temperature. σ_0 is the initial yield stress, and Q_1 , C_1 , Q_2 , and C_2 are hardening parameters. By using Eqs. (7) and (8), we can express the plastic rate-of-deformation tensor by means of the associated flow rule as

$$\mathbf{D}^p = \dot{p} \frac{\partial f}{\partial \boldsymbol{\sigma}} = \frac{3}{2} \dot{p} \frac{\boldsymbol{\sigma}'}{\sigma_{eq}}. \quad (11)$$

The equivalent plastic strain rate is defined by

$$\dot{p} = \begin{cases} 0 & \text{for } f \leq 0 \\ \dot{p}_0 \left(\left[\frac{\sigma_{eq}(\boldsymbol{\sigma})}{\sigma_y(p, T)} \right]^{1/c} - 1 \right) & \text{for } f > 0 \end{cases} \quad (12)$$

where c is a material parameter controlling the rate sensitivity, and \dot{p}_0 is a user defined strain rate. In the viscoplastic domain, $f > 0$, we obtain an expression for the equivalent stress as

$$\begin{aligned} \sigma_{eq}(\boldsymbol{\sigma}) \equiv \sqrt{\frac{3}{2}\boldsymbol{\sigma}' : \boldsymbol{\sigma}'} &= \sigma_y(p, T) \left[1 + \frac{\dot{p}}{\dot{p}_0} \right]^c \\ &= \left[\sigma_0 + \sum_{i=1}^2 Q_i (1 - \exp(-C_i p)) \right] \left[1 + \frac{\dot{p}}{\dot{p}_0} \right]^c [1 - T^{*m}]. \end{aligned} \quad (13)$$

The temperature change due to adiabatic heating is calculated using

$$\dot{T} = \frac{\chi}{\rho C_p} \boldsymbol{\sigma} : \mathbf{D}^p = \frac{\chi}{\rho C_p} \sigma_{eq} \dot{p} \quad (14)$$

where ρ is the density, C_p is the specific heat and χ is the Taylor-Quinney coefficient that represents the proportion of plastic work converted into heat. We typically assume $\chi = 0$ for isothermal conditions and $\chi = 0.9$ for adiabatic conditions (see e.g. Ref. [33]).

5.2. Failure criterion

A failure criterion proposed by Cockcroft and Latham (CL) [34] has been applied in this study. The criterion can be easily implemented in finite element codes and it only requires one uniaxial tensile test for calibration. The criterion as used here is uncoupled from the constitutive model. The CL criterion reads

$$D = \frac{W}{W_{cr}} = \frac{1}{W_{cr}} \int_0^p \langle \sigma_1 \rangle dp, \quad \langle \sigma_1 \rangle = \max(\sigma_1, 0), \quad (15)$$

where σ_1 is the major principal stress. Material failure takes place when the damage parameter, D , reaches unity. W_{cr} is the failure parameter, which can be found by integrating the major principal stress in a uniaxial tensile test over the entire equivalent plastic strain path to the plastic strain at failure, p_f . It can be seen from Eq. (15) that damage will not grow and failure cannot occur if there are no tensile stresses present.

Previously it has been shown that the CL criterion with only one parameter gives equally as good results as more elaborate criteria [35,36]. Also note that the criterion indirectly accounts for both the deviatoric and hydrostatic stress states, as shown in Fig. 16, through the relation

$$\sigma_1 = \left(\sigma^* + \frac{3 + \mu_\sigma}{3\sqrt{3 + \mu_\sigma^2}} \right) \sigma_{eq}, \quad (16)$$

where μ_σ and σ^* are the Lode parameter and the stress triaxiality, respectively, defined in terms of the principal stresses σ_1 , σ_2 , and σ_3 as

$$\mu_\sigma = \frac{2\sigma_2 - \sigma_1 - \sigma_3}{\sigma_3 - \sigma_1} \quad (17)$$

and

$$\sigma^* = \frac{\sigma_H}{\sigma_{eq}} = \frac{\sigma_1 + \sigma_2 + \sigma_3}{3\sigma_{eq}}. \quad (18)$$

Robustness of the CL criterion with respect to strain rate and temperature has been shown by Børvik et al. [37].

5.3. Calibrating the model parameters

Docol 600DL steel plates have also been used in previous studies. Gruben et al. [19] investigated ductile fracture behavior and Rakvåg et al. [38] considered strain rate effects. The initial yield stress σ_0 and hardening parameters (Q_1 , C_1 , Q_2 and C_2) in the

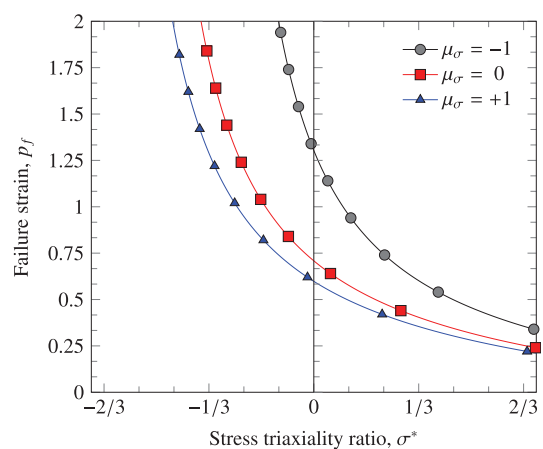


Fig. 16. Influence of the Lode parameter μ_σ and the stress triaxiality ratio σ^* on the failure strain for the failure parameter $W_{cr} = 473$ MPa used in this study.

Table 5

Calibrated material parameters for the extended Voce hardening rule and CL criterion.

σ_0 (MPa)	Q_1 (MPa)	C_1	Q_2 (MPa)	C_2	W_{cr} (MPa)
370.0	236.4	39.3	408.1	4.5	473.0

extended Voce hardening rule) were found to coincide in these two research programs. The tensile test results presented in Fig. 1a are somewhat inconsistent with the results obtained for the same material (but different batches and thicknesses) in Refs. [19,38], so a new calibration of the extended Voce hardening rule was made. Data from the extensometer measurements are only valid for displacements up to 4 mm, so by creating a virtual 40 mm extensometer in the DIC software we were able to get force-elongation measurements until specimen fracture. The test that exhibited the median elongation at the point of failure was chosen for further calibration. The scatter in the force level was negligible. A finite element model of the tensile test was made to be run in the explicit version of LS-DYNA 971 [39]. The mesh consists of 1602 8-node trilinear brick elements with selective reduced integration. To reduce the computational time, mass scaling was employed. The model has two elements over the thickness, giving an approximate element size in the gauge area of 0.4 mm.

The optimization itself was conducted in the optimization package LS-OPT [40]. This package reads e.g. LS-DYNA input files and optimizes the parameters of a constitutive relation based on a predefined target curve. The software runs sequential analyses on the same model with varying input parameters with the final goal of minimizing the mean-squared-error between the calculated force-elongation curve and the target curve. In this case we used the parameters Q_1 , C_1 , Q_2 , and C_2 of the extended Voce hardening rule which is compatible with the constitutive relation described in Section 5.1. 15 series of 8 simulations, i.e., a total of 120 simulations, were run to obtain the material parameters presented in this study. The initial yield stress at room temperature, σ_0 , was chosen as the stress that gives 0.2% plastic deformation in the reference test. Prior to the optimization an interpolation algorithm was run to ensure equal spacing between the data points of the target curve to prevent weighting of any parts of the curve during the simulations. The target curve (i.e., the force-elongation relation from the 40 mm virtual extensometers) and a simulation run with the optimized input parameters are shown in Fig. 1a. The equivalent stress-equivalent plastic strain curve until necking calculated from the DIC-measurements and the curve resulting from the optimized Voce parameters are shown in Fig. 1b, the agreement is, as seen, good. The hardening parameters that were found using LS-OPT are summarized in Table 5.

The CL failure criterion described in Section 5.2 was calibrated based on the numerical simulations described above. The equivalent plastic strain, p , and the major principal stress in the axial direction, σ_1 , were extracted from the element exposed to the largest plastic strain in the finite element analysis of the uniaxial tension test. This element also exhibited the largest value of W . The failure strain, p_f , was determined from the moment of failure in the numerical model that was adapted to match the force-elongation curves in Fig. 1a. To find the failure parameter, W_{cr} , the major principal stress was integrated over the equivalent plastic strain

path. This gave the CL failure parameter $W_{cr} = 473$ MPa (see Table 5). Fig. 2b compares the major surface strain from the representative DIC measurements to a finite element simulation. The correspondence between the two pictures suggests that the strain field and the neck are well captured in the numerical simulation even if the location of necking differs. The spread in elongation and fracture strain shown in Figs. 1 and 2a, respectively, suggests a slight spread in W_{cr} . Here, W_{cr} has only been calibrated from the tensile test that exhibited the median elongation to failure. This spread will at least to some extent affect the numerical results, but the main trends will remain the same.

The strain rate sensitivity of Docol 600DL was studied by Rakvåg et al. [38]. Because of difficulties involved in testing thin 0.7 mm specimens in a Split Hopkinson Tension Bar (SHTB), they tested 2 mm thick plates. The material was tested at five strain rates in the range 197 s^{-1} to 879 s^{-1} . The results revealed pronounced strain-rate sensitivity which increased with plastic strain. Thus the value of the parameter c in the constitutive model (see Eq. (13)) can vary significantly. Rakvåg et al. neglected the rate sensitivity in their main study due to low strain rates. Higher strain rates are expected in this study, so a rate hardening parameter $c = 0.01$ was chosen as a starting point. A study regarding the rate sensitivity is carried out in Section 6.

Table 6 summarizes the physical constants and general model parameters used in the finite element simulations. These are taken from the literature, while $m = 1$ indicates a linear degradation of material strength with increasing temperature which is commonly assumed in impact analyses [37]. The reference strain rate is set to $\dot{\rho}_0 = 5 \times 10^{-4} \text{ s}^{-1}$ which is close to the initial strain rate in the tensile tests.

6. Numerical study

6.1. Finite element models

All simulations were carried out using the explicit finite element code IMPETUS Afea Solver [41]. The program makes use of fully integrated higher order elements including cubic 64-node hexahedrons that are preferential to linear elements when describing bending. Whether we use linear elements, cubic elements, or a combination of the two is a trade-off between computational speed and the desired accuracy. A penalty-based node-to-surface contact algorithm is used in all simulations. Friction is disregarded in most of the simulations, but the effect of the frictional coefficient μ is investigated by varying its value in a parametric study. The boundaries are fixed by applying translational constraints to all edge nodes in all directions. Full thermal coupling was employed and a strain rate sensitivity parameter of $c = 0.01$ was chosen based on Ref. [38].

Screenshots of the mesh and impact area of the two models with a single 0.8 mm thick plate are shown in Fig. 17. From the experiments performed in this study we saw that the target plates behaved close to axisymmetric when impacted by blunt-ended impactors. We utilized this by running all analyses with a 10° slice of the entire plate with appropriate boundary conditions applied to the symmetry planes. Most simulations with the blunt-ended impactor were run with 745 cubic hexahedrons in the target plate. In the impact zone we have four elements over the thickness,

Table 6

Physical constants and model parameters for the Docol 600DL steel plates taken from the literature [33,37,38].

E (MPa)	ν (-)	ρ (kg/m^3)	α (K^{-1})	C_p ($\text{J}/(\text{kg K})$)	$\dot{\rho}_0$ (s^{-1})	c (-)	χ (-)	k ($\text{W}/(\text{m K})$)	T_0 (K)	T_m (K)	m (-)
210,000	0.33	7850	1.2×10^{-5}	452	5×10^{-4}	0.01	0.9	50	293	1800	1

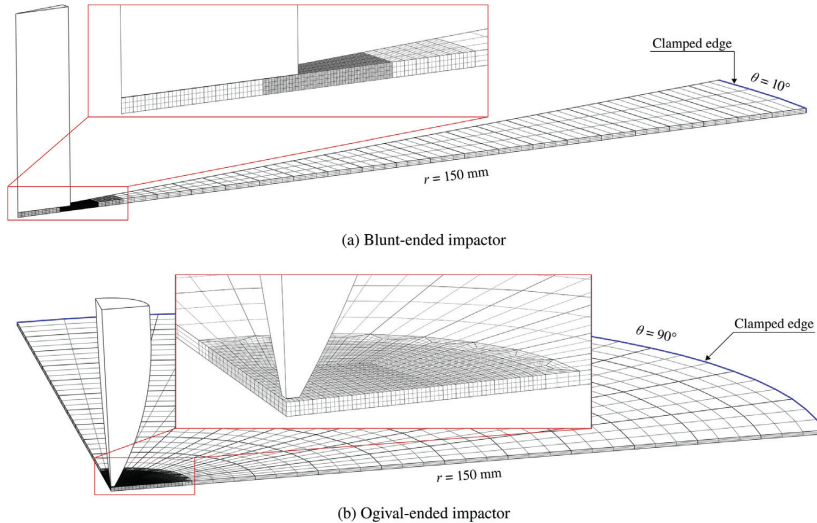


Fig. 17. Meshes applied in the IMPETUS Afea Solver for the 0.8 mm plates.

while we have one element over the thickness in the rest of the plate. Layered plates were modeled with a 0.02 mm gap; this is considered as in contact. Due to the cubic element formulation the number of nodes over the thickness in the impact zone was 13, i.e. a node spacing of 0.067 mm. All simulations with the ogival-ended impactor were run with a double-symmetric model. This was done so that we could describe the observed petaling while keeping the computational time at a reasonable level. Each target plate was discretized into 448 cubic hexahedron elements. The element size was approximately 0.8 mm × 0.8 mm × 0.8 mm in the impact zone and 30 mm × 10 mm × 0.8 mm at the clamped edge. In these simulations the cubic element formulation led to a node spacing in the thickness direction of 0.267 mm. Experience and previous studies have shown that mesh sensitivity is more pronounced in simulations with blunt-ended impactors than in simulations with ogival-ended impactors [16]. Thus, a more refined mesh was chosen for the plates struck by the blunt-ended impactor than for the plates struck by the ogival-ended impactor in this study.

The experiments carried out on the 1.8 mm thick plates were also simulated with the IMPETUS Afea Solver. The general inputs and material constants used for the 1.8 mm plates were identical to the 0.8 mm plates even though the material behavior was slightly different (see Section 3). Twice as many elements over the thickness were used to approximately preserve the node-spacing from the 0.8 mm plates.

Since only the part of the dropped-objects-rig actually striking the target plates was modeled (see Figs. 3 and 17), the added mass from the rest of the rig needed to be accounted for. This was done in the simulations by increasing the density of the impactors, with precautions taken to ensure that the masses matched the real values. The densities $\rho_{blunt} = 919.35 \times 10^3 \text{ kg/m}^3$ and $\rho_{ogival} = 1295.23 \times 10^3 \text{ kg/m}^3$ gave the correct respective masses of 9.82 kg and 9.78 kg. The tip of the ogival-ended projectile has been blunted in the numerical simulations (see Fig. 17b). This was done to avoid numerical issues. It is not expected to influence the results.

The hardening and failure parameters for the employed thermoelastic–thermoviscoplastic constitutive model can be found in Table 5, whereas the physical constants and model parameters are given in Table 6. The implementation of the CL criterion in IMPETUS

Afea Solver states that when the damage parameter, D in Eq. (15), has evolved from 0 to 1 in an integration point, the integration point loses its shear strength and we have local material failure. After local failure in a number of integration points (16 for cubic hexahedrons) the element is removed from the analysis. This is defined as element erosion.

The simulation times were highly dependent on the termination time of the analysis at hand, which is difficult to determine a priori. In many cases the analyses have been run longer than necessary. If we disregard this, most of the simulations took around 10 h to run on a NVIDIA Tesla Kepler K20c GPU.

6.2. Finite element results

Fig. 7 compares the ballistic limit curves from the numerical simulations to the experiments. Analyses have been run with identical initial velocities as in the experiments. Hence, each experiment has a corresponding simulation. Some additional simulations were run where this was deemed necessary to determine the entire ballistic curve. Plots from two typical simulations are shown in Figs. 18 and 19. The former illustrates how global deformation precedes membrane stretching and plug ejection in the plates struck by the blunt-ended impactor, while the latter shows the formation of petals which were also observed in the experiments on plates struck by the ogival-ended impactor.

Comparing Fig. 8a to b shows that the simulations reflect the trends observed in the experiments. However, the range in the ballistic limits is smaller in the numerical simulations than in the experimental data. This is due to an underestimation of the ballistic limit velocities for the multi-layered plates struck by the blunt-ended impactor in the numerical simulations. In addition, Fig. 8b shows the numerical results for the 1.8 mm plates. Also these results are in general underestimated and for the double-layered plates the ballistic limit velocity is actually higher for plates struck by the ogival-ended impactor than for the blunt-ended impactor.

Table 3 compares the ballistic limit velocities from the simulations to the experiments. The underestimation of the ballistic limit

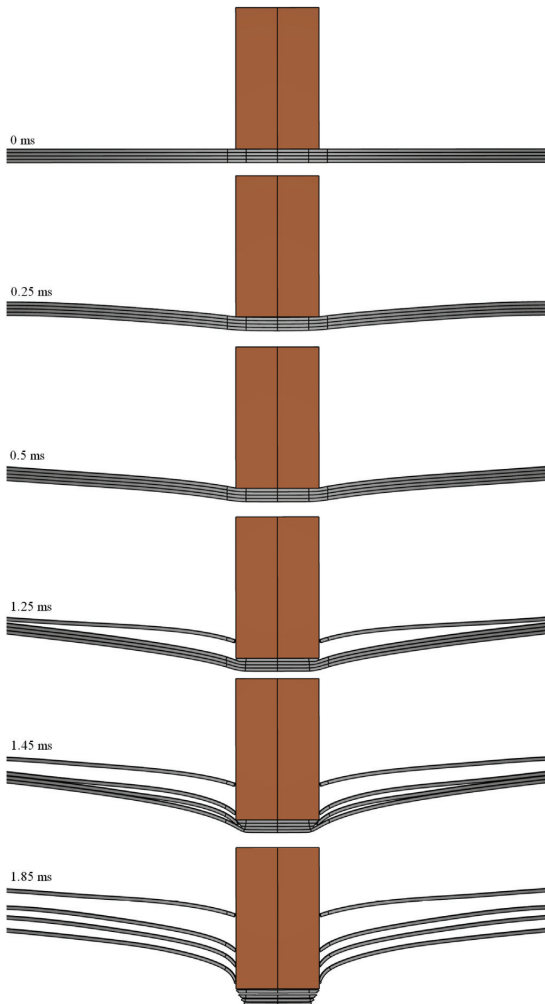


Fig. 18. Image series displaying the predicted perforation process of 4 plates by the blunt-ended impactor ($v_i = 14.0 \text{ m/s}$, $v_r = 10.5 \text{ m/s}$).

velocities for the blunt-ended impactor is seen, especially for the quadruple-layered plates. This means that the results are on the conservative side, which is preferred in design situations. The simulations involving the ogival-ended impactor gave excellent results in terms of ballistic limit velocity for the double-layered and triple-layered plates, but an underestimation of the capacity for the quadruple-layered plates and an overestimation of the capacity for the single plates. Table 4 compares the simulations to the experiments for the 1.8 mm plates. The trends are the same as for the 0.8 mm plates with the same discrepancy in ballistic limit velocity for the different impactor shapes.

Fig. 20a compares the force-time curve from a simulation to a typical experiment with the blunt-ended impactor, $v_i = 5.9 \text{ m/s}$ in both cases. The initial increase in force level, where bending dominates the behavior, is very similar in the simulation and the experiment. However, after about 1.5 ms the force level develops faster, and to a higher maximum level, in the simulation. Failure

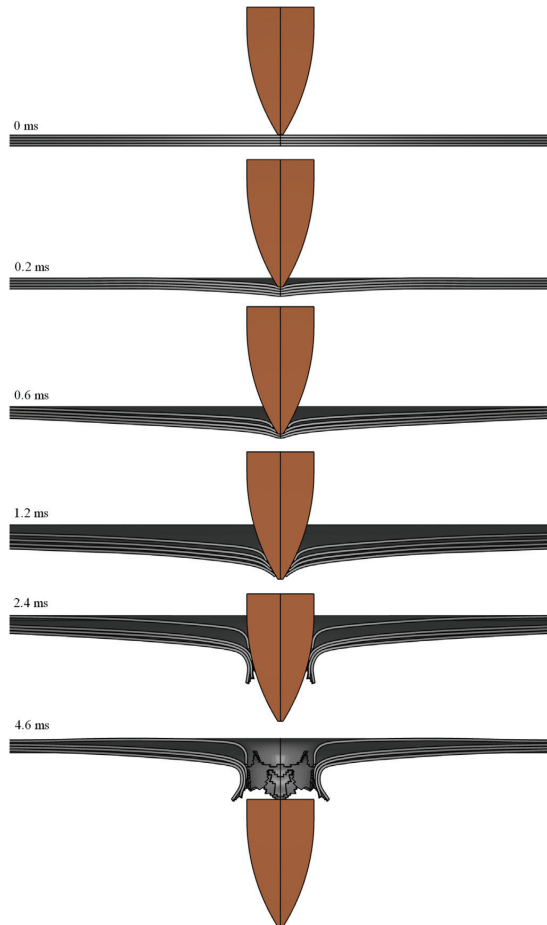


Fig. 19. Image series displaying the predicted perforation process of 4 plates by the ogival-ended impactor ($v_i = 14.0 \text{ m/s}$, $v_r = 11.6 \text{ m/s}$).

occurs prematurely, leading to higher predicted residual velocities than those found in the corresponding experiments.

Comparing the simulation in Fig. 20b to the corresponding experiment with the ogival-ended impactor ($v_i = 3.6 \text{ m/s}$) reveals that the initial increase in the force level is well captured by the simulation, but when the peak force is reached in the experiment, the force from the simulation continues to rise. The force drops gradually after the peak, and probably because we have neglected frictional effects, the force level drops faster and the impactor achieves complete perforation faster in the numerical simulation than in the experiment.

Even though the numerical results are acceptable in terms of ballistic limit velocity, Fig. 11 indicates that the numerical models have some shortcomings when it comes to describing the energy dissipation. The deflections at initial perforation are underestimated for both impactor shapes. The deflection values for the simulations with the ogival-ended impactor are most likely underestimated to some degree due to the use of element erosion. The deformation profiles are extracted from the state just after perforation which corresponds to the first state with eroded elements in the bottom plate.

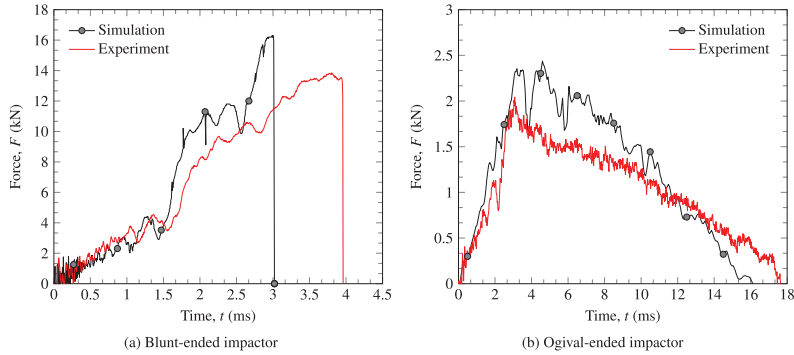


Fig. 20. Comparison of numerical and experimental results for (a) the blunt-ended impactor ($v_i = 5.9$ m/s, $v_r = 3.0$ m/s) and (b) the ogival-ended impactor ($v_i = 3.6$ m/s, $v_r = 1.9$ m/s).

6.3. Parametric study

The mesh sensitivity of the problem is investigated briefly for both the blunt-ended and the ogival-ended impactors by creating models with twice as many elements over the plate thickness as the original models used in this study. This increased the simulation times considerably. In the case of the blunt-ended impactor, simulations were run with initial velocities of 5.9 m/s and 5.4 m/s. The respective residual velocities obtained with the original model are 3.9 m/s and 2.4 m/s, while the refined mesh yielded 4.1 m/s and 2.5 m/s. For the simulations with the ogival-ended impactor the initial velocities 5.0 m/s and 3.6 m/s were investigated. The respective residual velocities went from 3.8 m/s to 4.0 m/s and from 1.5 m/s to 1.9 m/s when the mesh was refined. Thus an increase in the residual velocities was seen for the refined meshes regardless of impactor shape, caused by an earlier occurrence of failure. For both impactor shapes, the maximum force level dropped when the meshes were refined, and refining the grid size led to a force-time curve slightly closer to the experimental results. However, the maximum force only went from 16.1 kN to 15.6 kN for the blunt-ended impactor and from 2.5 kN to 2.3 kN for the ogival-ended impactor.

By keeping the node spacing constant and changing the cubic 64-node hexahedrons to linear 8-node hexahedrons we get nine times as many elements in the model. This modification results in smaller deflections, i.e., less energy absorbed, and thus larger residual velocities. According to Fig. 11, the displacement field is generally underestimated from the numerical simulations suggesting that the cubic 64-node hexahedrons predict a more realistic response than the linear 8-node hexahedrons.

In the bulk of the simulations the frictional coefficient was set to zero. Simulations were run with $\mu = 0.05$ and $\mu = 0.1$ to assess the influence of friction on the numerical results. By increasing μ , plastic strain and damage accumulate at the impactor–plate interface of the blunt-ended impactor. This resulted in earlier failure and lower capacity, contrasting the results from the simulations with the ogival-ended impactor where a higher μ led to a considerable reduction of the residual velocity of the impactor. The friction parameter is commonly set to zero or close to zero in ballistic analyses (see Refs. [21,42–44]). Although investigations show that friction can be negligible in some cases [45], the frictional effect can influence the solution in other cases like in this study where the impact velocity is low. According to Rosenberg and Dekel [22] friction is still one of the less understood phenomena in terminal ballistics and they report that the friction present around the shank of a cylindrical projectile is small but not always insignificant. Kpenyigba et al. [5] investigated how lubricating the contact surface affects a conical projectile perforating a 1 mm thick steel plate, and the residual velocities reported did not change significantly with lubrication. In this study the numerical investigation on the effect of μ yielded inconclusive results, and the effect of friction was therefore disregarded.

The influence of the parameter c controlling rate sensitivity in the thermoelastic–thermoviscoplastic model presented in Eq. (13) was investigated by comparing simulations with both impactor shapes for $c = 0$ and $c = 0.01$. Thermal softening, or the absence of such, was checked with adiabatic, isothermal, and thermally coupled formulations of the solver. The results in Table 7 show that introducing strain rate hardening increases the maximum force while it decreases the residual velocity as expected for both

Table 7

Summary of how temperature and strain rate affect the numerical simulations of the perforation process for impact on single plates. The residual velocity (v_r), peak force (F_{peak}), and the energy absorption (W) defined in Eq. (3) are given for each simulation.

Blunt-ended impactor ($v_i = 5.9 \text{ m/s}$)		Ogival-ended impactor ($v_i = 3.6 \text{ m/s}$)		
	Rate sensitive ($c = 0.01$)	Rate insensitive ($c = 0$)	Rate sensitive ($c = 0.01$)	Rate insensitive ($c = 0$)
Adiabatic	$v_r = 3.9 \text{ m/s}$	$v_r = 4.2 \text{ m/s}$	$v_r = 1.5 \text{ m/s}$	$v_r = 1.6 \text{ m/s}$
	$F_{peak} = 16.2 \text{ kN}$	$F_{peak} = 14.0 \text{ kN}$	$F_{peak} = 2.4 \text{ kN}$	$F_{peak} = 2.3 \text{ kN}$
	$W = 95.9 \text{ J}$	$W = 84.3 \text{ J}$	$W = 51.9 \text{ J}$	$W = 49.5 \text{ J}$
Coupled	$v_r = 3.9 \text{ m/s}$	$v_r = 4.2 \text{ m/s}$	$v_r = 1.5 \text{ m/s}$	$v_r = 1.6 \text{ m/s}$
	$F_{peak} = 16.3 \text{ kN}$	$F_{peak} = 14.0 \text{ kN}$	$F_{peak} = 2.4 \text{ kN}$	$F_{peak} = 2.4 \text{ kN}$
	$W = 96.9 \text{ J}$	$W = 84.7 \text{ J}$	$W = 52.0 \text{ J}$	$W = 50.1 \text{ J}$
Isothermal	$v_r = 2.7 \text{ m/s}$	$v_r = 4.0 \text{ m/s}$	$v_r = 1.5 \text{ m/s}$	$v_r = 1.6 \text{ m/s}$
	$F_{peak} = 17.4 \text{ kN}$	$F_{peak} = 15.2 \text{ kN}$	$F_{peak} = 2.4 \text{ kN}$	$F_{peak} = 2.3 \text{ kN}$
	$W = 134.9 \text{ J}$	$W = 92.4 \text{ J}$	$W = 51.0 \text{ J}$	$W = 49.8 \text{ J}$

impactor shapes. Differences in the force level and residual velocity are generally small, but in the case of isothermal conditions the absence of thermal softening delays the onset of initial fracture for the plate struck by the blunt-ended impactor leading to a low residual velocity. This was also observed by Grytten et al. [20]. Comparing the results to the corresponding experiments shows that an isothermal formulation combined with $c = 0.01$ gave the best results for the blunt-ended impactor. For the ogival-ended impactor the effect of temperature and strain-rate did not significantly change the results.

Measures were taken to ensure full clamping of the boundary in the experiments, and no deformation was seen around the bolted holes. However, studies have shown that the boundary behaves somewhere between fixed and simply supported, and that the effect of the boundaries increases as the impact velocity decreases [46]. In other words, as we approach quasi-static loading, more of the plate will be affected. The displacement profiles shown in Figs. 5 and 6 indicate that the entire plate is involved in the energy dissipation process for the blunt-ended impactor, but global deformation is less marked for the ogival-ended impacts. Simulations were therefore also run with simply supported boundaries. In the simulations with the blunt-ended impactor a simply supported formulation resulted in a lower residual velocity than a fixed boundary formulation. In the simulations using the ogival-ended impactor the residual velocity did not change noticeably for the simply supported simulation. The effect of boundary conditions on the residual velocity was found to be small in this study, so the conservative fixed boundary formulation has been chosen.

7. Concluding remarks

In this paper an experimental program concerning low-velocity impact on the dual-phase steel Docol 600DL was presented. The program includes material testing and calibration supported by DIC measurements, subsequent impact experiments in a dropped-objects-rig, and 3D finite element simulations. The bulk of the impact experiments were done on various layered configurations of 0.8 mm thick plates with a span of 300 mm. In addition, a smaller experimental program with 1.8 mm thick plates with the same span was carried out for comparison.

The impact experiments revealed that the thin plates' ability to resist perforation was greater when they were struck by a blunt-ended impactor than when they were struck by an ogival-ended impactor. This can be seen by comparing the ballistic limit velocities, which are higher when using the blunt-ended impactor. An almost linear relationship is found between the total plate thickness, i.e., number of layers, and the ballistic limit velocity for the respective impactors.

The blunt-ended impactor activates the entire plate in the energy dissipation process before the final failure happens in shear/plate thinning. On the other hand, plates struck with the ogival-ended impactor display a petaling fracture pattern, a significantly smaller global deformation, and less energy is absorbed by the plate, resulting in a lower ballistic limit. The failure mechanisms hardly vary when the plates are laminated. The distinctive petaling pattern from the single plate struck by the ogival-ended impactor can be found in every plate in every configuration, the same being true for the bending, thinning, and shear failure caused by the blunt-ended impactor.

The same failure mechanisms from the 0.8 mm plates are observed in the impacts on the thicker 1.8 mm plates. However, the experimental results indicate that the energy absorption is higher for one thick monolithic plate than for layered plates of equal thickness. This is particularly clear for the ogival-ended impactor where the ballistic velocity and absorbed energy increased

noticeably for the monolithic plate. Relating these findings to earlier research shows that layering might not be an advantageous strategy to improve the capacity of metallic plates subjected to low-velocity impact.

In the finite element simulations the behavior of the impacted plates in terms of plate thickness and layering was described with reasonable accuracy considering the complexity of the problem. This shows that a finite element model can predict failure modes and capture the trends present during low-velocity impact. That being said, the numerous mechanisms such as bending, membrane stretching, thinning, shear bands, and petaling, and uncertain factors like boundary conditions, thermal behavior, mesh sensitivity, friction, and strain rate make this low-velocity impact problem difficult to predict numerically.

Acknowledgments

The financial support for this work from the Norwegian Defence Estates Agency and the Structural Impact Laboratory (SIMLab), Centre for Research-based Innovation (CRI) at the Norwegian University of Science and Technology (NTNU) is gratefully acknowledged. The authors would also like to thank Dr. Egil Fagerholt for assistance with the DIC measurements.

References

- [1] Zukas JA. *Impact dynamics*. 1st ed. New York: John Wiley & Sons, Inc.; 1982.
- [2] Corbett GG, Reid SR, Johnson W. Impact loading of plates and shells by free-flying projectiles: a review. *Int J Impact Eng* 1996;18:141–230.
- [3] Backman ME, Goldsmith W. The mechanics of penetration of projectiles into targets. *Int J Eng Sci* 1978;16:1–99.
- [4] Børvik T, Langseth M, Hopperstad OS, Malo KA. Perforation of 12 mm thick steel plates by 20 mm diameter projectiles with flat, hemispherical and conical noses. Part I: experimental study. *Int J Impact Eng* 2002;25:19–35.
- [5] Kpenyigba KM, Jankowiak T, Rusinek A, Pesci R. Influence of projectile shape on dynamic behavior of steel sheet subjected to impact and perforation. *Thin Walled Struct* 2013;65:93–104.
- [6] Iqbal MA, Gupta PK, Deore VS, Tak SK, Tiwari G, Gupta NK. Effect of target span and configuration on the ballistic limit. *Int J Impact Eng* 2012;42:11–24.
- [7] Gupta NK, Iqbal MA, Sekhon GS. Experimental and numerical studies on the behavior of thin aluminum plates subjected to impact by blunt- and hemispherical-nosed projectiles. *Int J Impact Eng* 2006a;32:1921–44.
- [8] Gupta NK, Iqbal MA, Sekhon GS. Effect of projectile nose shape, impact velocity and target thickness on the deformation behavior of layered plates. *Int J Impact Eng* 2006b;32:37–60.
- [9] Woodward RL, Cimpoeru SJ. A study of the perforation of aluminium laminate targets. *Int J Impact Eng* 1998;21:117–31.
- [10] Dey S, Børvik T, Teng X, Wierzbicki T, Hopperstad OS. On the ballistic resistance of double-layered steel plates: an experimental and numerical investigation. *Int J Solids Struct* 2007;44:6701–23.
- [11] Ben-Dor G, Dubinsky A, Elperin T. Investigation and optimization of protective properties of metal multi-layered shields: a review. *Int J Prot Struct* 2012;3:275–91.
- [12] Langseth M, Larsen PK. Dropped objects' plugging capacity of steel plates: an experimental investigation. *Int J Impact Eng* 1990;9:289–316.
- [13] Wen HM, Jones N. Low-velocity perforation of punch-impact-loaded metal plates. *J Pressure Vessel Technol, Trans ASME* 1996;118:181–7.
- [14] Mohotti D, Muneeb A, Ngo T, Lu J, Mendis P, Ruan D. Out-of-plane impact resistance of aluminium plates subjected to low velocity impact. *Mater Des* 2013;50:413–26.
- [15] Abdulhamid H, Kolopp A, Bouvet C, Rivallant S. Experimental and numerical study of AA5086-H111 aluminum plates subjected to impact. *Int J Impact Eng* 2013;51:1–12.
- [16] Rusinek A, Rodriguez-Martinez JA, Zaera R, Klepaczko JR, Arias A, Sauvelet C. Experimental and numerical study of the perforation process of mild steel sheets subjected to perpendicular impact by hemispherical projectiles. *Int J Impact Eng* 2009;36:565–87.
- [17] SSAB EMEA AB, SE-781 84 Borlange, Sweden, Datasheet 13-02-14 GB8201 DOCOL; Cited 2014-03-20. <http://www.ssab.com/en/Brands/Docol1/Products/Docol-600-DL/>.
- [18] Fagerholt E, Børvik T, Hopperstad OS. Measuring discontinuous displacement fields in cracked specimens using digital image correlation with mesh adaptation and crack-path optimization. *Opt Lasers Eng* 2013;51:229–310.
- [19] Gruben G, Fagerholt E, Hopperstad OS, Børvik T. Fracture characteristics of a cold-rolled dual-phase steel. *Eur J Mech – A/Solids* 2011;30:204–18.
- [20] Grytten F, Børvik T, Hopperstad OS, Langseth M. Low velocity perforation of AA5083-H116 aluminium plates. *Int J Impact Eng* 2009;36:597–610.

- [21] Børvik T, Langseth M, Hopperstad OS, Malo KA. Ballistic penetration of steel plates. *Int J Impact Eng* 1999;22:855–86.
- [22] Rosenberg Z, Dekel E. Terminal ballistics. Berlin Heidenberg: Springer-Verlag; 2012. 23–25, 95–96.
- [23] Børvik T, Hopperstad OS, Pedersen KO. Quasi-brittle fracture during structural impact of AA7075-T651 aluminium plates. *Int J Impact Eng* 2010;37:537–51.
- [24] CEAST 9350. Instructions for use and maintenance. 1st ed. Instron; 2010.
- [25] Gruben G. Private communication. 2014. Trondheim.
- [26] Gruben G, Vysochinskij D, Coudert T, Reyes A, Lademo OG. Determination of ductile fracture parameters of a dual-phase steel by optical measurements. *Strain* 2013;49:221–32.
- [27] Recht RF, Ipsen TW. Ballistic perforation dynamics. *J Appl Mech* 1963;30: 384–90.
- [28] Langseth M, Larsen PK. Dropped objects' plugging capacity of aluminium alloy plates. *Int J Impact Eng* 1994;15:225–41.
- [29] Wierzbicki T. Petalling of plates under explosive and impact loading. *Int J Impact Eng* 1999;22:935–54.
- [30] Lee YW, Wierzbicki T. Fracture prediction of thin plates under localized impulsive loading. Part I: dishing. *Int J Impact Eng* 2005a;31:1253–76.
- [31] Lee YW, Wierzbicki T. Fracture prediction of thin plates under localized impulsive loading. Part II: discing and petalling. *Int J Impact Eng* 2005b;31: 1277–308.
- [32] Rosenberg Z, Dekel E. On the deep penetration and plate perforation by rigid projectiles. *Int J Solid Struct* 2009;46:4169–80.
- [33] Børvik T, Hopperstad OS, Berstad T, Langseth M. A computational model of viscoplasticity and ductile damage for impact and penetration. *Eur J Mech A/ Solids* 2001;20:685–712.
- [34] Cockcroft MG, Latham DJ. Ductility and the workability of metals. *J Inst Metals* 1968;96:33–9.
- [35] Dey S, Børvik T, Hopperstad OS, Langseth M. On the influence of fracture criterion in projectile impact of steel plates. *Comput Mater Sci* 2006;38: 176–91.
- [36] Kane A, Børvik T, Berstad T, Benallal A, Hopperstad OS. Failure criteria with unilateral conditions for simulation of plate perforation. *Eur J Mech – A/Solids* 2011;30:468–76.
- [37] Børvik T, Dey S, Clausen AH. Perforation resistance of five different high-strength steel plates subjected to small-arms projectiles. *Int J Impact Eng* 2009;36:948–64.
- [38] Rakvåg KG, Underwood NJ, Schleyer GK, Børvik T, Hopperstad OS. Transient pressure loading of clamped metallic plates with pre-formed holes. *Int J Impact Eng* 2013;53:44–55.
- [39] LSTC, LS-DYNA; Cited 2014-20-01. <http://www.lstc.com/products/ls-dyna>.
- [40] LSTC, LS-OPT; Cited 2014-20-01. <http://www.lstc.com/products/ls-opt>.
- [41] IMPETUS Afea AS., IMPETUS Afea solver; Cited 2014-20-01. <http://www.impetus-afea.com>.
- [42] Holmen JK, Johnsen J, Jupp S, Hopperstad OS, Børvik T. Effects of heat treatment on the ballistic properties of AA6070 aluminium alloy. *Int J Impact Eng* 2013;57:119–33.
- [43] Johnsen J, Holmen JK, Myhra OR, Hopperstad OS, Børvik T. A nano-scale material model applied in finite element analysis of aluminium plates under impact loading. *Comput Mater Sci* 2013;79:724–35.
- [44] Arias A, Rodriguez-Martinez JA, Rusinek A. Numerical simulations of impact behaviour of thin steel plates subjected to cylindrical, conical and hemispherical non-deformable projectiles. *Eng Fract Mech* 2008;75:1635–56.
- [45] Børvik T, Olovsson L, Dey S, Langseth M. Normal and oblique impact of small arms bullets on AA6082-T4 aluminium protective plates. *Int J Impact Eng* 2011;38:577–89.
- [46] Grytten F, Fagerholt E, Auestad T, Førre B, Børvik T. Out-of-plane deformation measurements of an aluminium plate during quasi-static perforation using structured light and close-range photogrammetry. *Int J Solids Struct* 2007;44: 5752–73.

Part 2

Jens Kristian Holmen, Tore Børvik, Ole Runar Myhr, Hallvard Gustav Fjær,
Odd Sture Hopperstad

Perforation of welded aluminum components: Microstructure-based modeling and experimental validation

International Journal of Impact Engineering 84 (2015) 96–107.



Perforation of welded aluminum components: Microstructure-based modeling and experimental validation



Jens Kristian Holmen ^{a,* 1}, Tore Børvik ^a, Ole Runar Myhr ^b, Hallvard Gustav Fjær ^c, Odd Sture Hopperstad ^a

^a Structural Impact Laboratory (SIMLab), Department of Structural Engineering, Norwegian University of Science and Technology, NO-7491, Trondheim, Norway

^b Hydro Aluminium, Research and Technology Development (RTD), NO-6601, Sunndalsøra, Norway

^c Institute for Energy Technology, NO-2027, Kjeller, Norway

ARTICLE INFO

Article history:

Received 29 January 2015

Received in revised form

7 May 2015

Accepted 14 May 2015

Available online 12 June 2015

Keywords:

Ballistics

Impact

Aluminum alloy

MIG welding

Numerical methods

ABSTRACT

Perforation of welded aluminum structures by small-arms bullets is studied both experimentally and numerically in this paper. From the chemical composition, artificial aging history, and welding procedure, the spatial distribution of the flow stress at ambient temperature of MIG-welded AA6082-T6 aluminum extrusions was determined by using a thermal finite element model and a nano-scale material model. The resulting flow-stress curves which are functions of the distance from the weld center line were used in a mechanical 3D finite element model to investigate the effect of the heat affected zone (HAZ) on the ballistic properties of welded aluminum extrusions. For experimental validation, 10 mm, 20 mm and 30 mm thick extruded profiles were processed and welded to correspond to the numerical method. Hardness measurements and ballistic impact experiments were performed in the weld metal, HAZ, and base material. Uniaxial tension tests were conducted for the base material of the 10 mm and 30 mm profiles. These tests provided sufficient data for experimental validation of the numerical method. Temperature distribution, hardness values, equivalent stress-strain curves, and ballistic limit curves are reported from both the experiments and the numerical simulations. In general, the experimental results correspond well with the numerical predictions and the predicted ballistic limit velocities are within 10% of the experimental ones, suggesting that this method is a possible alternative to performing expensive and time consuming experimental testing in the early stages of the design of protective aluminum structures. The HAZ was found to impair the ballistic performance locally, but the difference between the ballistic limit for the base material and HAZ was never more than 10% in this study.

© 2015 Elsevier Ltd. All rights reserved.

1. Introduction

Most studies concerning the ballistic capabilities of structures involve perpendicular impact on flat, flawless surfaces where the effects of connections are disregarded [1–5]. However, size and shape limitations inherent in ordinary construction processes make the presence of e.g. welds, nuts, or bolts inevitable. Consequently, knowledge about connections is essential in any design situation. In the design of protective structures against small-arms bullets, thin plates made of steel are widely used due to their advantageous

combination of strength, hardness, ductility, and relatively low price compared to most other armor materials [6]. However, when areal mass is taken into account, high-strength aluminum alloys can rival the ballistic properties of high-strength steels [7,8].

Welding is a common and effective joining procedure, but welding of aluminum generates a zone which may be weak relative to the base material. This zone is known as the heat affected zone (HAZ), and it may cause a so-called ballistic window in protective structures. Usually material strength governs ballistic performance [6,9], so special attention is required in the design of welded aluminum protective structures.

The strength and work hardening of Al–Mg–Si aluminum alloys can be predicted with reasonable accuracy by nano-scale material models [10–13]. The application of such a model was shown by Johnsen et al. [14], where the stress-strain behavior of four different

* Corresponding author. Tel.: +47 93 04 58 37.

E-mail address: jens.k.holmen@ntnu.no (J.K. Holmen).

1 URL: www.ntnu.edu/simlab.

heat treatments (tempers) of the wrought aluminum alloy AA6070 was determined with a nanostructure model, NaMo. The model was able to predict the yield strength and work hardening of the different tempers. Subsequently, mechanical non-linear finite element simulations, using the yield strength and work-hardening determined with NaMo as input, accurately described the ballistic behavior. This correlation suggests that employing the predictive capabilities of nano-scale material modeling in combination with tools that can provide thermal histories in all material points due to welding can dramatically reduce the need for expensive and time-consuming experimental programs.

Computational models which were designed to incorporate elements of the manufacturing process for conventionally or friction-stir welded steel and aluminum protective structures have also been of interest for several years [15–17]. These techniques are often called through-process modeling. In some cases, the ballistic behavior is included in the model [18–21].

There are two main objectives of this paper. First, we investigate how welding affects the ballistic properties of aluminum extrusions of various thicknesses through an extensive experimental program for 10 mm, 20 mm and 30 mm thick profiles, including tension tests for the 10 mm and 30 mm profiles; hardness measurements of the base material, HAZ, and weld for all thicknesses; and ballistic impact experiments. In the ballistic tests, armor piercing (AP) bullets are fired at the welded test specimens at various distances from the weld center line. Second, and most important in this study, a purely numerical method is demonstrated. The numerical approach is performed independently from the experiments. Hence, the experimental results are only used for validation purposes in this part of the paper. The heat distribution from multi-pass welding is calculated numerically by the thermal finite element program WELDSIM [22]. Results from selected points in these analyses are used as inputs to NaMo [23] to determine the yield strength and hardening behavior of the material as functions of distance from the weld center line, before the non-linear finite element code IMPETUS Afea Solver [24] is employed to solve the impact problem itself. All the calculations can be done without carrying out a single experiment.

Sections 2 and 3 present an experimental program in which the material processing, welding procedure, material testing, and ballistic testing are carried out to obtain an experimental basis for comparison with, and validation of, the subsequent numerical results. Section 4 outlines the numerical scheme and provides a description of the use of WELDSIM, NaMo and IMPETUS Afea Solver. In Section 5 the numerical predictions are presented, discussed, and compared to the experimental results. The main observations and conclusions are summarized in Section 6.

2. Material

2.1. Material processing and welding

Extruded 10 mm, 20 mm and 30 mm thick profiles made of AA6082-T6 were investigated in this study. The measured chemical compositions of the extrusions provided by Hydro Aluminium and the composition window of AA6082 are shown in Table 1. Due to

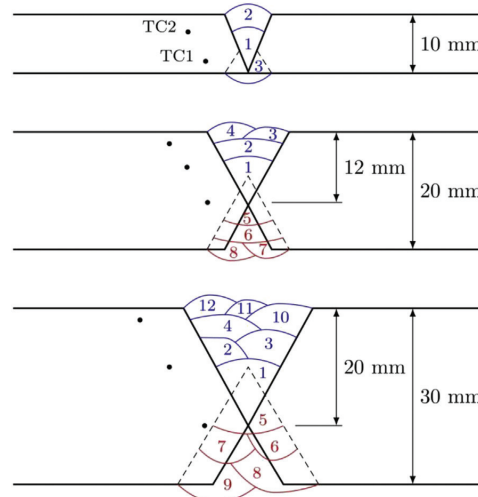


Fig. 1. Numbering of the weld-seams in the multi-pass welding procedure. Placements of the thermocouples are indicated with dots.

the varying profile thicknesses, the artificial aging to obtain the peak strength temper T6 varied. The 10 mm extrusion was held at 175 °C for 5 h and 30 min, while the 20 mm and 30 mm thick extrusions were held at 185 °C for 5 h and 10 min.

The flat extruded profiles were automatically welded to each other with MIG welding at Marin Aluminium AS. Precautions were taken to ensure that the welding process was in accordance with EN 1090-3 [25]. Numbering of the various weld seams in the multi-pass welding procedures is shown in Fig. 1. In all welding procedures the temperature of the HAZ was measured to be below 100 °C before the next weld seam was initiated. The welding consumable was a Safra 5183 welding wire designed for high corrosion environments such as ship constructions and offshore applications ($\sigma_{0.2} \geq 125$ MPa [26]). Complex thermal histories were introduced during welding due to the application of three weld passes for the 10 mm profile, eight for the 20 mm profile, and twelve for the 30 mm profile. The temperature-time histories were measured by thermocouples. The placement of these thermocouples is shown in Fig. 1, while selected results from the temperature measurements are shown later in the paper.

2.2. Material testing

Three tensile tests of the base material were performed in both the extrusion direction (0°) and the cross-weld direction (90°) for the 10 mm and 30 mm thick extruded profiles. Two typical curves from the 0°-direction are shown in Fig. 2. A Zwick Roell 30 kN tensile testing machine was used with a crosshead velocity of 1.2 mm/min. This corresponds to an initial strain rate of 5×10^{-4} s⁻¹ for the circular test specimens with an initial

Table 1
Chemical composition of the various profiles, and composition window for AA6082 in wt-%.

	Si	Mg	Mn	Fe	Ti	Zn	Cu	Cr	Al
Measured – 10 mm profile	0.93	0.60	0.55	0.18	0.011	0.002	0.008	0.011	Balance
Measured – 20 mm profile	0.99	0.63	0.56	0.17	0.018	0.006	0.025	0.011	Balance
Measured – 30 mm profile	0.97	0.63	0.54	0.16	0.013	0.004	0.004	0.013	Balance
Composition window AA6082	0.7–1.3	0.6–1.2	0.4–1.0	0.50	0.10	0.20	0.10	0.25	Balance

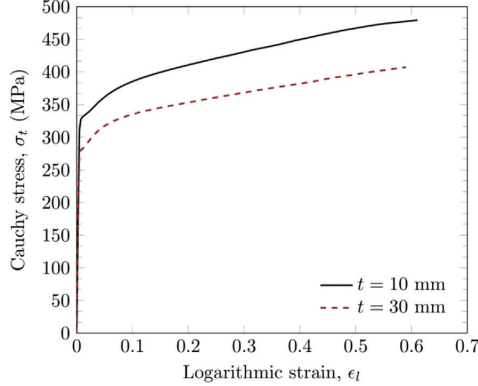


Fig. 2. Typical Cauchy stress-logarithmic strain curves from experimental tension tests taken from a 10 mm thick profile and a 30 mm thick profile.

gauge-length of 70 mm and an initial diameter, $d_0 = 6 \text{ mm}$ (see e.g. Holmen et al. [9] for the specimen geometry). Diameter reduction was continuously measured in two perpendicular directions all the way to fracture by a laser-scan micrometer [27]. Assuming plastic incompressibility the Cauchy stress σ_t and logarithmic strain ϵ_l are calculated from the measured force F and the diameters in the thickness direction of the extrusion (d_z) and transverse direction of the specimen (d_{\perp}) as

$$A = \frac{\pi}{4} d_z d_{\perp}, \quad \sigma_t = \frac{F}{A}, \quad \epsilon_l = \ln \frac{A_0}{A} \quad (1)$$

where A_0 is the initial area of the specimen. There is no significant difference in yield strength, flow stress or failure strain obtained from the tests in the 0° and 90° -directions for the 10 mm thick profile. Some anisotropy was seen for the yield strength of the 30 mm thick profile (the 90° -direction is approximately 25 MPa weaker than the 0° -direction). The scatter between repeated tests was less than 1% in yield stress and less than 4% in failure strain.

To pinpoint the location of the HAZ and to reveal the strength differences caused by the temperature history, hardness testing was conducted. The specimens are shown in Fig. 3, and they were tested with 5 kg of pressure for 15 s each in a Struers DuraScan fully automatic Vickers hardness testing machine. Hardness measurements were conducted along three horizontal lines across the weld, as well as along one vertical line in the thickness direction of the base material. Plots of the Vickers hardness can be seen in Fig. 4. An investigation of these curves shows that the 10 mm and 20 mm profiles exhibit practically equal hardness distributions, while the

30 mm profile is markedly weaker. Further investigation of Fig. 4 reveals that the lowest hardness values for each through-thickness position of the cross section follow a line offset from the fusion line, approximately 6 mm for the 20 mm thick profile (Fig. 4d) and 7 mm for the 30 mm thick profile (Fig. 4f). For the 10 mm thick profile the lowest hardness values are located along a nearly straight vertical line (Fig. 4b). The average hardness and the sample standard deviation (s) in the base material for the 10 mm, 20 mm and 30 mm thick extruded profiles are 110 HV ($s = 0.4 \text{ HV}$), 105 HV ($s = 1.3 \text{ HV}$) and 89 HV ($s = 1.2 \text{ HV}$), respectively, showing that the hardness (and strength) decreases as the extrusion thickness increases. However, based on these measurements the material behavior of the 10 mm and 20 mm extrusions is assumed to be equal.

The reason for the observed lower base-metal hardness of the 30 mm thick extrusion compared with the two other thicknesses is a lower cooling rate following the extrusion process for this relatively thick profile. 6082-type alloys are known to be quench sensitive, and since the cooling rate decreases with increasing thickness, it has probably been sufficiently slow to cause severe precipitation of coarse non-hardening particles during the cooling stage as described in Ref. [28].

3. Ballistic experiments

The ballistic impact experiments were performed in the ballistic laboratory at SIMLab, NTNU. The 7.62 mm AP-bullets shown in Fig. 5 were fired from a smooth-bore Mauser rifle inside a 16 m^3 protective tank. The bullet velocity was controlled by adjusting the amount of powder in the cartridge before each shot. Detailed descriptions of the ballistic setup and bullet are provided by Børvik et al., [6,30,31]. All shots were fired from a safe distance using a magnetic trigger, and the initial and residual velocities of the bullet were measured optically with a Phantom v1610 high speed camera operating at 75,000 fps. The welds were milled flush to obtain a constant thickness before ballistic testing. Pictures of the perforation process are shown in Fig. 6. In most of the tests the jacket was completely ripped off the core and fragmented into several pieces, but the core itself remained rigid and undamaged (by visual inspection) during impact in all tests. A total of 25 shots were fired at the various parts of the respective profiles, i.e., 8–9 shots for each thickness. One shot hit directly in each weld, whereas three or four shots hit the base material and the HAZ. A shooting-map for the 10 mm thick profile is shown in Fig. 7, and the results are plotted in Fig. 8. Every shot obtained full perforation of the profiles so the ballistic limit velocity (v_{bl}) was estimated by minimizing the mean-squared-error between the solid lines and data points shown in Fig. 8. The solid lines estimate the residual velocity (v_r) based on a model originally proposed by Recht and Ipson [32].

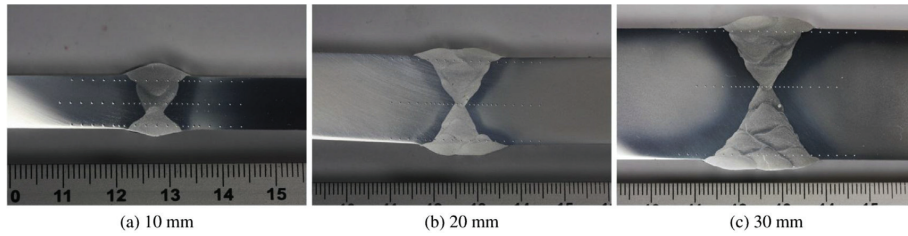


Fig. 3. Pictures of the cross section of the welds. The dots are indentations made by the hardness-test machine.

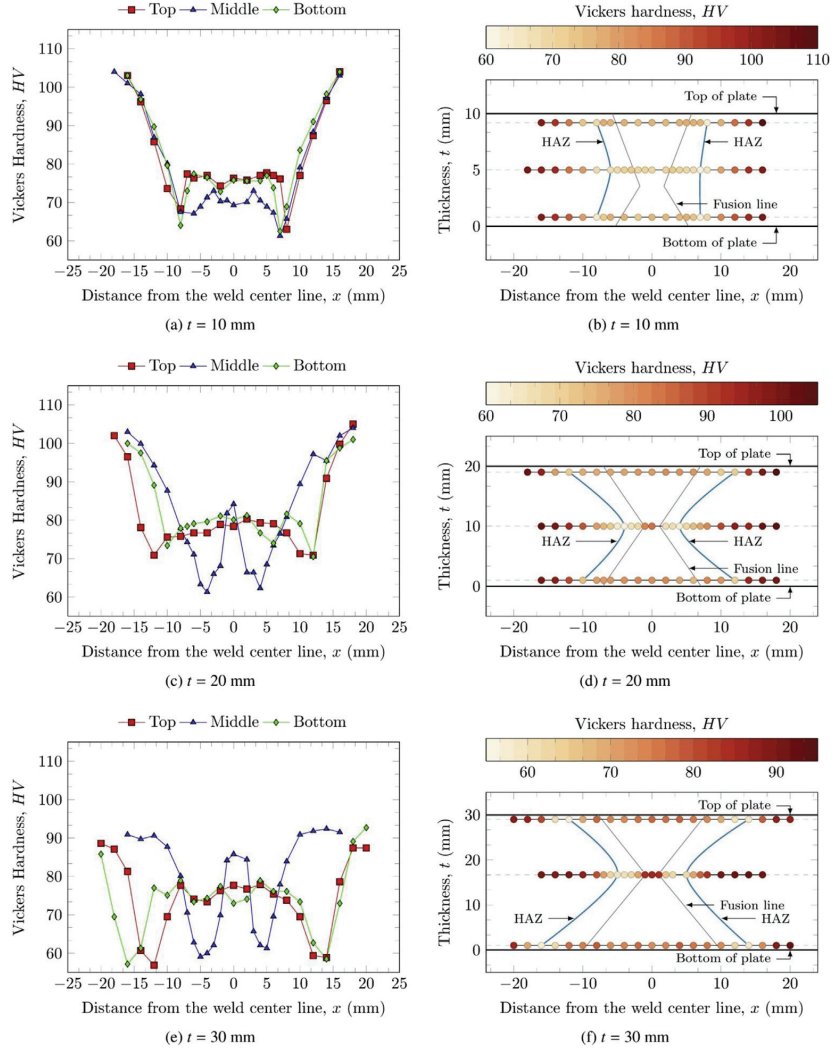


Fig. 4. Overview of the hardness measurements: (a), (c) and (e) show the Vickers hardness value as the ordinate for the three tests strings for each profile; (b), (d) and (f) show the Vickers hardness value for each indentation represented by a color. The lowest HV measurements in the HAZ and the fusion lines are indicated [29]. (For interpretation of the references to color in this figure legend, the reader is referred to the web version of this article.)

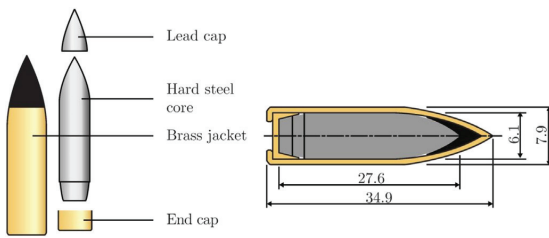


Fig. 5. Geometry of the AP-bullet used in the experiments.

$$v_r = \left(v_i^2 - v_{bl}^2 \right)^{1/2} \quad (2)$$

where v_i and v_{bl} are the initial velocity and ballistic limit velocity, respectively. This simple equation, also known as the Recht–Ipson model for rigid sharp projectiles, has been shown to represent perforation experiments with sharp projectiles on ductile targets accurately [33]. Note that the Recht–Ipson model was originally derived for rigid penetrators, which seems like a reasonable assumption in these tests.

It can be seen in Fig. 8 that welding affects the ballistic properties of the aluminum alloy, but the effect is not large. It also seems that there is a rather linear relationship between thickness and ballistic limit velocity. For the 10 mm profile the base material is the

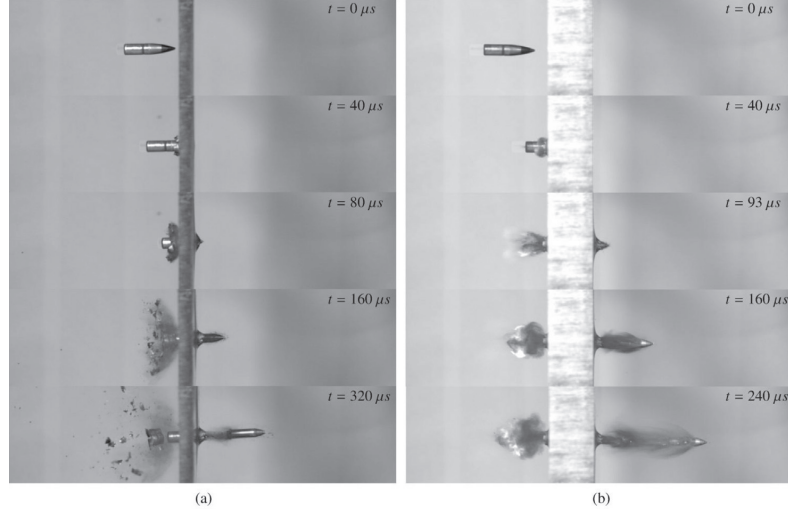


Fig. 6. Sequences of images showing the perforation process of the base material of: (a) 10 mm thick AA6082-T6 extrusion ($v_i = 390.6 \text{ m/s}$, $v_r = 179.2 \text{ m/s}$) and (b) 30 mm thick AA6082-T6 extrusion ($v_i = 726.8 \text{ m/s}$, $v_r = 457.2 \text{ m/s}$).

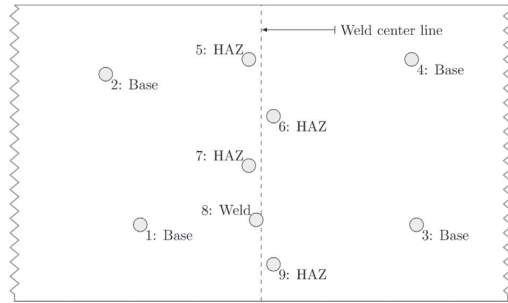


Fig. 7. Shooting-map of the 10 mm extrusion.

strongest, and impacts in the weld and HAZ give 3% and 10% lower ballistic limit velocities, respectively. Impacts on the 20 mm profile show the same trend, i.e., the base material is the strongest. In this profile, however, the weld and HAZ exhibit equal resistance against perforation and their ballistic limit velocities are both 6% lower than for the base material. Looking at the 30 mm thick profile we see that the weld is actually slightly stronger than the base material with a 1% increase in the ballistic limit velocity. Also here the HAZ is the weakest with a 3% lower ballistic limit velocity than the base material. A clear correlation can be seen between the hardness measurements in Fig. 4 and the ballistic curves in Fig. 8. The hardness of the weld metal is significantly lower than that of the base material for the 10 mm and 20 mm thick profiles, whereas for the 30 mm profile the weld metal hardness is almost at the same level as the base material. The HAZ is the weakest zone in every case.

Examples of some typical post-perforation bullet-holes are shown in Fig. 9. As these pictures indicate, the predominant failure mode in all the experiments was ductile hole-growth which was

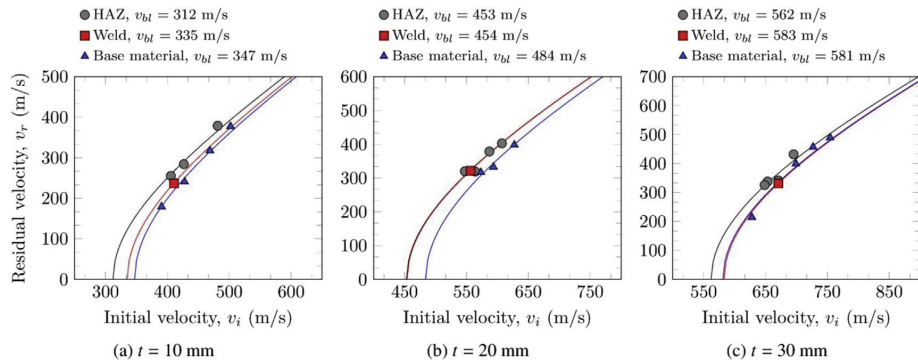


Fig. 8. Ballistic curves obtained experimentally from (a) the 10 mm thick profile, (b) the 20 mm thick profile, and (c) the 30 mm thick profile.

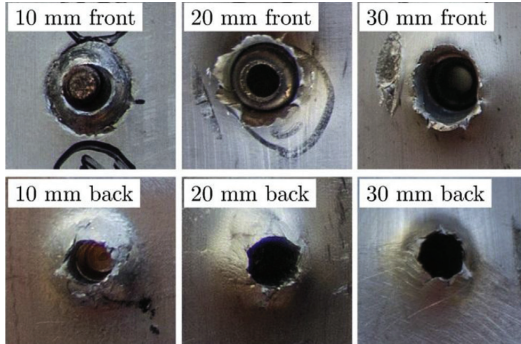


Fig. 9. Some typical bullet holes from impacts on the base material.

sometimes accompanied by moderate rear-face petaling without fragmentation.

It should be noted that these results are based on a limited set of data, in particular for impact in the welds with only one hit for each profile. It was hard to directly hit the weld, and due to limited amount of material available for testing the shots were fired in close proximity to each other. However, at least one projectile diameter (but normally 3–4) was left between each point of impact. Based on the results presented in Fig. 8, this did not seem to have any noticeable effect on the ballistic data.

4. Numerical methods

4.1. Outline

The three-step numerical procedure employed in this paper is illustrated in Fig. 10. First a thermal solver (WELDSIM) is used to predict the thermal field from the welding. Then a nano-scale material model (NaMo) makes use of the chemical composition

and the complete temperature history from aging and welding as input in order to calculate the flow-stress curves which are used by a mechanical finite element solver (IMPETUS Afea Solver) to simulate the ballistic experiments. No experimental data whatsoever has been used for calibration of the numerical models in this section. The numerical calculations are limited to the 10 mm thick extrusion since the procedure will essentially be identical for thicker profiles.

4.2. WELDSIM

The evolution of the temperature field during the welding was simulated with the thermal solver WELDSIM [22,23,34]. WELDSIM can be used to predict the evolution of temperatures, microstructure parameters and stresses during the welding process. However, in this analysis only the thermal module was applied. Symmetry along the weld center line was assumed and a 0.8 m section of the actual extrusion length of 2 m was included in the solution domain. By applying a typical arc efficiency for MIG-welding of 0.8 (i.e., the net power fraction received by the weldment when taking into account losses due to convection and radiation) and the recorded values of current, voltage and welding speed, the simulated temperature-time histories were very close to the measured temperature-time histories, as shown in Fig. 11.

The handling of multi-pass welding has previously been applied for simulation of steel welding [35,36]. The weld metal domains are predefined by the preprocessing. Elements in domains corresponding to weld metal becoming deposited in later passes are not activated during the first pass. The weld groove for the third pass was in this case made after welding of the first two passes. This was accounted for in the simulation by redefining this domain to become a filler metal domain in a restart simulation of the third weld pass. A temperature field from this pass is depicted in Fig. 12 together with the finite element mesh illustrating the activation of elements in the weld.

In Fig. 13, the peak temperatures in a central cross-section and at the top surface of the solution domain are shown. The

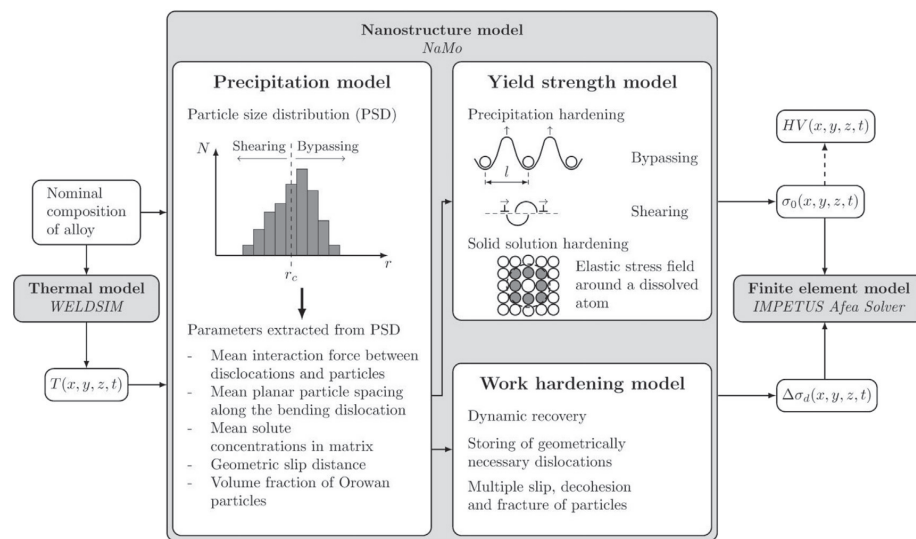


Fig. 10. Overview of the relative dependencies of the numerical models applied in this current study.

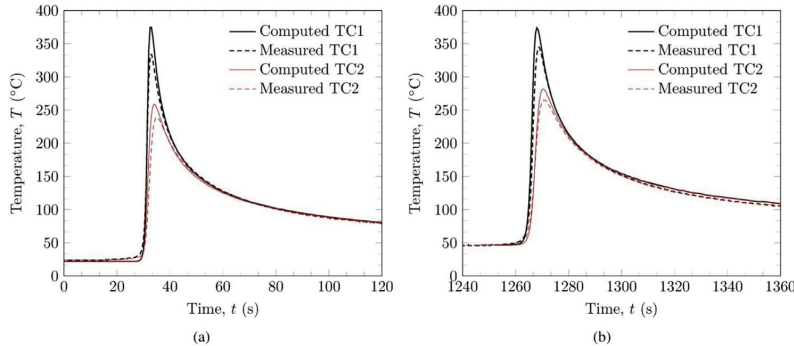


Fig. 11. Comparison of computed temperatures and temperatures measured by thermocouples (TC): (a) during the first weld pass, and (b) during the second weld pass.

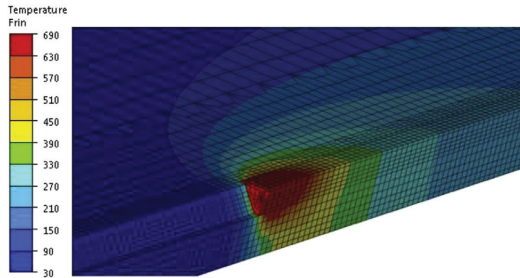


Fig. 12. The temperature field in $^{\circ}$ C during the third weld pass.

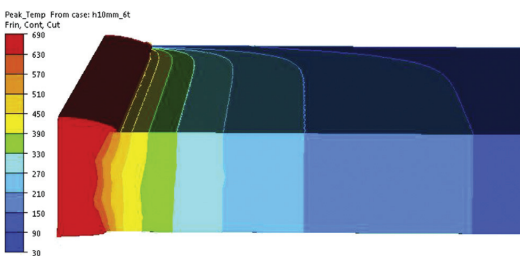


Fig. 13. Peak temperatures in $^{\circ}$ C shown on a central cross-section and the top surface of the solution domain.

leftmost contour line corresponds to the computed fusion line. This appears to be in good agreement with the picture shown in Fig. 3a.

4.3. Microstructural changes during welding and natural aging

The microstructure changes taking place during welding and room temperature storing are explained in Fig. 14, which is based on Myhr et al., [28,37]. During artificial aging, a high density of fine, needle-shaped β' particles form uniformly in the matrix, which is the dominating hardening phase in T6 heat-treated Al–Mg–Si alloys. However, since these precipitates are thermodynamically unstable in a welding situation, the smallest ones start to dissolve in parts of the HAZ where the peak temperature has been above approximately 250 $^{\circ}$ C, while the larger ones continue to grow. Close to the weld fusion line, i.e. Zone 1 in Fig. 14, full reversion of the β''

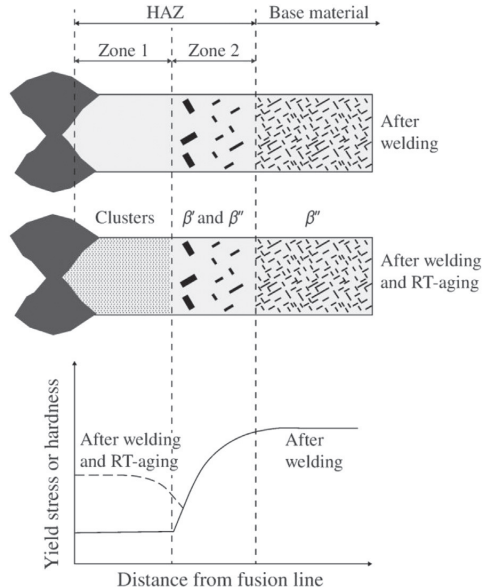


Fig. 14. Microstructural changes during welding and natural aging.

particles is achieved. At the same time, coarse rod-shaped β' precipitates may form in the intermediate peak temperature range between 250 $^{\circ}$ C and 480 $^{\circ}$ C, as indicated in Zone 2 in the figure. These β' precipitates will grow rapidly in the presence of the abundant solute being supplied from the small, dissolving β'' precipitates.

If welding is succeeded by room temperature storing, natural aging leads to cluster formation in the high peak temperature regions of the HAZ corresponding to Zone 1 in Fig. 14. It occurs depending both on the matrix vacancy concentration and the level of Mg and Si in solid solution. Accordingly, the cluster formation would be expected to be most extensive in the fully reverted region close to the weld fusion line owing to the combined effect of a high solute content and a high concentration of quenched-in vacancies. Conversely, the cluster formation will be suppressed in parts of the HAZ where the peak temperature is lower because the aluminum matrix in these regions will be depleted of vacancies and solute.

This eventually leads to the development of a permanent soft region within the HAZ after prolonged room temperature storing in agreement with experimental observations.

4.4. Nanostructure model (NaMo)

Fig. 10 describes the components of the nano-scale material model NaMo which is a combined precipitation, yield strength and work hardening model for age-hardening aluminum alloys [12,13]. The present version is comprehensively verified and validated for 6xxx series aluminum alloys [11–14,28,37,38]. The three sub-models shown in **Fig. 10** are fully integrated in a computer code, where the outputs from the precipitation model are inputs to both the yield-strength model and the work-hardening model that assume isotropic material behavior.

To run a simulation, the alloy composition and the temperature-time history must be specified. In the current study, the temperature-time history is obtained from WELDSIM. Based on the acquired information the complete room-temperature flow-stress curve is calculated by the program. The first step of a simulation is to invoke the precipitation model that calculates the evolution of the hardening precipitates by nucleation, growth or dissolution, and coarsening [11,12,28]. **Fig. 10** shows a discrete particle size distribution (PSD), where each column corresponds to a certain number density of particles within the specific size class. The PSD changes continuously during heat treatment and welding as calculated by the precipitation model. Based on the PSD, the essential precipitation parameters can be extracted and transferred to the yield-strength and work-hardening models as illustrated in **Fig. 10**.

In the yield-strength model, the overall macroscopic yield stress σ_0 is given as

$$\sigma_0 = \sigma_i + \sigma_p + \sigma_{ss} \quad (3)$$

where σ_i corresponds to the intrinsic yield stress of pure aluminum, σ_p is the overall precipitation hardening contribution, and σ_{ss} is the contribution from alloying elements in the solid solution. The simplified method described in Ref. [39] is adopted here to predict the effect of cluster formation and the associated yield strength increase during room temperature storing in regions where the peak temperature has been sufficiently high to cause partial or complete dissolution of the hardening β' particles during the welding, i.e. Zone 1 in **Fig. 14**. In order to compare the predicted strength in the HAZ against hardness measurements, a conversion from yield strength (in MPa) to hardness HV (in VPN) via a simple regression formula from Ref. [11] is necessary

$$HV = 0.33\sigma_0 + 16.0 \quad (4)$$

The work-hardening model predicts the individual evolution of statistically stored and geometrically necessary dislocations, respectively, based on well-established evolution laws. The evolution of statistically stored dislocations is predicted as the balance between statistical storage and dynamic recovery of dislocations, while the generation of geometrically necessary dislocations during plastic deformation is assumed to be associated with non-shearable particles. When the two contributions to the overall dislocation density are predicted, the resulting net contribution from dislocation hardening $\Delta\sigma_d$ is calculated from a response equation as a function of the plastic strain, as described in Ref. [12]. Finally, the flow stress σ_f is calculated as follows

$$\sigma_f = \sigma_0 + \Delta\sigma_d \quad (5)$$

Here σ_0 and $\Delta\sigma_d$ are the room temperature yield stress and the net contribution from dislocation hardening, respectively. This allows the complete stress-strain curve to be calculated and transferred to the IMPETUS Afea Solver.

The flow-stress curves for various distances from the weld center line resulting from NaMo simulations are presented in **Fig. 15**, while **Fig. 16** compares the experimental hardness distribution to the values predicted by NaMo for the 10 mm profile using Eq. (4). It is interesting to note that one week of room temperature storage has a pronounced effect on the predicted hardness distribution in the regions close to the weld.

To see how well the numerical method coincides with the experimental results for the base material, the hydrostatic contribution to the true stress-strain curve in **Fig. 2** has been removed by use of the Bridgman correction [40] and plotted together with the flow-stress curve obtained from NaMo for the base material. The comparison is shown in **Fig. 17**. The correspondence is seen to be good, especially for plastic strains up to 0.3, as shown in **Fig. 17b**.

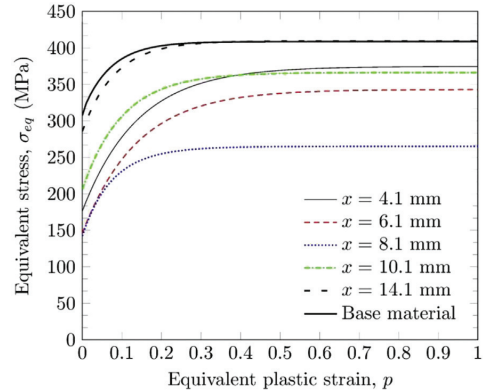


Fig. 15. The resulting flow-stress curves obtained from NaMo. These curves determine the hardening behavior in the constitutive model used in IMPETUS Afea Solver. Here x is defined as the distance from the weld center line.

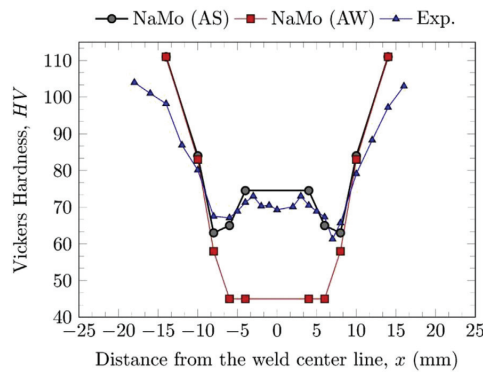


Fig. 16. Vickers hardness values obtained from NaMo compared to an experimental curve. NaMo (AS) = hardness values after one week of storage at room temperature while NaMo (AW) = hardness values directly after welding.

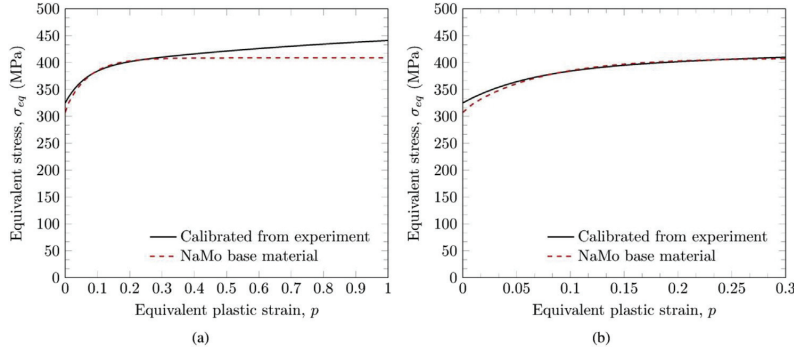


Fig. 17. Equivalent stress-equivalent plastic strain curves taken from the numerical work (WELDSIM and NaMo) and a Bridgman-corrected curve from the experiments for (a) $p \in [0:1]$, and (b) $p \in [0:0.3]$.

4.5. IMPETUS Afea Solver

The explicit finite element code IMPETUS Afea Solver [24] was used to simulate the impact process in this paper. A modified Johnson–Cook constitutive relation was chosen to represent the material behavior in the mechanical finite element simulations, i.e., the von Mises yield criterion, the associated flow rule, and an isotropic hardening rule are assumed [41]. This can be done because the material was found to be practically isotropic, see Section 2. Thus, the constitutive relation is expressed as

$$\sigma_{eq} = \left(\sigma_0 + \sum_{i=1}^2 Q_i (1 - \exp(-C_i p)) \right) (1 + \dot{p}^*)^c (1 - T^{*m}) \quad (6)$$

where σ_{eq} is the equivalent stress, p is the equivalent plastic strain, $\dot{p}^* = \dot{p}/\dot{p}_0$ is the dimensionless plastic strain rate and $T^* = (T - T_r)/(T_m - T_r)$ is the homologous temperature. Here \dot{p}_0 is a reference strain rate, T is the absolute temperature, T_r is the ambient temperature and T_m is the melting temperature. Adiabatic heating was assumed in all simulations, and the incremental temperature evolution is calculated using

$$\Delta T = \int_0^p \frac{\chi}{\rho C_p} \sigma_{eq} dp \quad (7)$$

where χ is the Taylor–Quinney coefficient, C_p is the specific heat, and ρ is the material density. The parameters σ_0 , Q_i , C_i , Q_2 and C_2 of the isotropic hardening rule are summarized in Table 2. They were found by curve-fitting to the equivalent stress-equivalent plastic strain curves obtained by NaMo in Section 4.4. All other model parameters are taken from the literature and given in Table 3. The strain-rate sensitivity of a similar material was investigated by

Chen et al. [42] and found to be almost negligible, justifying the low value of c used in the simulations. A linear degradation of strength is introduced in the model through the homologous temperature parameter $m = 1$. This is common in impact analyses; see e.g. Børvik et al. [6].

By recognizing that high-velocity impact is an extremely localized process, virtually unaffected by the boundary [43], we only need to model a part of the profile. To save additional computational time, the inherent symmetry of the problem was exploited by modeling only 30° of the target and projectile. A picture of the calculation model and its mesh is shown in Fig. 18. Ten cubic elements, known to be excellent in describing bending, were used over the target thickness, i.e., an element size of 1 mm. Note that by using the cubic elements the effective node spacing was: $\Delta z = 0.33$ mm, giving 31 nodes over the thickness. Sufficient information to calibrate a failure criterion could not be extracted from NaMo, so to allow the projectile to pass through the material a pinhole with a radius of 0.25 mm was introduced in the target's mesh. The pinhole enables us to effectively circumvent the need for a fracture criterion in ballistic perforation using pointed-nose projectiles, and its size was chosen as small as possible without introducing numerical difficulties. In problems where ductile hole growth is expected to be the predominant failure mode the effect of such a pinhole is observed to be small [14,44], allowing us to employ relatively large fully integrated cubic 64-node hexahedron elements with 3rd-order shape functions since the absence of element erosion prevents mass loss resulting in an artificial reduction of the capacity. Contact was taken care of by a penalty based node-to-surface algorithm. The effect of friction is disregarded in many studies, however, with ogival-ended projectiles frictional forces do exist. Zukas [45] recommended 0.01 to be used as a dynamic friction coefficient. Ravid and Bodner [46] found that a friction coefficient of 0.1 is proposed in the literature for metal working applications, but they themselves advocated a value of 0.05 for impact situations. We realize that there might be frictional forces between the bullet and the plate, so in this study it was decided to use a frictional coefficient of 0.05 in the contact algorithm (see also [47]). However, it should be mentioned that

Table 2
Parameters for the isotropic hardening rule fitted to the equivalent stress—equivalent plastic strain curves computed by NaMo (cf. Fig. 15).

Distance from center weld (mm)	σ_0 (MPa)	Q_1 (MPa)	C_1	Q_2 (MPa)	C_2	Comment
0.0 mm and 4.1 mm	176.3	198.4	7.2	—	—	At fusion line
6.1 mm	146.0	187.1	7.2	—	—	
8.1 mm	142.1	19.7	23.3	103.2	11.7	Weakest
10.1 mm	205.8	69.5	11.5	91.1	8.7	
14.1 mm	285.6	125.0	12.2	—	—	
Base material	307.3	4.3	278.7	97.1	14.1	Strongest

Table 3
Physical constants and model parameters used in IMPETUS Afea Solver [9].

E (MPa)	ν	ρ (kg/m ³)	m	c	\dot{p}_0 (s ⁻¹)	T_r (K)	T_m (K)
70,000	0.3	2700	1	0.001	5×10^{-4}	293	923

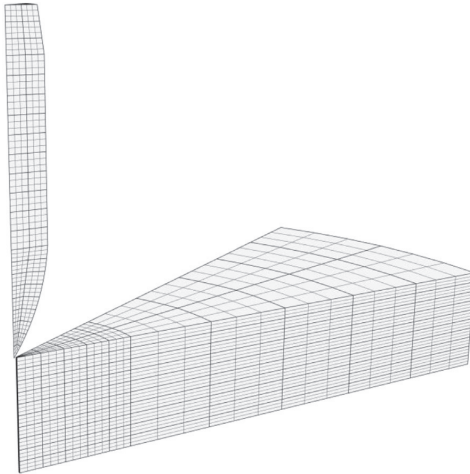


Fig. 18. Solid element mesh used for the 10 mm thick profile in the IMPETUS Afea Solver. Two symmetry planes were assigned to enable modeling of only a 30° wedge.

including frictional effects in the sliding contact might contribute to non-conservative results [14,43].

The AP-bullet was represented by its steel core with a rigid material formulation in all simulations, requiring only the density for steel, $\rho = 7850 \text{ kg/m}^3$ as material input. Previous works have shown that the change in residual velocity is not significant if the entire AP-bullet with correct material input or only the core is used [6–9].

One finite element model was made with each of the material curves described by the parameters in Table 2. In other words, no attempt was made to describe the variation of the material parameters as a function of distance from the weld center line. NaMo does not provide material behavior from the center of the weld. Thus, in the simulations marked weld we have assumed the same behavior as at the location $x = 4.1 \text{ mm}$ from the weld center line.

5. Results and Discussion

Fig. 19 shows the evolution of the equivalent plastic strain for a typical simulation of impact on the base material. Observe that no plastic strains accumulate outside a zone roughly one projectile

radius ($r = 3.05 \text{ mm}$) from the edge of the hole. This is consistent with the corresponding experiments. For impacts with lower velocities a zone of approximately one projectile diameter ($d = 6.10 \text{ mm}$) is affected.

The numerical results are compared to the experimental results for the 10 mm thick profile in Fig. 20. For the base material, Fig. 20a, the ballistic limit velocity found numerically ($v_{bl} = 344 \text{ m/s}$) is almost identical to the ballistic limit velocity found experimentally ($v_{bl} = 347 \text{ m/s}$). Such a match is in many ways coincidental seeing that many uncertainties exist in the experimental results and that a number of assumptions have been applied in the numerical model. In any case, the agreement between the experimental results and the numerical predictions is excellent.

Fig. 20b shows the results from the weld center line. Only one shot was fired directly at the weld-seam in the 10 mm thick profile. Furthermore, the constitutive behavior of the weld used in IMPETUS Afea Solver is presumed to be equal to the behavior of the material at a location 4.1 mm from the center of the weld. This seems to be a rational assumption based on the results from the hardness tests in Fig. 16. Here the numerically obtained ballistic limit velocity ($v_{bl} = 312 \text{ m/s}$) underestimates the ballistic limit velocity ($v_{bl} = 335 \text{ m/s}$) found from experiments with 6.9%.

Comparing results obtained from the HAZ, as seen in Fig. 20c, is more involved. In this area, only one ballistic limit velocity is available from the experiments, but several ballistic limit velocities have been found numerically since NaMo provided input to the constitutive model from multiple points at various distances x from the weld center line. The 7.62 mm AP-bullet has a finite diameter, so each impact will encompass several of the zones corresponding to the material behavior predicted by NaMo. By inspecting Fig. 20c we see that the experimentally obtained ballistic limit curve is surrounded by the curves obtained from simulations. The curves with the lowest and highest ballistic limit velocities are extracted 8.1 mm and 14.1 mm from the weld center line, respectively, which is also suggested in Fig. 15. These points represent the lower and upper bounds for the results from the HAZ. The v_{bl} for the experiment is 312 m/s, while the average of all the numerical values is $v_{bl} = 309.0 \text{ m/s}$, i.e., only 1.0% lower. To employ an average value for the numerical results is a crude way of simulating that the bullet hits several zones in the HAZ at the same time. Nevertheless, it illustrates the accuracy of the solution method. Another way of incorporating the zones would be to extract the spatially varying material parameters from NaMo and use this to assign the correct behavior to each integration point in the IMPETUS Afea Solver. That is left for further work.

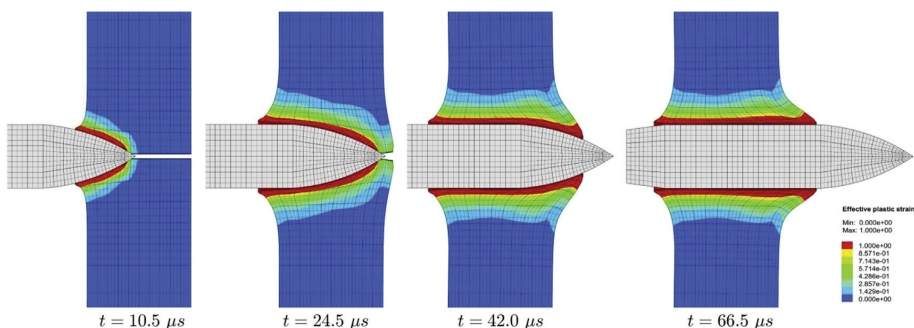


Fig. 19. A typical perforation process displayed as a timelapse. The colors show accumulated plastic strain in the range $\epsilon \in [0;1]$, and the mesh is reflected about the center line to illustrate the pinhole ($v_i = 450.0 \text{ m/s}$, $v_r = 290.0 \text{ m/s}$). (For interpretation of the references to color in this figure legend, the reader is referred to the web version of this article.)

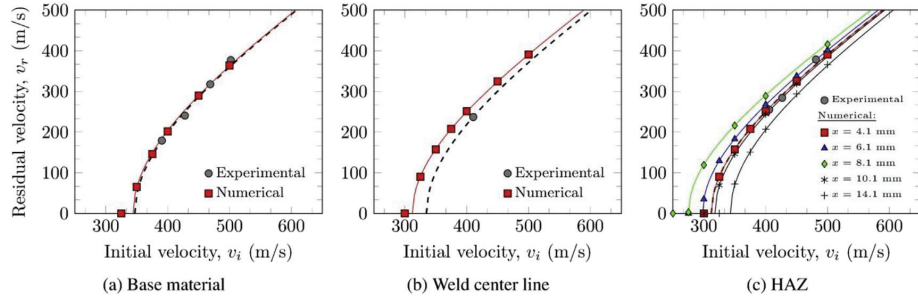


Fig. 20. Experimental ballistic curves from (a) the base material, (b) the center of the welding zone, and (c) the HAZ; compared to purely numerical simulations.

Fig. 21 shows the bullet's residual velocity as a function of mesh density. Two cubic elements over the thickness yield no perforation. A softer response is achieved with an increasing mesh density, but no change in residual velocity can be seen if the number of elements over the thickness is increased above 10 elements. A typical analysis took approximately 3 min to run with 10 cubic elements over the thickness, but with 30 cubic elements over the target thickness the analysis time increased to over 60 min.

By replacing a fracture criterion with a pinhole, we presume that only ductile hole-growth takes place. This is, with the exception of some rear-face petaling, true for the tests performed in this study. If more brittle failure mechanisms like rear-face spalling or fragmentation take place, a fracture criterion must be implemented to describe the more complex failure mode. However, for relatively thick profiles the rear-face petaling observed in this paper is generally not considered as a major energy dissipating mechanism [19], and a pinhole can safely be adopted.

The effect of the size of the pinhole is shown in **Fig. 22**. It is evident that for the conditions investigated in this study the radius of the pinhole affects the results. A linear decrease in residual velocity from 225.4 m/s to 201.2 m/s (i.e., 11%) is seen when reducing the pinhole radius from 1 mm to 0.20 mm. The maximum equivalent plastic strain in the analysis goes towards infinity for pinhole radius less than 0.2 mm because of unphysical element deformation. This is a numerical effect, and we conclude that the analyses cease to be valid below this pinhole size. Comparing these results to results seen in the literature (e.g., Camacho and Ortiz [44] and Chen [48]) indicates that significantly smaller pinholes than those used here can be applied in 2D axisymmetric simulations and in simulations where friction is omitted.

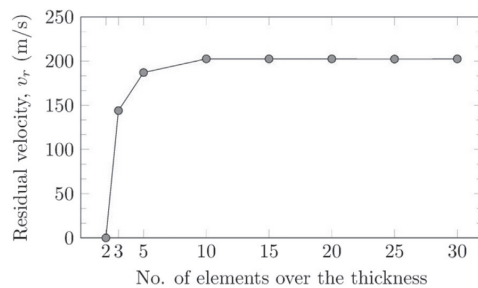


Fig. 21. Results from the mesh-sensitivity study with initial velocity $v_i = 400$ m/s, and pinhole radius $r = 0.25$ mm.

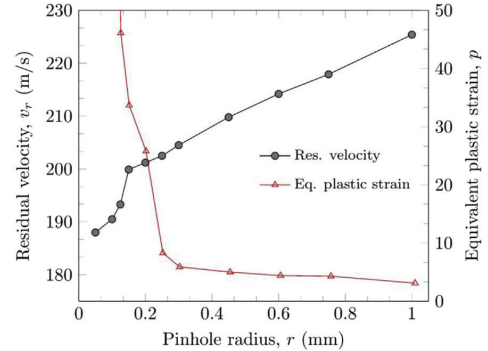


Fig. 22. Results from the pinhole study with initial velocity $v_i = 400$ m/s, and 10 elements over the thickness.

6. Conclusions

In the experimental part of this paper, MIG-welded 10 mm, 20 mm and 30 mm thick AA6082-T6 aluminum extruded profiles were impacted by small-arms bullets to determine the effect of the heat affected zone (HAZ) on their ballistic limit velocity. In the tests, 7.62 mm AP-bullets were fired at the base material, weld metal and the HAZ with varying initial velocities. In all tests, the predominant failure mode was ductile-hole growth. The ballistic limit velocities were calculated with the Recht-Ipson equation for rigid sharp projectiles. We found a linear relationship between ballistic limit velocity and extrusion thickness for the respective targets. For all profiles the base material exhibited the highest ballistic limit velocity while the HAZ exhibited the lowest. The reduction of capacity was highest for the 10 mm thick profile where a 10% decrease in the ballistic limit velocity in the HAZ was observed.

No experimental data was used in the numerical part of the paper. Here, the simulated temperature evolution during welding, the chemical composition and the artificial aging history were used to calculate the spatial distribution of the flow stress and subsequently the ballistic limit curves for the 10 mm thick profile. The thermal finite element model WELDSIM estimated accurately the temperature evolution during welding. A nanostructure model (NaMo) then calculated the flow-stress curves that were used as input to the IMPETUS Afea Solver. The final results, provided as ballistic limit velocities, are in very good agreement with the experimental results, especially if we consider that no experimental data whatsoever was used to calibrate the models. The

trends from the simulations reflect the trends seen in the experiments, and the deviation is never more than 10%.

This paper shows that we can predict the ballistic behavior of AA6xxx aluminum alloys subjected to complex thermal histories without carrying out a single experiment. The fact that the numerical method described here gives results within 10% of the corresponding experiments suggests that this method can be very useful in the early design phase.

Acknowledgment

The financial support for this work from the Structural Impact Laboratory (SIMLab), Centre for Research-based Innovation (CRI) at the Norwegian University of Science and Technology and the Norwegian Defence Estates Agency (NDEA), is gratefully acknowledged. The authors would like to thank Dr. Ida Westermann at SINTEF Materials and Chemistry for carrying out the hardness measurements, Mr. Trond Auestad for managing the ballistic tests, and Mr. Steffen Breivik and Mr. Espen Frøyen for their significant contribution in both experimental work and graphical design. The authors would also like to thank Mr. Steinar Lundberg at Hydal Aluminium Profiler AS as well as Mr. Nils Jakob Tjøstheim at Hydro Aluminium for planning and managing the welding process and the temperature measurements, respectively.

References

- [1] Zukas JA. Impact effects in multilayered plates. *Int J Solids Struct* 2001;38:3321–8.
- [2] Børvik T, Hopperstad OS, Berstad T, Langseth M. Numerical simulation of plugging failure in ballistic penetration. *Int J Solids Struct* 2001;38:6241–64.
- [3] Dey S, Børvik T, Teng X, Wierzbicki T, Hopperstad OS. On the ballistic resistance of double-layered steel plates. *Int J Solids Struct* 2007;44:6701–23.
- [4] Rusinek A, Rodrigues-Martinez JA, Arias A, Klepaczko JR, Lopez-Puente J. Influence of conical projectile diameter on perpendicularly impact of thin steel plate. *Eng Fract Mech* 2008;75:2946–3967.
- [5] Iqbal MA, Gupta NK. Ballistic limit of single and layered aluminum plates. *Strain* 2011;47:205–19.
- [6] Børvik T, Dey S, Clausen AH. Perforation resistance of five different high-strength steel plates subjected to small-arms projectiles. *Int J Impact Eng* 2009;36:948–64.
- [7] Børvik T, Forrestal MJ, Warren TL. Perforation of 5083-H116 aluminum armor plates with ogive nose rods and 7.62 mm APM2 bullets. *Exp Mech* 2010;50:969–78.
- [8] Forrestal MJ, Børvik T, Warren TL. Perforation of 7075-T651 aluminum armor plates with ogive nose rods and 7.62 mm APM2 bullets. *Exp Mech* 2010;50:1245–51.
- [9] Holmen JK, Johnsen J, Jupp S, Hopperstad OS, Børvik T. Effects of heat treatment on the ballistic properties of AA6070 aluminum alloy. *Int J Impact Eng* 2013;58:119–33.
- [10] Deschamps Y, Brechet Y. Influence of predeformation and ageing of an Al–Zn–Mg alloy-II. Modeling of precipitation kinetics and yield stress. *Acta Mater* 1999;47:293–305.
- [11] Myhr OR, Grong Ø, Andersen SJ. Modelling of the age hardening behavior of Al–Mg–Si alloys. *Acta Mater* 2001;49:65–75.
- [12] Myhr OR, Grong Ø, Pedersen KP. A combined precipitation, yield strength and work hardening model for Ag–Mg–Si alloys. *Metall Mater Trans* 2010;41A:2276–89.
- [13] Myhr OR, Grong Ø. Modeling of metallurgical microstructure evolution in fusion welding. *ASM Handb* 2011;41A:797–818.
- [14] Johnsen J, Holmen JK, Myhr OR, Hopperstad OS, Børvik T. A nano-scale material model applied in finite element analysis of aluminium plates under impact loading. *Comput Mater Sci* 2013;79:724–35.
- [15] Kamp N, Sullivan A, Tomasi R, Robson JD. Modelling of heterogeneous precipitate distribution evolution during friction stir welding process. *Acta Mater* 2006;54:2003–14.
- [16] Kamp N, Sullivan A, Robson JD. Modelling of friction stir welding of 7xxx aluminium alloys. *Mater Sci Eng A* 2007;466:246–55.
- [17] Grujicic M, Arakere A, Yen C, Cheeseman BA. Computational investigation of hardness evolution during friction-stir welding of AA5083 and AA2139 aluminum alloys. *J Mater Eng Perform* 2011;20:1097–108.
- [18] Grujicic M, Arakere A, Pandurangan B, Hariharan A, Yen C, Cheeseman BA. Development of a robust and cost-effective friction stir welding process for use in advanced military vehicles. *J Mater Eng Perform* 2011;20:11–23.
- [19] Grujicic M, Pandurangan B, Arakere A, Yen C, Cheeseman BA. Friction stir Weld failure mechanisms in aluminum-armor structures under ballistic impact loading conditions. *J Mater Eng Perform* 2014;22:30–40.
- [20] Grujicic M, Snipes JS, Galgalikar R, Ramaswami S, Yavari R, Yen C, et al. Ballistic-failure mechanisms in gas metal arch welds of mil A46100 armor-grade steel: a computational investigation. *J Mater Eng Perform* 2014;23:3108–25.
- [21] Sullivan A, Derry C, Robson JD, Horsfall I, Prangnell PB. Microstructure simulation and ballistic behavior of weld zones in friction stir welds in high strength aluminium 7xxx plate. *Mater Sci Eng A* 2011;528:3409–22.
- [22] Fjær HG, Myhr OR, Klokkehaug S, Holm S. Advances in aluminum weld simulations applying WeldSim. In: Siewert TA, Pollock C, editors. Proceedings of the 11th International Conference on Computer Technology in Welding, 973. Washington, USA: NIST Special Publication; 2001. p. 251–63.
- [23] Myhr OR, Klokkehaug S, Grong Ø, Fjær HG, Klukken AO. Modelling of microstructure evolution, residual stresses and distortions in 6082-T6 aluminum weldment. *Weld J* 1998;77:286–92.
- [24] IMPETUS Afea AS. IMPETUS Afea Solver: <http://www.impetus-afea.com> [cited 2014-20-10].
- [25] CEN, European Committee for Standardization. Execution of steel structures and aluminium structures. Part 3: technical requirements for aluminium structures. 2008. EN 1090–3.
- [26] Safra SPA: <http://www.safraspa.it> [cited 2014-20-10].
- [27] Fournier M, Børvik T, Benallal A, Lademo OG, Hopperstad OS. On the plastic anisotropy of an aluminium alloy and its influence on constrained multiaxial flow. *Int J Plast* 2011;27:2005–25.
- [28] Myhr OR, Grong Ø, Fjær HG, Marioara CD. Modelling of the microstructure and strength evolution in Al–Mg–Si alloys during multistage thermal processing. *Acta Mater* 2004;52:4997–5008.
- [29] Breivik SMW, Thomsen EF. Perforation of welded aluminium structures. Master's thesis. Trondheim: SIMLab, Department of Structural Engineering, Norwegian University of Sciences and Technology; 2014.
- [30] Børvik T, Langseth M, Hopperstad OS, Malo KA. Ballistic penetration of steel plates. *Int J Impact Eng* 1999;22:855–86.
- [31] Børvik T, Hopperstad OS, Langseth M, Malo KA. Effect of target thickness in blunt projectile penetration of weldox 460 E steel plates. *Int J Impact Eng* 2003;28:413–64.
- [32] Recht RF, Ipsen TW. Ballistic perforation dynamics. *J Appl Mech* 1963;30:384–90.
- [33] Rosenberg Z, Dekel E. On the deep penetration and plate perforation by rigid projectiles. *Int J Solids Struct* 2009;45:4169–80.
- [34] Fjær HG, Liu J, M'Hamdi M, Lindholm D. On the use of residual stresses from welding simulations in failure assessment analysis for steel structures. Chapter 8: mathematical modelling of weld phenomena. Verlag der Techn. Univ. Graz; 2007. p. 998–1011.
- [35] Fjær HG, Bjørneklett BI, Myhr OR. Microstructure based modeling of Al–Mg–Si alloys in development of local heating processes for automotive structures. In: Trends in materials and manufacturing technology for transportation industry and powder metallurgy research and development in the transportation industry; Warrendale, PA, USA: 2005.
- [36] Fjær HG, Aune R, M'Hamdi M. Modelling the development of stresses during single and multipass welding of a ferritic steel in an instrumented restraint cracking test. In: Modelling of casting, welding, and advanced solidification processes-XII. USA: TMS; 2009. p. 571–8.
- [37] Myhr OR, Grong Ø, Klokkehaug S, Fjær HG. Modelling of the microstructure and strength evolution during ageing and welding of Al–Mg–Si alloys. In: Cerja H, editor. Chapter 6: mathematical modelling of weld phenomena. The Institute of Materials; 2002. p. 337–63.
- [38] Dørum C, Lademo OG, Myhr OR, Berstad T, Hopperstad OS. Finite element analysis of plastic failure in heat-affected zone of welded aluminium connections. *Comput Struct* 2010;88:519–28.
- [39] Myhr OR, Grong Ø. Novel modelling approach to optimisation of welding conditions and heat treatment schedules for age hardening Al alloys. *Sci Technol Weld Join* 2009;14:621–32.
- [40] Bridgman PW. The stress distribution at the neck of a tensile specimen. *Trans Am Soc Metals* 1944;32:553–72.
- [41] Børvik T, Hopperstad OS, Berstad T, Langseth M. A computational model of viscoplasticity and ductile damage for impact and penetration. *Eur J Mech A/Solids* 2001;20:685–712.
- [42] Chen Y, Clausen AH, Hopperstad OS, Langseth M. Stress-strain behavior of aluminium alloys at a wide range of strain rates. *Int J Solids Struct* 2009;46:3825–35.
- [43] Børvik T, Olovsson L, Dey S, Langseth M. Normal and oblique impact of small arms bullets on AA6082-T4 aluminium protective plates. *Int J Impact Eng* 2011;38:577–89.
- [44] Camacho GT, Ortiz M. Adaptive Lagrangian modelling of ballistic penetration of metallic targets. *Comput Methods Appl Mech Eng* 1997;142:269–301.
- [45] Zukas JA. High velocity impact dynamics. 1st ed. New York: John Wiley & Sons, Inc; 1990.
- [46] Ravid M, Bodner SR. Dynamic perforation of viscoplastic plates by rigid projectiles. *Int J Eng Sci* 1983;21:577–91.
- [47] Børvik T, Hopperstad OS, Berstad T, Langseth M. Perforation of 12 mm thick steel plates by 20 mm diameter projectiles with blunt, hemispherical and conical noses, Part II: numerical simulations. *Int J Impact Eng* 2002;27:37–64.
- [48] Chen EP. Finite element simulation of perforation and penetration of aluminum targets by conical-nosed steel rods. *Mech Mater* 1990;10:107–15.

Part 3

Jens Kristian Holmen, Joakim Johnsen, Odd Sture Hopperstad, Tore Børvik

Influence of fragmentation on the capacity of aluminum alloy plates subjected to ballistic impact

European Journal of Mechanics A/Solids 55 (2016) 221–233.



Influence of fragmentation on the capacity of aluminum alloy plates subjected to ballistic impact



Jens Kristian Holmen*, Joakim Johnsen, Odd Sture Hopperstad, Tore Børvik

Structural Impact Laboratory (SIMLab) and Centre for Advanced Structural Analysis (CASA), Department of Structural Engineering, Norwegian University of Science and Technology, Norway

ARTICLE INFO

Article history:
Received 8 July 2015
Accepted 25 September 2015
Available online 9 October 2015

Keywords:
Ballistic impact
Fragmentation
Node-splitting

ABSTRACT

In this paper, the perforation resistance of 20 mm thick aluminum plates subjected to moderate velocity impacts is examined experimentally and numerically. Plates made of four different tempers of aluminum alloy AA6070 were struck by ogive-nosed and blunt-nosed cylindrical projectiles with a diameter of 20 mm. We show that for this alloy material strength is not the decisive factor for the plates' resistance against perforation, but that a combination of ductility and strength, which inhibits fragmentation of the target plate, might be more important. Interpreting the results with previously obtained experimental data in mind sheds new light upon the role fragmentation plays for the capacity of metal plates undergoing impact loading. Increasing the material strength increases the probability of fragment ejection, which is unfavorable for the capacity. A novel 3D node-splitting technique which is available in the finite element code IMPETUS Afea Solver was employed to describe possible fragmentation and debris ejection in the numerical simulations. By using the node-splitting approach instead of element erosion, an improvement in the qualitative description of fracture for the least ductile tempers can be obtained without compromising the predicted component behavior for the more ductile tempers.

© 2015 Elsevier Masson SAS. All rights reserved.

1. Introduction

For impacts by small-arms bullets it has been observed both experimentally and numerically that material strength is the single most important parameter when it comes to perforation resistance (Børvik et al., 2009; Holmen et al., 2013). However, results from studies with larger projectiles at lower impact velocities suggest that the capacity of plates subjected to projectile impact is not only dependent upon material strength, but also upon the local ductility (Børvik et al., 2010a,b; Forrestal et al., 2010; Rodríguez-Millán et al., 2014). Consequently, structural materials with a balanced combination of strength and ductility may, under certain impact conditions, be equally good or even better energy absorbers than special alloys having high strength at the expense of ductility.

Accurate numerical descriptions of failure and fracture are important not only for ballistic impact, but also for analyses of events like metal forming operations and accidentally applied loads such as dropped objects, bird-strikes, explosions and collisions. Hence, criteria to predict the onset of failure are plentiful in the

literature. Some models, like Gurson-type models (Gurson, 1977; Nahshon and Hutchinson, 2008), account explicitly for void growth in ductile materials, while others define a fracture surface (Johnson and Cook, 1985) or assume that plastic straining amplified by a factor (e.g. depending on the stress state) drives the damage (Cockcroft and Latham, 1968). Having chosen a failure criterion, the next step is to introduce fracture into a numerical finite element model. To this end, element erosion is the most common method, but node separation, or node-splitting, is advantageous in many ways and has been applied to various problems in past studies (Xu and Needleman, 1994; Camacho and Ortiz, 1996; Komori, 2001; Ruggiero et al., 2014; Moxnes et al., 2014; Olovsson et al., 2015). For ballistic impact, fragmentation and debris ejection are poorly described by conventional methods and node-splitting appears to be a promising strategy to capture these phenomena.

Aluminum can through alloying and heat treatments obtain a great number of useful properties with respect to perforation resistance, but it is still not fully clear from the existing literature which properties are most crucial for the capacity under various impact conditions. The purpose of this study is therefore two-fold. In the experimental part the main objective is to investigate the effects of yield stress, strain hardening and ductility on the ballistic properties of 20 mm thick rolled plates made of the aluminum alloy

* Corresponding author. Tel.: +47 93 04 58 37.

E-mail address: jens.k.holmen@ntnu.no (J.K. Holmen).

URL: <http://www.ntnu.edu/casa>

Table 1
Chemical composition of the aluminum alloy AA6070 (wt-%).

Si	Mg	Fe	Cu	Mn	Al
1.38	1.23	0.22	0.26	0.54	Balance

AA6070. Four different heat treatments which emphasize variations in the above mentioned properties are applied to the plates. The plates are then struck by ogive-nosed and blunt-nosed cylindrical projectiles with a diameter of 20 mm and a mass of 197 g in the intermediate velocity regime, and the results are discussed in terms of their strength and ductility. In the numerical part the main objective is to evaluate and compare the predictive capabilities of a novel 3D node-splitting technique versus element erosion considering the current experimental results involving fragmentation for some of the tempers. The former numerical method has recently been implemented in the non-linear finite element code IMPETUS Afea Solver (IMPETUS Afea AS, 2015), and appears very appealing in situations where fragmentation and crack propagation in finite element models may occur. In this part we use a rather simple base model to be able to compare the different computational failure methods and to study how they capture fragmentation. We do not expect, or seek, a one-to-one relation between the experiments and the simulations.

The quasi-static material behavior and the perforation behavior of AA6070 aluminum plates struck by 7.62 mm armor piercing (AP) bullets were studied previously by the authors in Holmen et al. (2013). Herein, projectiles of diameter 20 mm have been used to strike the material plates. This provokes different perforation mechanisms compared to the smaller AP-bullets and it shows that perforation resistance is not a function only of material strength.

2. Material

Table 1 shows the chemical composition of the aluminum alloy AA6070 which was delivered by Hydro Aluminium Rolled Products in Bonn, Germany. After hot-rolling to a thickness of 20 mm, the plates were heat treated as described in Table 2 to achieve the following tempers: temper O (annealed), temper T4 (naturally aged), temper T6 (peak strength) and temper T7 (over-aged). Micrographs showed that the grain structure was not significantly altered by the thermal processing (Holmen et al., 2013).

Tripligate quasi-static tension tests were performed on smooth axisymmetric specimens taken from three different material directions to characterize the mechanical properties of the various tempers. A total of 36 quasi-static tension tests were carried out. The geometry can be found in Fig. 1. All specimens were taken from the center of the plates and the tensile axes were oriented 0°, 45° and 90° with respect to the rolling direction. The tension tests were conducted in a 20 kN DARTEC servo-hydraulic universal testing machine at an initial strain rate of $\dot{\varepsilon} = 5 \times 10^{-4} \text{ s}^{-1}$. Outputs from the testing include the force F and continuous measurements of the diameter reduction in two perpendicular directions by a laser

micrometer (Fourmeau et al., 2011). Based on these measurements the average true stress-strain curves were calculated as follows

$$\sigma_t = \frac{F}{A} = \frac{4F}{\pi D_z D_{\perp}}, \quad \varepsilon_t = \ln \frac{A_0}{A} \quad (1)$$

where σ_t is the Cauchy (true) stress, ε_t is the logarithmic (true) strain, and A is the current area. D_z and D_{\perp} are the current diameters in the thickness direction of the plate and the transverse direction of the sample, respectively.

Fig. 2 shows the true stress-strain curves to failure for typical smooth tension tests from all tempers in different specimen orientations. No significant disparity in yield and flow stress can be identified between the tests for each temper, but the failure strain, here defined as the true strain at maximum true stress, is highly dependent upon the specimen orientation. This is illustrated by temper T6 for which the failure strain ε_f in the rolling direction (0°) is almost six times as high as in the transverse direction (90°).

Generally speaking, the mechanical behavior varies dramatically from the ductile annealed temper O with low yield stress, through the naturally aged temper T4 which exhibits considerable strain hardening, to the stronger and less ductile peak strength temper T6 and over-aged temper T7 with moderate strain hardening.

3. Component testing

3.1. Setup

The ballistic impact experiments were performed in a compressed gas-gun facility of which a detailed description can be found in Borvik et al. (1999). In the tests, the projectiles were accelerated by compressed air. The air was rapidly released by the rupture of membranes that were designed to withstand a certain pressure, making it possible to determine, in advance, the approximate striking velocity of the projectile. Accurate optical measurements of the initial velocity v_i and the residual velocity v_r of the projectile were obtained either by a Photron FASTCAM SA1.1 high-speed camera operating at 40,000 fps or a Phantom v1610 high-speed camera at 50,000 fps. These cameras were also used to capture high-resolution videos of the penetration and perforation process.

Ogive-nosed and blunt-nosed cylindrical projectiles as shown in Fig. 3 were used in this study. The projectiles have diameter 20 mm and a nominal weight of 197 g. They are made of hardened tool steel with nominal yield stress σ_0 of about 1900 MPa (HRC 52). The ogive nose has a caliber radius head (CRH) of 3. Nine-piece sabots consisting of polystyrene with a hard polycarbonate outer shell were used to ensure satisfactory acceleration conditions inside the firing barrel.

The target plate dimensions were 300 mm × 300 mm × 20 mm, and one shot was fired at the center of each plate. We securely fastened the target plates to a rigid boundary by clamping the top and bottom parts of the plates with horizontal beams while keeping the vertical sides free. The free span between the clamps was 200 mm in the vertical direction in all tests.

Table 2
Heat treatments of aluminum alloy AA6070.

Temper	Solutionizing	Cooling	Annealing/Artificial aging	Cooling
AA6070-O	90 min at 560 °C (+5 °C)	Water quench	24 h at 350 °C (+5 °C)	Slow cooling
AA6070-T4	90 min at 560 °C (-5 °C)	Water quench	—	—
AA6070-T6	90 min at 560 °C (+5 °C)	Water quench	64 h at 160 °C (+5 °C)	Slow cooling
AA6070-T7	90 min at 560 °C (-5 °C)	Water quench	8 h at 200 °C (+5 °C)	Slow cooling

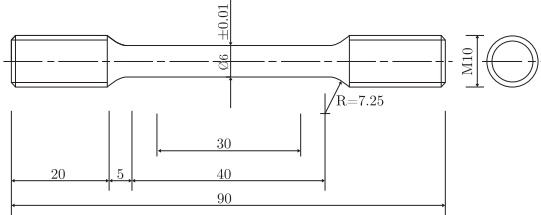


Fig. 1. Specimens used to characterize the mechanical behavior. All measures are in mm.

3.2. Experimental results

A summary of the experimental results is provided in [Table 3](#). It should at this point be emphasized that the main objective of these experiments was not to find the ballistic limit velocity of the various tempers, but to investigate the effect of yield stress, strain hardening and ductility on the ballistic properties of the alloy at constant impact velocities. Still, [Table 3](#) reports the estimated ballistic limit velocity v_{bl} and the model parameters a and p found from a least-squared-error curve fit to the generalized Recht-Ipson model ([Recht and Ipson, 1963](#)):

$$v_r = a(v_i^p - v_{bl}^p)^{1/p} \quad (2)$$

The ogive-nosed projectiles were accelerated to initial velocities $v_i \approx 250$ m/s and $v_i \approx 300$ m/s. The former proved to be very close to the ballistic limit velocity v_{bl} for temper T4 and T7 for which the respective residual velocities v_r were 18 m/s and 39 m/s. The peak strength temper T6 has slightly lower capacity and temper O is the weakest, as expected from the yield stresses given in [Table 4](#). High-speed camera images just after complete perforation of the plates in various tempers are shown in [Fig. 4](#). The pitch was measured by the high-speed cameras just before impact, and found to be below 3° in all tests. Thus, the small pitch is not expected to have any significant effect on the results ([Backman and Goldsmith, 1978](#)). [Fig. 5](#) shows the residual velocity v_r as a function of the initial velocity v_i for the impact tests with ogive-nosed projectiles. It is clearly seen that the estimated perforation resistance of the plates does not increase uniquely with the yield stress. This is in some contrast to the observations from other studies using small-arms

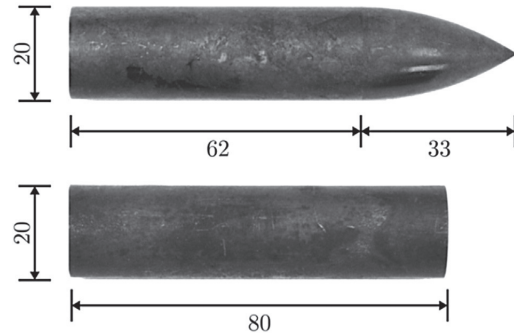


Fig. 3. Pictures of the ogive-nosed projectile (top) and blunt-nosed projectile (bottom). All measures are in mm.

bullets in the ordnance velocity regime ([Børvik et al., 2009](#); [Holmen et al., 2013](#)).

The blunt-nosed projectiles were accelerated to initial velocities of $v_i \approx 200$ m/s and $v_i \approx 250$ m/s. High-speed camera images just after complete perforation can be seen in [Fig. 6](#). For this nose shape, temper T4 exhibited the greatest resistance against perforation followed by temper T7, temper O and temper T6, in that order. The inconsistent correlation between strength and perforation resistance is also evident for the blunt-nosed projectiles, see [Fig. 7](#). The ballistic velocities are lower for blunt-nosed than for ogive-nosed projectiles suggesting that blunt-nosed projectiles are more detrimental to plates of intermediate thicknesses than ogive-nosed projectiles ([Backman and Goldsmith, 1978](#); [Gupta et al., 2007](#)).

[Fig. 8](#) shows close-up images of the bullet holes after perforation. The tiny petals that can be seen around the circumference of the entry holes in [Fig. 8\(a\)](#) develop because the pointed tip of the ogive-nosed projectile pushes material aside perpendicular to the flight direction. The blunt-nosed projectiles in [Fig. 8\(b\)](#), on the other hand, left flawless entry holes that are attributed to the plugging failure. It is clear that the amount of fragmentation increases as the failure strain decreases and the strength increases (see [Fig. 2](#)). Increasing the velocity also results in increased fragmentation. Apart from the scarce petaling in [Fig. 8\(a\)](#) the exit holes for the two nose shapes show the same trend. Temper O demonstrates ductile, but different, perforation mechanisms for the two

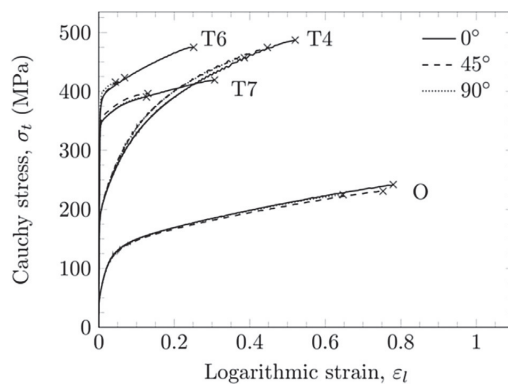


Fig. 2. True stress–strain curves from tension tests in three directions for the different tempers, where × marks the point of failure in each test.

Table 3

Results from the impact experiments on the four different tempers in this study, v_i is the initial velocity, v_r is the residual velocity, m_{pl} is the mass of the ejected plug, v_{bl} is the ballistic limit velocity, and a and p are the Recht–Ipson parameters.

Temper	Test	v_i (m/s)	v_r (m/s)	m_{pl} (g)	v_{bl} (m/s)	a	p
AA6070-O	Ogive-1	248.2	163.0	—	201.5	1.00	2.30
AA6070-O	Ogive-2	290.0	226.5	—	—	—	—
AA6070-T4	Ogive-1	246.5	18.2	—	246.0	1.00	2.11
AA6070-T4	Ogive-2	295.9	173.1	—	—	—	—
AA6070-T6	Ogive-1	247.4	107.6	—	216.7	1.00	1.84
AA6070-T6	Ogive-2	291.5	182.0	—	—	—	—
AA6070-T7	Ogive-1	250.0	39.4	—	248.0	1.00	2.19
AA6070-T7	Ogive-2	298.3	180.7	—	—	—	—
AA6070-O	Blunt-1	186.5	95.3	13.54	155.1	0.92	2.00
AA6070-O	Blunt-2	252.2	183.0	13.04 ^a	—	—	—
AA6070-T4	Blunt-1	195.5	84.3	11.62	173.9	0.92	2.00
AA6070-T4	Blunt-2	250.2	165.8	9.70 ^a	—	—	—
AA6070-T6	Blunt-1	198.9	120.9	12.64	144.4	0.89	2.00
AA6070-T6	Blunt-2	246.8	177.8	11.44	—	—	—
AA6070-T7	Blunt-1	197.2	98.6	13.02	166.5	0.93	2.00
AA6070-T7	Blunt-2	249.0	172.7	12.10	—	—	—

^a The entire plug was not located after the test.

Table 4

The optimized model parameters for the extended Voce hardening rule and the CL failure criterion for the different tempers of aluminum alloy AA6070 found from the rolling direction.

Temper	$\sigma_{0.2}$ (MPa)	σ_0 (MPa)	Q_1 (MPa)	C_1	Q_2 (MPa)	C_2	W_{cr} (MPa) Experiment	W_{cr} (MPa) Simulation
AA6070-O	50.5	38.8	79.5	56.9	88.2	4.0	151.0	179.0
AA6070-T4	186.5	172.7	35.6	80.6	247.7	6.5	211.0	244.0
AA6070-T6	372.5	350.0	30.1	185.9	72.8	7.7	115.0	130.0
AA6070-T7	341.0	292.5	55.3	317.2	31.1	10.0	128.0	170.0

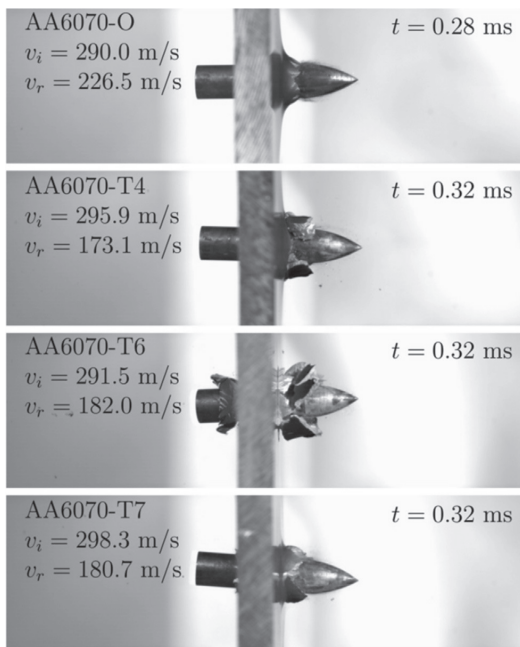


Fig. 4. Pictures just after perforation for the four different tempers using the ogive-nosed projectiles fired at $v_i \approx 300$ m/s.

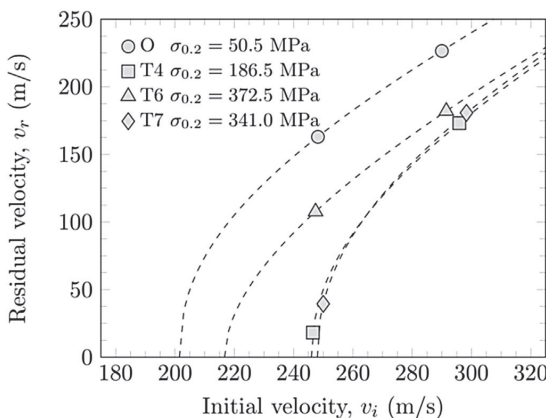


Fig. 5. Residual velocity plotted against initial velocity for the tests with ogive-ended projectiles. The dotted lines are Recht–Ipson fits to the data.

nose-shapes: ejection of a clean plug by the blunt-nosed projectile and radial hole-growth for the ogive-nosed projectile. As the yield stress increases through temper T4 and T7, indications of fragmentation can be seen, and more so for increasing velocity. Temper T6 experienced severe fragmentation and a characteristic halo of ejected debris was seen for both nose shapes for this temper.

Sliced plates of temper O and T6 struck by ogive-nosed projectiles at approximately the same initial velocity are shown in Fig. 9. The pictures confirm that the perforation process was ductile for temper O and that the perforation mode for temper T6 was a combination of ductile-hole growth and scabbing. Scabbing is in the literature also called discing and it involves tensile fractures in the plane of the plate initiated by for example local inhomogeneities. Further explanations can be found in Backman and Goldsmith (1978) and Woodward (1984). A significant portion of the back part of the temper T6 plate has been detached and ejected as fragments. The start of the delamination process can be seen as distinct cracks emanating from the projectile's path.

4. Material modeling

4.1. Constitutive relation

A modified version of the Johnson–Cook constitutive model, in which the quasi-static strain hardening is described by an extended

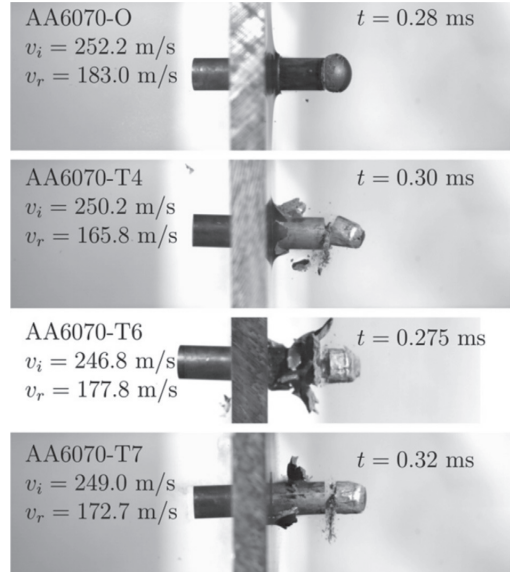


Fig. 6. Pictures just after perforation for the four different tempers using the blunt-nosed projectiles fired at $v_i \approx 250$ m/s.

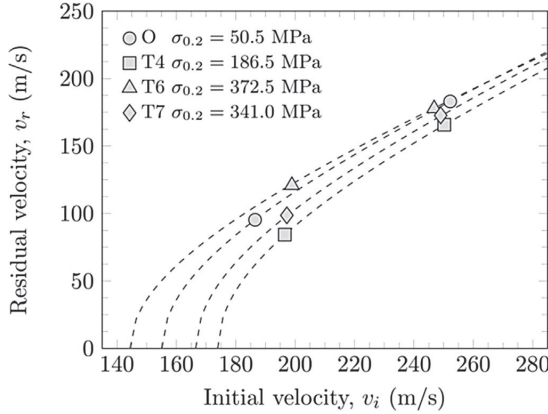


Fig. 7. Residual velocity plotted against initial velocity for the tests with blunt-ended projectiles. The dotted lines are Recht–Ipson fits to the data.

Voce rule, is employed in the following (Johnson and Cook, 1983; Børvik et al., 2001). We assume associated flow and isotropic hardening, and the von Mises equivalent stress σ_{eq} is expressed as

$$\sigma_{eq} = \left(\sigma_0 + \sum_{i=1}^2 Q_i (1 - \exp(-C_i p)) \right) (1 + \dot{p}^*)^c (1 - T^{*m}) \quad (3)$$

where σ_0 is the initial yield stress, Q_i and C_i are hardening parameters, p is the equivalent plastic strain and $\dot{p}^* = \dot{p}/\dot{p}_0$ is a

dimensionless plastic strain rate, where \dot{p}_0 is a user-defined reference strain rate. The homologous temperature is given as a function of the current temperature T , the melting temperature T_m , and the ambient temperature T_r as $T' = (T - T_r)/(T_m - T_r)$. The model parameters c and m control the rate sensitivity and the thermal softening of the material, respectively. The deformation process is assumed to take place under adiabatic conditions. Plastic dissipation then leads to heating of the body and the temperature rate is estimated as

$$\dot{T} = \frac{\chi}{\rho C_p} \sigma_{eq} \dot{p}, \quad (4)$$

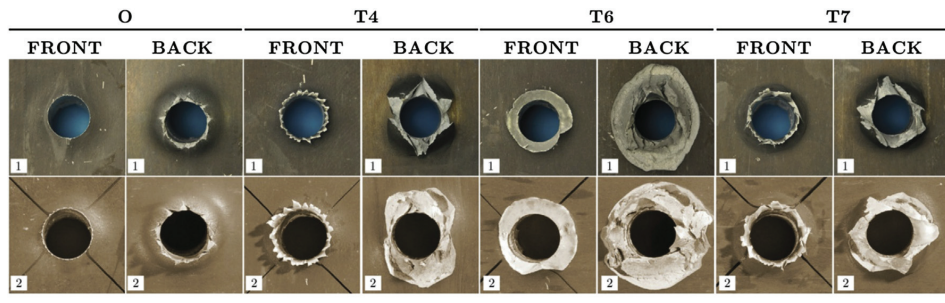
where ρ is the material density, C_p is the specific heat of the material and χ is the Taylor–Quinney coefficient that represents the proportion of plastic dissipation converted into heat.

4.2. Failure criterion

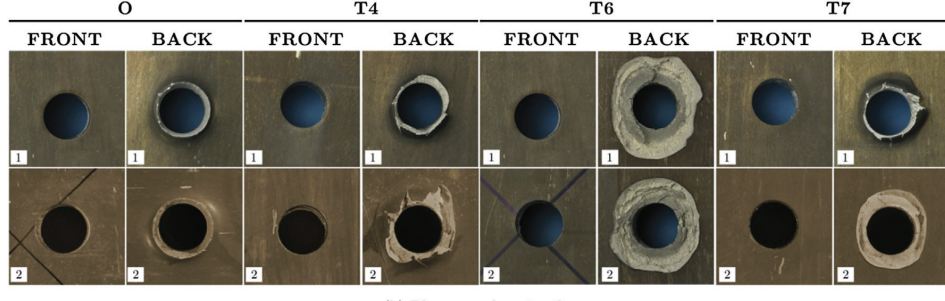
The empirical, one-parameter Cockcroft and Latham (CL) fracture criterion (Cockcroft and Latham, 1968) is adopted here in the form

$$D \equiv \frac{1}{W_{cr}} \int_0^p \langle \sigma_1 \rangle dp = \frac{1}{W_{cr}} \int_0^p \left\langle \sigma^* + \frac{3 + \mu_\sigma}{3\sqrt{3 + \mu_\sigma^2}} \right\rangle \sigma_{eq} dp \quad (5)$$

where W_{cr} is the failure parameter, σ_1 is the major principal stress, and $\langle a \rangle = \frac{1}{2}(a + |a|)$ for any real number a . The parameters σ^* and μ_σ are the stress triaxiality and the Lode parameter, respectively, defined by



(a) Ogive-nosed projectiles



(b) Blunt-nosed projectiles

Fig. 8. Close-ups of bullet holes from impacts by (a) ogive-nosed projectiles and (b) blunt-nosed projectiles.

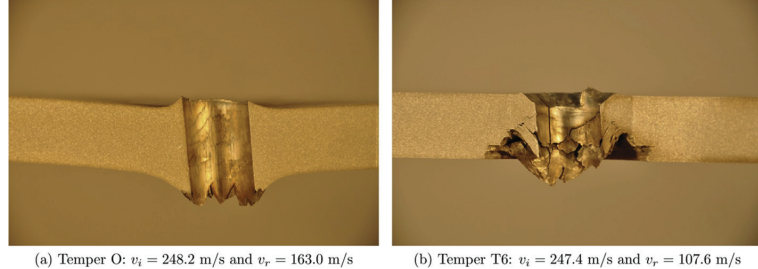


Fig. 9. Pictures of cross sections of the 20 mm thick AA6070 aluminum alloy plates struck by ogive-nosed projectiles. (a) Shows temper O and (b) shows temper T6.

$$\sigma^* = \frac{\sigma_H}{\sigma_{eq}}, \quad \mu_\sigma = \frac{2\sigma_2 - \sigma_1 - \sigma_3}{\sigma_3 - \sigma_1} \quad (6)$$

where $\sigma_1 \geq \sigma_2 \geq \sigma_3$ are the ordered principal stresses and $\sigma_H = (\sigma_1 + \sigma_2 + \sigma_3)/3$ is the hydrostatic stress. It transpires that the damage D is driven by plastic dissipation and amplified by a factor that depends on the stress state through the parameters σ^* and μ_σ . For sufficiently low stress triaxiality, damage will not develop. The failure parameter W_{cr} is readily found by integrating the major principal stress σ_1 over the equivalent plastic strain path p to failure in a uniaxial tension test. The CL failure criterion has been successfully used to model perforation in cases of impact in several past studies, e.g., Børvik et al. (2009), Børvik et al. (2010a), Holmen et al. (2013).

5. Finite element modeling

5.1. Finite element code

The explicit finite element method is, regardless of its shortcomings, the most common simulation tool for ballistic impact. However, meshless methods like the discrete element method (DEM), smooth particle hydrodynamics (SPH) or element-free Galerkin methods (EFG) can also be employed to simulate problems with large deformations and failure. In the current study we compare element erosion to node-splitting. These computational failure methods are relevant for finite elements which have been used herein. The simulations were conducted with the 3D nonlinear explicit finite element code IMPETUS Afea Solver (IMPETUS Afea AS, 2015). This code is specifically designed to predict large deformations under extreme loading conditions and it is compatible with graphic processing units (GPUs). All simulations reported in the following were run on a NVIDIA Tesla Kepler K20c GPU.

5.2. Higher order elements and node-splitting technique

In the impact simulations, 64-node hexahedral elements are applied. Such elements are historically not recommended for use in dynamic problems with large deformations due to noisy solutions (Belytschko et al., 2000). However, in the IMPETUS Afea Solver their interpolation functions are not isoparametric, and they are designed to minimize the high frequency spectra on an element level. The dispersion in wave propagation is small. The elements are well suited for explicit solvers using the central difference scheme (Olovsson, 2015). The main advantage in ballistic modeling is their capability to handle extreme deformations.

Node-splitting is a method for describing fracture and crack propagation in finite element models. Instead of removing failed elements from the simulations as conventional methods of element

erosion do, the node-splitting method allows cracks to propagate between the elements as they separate at material failure. The technique permits use of larger elements than what is possible with element erosion since material failure is no longer analogous with deletion of an entire element, thus mass and energy loss can be reduced. However, the direction of the crack growth is dependent on both the mesh size and orientation so employing large elements is still associated with problems for penetration and perforation simulations.

The algorithm that is available in IMPETUS Afea Solver (IMPETUS Afea AS, 2015) splits the nearest exterior node into two nodes and creates new element faces perpendicular to either the direction of maximum principal strain or the direction of maximum principal stress when an integration point reaches its failure criterion (e.g. $D = 1$ in Eq. (5)). The interior nodes in the 64-node hexahedral elements cannot be split. In proportional loading, strain-based and stress-based node-splitting will give the same result (Olovsson, 2015). The main advantage of strain-based node-splitting is that this method is less sensitive to numerical noise, while it may give completely erroneous results in some cases. One such case is spalling, where a compressive stress wave is followed by a tensile stress wave and the direction of maximum principal strain is often orthogonal to the maximum principal stress at the time of spalling. In this work, we have tried out and evaluated these two options for node-splitting already implemented in IMPETUS Afea Solver.

5.3. Material model calibration and validation

Most of the material and model parameters for aluminum alloy AA6070 were determined in Holmen et al. (2013) and they are given in Tables 4 and 5. Note that only the tension tests performed in the rolling direction of the plate were used in the calibration although the failure strains are significantly lower in the 45° and 90° directions. Modeling of anisotropic fracture is not within the scope of this paper even though it might be important. All numerical models are isotropic in this study, and thus we do not expect to capture the exact crack pattern. In Børvik et al. (2010a) material parameter sets from various material orientations were applied in simulations of impacts by both ogive-nosed and blunt-nosed projectiles. For blunt-nosed projectiles the ballistic limit velocity was virtually unaffected by the parameter set, but for the ogive-nosed projectiles a threefold increase in the CL parameter

Table 5

Physical constants and model parameters that were used in the IMPETUS Afea Solver (Holmen et al., 2013).

E (MPa)	ν	ρ (kg/m^3)	c	\dot{p}_0 (s^{-1})	C_p ($\text{J}/\text{kg K}$)	T_r (K)	T_m (K)	m	μ
70,000	0.3	2700	0.0125	5×10^{-4}	910	293	893	1.0	0.025

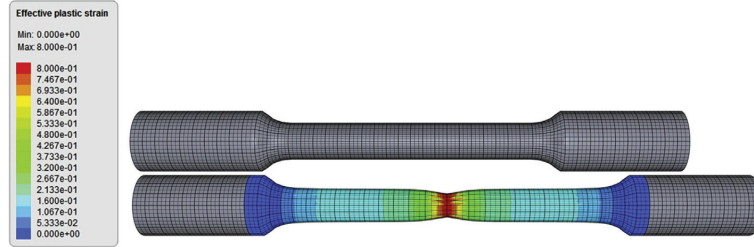


Fig. 10. Validation simulation of tension test: initial mesh compared to the deformed mesh at the last state before failure. The fringes represent effective plastic strain.

increased the ballistic limit velocity by 13.5%. We expect similar results for temper T6 and T7 in this study.

The smooth tension tests were simulated to validate the calibration of the material model. The mesh can be seen in Fig. 10. Cubic 64-node hexahedral elements of roughly the same size as those used in the subsequent ballistic simulations were used in the entire specimen. The analysis-time was scaled by a factor 10^{-4} , and the kinetic energy that was present in the simulations was compared to the plastic dissipation and found to be negligible. Temperature and strain-rate effects were disregarded since the tests were conducted at a quasi-static strain rate. Fig. 11 shows force-diameter reduction curves from the simulations compared to typical experiments. The correspondence is excellent, which was expected since the material model was in fact calibrated based on these experiments. Failure, on the other hand, initiates too early in the simulations. The CL failure parameters determined in Holmen et al. (2013) were solely based on the experimental data where homogeneous stress and strain distributions over the cross section were presumed. In reality, failure initiates at the center of the neck where the stress triaxiality is most severe (Mackenzie et al., 1977). A more accurate calibration of the failure parameter can be achieved by using inverse modeling with a finite element model. With this approach W_{cr} is found by numerically integrating the first principal stress at the central integration point over the equivalent plastic strain until the point of failure in the experiments. Failure is, as previously stated, defined as the true strain at the maximum value

of the true stress in this study. The results can be seen in Fig. 11. The CL failure parameters obtained using this approach are also provided in Table 4 where they are compared to the parameters obtained from a direct calibration of the experimental data. As seen, the experimental-numerical approach predicts a higher value of the CL failure parameter than the purely experimental approach.

5.4. Ballistic impact modeling

Perforation simulations of the experiments with both the ogive-nosed and the blunt-nosed projectiles were conducted using the constitutive models described in Section 4 and the parameters provided in Tables 4 and 5. The projectiles were undeformed after the experimental tests so in the numerical part of this study they were in most simulations assumed rigid with density $\rho = 7850 \text{ kg/m}^3$. Contact was modeled with a penalty based node-to-surface algorithm and a penalty stiffness such that the contact penetrations were minimized while retaining a reasonable time step. Friction coefficients of $\mu = 0$, $\mu = 0.025$ and $\mu = 0.05$ were considered in the simulations. The strain rate sensitivity for similar aluminum alloys has been shown to be almost negligible at ambient temperatures (Chen et al., 2009), but at higher temperatures the material behavior is markedly affected by the strain rate (Vilamosa et al., 2015). High temperatures are expected in this problem so values of c between 0.001 and 0.015 were investigated. A minimum time step of 3 ns was specified in every analysis to remove overly distorted elements that could cause error termination.

Most of the simulations were run with one symmetry plane. This saves computational time without unnecessarily constraining the solution. The base mesh shown in Fig. 12 has 10 cubic hexahedral elements (with 64 nodes each) over the thickness in the impact zone which is equivalent to a node-spacing of 0.67 mm. This gave a total of 5020 elements in the plate, out of which 1700 were cubic hexahedral and 3320 were linear hexahedral. A finer mesh with 20 cubic hexahedral elements over the thickness is also shown in Fig. 12. This corresponds to a node-spacing of 0.33 mm and it has a total of 7640 cubic hexahedral elements and 6872 linear hexahedral elements. Additional meshes with 5, 8 and 15 elements over the thickness were also created and used in a mesh-sensitivity study.

Although the CL failure criterion was used to identify the point of material failure in every simulation, the way failure was introduced into the finite element model was varied. Four methods were considered:

- (1) The standard element erosion algorithm where all the components of the stress tensor are set to zero when $D = 1$ in 16 out of 64 integration points of the element

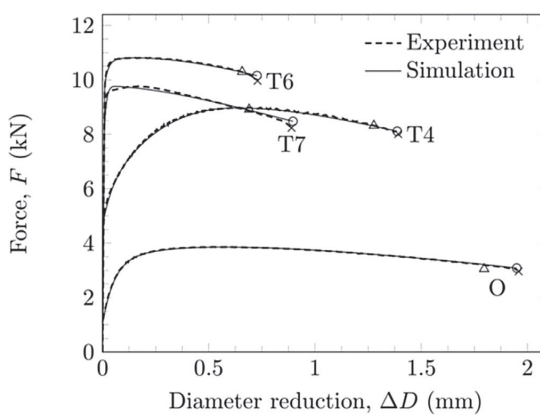


Fig. 11. Numerical simulations of the tension test in the rolling direction compared to the experimental results. The crosses depict failure in the experiments, while the triangles and the circles depict failure in the numerical simulations with experimentally determined and numerically determined W_{cr} respectively.

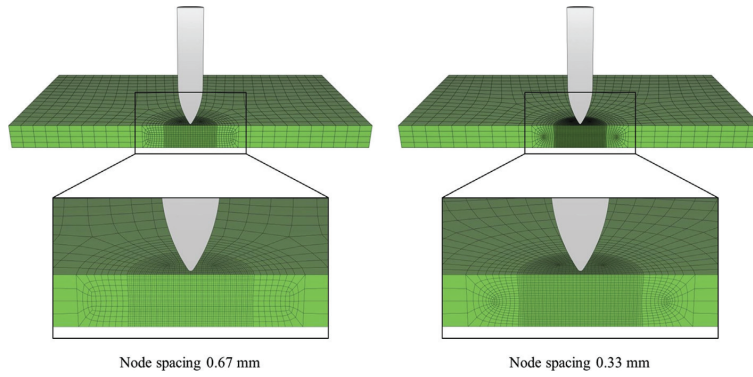


Fig. 12. Solid element meshes used in the ballistic simulations with ogive-nosed and blunt-nosed projectiles.

- (2) An element erosion algorithm where the shear strength in an integration point vanishes when $D = 1$, but the element can still take compressive stresses and is not removed from the analysis until the minimum time step is violated
- (3) The strain-based node-splitting algorithm where new surfaces are created between elements perpendicular to the direction of maximum principal strain when $D = 1$ in one integration point.
- (4) The stress-based node-splitting algorithm where new surfaces are created between elements perpendicular to the direction of maximum principal stress when $D = 1$ in one integration point.

The failure methods are summarized in [Table 6](#). Simulations corresponding to every experiment from Section 3 were run with the various numerical formulations of failure described above.

5.5. Initial numerical study

The effects that the boundary conditions, symmetry condition, projectile material formulation, friction, strain rate sensitivity, and mesh refinement have on the perforation resistance were checked in a series of initial simulations. Temper O was chosen because it showed no signs of fragmentation in the experimental tests, which simplifies the numerical description. However, the mesh-sensitivity study also includes simulations with element erosion, strain-based node-splitting and the temper T6 material formulation. Both ogive-nosed and blunt-nosed projectiles were investigated.

First, the entire target plate, projectile, clamping beams and the pre-stressed bolts as shown in [Fig. 13](#) were modeled. Pre-stressing was done in a separate analysis in which the clamping length of the bolts was reduced until the stress in the bolts reached a prescribed value. Bolt stresses of 50 MPa and 100 MPa respectively did not alter the residual velocity of the projectile after perforation. By removing the clamps and constraining the top and bottom edges of

the plate in x , y , and z directions we obtained the same residual velocity. Modeling only half the plate and introducing a plane of symmetry yielded the same residual velocity again and we conclude that the far-field boundary conditions are of minor importance in this particular problem. To further evaluate the artificial constraint imposed by the symmetry plane, simulations with node-splitting were run both with and without the symmetry condition. We used the material parameters for temper T6 and an ogival-nosed projectile. The overall fracture patterns are hardly affected by the imposed symmetry, and the residual velocity is not affected. Thus, we conclude that a model with one symmetry plane is sufficient for the application in this study.



Fig. 13. The complete model as seen in the IMPETUS Afea Postprocessor.

Table 6

Overview of the failure methods used in this study.

Initiation of failure at $D = 1$		Removes the element
(1) Element erosion	Removes the deviatoric strength of the integration point	When 16 of 64 integration points reach $D = 1$
(2) No erosion	Removes the deviatoric strength of the integration point	When $\Delta t \leq 3ns$
(3) Strain-based node-splitting	Creates new element faces in the direction of the maximum principal strain	When $\Delta t \leq 3ns$
(4) Stress-based node-splitting	Creates new element faces in the direction of the maximum principal stress	When $\Delta t \leq 3ns$

Although the projectiles were inspected after the tests, and no permanent deformation was visible, the energy dissipation in both the ogive-nosed and blunt-nosed projectiles was checked. The projectiles were assigned rigid ($\rho = 7850 \text{ kg/m}^3$), elastic ($E = 210,000 \text{ MPa}$, $v = 0.3$) and elastic-perfectly plastic ($\sigma_0 = 1900 \text{ MPa}$) material parameters. Changing the parameters did not significantly change the residual velocity of the ogive-nosed projectile, and only a slight difference was seen for the blunt-nosed projectile at the highest impact velocity. A rigid material formulation was therefore applied in all subsequent simulations.

The individual and combined effects of friction and strain rate sensitivity were also studied. Including Coulomb friction with a coefficient of $\mu = 0.05$ in the model slows the ogive-nosed projectile down significantly compared to the frictionless simulation; the frictional coefficient had almost no impact on the residual velocity for the blunt-nosed projectile. Increasing the strain-rate sensitivity parameter c affected the simulations with both nose shapes, but the ogive-nosed projectile the most. The parameter combination $\mu = 0.025$ and $c = 0.0125$ represents a compromise and the values lie within the spread seen in available literature (Ravid and Bodner, 1983; Zukas, 1990; Chen, 1990; Rusinek et al., 2009). Hence, they are used in the rest of the simulations in this study.

Lastly, the influence of the mesh density was investigated. A substantial mesh-sensitivity study was undertaken where 5, 8, 10, 15 and 20 elements over the thickness were used, resulting in node spacings from 1.33 mm to 0.33 mm. The projectile was assumed rigid and the material parameters that were found in the preceding discussion were used. Both ogive-nosed ($v_i \approx 300 \text{ m/s}$) and blunt-nosed ($v_i \approx 250 \text{ m/s}$) projectiles striking plates in tempers O and T6 were checked. Conventional element erosion (1) and the strain-based node-splitting algorithm (3) were applied. Results from the mesh sensitivity study are shown in Fig. 14. It seems that the residual velocity of the ogive-nosed projectile is not significantly influenced by the grid size, regardless of failure method. The fact that the results are not very sensitive upon the mesh size in 3D models has also been observed previously by Børvik et al. (2010a). We believe that this is because the projectile is sufficiently large compared to the elements in the plate, which activates a larger portion of the plate than a smaller projectile would. Also the results for the blunt-nosed projectile exhibit low grid-size dependence. The exception is the simulation for temper T6 using strain-based node-splitting, where the residual velocity increases by 11.4% when the number of elements over the thickness increases from 8 to 20. We believe that this is caused by the node-splitting technique's sensitivity to node placement and mesh orientation. In the

mesh with 10 elements over the thickness, the perimeter of the projectile coincides with a row of nodes.

5.6. Ballistic impact-simulation results

Results from the numerical simulations are first presented for the ogive-nosed projectiles and then for the blunt-nosed projectiles. The main focus in this study is the quantitative difference between the simulations employing the various failure methods and not the prediction of the estimated ballistic limit velocity. How well the methods predict the perforation mechanisms seen in the experimental tests is also emphasized. Since this study evaluates differences between numerical implementations of failure in finite element models, we have tried to keep the models as similar as possible and no further tuning has been done after the calibration.

Every ballistic test reported in Section 3 was simulated with the ogive-nosed projectile and a relatively coarse plate mesh, i.e., 10 cubic hexahedral elements over the thickness. This grid size was chosen because it seemed like a reasonable trade-off between accuracy and computational efficiency. The normalized ballistic limit velocities ($v_{bl,sim}/v_{bl,exp}$) from the simulations with ogive-nosed projectiles are shown as functions of temper configuration in Fig. 15. Here we clearly see that for tempers that exhibited no or little fragmentation experimentally (temper O and temper T4), the four failure methods gave approximately the same results. A larger spread in results can be seen for temper T7 and especially temper T6. Fig. 16 shows pictures from the perforation process for the annealed temper O and the peak-strength temper T6 taken from simulations employing element erosion and stress-based node-splitting. There are obvious differences between the predicted perforation mechanisms. The element erosion technique can only describe ductile-hole growth, and fragmentation is poorly described for the low-ductility temper T6. Node-splitting, on the other hand, captures the ejected fragments much better for temper T6, while predicting a relatively ductile perforation mechanism for temper O.

In the same manner as for the ogive-nosed projectiles, every experimental test with the blunt-nosed projectile was simulated with 10 elements over the thickness in the plate mesh. Fig. 17 shows the normalized ballistic limit velocities ($v_{bl,sim}/v_{bl,exp}$) as functions of the temper configuration. Failure methods (1) element erosion and (2) no erosion predicted in general similar results for the simulations with blunt-nosed projectiles. Plugging failure is a shear dominated problem and whether an element is removed from the analysis or its shear resistance is removed makes hardly any difference on the final result. Analysis times were on the other hand

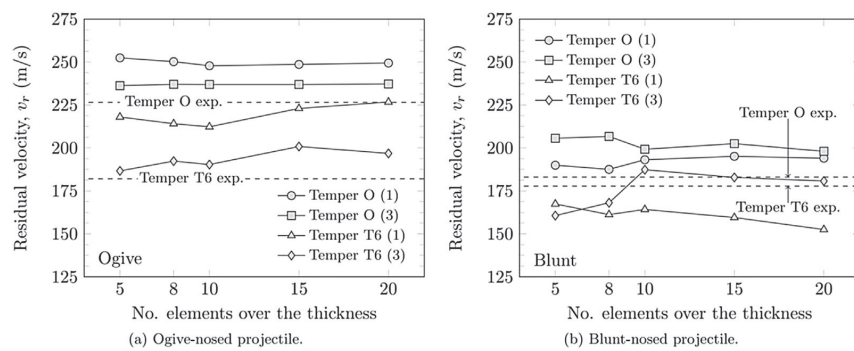


Fig. 14. Results from the mesh sensitivity study. The initial velocity for the ogive-nosed projectile is approximately 300 m/s while the initial velocity for the blunt-nosed projectile is approximately 250 m/s.

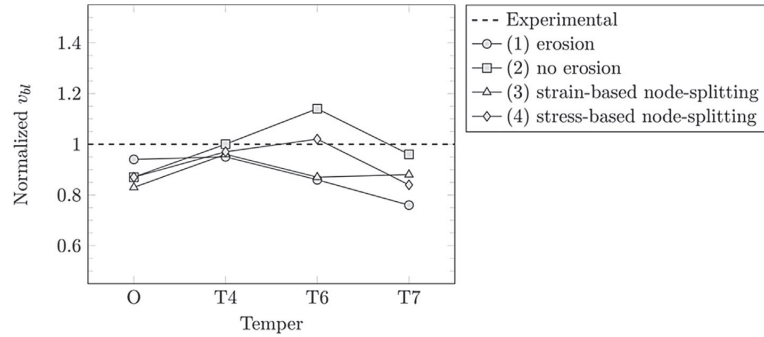


Fig. 15. Normalized ballistic limit velocities $v_{bl,exp}/v_{bl,sim}$ shown as functions of temper for impacts with the ogive-nosed projectiles and 10 elements over the plate thickness.

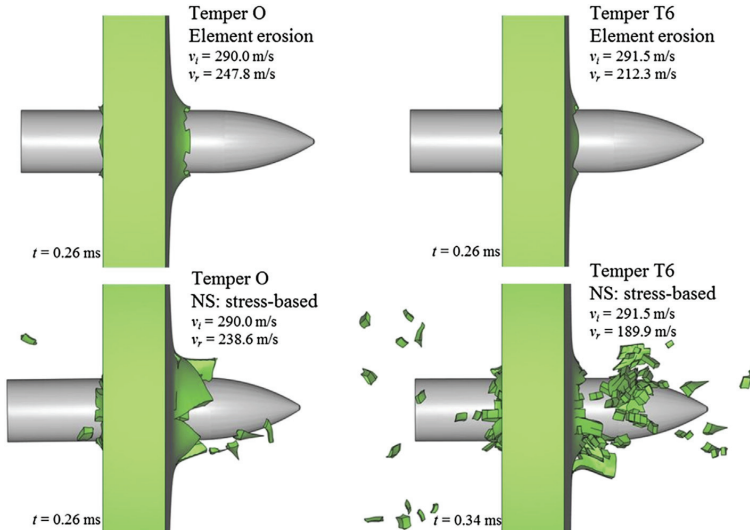


Fig. 16. Images from after perforation by the ogive-nosed projectile for tempers O and T6 with conventional element erosion and stress-based node-splitting.

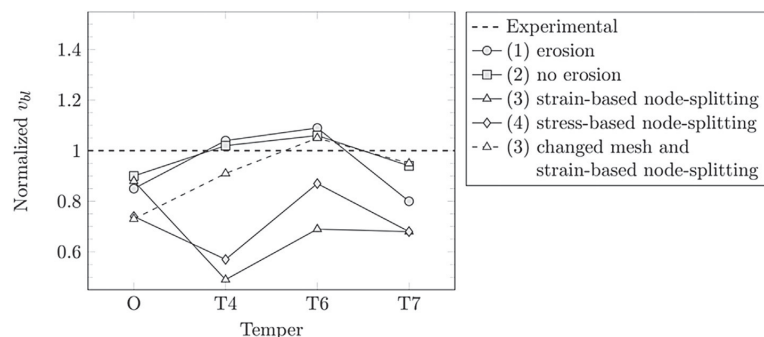


Fig. 17. Normalized ballistic limit velocities $v_{bl,exp}/v_{bl,sim}$ shown as functions of temper for impacts with the blunt-nosed projectiles and 10 elements over the plate thickness.

significantly shorter for method (1) *element erosion*. *Strain-based node-splitting* (3) and *stress-based node-splitting* (4) generally predicted significantly higher residual velocities than methods (1) and (2). Node-splitting and element erosion are two fundamentally different ways of incorporating fracture in a finite element model; and where element erosion is generally recognized to be sensitive to the grid size, node-splitting seems sensitive to the node placement and mesh orientation. In the standard mesh, the perimeter of the projectile coincided with a row of nodes in the plate which facilitated fracture, especially at low impact velocities. We changed the node placement slightly from the standard mesh with 10 elements over the thickness (see Fig. 18) to investigate the influence of mesh orientation. For the simulations with the ogive-nosed projectiles the results did not change. With the blunt-nosed projectiles with failure method (1) *element erosion* and (2) *no erosion* no change was seen in the results, but with method (3) *strain-based node-splitting* and (4) *stress-based node-splitting* the results were significantly different. The normalized ballistic limit velocities for (3) *strain-based node-splitting* are plotted in Fig. 17 for comparison. This suggests that care must be taken when employing node-splitting and regular meshes, at least for impacts with blunt-nosed projectiles.

Fig. 19 shows pictures from the simulations for temper O plates and temper T6 plates after complete perforation when using element erosion and stress-based node-splitting. We see from the shape and size of the plugs that the element erosion method predicts reasonably shaped plugs, but due to the relatively large elements employed and the fact that elements need to be removed to obtain perforation the plugs are too small. Node-splitting predicts plugs of correct size since virtually no elements have been removed from the analyses. Some fragmentation can be seen for the simulation of temper T6, but not as much as in the experiments shown in Fig. 6.

Lastly, Fig. 20 compares cross sections of simulations run with element erosion and strain-based node-splitting. The only difference in the input file from the simulation depicted in Fig. 20(b) to that in (a) is that node-splitting was activated in the former. However, the fracture mechanisms are not similar at all. The cross section using element erosion looks like temper O in Fig. 9(a), i.e., it looks completely ductile. This was the case for every simulation with element erosion. By activating node-splitting we see that the fragments are flying from the plate, and that the delamination shown for temper T6 in Fig. 9(b) is reproduced with good accuracy in the numerical model, especially when considering the simplicity of the isotropic material model and the coarse element mesh.

6. Discussion

Blunt-nosed projectiles were in the experimental part of this paper found to cause failure by plugging, while ogive-nosed projectiles mainly perforated the plates by ductile-hole growth. This has frequently been observed in the literature (Børvik et al., 2010a; Backman and Goldsmith, 1978; Børvik et al., 2002), and it explains the differences in perforation capacity of the plates when they are struck by the different projectiles. A plate struck by a blunt-nosed projectile of the same approximate diameter as its thickness is susceptible to adiabatic shear banding which is a low-energy failure mode (Dodd and Bai, 2015). Ductile hole-growth requires, on the other hand, radial displacement of material that often induces large plastic strains, which in turn dissipates more energy than plugging (Backman and Goldsmith, 1978; Forrestal et al., 1990).

Ballistic testing of five different high-strength steels by Børvik et al. (2009) showed that material strength is the most important parameter for plates struck by small-arms bullets at ordnance velocity. The five steel types had comparable hardening curves and sufficient ductility to prevent significant fragmentation, thus the capacity was found to be a linear function of the yield stress. A similar relationship between strength and ballistic capacity was also shown by Holmen et al. (2013) where small-arms bullets were fired at aluminum alloy plates of the same type as in the current paper. As shown in Fig. 2, the hardening varied between the tempers, and some fragmentation was observed for tempers T6 and T7 at the highest impact velocities when struck by small-arms bullets. Forrestal et al. (2010) and Børvik et al. (2010b) observed the same trend for the aluminum alloys AA7075-T651 and AA5083-H116, i.e., that strength governs the capacity for plates struck by small-arms bullets where the amount of fragmentation is limited.

The ratio between target thickness h_0 and projectile diameter D in Børvik et al. (2009), Holmen et al. (2013), Forrestal et al. (2010), Børvik et al. (2010b) discussed above was $h_0/D = 3.28$. If we consider impact conditions where the projectile diameter is large compared to the plate thickness, as it is in this study where $h_0/D = 1$, we see that strength does not necessarily determine the capacity. This was experimentally demonstrated by striking 20 mm thick AA7075-T651 and AA5083-H116 plates using both 7.62 mm AP-bullets and 20 mm ogive-nosed projectiles (Forrestal et al., 2010; Børvik et al., 2010b). Limited plate fragmentation was seen when the relatively small AP-bullets struck the plates at ordnance velocity, and the capacity expressed as the ballistic limit velocity was in favor of the stronger AA7075 alloy: 628 m/s compared to 492 m/s. Even though their respective yield stresses were 520 MPa

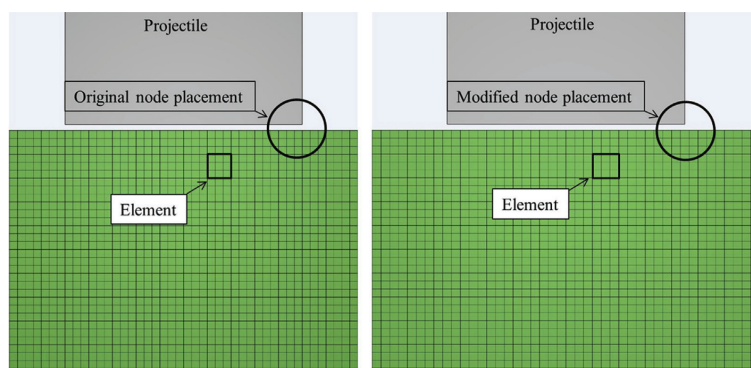


Fig. 18. Illustration of the original and the modified node placements.

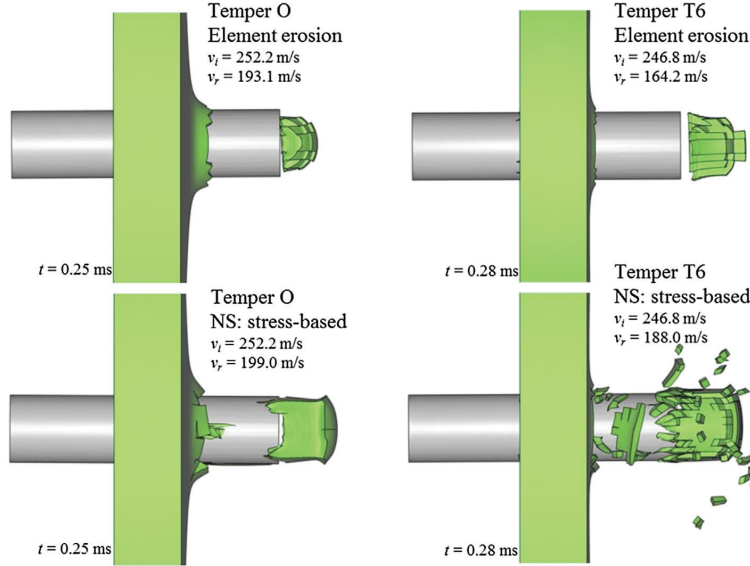


Fig. 19. Images from after perforation by the blunt-nosed projectile for temps O and T6 with conventional element erosion and stress-based node-splitting.

and 244 MPa, the ballistic limit velocities when the plates were struck by the large 20 mm ogive-nosed projectiles were 209 m/s and 244 m/s, i.e., a 20% difference in favor of the apparently weaker AA5083 alloy (Børvik et al., 2010a,b). This is attributed to the quasi-brittle behavior of the AA7075 aluminum alloy under certain impact conditions (Børvik et al., 2010a). The same type of behavior was observed in the experimental part of this paper; temper T6 has the highest yield stress, but it is the second weakest and weakest temper when it comes to preventing perforation by the ogive-nosed and blunt-nosed projectiles, respectively. This is in contrast to the results reported for 7.62 mm AP-bullets in Holmen et al. (2013). It appears that strength governs the perforation capacity as long as the structural component is sufficiently ductile not to fragment, and the component ductility seems to be determined by

the relationship between projectile size, target thickness, impact velocity, and material behavior. If the projectile diameter is small compared to the plate thickness, then the material is constrained and fragmentation is less severe. Revisiting the images in Figs. 8 and 9 while keeping in mind the failure strains (in the rolling direction) for the various tempers, i.e., $\epsilon_{f,O} = 0.79$, $\epsilon_{f,T4} = 0.52$, $\epsilon_{f,T6} = 0.26$ and $\epsilon_{f,T7} = 0.32$ we see that severe fragmentation indeed correlates with low failure strains.

The importance of accurately capturing the fragmentation in numerical simulations was highlighted in the preceding discussion, and to this end, the node-splitting methods described in Section 5.2 appear promising although more validation of the approach still is required. For the tests that exhibited ductile behavior, the results obtained using node-splitting were similar to the ones obtained

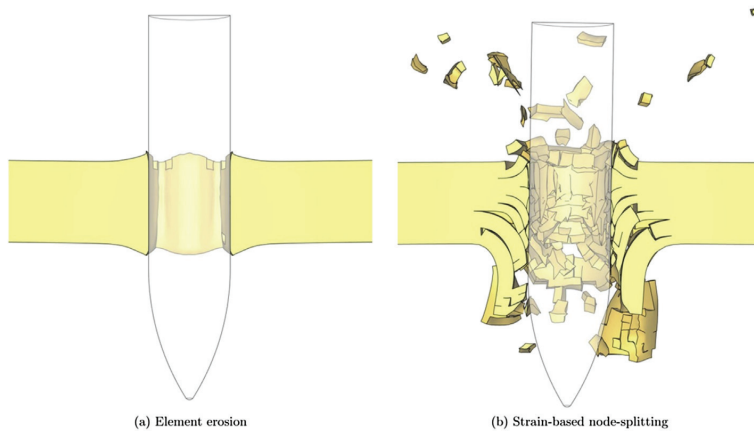


Fig. 20. Images from simulations of temper T6 with (a) element erosion ($v_i = 247.4 \text{ m/s}$ and $v_r = 151.0 \text{ m/s}$) and (b) strain-based node-splitting ($v_i = 247.4 \text{ m/s}$ and $v_r = 129.7 \text{ m/s}$).

with element erosion, but for the tests that behaved in a more quasi-brittle manner the delamination and fragmentation processes were more aptly described and the experimental trends were better captured particularly for the ogive-nosed projectile.

7. Conclusions

The experimental test program presented in this paper includes material tests and ballistic impact tests of 20 mm thick AA6070 aluminum alloy plates that underwent four different heat treatments. It was shown that material strength is not the most important parameter for the capability of plates made of this alloy to resist penetration and perforation. Ductility is seen to be as important as the strength, since fragmentation occurs for the temper with the highest strength and the lowest ductility. The amount of fragmentation seems to be controlled by the relationship between the plate thickness and the projectile diameter/velocity, and the ductility of the material. The experiments further confirmed that the capacity of a plate when subjected to impact by blunt-nosed projectiles is lower than it is for ogive-nosed projectiles due to the formation of adiabatic shear bands.

A Johnson–Cook type plasticity model and the one-parameter Cockcroft–Latham failure criterion were used in the numerical part of this paper where methods of incorporating failure and fracture into a finite element simulation were compared. Element erosion and node-splitting in various forms were checked and it was found that although the methods predicted similar results when the plate material was ductile, node-splitting was able, at least qualitatively, to capture the effect of fragmentation with a rather coarse element mesh. Node-splitting also makes it possible to model failure and fracture quite accurately while employing relatively large elements, but this is not necessarily an advantageous strategy for penetration and perforation problems involving shear localization.

For small-arms bullets striking steel plates, the target material has sufficient ductility to avoid fragmentation, and strength governs the perforation resistance. Aluminum is commonly less ductile than steel, but strength remains the most important parameter as long as fragmentation is limited. When fragmentation is present, ductility and strain hardening behavior are important and have to be considered to predict the perforation behavior. It is thus important in the design of protective structures to consider all aspects of material behavior and the size and shape of the projectile; not only the apparent strength given by the material's yield stress.

Acknowledgments

The financial support for this work comes from the Structural Impact Laboratory (SIMLab), Centre for Research-based Innovation (CRI) at the Norwegian University of Science and Technology and the Norwegian Defence Estates Agency. The authors would like to express their gratitude to Hydro Aluminium, in particular Dr. Simon Jupp, and to Dr. Lars Olovsson at IMPETUS Afea AB for valuable input.

References

- Backman, M.E., Goldsmith, W., 1978. The mechanics of penetration of projectiles into targets. *Int. J. Eng. Sci.* 16, 1–99.
- Belytschko, T., Liu, W.K., Moran, B., 2000. *Nonlinear Finite Elements for Continua and Structures*, first ed. John Wiley & Sons, Inc.
- Børvik, T., Langseth, M., Hopperstad, O.S., Malo, K.A., 1999. Ballistic penetration of steel plates. *Int. J. Impact Eng.* 22, 855–886.
- Børvik, T., Hopperstad, O.S., Berstad, T., Langseth, M., 2001. A computational model of viscoplasticity and ductile damage for impact and penetration. *Eur. J. Mech. – A/Solids* 5, 685–712.
- Børvik, T., Langseth, M., Hopperstad, O.S., Malo, K.A., 2002. Perforation of 12 mm thick steel plates by 20 mm diameter projectiles with flat, hemispherical and conical noses. Part I: experimental study. *Int. J. Impact Eng.* 27, 19–35.
- Børvik, T., Dey, S., Clausen, A.H., 2009. Perforation resistance of five different high-strength steel plates subjected to small-arms projectiles. *Int. J. Impact Eng.* 36, 948–964.
- Børvik, T., Hopperstad, O.S., Pedersen, K.O., 2010a. Quasi-brittle fracture during structural impact of AA7075-T651 aluminium plates. *Int. J. Impact Eng.* 37, 537–551.
- Børvik, T., Forrestal, M.J., Warren, T.L., 2010b. Perforation of 5083-H116 aluminum armor plates with ogive-nose rods and 7.62 mm APM2 bullets. *Exp. Mech.* 50, 969–978.
- Camacho, G.T., Ortiz, M., 1996. Computational modeling of impact damage in brittle materials. *Int. J. Solids Struct.* 33, 2899–2938.
- Chen, Y., Clausen, A.H., Hopperstad, O.S., Langseth, M., 2009. Stress-strain behavior of aluminium alloys at a wide range of strain rates. *Int. J. Solids Struct.* 46, 3825–3835.
- Chen, E.P., 1990. Finite element simulation of perforation and penetration of aluminium targets by conical-nosed steel rods. *Mech. Mater.* 10, 107–115.
- Cockcroft, M.G., Latham, D.J., 1968. Ductility and the workability of metals. *J. Inst. Metals* 96, 33–39.
- Dodd, B., Bai, Y., 2015. *Introduction to Adiabatic Shear Localization*. Revised edition. Imperial College Press.
- Forrestal, M.J., Luk, V.K., Brar, N.S., 1990. Perforation of aluminum armor plates with conical-nose projectiles. *Mech. Mater.* 10, 97–105.
- Forrestal, M.J., Børvik, T., Warren, T.L., 2010. Perforation of 7075-T651 aluminum armor plates with 7.62 mm APM2 bullets. *Exp. Mech.* 50, 1245–1251.
- Fourmeau, M., Børvik, T., Benallal, A., Lademo, O.G., Hopperstad, O.S., 2011. On the plastic anisotropy of an aluminium alloy and its influence on constrained multiaxial flow. *Int. J. Plasticity* 27, 2005–2025.
- Gupta, N.K., Iqbal, M.A., Sekhon, G.S., 2007. Effect of projectile nose shape, impact velocity and target thickness on deformation behavior of aluminum plates. *Int. J. Solids Struct.* 44, 3411–3439.
- Gurson, A.L., 1977. Continuum theory of ductile rupture by void nucleation and growth – Part I. Yield criteria and flow rules for porous ductile media. *J. Eng. Mater. Technol.* 99, 2–15.
- Holmen, J.K., Johnsen, J., Jupp, S., Hopperstad, O.S., Børvik, T., 2013. Effects of heat treatment on the ballistic properties of AA6070 aluminium alloy. *Int. J. Impact Eng.* 57, 119–133.
- IMPETUS Afea AS. IMPETUS Afea Solver: <http://www.impetus-afea.com> [cited: 2015-02-01].
- Johnson, G.R., Cook, W.H., 1983. A constitutive model and data for metals subjected to large strains, high strain rates and high temperatures. In: Proceedings of the 7th International Symposium on Ballistics, pp. 541–547.
- Johnson, G.R., Cook, W.H., 1985. Fracture characteristics of three metals subjected to various strains, strain rates, temperatures and pressures. *Eng. Fract. Mech.* 21, 31–48.
- Komori, K., 2001. Simulation of shearing by node separation method. *Comput. Struct.* 79, 197–207.
- Mackenzie, A.C., Hancock, J.W., Brown, D.K., 1977. On the influence of state of stress on ductile failure initiation in high strength steels. *Eng. Fract. Mech.* 9, 167–188.
- Moxnes, P., Prytz, A.K., Frøyland, Ø., Kløkkehaug, S., Skriudalen, S., Friis, E., Tetland, J.A., Dørum, C., Ødegårdstuun, G., 2014. Experimental and numerical study of the fragmentation of expanding warhead casings by using different numerical codes and solution techniques. *Def. Technol.* 10, 161–176.
- Nahshon, K., Hutchinson, J.W., 2008. Modification of the Gurson Model for shear failure. *Eur. J. Mech. A/Solids* 27, 1–17.
- Olovsson, L., Limido, J., Lacome, J.-L., Hanssen, A.G., Petit, J., 2015. Modeling fragmentation with new higher order finite element technology and node splitting. In: Proceedings of the 11th International Conference on the Mechanical and Physical Behaviour of Materials under Dynamic Loading, pp. 1–6, 04050.
- Olovsson, L., 2015. IMPETUS Afea AB, Huddinge, Sweden. Private communication.
- Ravid, M., Bodner, S.R., 1983. Dynamic perforation of viscoplastic plates by rigid projectiles. *Int. J. Eng. Sci.* 21, 577–591.
- Recht, R.F., Ipson, T.W., 1963. Ballistic perforation dynamics. *J. Appl. Mech.* 30, 384–390.
- Rodríguez-Millán, M., Vaz-Romero, A., Rusinek, A., Rodríguez-Martínez, J.A., Arias, A., 2014. Experimental study on the perforation process of 5754-H111 and 6082-T6 aluminium plates subjected to Normal impact by conical, hemispherical and Blunt projectiles. *Exp. Mech.* 54, 729–742.
- Ruggiero, A., Iannitti, G., Testa, G., Limido, J., Lacome, J.L., Olovsson, L., Ferraro, M., Bonora, N., 2014. High strain rate fracture behavior of fused silica. *J. Phys. Conf. Ser.* 500, 1–4.
- Rusinek, A., Rodríguez-Martínez, J.A., Zaera, R., Klepaczko, J.R., Arias, A., Sauvelet, C., 2009. Experimental and numerical study on the perforation process of mild steel sheets subjected to perpendicularly impact by hemispherical projectiles. *Int. J. Impact Eng.* 36, 565–587.
- Vilamosa, V., Clausen, A.H., Børvik, T., Skjervold, S., Hopperstad, O.S., 2015. Behaviour of Al-Mg-Si alloys at a wide range of temperatures and strain rates. *Int. J. Impact Eng.* 86, 223–239.
- Woodward, R.L., 1984. The interrelation of failure modes observed in the penetration of metallic targets. *Int. J. Impact Eng.* 2, 121–129.
- Xu, X.-P., Needleman, A., 1994. Numerical simulations of fast crack growth in brittle solids. *J. Mech. Phys. Solids* 42, 1397–1434.
- Zukas, J.A., 1990. *High Velocity Impact Dynamics*, first ed. John Wiley & Sons, Inc.

Jens Kristian Holmen, Jan Ketil Solberg, Odd Sture Hopperstad, Tore Børvik

Ballistic perforation of layered and surface-hardened steel plates

Presented at the 1st International Conference on Impact Loading of Structures and Materials, Turin, Italy, 2016.

Part 4



Ballistic perforation of layered and surface-hardened steel plates

J.K. Holmen¹, J.K. Solberg², O.S. Hopperstad¹, T. Børvik¹

¹ Structural Impact Laboratory (SIMLab), Department of Structural Engineering, Norwegian University of Science and Technology, Trondheim, Norway

² Department of Materials Science and Engineering, Norwegian University of Science and Technology, Trondheim, Norway

Abstract

In this study, we investigate the ballistic resistance of hot-rolled structural steel plates with a nominal yield stress of 355 MPa. Ballistic experiments were conducted on monolithic and laminated configurations both in the as-received (AR) and in a surface-hardened (SH) state. In the SH state we made the surface stronger while keeping the center of the plates relatively unchanged from the AR state. This was done in an attempt to improve the ballistic properties of the plates without compromising their ductility. Quasi-static uniaxial tension testing and Vickers hardness testing were done to calibrate a constitutive model for numerical simulations. The ballistic tests revealed that the capacity was highest for a monolithic, surface-hardened plate. Plate layering decreased the capacity more for SH plates than for AR plates.

Keywords: Ballistic impact, Finite element analysis, Node splitting

1. Introduction

Børvik et al. [1] reported that perforation resistance is a linear function of the material strength. This observation seems to hold as long as the local ductility is sufficient to prevent fragmentation [2]. As shown by Lou et al. [3], a possible method for increasing the capacity of initially ductile steel plates is to case-harden them. This process strengthens the surface while retaining the core's ductility. Steels with 0.13-0.20% carbon and a ferrite/pearlite structure are normally carburized by placing the specimen in a carbon-rich environment at a temperature between 850 °C and 950 °C. At this elevated temperature the steel will transform into an austenite structure that can contain more carbon than the initial ferrite/pearlite structure leading to diffusion of carbon atoms into the surface of the specimen. After cooling and subsequent heat treatment the result is steel with a strong martensitic surface and a softer ferritic or martensitic core [4]. The main objectives of this research are (1) to investigate how the capacity of laminated plates compares to that of monolithic plates of equal thickness, and (2) to investigate how the capacity of the plates are affected by increasing the surface hardness.

2. Target Material

Hot-rolled NVE36 structural steel plates with a nominal yield stress of 355 MPa were used in this study. They were delivered as 300 × 300 mm square plates of varying thickness. We considered 12 mm, 6 mm and 4 mm thick plates, in either a monolithic configuration (12 mm) or laminated configurations (2×6 mm and 3×4 mm), i.e., all configurations had a total thickness of 12 mm. The plates were first tested in the as-received (AR) condition. Some plates were surface hardened (SH) in a carbon-rich environment at elevated temperatures. This was done to obtain varying hardness over the target thickness. The surface-hardening procedure started by subjecting the plates to carburization in a pit furnace at 920 °C for 4 h for the 4 mm thick plates, 6 h for the 6 mm and 12 mm thick plates before air cooling back to room temperature. They were then reheated to 920 °C for a shorter time-period, where precautions were taken to ensure that the plates were hot through the thickness for at least 10

min, before they were quenched in a 10% NaOH solution. Lastly, all the plates were annealed at 245 °C for 2 h.

3. Experimental Work

3.1 Material tests

Uniaxial tension specimens were extracted from the center of the 12 mm thick AR and SH plates. The specimens had a diameter of 6 mm and an initial gauge length of 40 mm. We continuously measured the force F and the current area A from which the average true stress-strain curves were calculated (Figure 1(a)). Figure 1(b) shows the measured hardness distributions over the thickness of the 12 mm thick plates. The distributions were found with standard hardness testing. Indents were made with a 0.2 kg diamond-shaped indenter on a sample approximately 15 mm from the edge of a penetration channel. We left 80 µm between each indent near the surface, but the indentation interval was increased near the center of the sample.

3.2 Ballistic tests

We securely fastened the 300 × 300 mm square target plates to a rigid setup with two horizontal beams, leaving the vertical sides free. A smooth-bore Mauser rifle fired 7.62 mm armor piercing (AP) bullets at predefined velocities between 465 m/s and 915 m/s. The nominal mass of the 7.62 mm AP-bullet was 10.5 g and it consisted of a brass jacket, a lead cap and an ogive-nosed hardened steel core with a nominal mass of 5.0 g. Maximum nine shots were fired into each plate configuration. The impact event was captured by a high-speed camera with a frame rate of 75,000 fps. These videos were also used to optically measure the initial (v_i) and the residual (v_r) velocity in each test (Figure 2(a)).

3.3 Experimental results

The hardness tests showed that it was hard to reproduce the exact hardness profile although the surface-hardening procedure was done with care. This means that the approach does not necessarily work on a large scale. Surface hardening strengthened the entire thickness of the plate, but the edges more than the core (Figure 1(b)). The work hardening is slightly higher for the SH plates than for the AR plates and the failure strain is lower. The 6 mm and 4 mm plates were also hardened. The hardness profiles were similar, but the core hardness was higher overall for these thicknesses. The ballistic limit velocities were determined from numerical fits to the generalized Recht-Ipson model [5]. Figure 2(b) shows that the ballistic limit velocity for the SH plates are between 20% and 30% higher than for the AR plates. We also see that the ballistic limit velocity decreases for configurations with more layers for the SH plates, but that layering the AR plates is less detrimental to the capacity.

Table 1: Model parameters (Note that A varies over the thickness for the SH plates.)

	A (MPa)	Q_1 (MPa)	C_1	Q_2 (MPa)	C_2	W_{cr} (MPa)	c	\dot{p}_0	m
AR	333.1	236.3	16.5	416.5	1.2	848			
SH	535.8	381.8	68.7	394.4	1.9	925	0.0114	5.0×10^{-4}	0.94

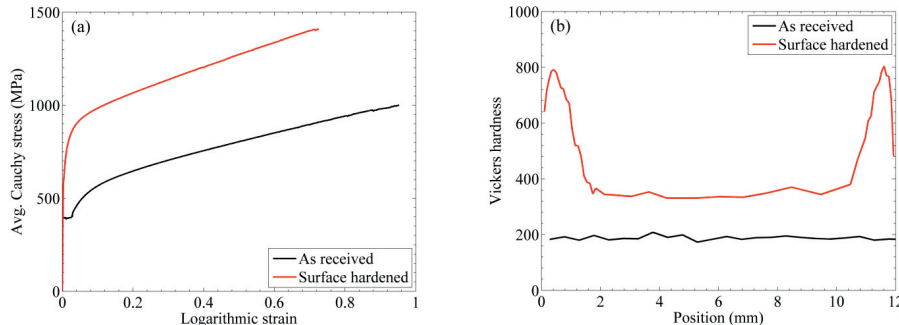


Figure 1: (a) Stress-strain curves to failure and (b) hardness distribution for the 12 mm plates.

4. Numerical Simulations

4.1 Material modeling

A modified Johnson-Cook (MJC) constitutive model [6][7] was used in the simulations, i.e.,

$$\sigma_{eq} = \left(A + \sum_{i=1}^2 Q_i (1 - \exp(-C_i P)) \right) \left(1 + \frac{\dot{p}}{\dot{p}_0} \right)^c \left(1 - \left(\frac{T - T_r}{T_m - T_r} \right)^m \right) \quad (1)$$

where σ_{eq} is the von Mises equivalent stress, (A , Q_i , C_i , c , m) are material constants, p and \dot{p} are the equivalent plastic strain and strain rate, \dot{p}_0 is a reference strain rate, T is temperature, T_r is the reference temperature and T_m is the melting temperature. Note that for the SH plates, A varies as a function of the plate thickness. We further assume adiabatic conditions. Failure was modeled with the Cockcroft-Latham (CL) [8] criterion where damage (D) accumulates as a function of the major principal stress (σ_1) and the equivalent plastic strain as

$$D = \frac{1}{W_{cr}} \int_0^{p_f} \langle \sigma_1 \rangle dp \quad (2)$$

where W_{cr} is the CL failure parameter that completely defines the failure model. All the material parameters for the AR configuration were found from the uniaxial tension tests by inverse modeling. The CL failure parameter was found by integrating the major principal stress over the equivalent plastic strain to failure. Since tension testing of the hardened surface layer is difficult to perform, we had to make three assumptions to obtain the material parameters as a function of the thickness in the SH plates: (1) the CL parameter is constant for each plate, (2) the slope of the hardening curve does not change over the cross section, and (3) the Vickers hardness is proportional to the tensile strength. This entails that the only two parameters to vary across the cross section are, in fact, the yield stress and the failure strain. Table 1 shows a selection of the material parameters used in the simulations of AR and SH plates. Bullet material data and other parameters for steel can be found in Børvik et al. [1].

4.2 Finite elements models

We conducted the simulations with the commercial, nonlinear explicit finite element code IMPETUS Afea Solver [9]. 64-node hexahedral elements and a node-splitting algorithm were applied in all simulations; their main advantage in ballistic modeling is their ability to handle extreme deformations. We only simulated the impacts of the 12 mm thick plates for which the goal was to determine the ballistic limit velocity (v_b). Figure 3 shows some images from simulations before and during the penetration process where both the varying yield stress and the model's capability to describe fragmentation are illustrated.

4.3 Numerical results

Figure 2(a) and (b) show the results from the numerical simulations compared to the experiments. The simulations are conservative and the estimated ballistic velocities are 8.2% and 6.8% below the experimental ballistic velocities for the AR and SH plates, respectively.

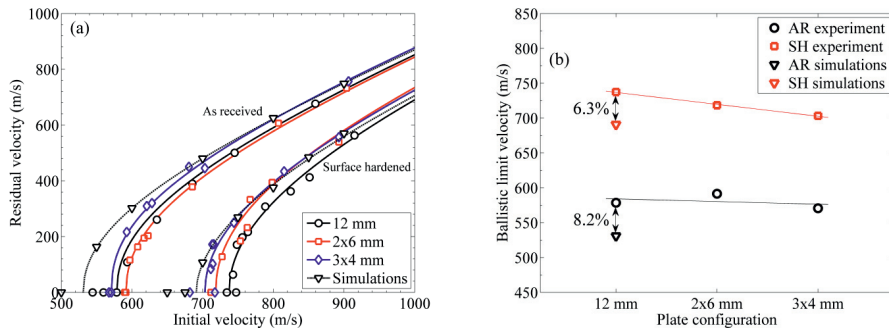


Figure 2: (a) Experimentally determined ballistic limit curves for all configurations compared to the simulations. (b) Ballistic limit velocity as a function of layer-configuration.

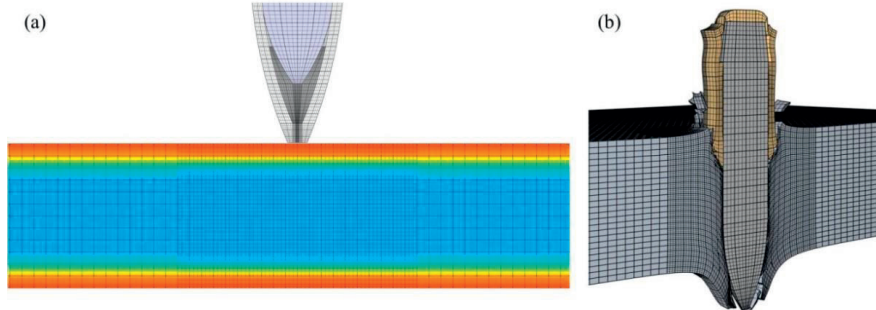


Figure 3: (a) Illustration of the varying yield stress in the FE model, and (b) picture from simulation.

5. Concluding Remarks

Experimentally, the ballistic limit velocity was highest for the monolithic and surface-hardened plates. Plate layering degraded the capacity more for SH plates than for AR plates. By inspecting the plates after perforation we saw that the layered AR plates developed a global dishing shape that cannot be seen in the SH plates. This global dish dissipates energy and is probably the reason why layering is less disadvantageous for AR plates than for SH plates. Ductile-hole growth was the only perforation mechanism seen for the AR plates. The SH plates exhibited fragmentation, radial-crack growth and, for the triple-layered plates, circumferential cracking, giving a larger experimental scatter in terms of residual velocity. The strong, but relatively brittle, surface layers were especially prone to cracking and in some cases, delamination between this layer and the ductile core was identified. In general, the numerical simulations captured the trends from the experiments. The ductile-hole growth is straightforward to describe numerically. A node-splitting algorithm was employed to capture the fragmentation seen in the SH plates.

Acknowledgements

The research was supported by SFI-CASA at the Norwegian University of Science and Technology. The authors would also like to thank former master's students Erlend Orthe and Henrik Thorsen for their valuable assistance.

References

- [1] T. Børvik, A. Clausen and S. Dey, *Perforation resistance of five different high-strength steel plates subjected to small arms projectiles*, International Journal of Impact Engineering, **Vol. 36**, pp. 948-964, July 2009.
- [2] J.K. Holmen, J. Johnsen, O.S. Hopperstad and T. Børvik, *Influence of fragmentation on the capacity of aluminum alloy plates subjected to ballistic impact*, European Journal of Mechanics A/Solids, **Vol. 55**, pp. 221-233, January – February 2016.
- [3] D. Lou, J.K. Solberg and T. Børvik, *Surface strengthening using a self-protective diffusion paste and its application for ballistic protection of steel plates*, Materials and Design, **Vol. 30**, pp. 3525-3536, October 2009.
- [4] G. Dieter, *Mechanical Metallurgy: SI Metric Edition*, McGraw-Hill Book Company, London, 1988.
- [5] R.F. Recht and T.W. Ipson, *Ballistic perforation dynamics*, Journal of Applied Mechanics, **Vol. 30**, pp. 384-390, 1963.
- [6] G.R. Johnson and W.H. Cook, *A constitutive model and data for metals subjected to large strains, high strain rates and high temperatures*, In: Proceedings of the 7th International Symposium on Ballistics, pp. 541-547, April 1983.
- [7] T. Børvik, O.S. Hopperstad, T. Berstad and M. Langseth, *A computational model of viscoplasticity and ductile damage for impact and penetration*, European Journal of Mechanics A/Solids, **Vol. 20**, pp. 685-712, September – October 2001.
- [8] M.G. Cockcroft and D.J. Latham, *Ductility and the workability of metals*, Journal of the Institute of Metals, **Vol. 96**, pp. 33-39, 1968.
- [9] IMPETUS Afea AS, *Impetus Afea Solver*: <http://www.impetus-afea.com> [cited: 2016-01-26].

Jens Kristian Holmen, Tore Børvik, Odd Sture Hopperstad

**Experiments and simulations of empty and sand-filled
aluminum alloy panels subjected to ballistic impact**

Submitted for possible journal publication.

Part 5

Experiments and simulations of empty and sand-filled aluminum alloy panels subjected to ballistic impact

J.K. Holmen*, T. Børvik and O.S. Hopperstad

*Structural Impact Laboratory (SIMLab) and Centre for Advanced Structural Analysis (CASA),
Department of Structural Engineering, Norwegian University of Science and Technology (NTNU),
Trondheim, Norway*

ABSTRACT

A discrete particle method can in combination with the finite element method be used to predict the interaction between structures and granular media during ballistic impact. By applying a discrete particle method to model granular materials, issues like mesh distortion, element deletion and continuum constitutive equations can be avoided. This study presents experiments and numerical simulations on the perforation of empty and sand-filled aluminum alloy panels subjected to impacts by small-arms bullets. The simulations of the sand-filled panels were conducted using a combined discrete particle–finite element approach that accounts for the coupling between structure and sand. The ballistic capacity of the sand-filled aluminum panels was more than 40 % higher than that of the empty aluminum panels. Overall, the results from the numerical simulations capture the trends from the experiments. The predicted ballistic capacity for the empty panels was within 5 % of the experimentally determined value and the critical velocity for the sand-filled panels was predicted within 11 % of the experimentally determined critical velocity. The scatter found in the experiments was also captured in the simulations.

Keywords: Small-arms bullets; Ballistic tests; Discrete particle method; Finite element method; Granular materials; Protective structures; Soil-structure coupling

* Corresponding author: + 47 93 04 58 37 (Jens Kristian Holmen)
Email address: jens.k.holmen@ntnu.no (Jens Kristian Holmen)
URL: www.ntnu.edu/casa

1. INTRODUCTION

Extruded aluminum panels are used in a number of engineering structures due to their low weight-to-stiffness ratio. Børvik et al. [1][2] showed experimentally that AA6005-T6 aluminum panels filled with granular materials can be used to mitigate the possibly lethal effects of explosions or impacts by projectiles or debris. The resistance against explosions was simulated with a finite element model where the response of the granular material was approximated by a constitutive model originally intended for foams. However, the foam model was not deemed accurate enough for perforation simulations, so the ballistic behavior was not analyzed numerically in that study. A significant grain-size effect was revealed in experiments with gravel. Here, grains larger than 2 mm were found to have greater resistance against perforation than typical sand with median grain diameter smaller than 2 mm. The material parameters for the AA6005-T6 aluminum panels were determined some years earlier and numerical simulations of ballistic perforation of empty panels by 20 mm ogival-nosed projectiles were presented in Ref. [3].

In the current study we use the same AA6005-T6 aluminum panels as were used in Refs. [1][2][3]. They are in the numerical simulations modeled as a continuum with finite elements. The granular material (sand), on the other hand, is modeled with a discrete particle method as rigid spherical particles that transfer forces through contact and friction. This method was proposed by Olovsson et al. [4][5] and was initially developed to handle the gas-fabric contact issues in airbag-deployment simulations before it was applied to represent close-range blast loading and the interaction between high explosives, air and sand. The discrete particle method is available in the explicit nonlinear finite element code IMPETUS Afea Solver [6] and it was thoroughly described and used for combined sand impact and blast loading on structures by Børvik et al. [7] and Wadley et al. [8]. More recently, Holloman et al. [9][10] applied the discrete particle method to gain insight into the impulse transfer between sand ejecta from buried charges and structural components. The case of deep penetration by small-arms bullets into granular materials was studied in detail by Børvik et al. [11] and the results from these simulations showed that the method was able to describe many of the phenomena that were seen experimentally.

Discrete numerical modeling of granular materials has been researched extensively since Cundall and Strack [12] presented their distinct element model in 1979. Combined discrete particle–finite element approaches like the one presented above have been used, e.g., by

Oñate and Rojek [13]. Solid materials such as rock and concrete can also be represented by discrete particles by introducing a cohesive law between individual particles [14]. On an even lower scale, agglomerates of discrete sub-particles can represent larger particles to model cracking and fracture in granular materials as shown by Cil and Alshibli [15]. Discrete particles methods have the advantage of needing relatively few input parameters and the complicated bulk material behavior arises as a consequence of relatively simple assumptions on the particle level [16]. Continuum models, on the other hand, require constitutive equations for the bulk sand and numerical issues might arise in the mesh discretization and with element erosion. Heterogeneity is also difficult to capture. Individual sand grains can in some cases be represented by finite elements to allow for crushing. This has been shown to be important in high velocity penetration of sand [17][18][19], but the added complexity comes at a significant computational cost.

High strain rate behavior of sand and its behavior during rapid penetration has been carefully reviewed by Omidvar et al. [20][21]. It is clear from centuries of research that the resistance of sand against a high-velocity intruder such as a bullet is affected by a myriad of parameters on several scales. The most relevant for perforation problems are the shape, trajectory, obliquity, mass and velocity of the bullet; and the packing density, grain size and moisture content of the sand. In addition, the frictional effects between the bullet and the sand come into play.

The objective of this study is to evaluate a numerical technique for design of protective structures consisting of sand in combination with ordinary solid materials. To this end we first experimentally determine to which degree filling an aluminum panel with sand increases its capacity against perforation by small-arms bullets; we present a simple calibration method for the discrete particle model; and lastly we use the calibrated discrete particle model in combination with finite elements to simulate the entire problem including the sand–structure interaction. By using this approach, it is now possible to predict the response and optimize the design of protective structures consisting of a combination of a solid structure and a discrete filling.

2. EXPERIMENTAL STUDY

2.1 Component test setup

All the ballistic tests were conducted in a ballistic laboratory where a smooth-bored 7.62×63 mm Mauser rifle launched the armor piercing (AP) bullets shown in Figure 1

toward the target panels shown in Figure 2 at predefined approximate velocities between 400 m/s and 900 m/s. The nominal mass of the complete bullet was 10.5 g and it consisted of a brass jacket, a lead cap and an ogive-nosed hardened steel core with a nominal mass of 5.0 g, a caliber radius head (CRH) of 3 and a Rockwell C hardness of 63. During testing, 300 mm long sections of the panels were mounted in a rigid frame, and only the bottom and top 30 mm were constrained in the direction of perforation. For the impact conditions considered here the boundary conditions are believed to be of minor importance. The impact point was chosen 27.5 mm from the center line of the panel as indicated in Figure 2, meaning that the projectile also had to perforate the oblique web. For the tests without any sand, at most 10 shots were fired at a 300 mm high profile, leaving 50 mm between each shot. For the remaining tests, sand was filled inside the cavities of similar profiles and the sides of the panels were gently tapped with a rubber hammer to compact the sand. The panels were mounted on a specially designed steel plate and another steel plate was put on top of the panels before each test. At least 70 mm was left between each impact point and the sand was replaced at irregular intervals. Small pitch angles, $\alpha \leq 3^\circ$, were observed in some of the tests. This is commented upon in Section 3. No spin was given to the bullet, the effects of which were commented on by Børvik et al. [11]. Initially, 49 tests were performed, but nine additional tests were conducted on the B95 sand to further investigate the repeatability of the test setup giving 58 component tests in total.

Two Phantom v1610 high-speed video cameras were used to capture the perforation process. A Nikon 80-200 1:2.8D lens and a Nikon 70-300 1:4.5-5.6G lens were mounted on the cameras, an exposure time of 0.001 ms was used and an area of approximately 150 mm x 75 mm was covered by each camera. Two Cordin Model 659 flashes were used as light sources. A resolution of 512×304 pixels and a frame rate of 80,000 frames per second for both cameras were sufficient to optically measure the initial and residual velocities of the bullets.

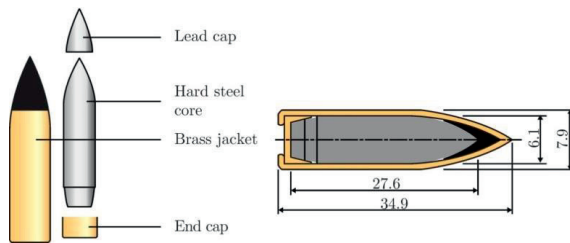


Figure 1: Geometry of the AP-bullet used in this study.

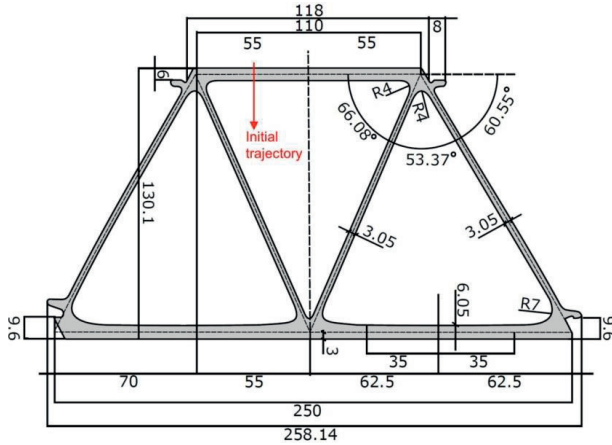


Figure 2: Geometry of the AA6005-T6 aluminum panel and an indication of the initial bullet trajectory/impact point.

2.2 Sand characteristics

Three types of sand delivered from AB Baskarpsand in Sweden were used in this study: B15, B55 and B95 with respective median grain sizes (diameters) of 0.15 mm, 0.55 mm and 0.95 mm. The main constituents of the sand are quartz (SiO_2) and alumina (Al_2O_3), with minor fractions of other elements. B15 consists of 88.5 % quartz and 6.3 % alumina; B55 consists of 90.1 % quartz and 5.3 % alumina; while B95 consists of 77.1 % quartz and 12.5 % alumina. Table 1 provides some material data for the sand. The grain size curves that show the proportion of grains smaller than a certain size are shown in Figure 3 and the grain size distribution is visualized in Figure 4. The moisture content was measured to be less than 0.5 % for all the sand types. Figure 3 and Figure 4 also show that B95 sand is the least uniform material. This means that the porosity is lower than for B55 and B15 which is why the bulk density is highest for this sand type. The bulk density in Table 1 was measured with a 1000 cm^3 container normally used for concrete aggregates. However, in relation to the additional ballistic tests we measured the bulk density of the B95 sand when it was filled in the aluminum panels just before impact-testing: no measurement differed more than 2 % from the reported value.

Table 1: Material properties for the sand

Sand type	Median grain size (mm)	Compacted density (kg/m^3)	Particle density (kg/m^3)	Moisture content (%)
B15	0.15	1629	2600-2700	0.42
B55	0.55	1695	2600-2700	0.32
B95	0.95	1731	2600-2700	0.30

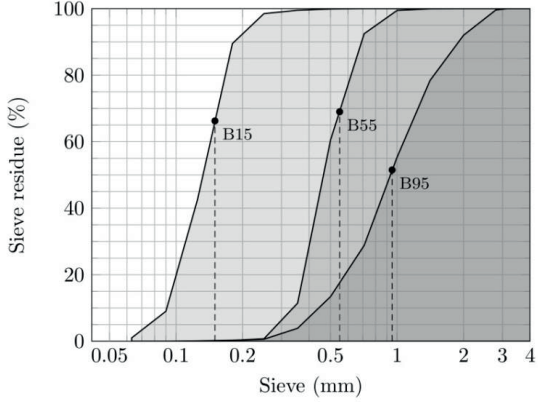


Figure 3: Grain size curves for the three sand types. The median grain sizes are indicated with dashed lines.

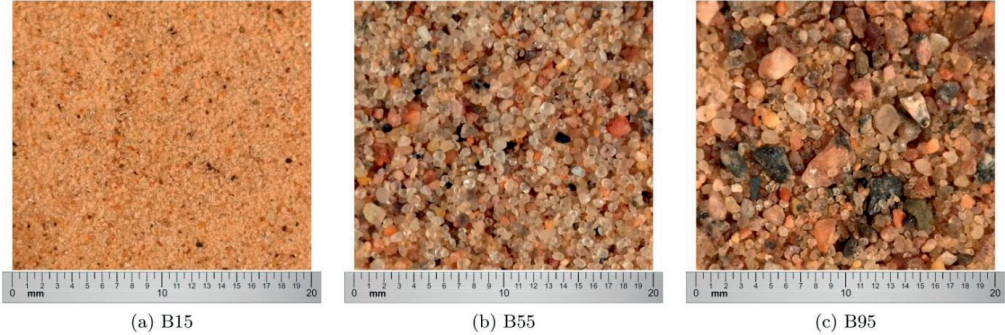


Figure 4: Visualization of the grain size distribution for the three sand types.

2.3 Results from the tests on empty aluminum panels

The residual velocities v_r from the tests on the empty aluminum panels plotted against their respective initial velocities v_i are shown in Figure 5. The solid line was calculated from a generalized version of an analytical model originally proposed by Recht and Ipson [22], also called the Lambert and Jonas equation [23],

$$v_r = a(v_i^p - v_{bl}^p)^{1/p} \quad (1)$$

where the model parameters a and p , as well as the ballistic limit velocity v_{bl} were simultaneously obtained with a least-squared-error fit to the experimental data points. With $a = 0.94$ and $p = 2.06$ the ballistic limit velocity, which is a common ballistic capacity measure, of the empty panels was found to be $v_{bl} = 450.1$ m/s.

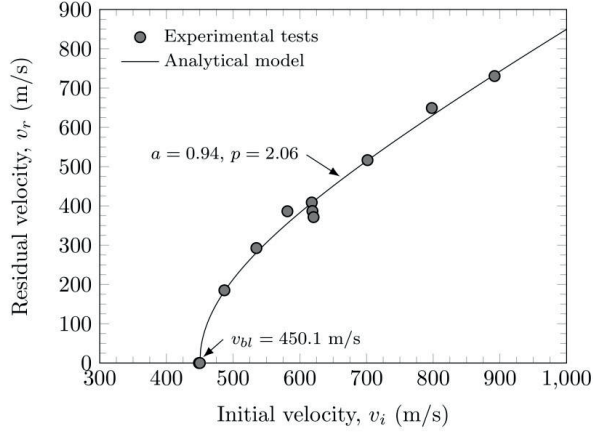


Figure 5: Results from ballistic tests of the AA6005-T6 aluminum alloy panels without sand.

A total of eleven shots were fired at the empty panels. A cross section showing the penetration channels from two tests is presented in Figure 6. The entry holes were similar for every test and ductile-hole enlargement was the main perforation mechanism. No evidence was found of stripping of the brass jacket during perforation of the front plate in any of the tests. The flight trajectory after impact was unstable for low initial velocities. The bullet did in some cases deviate significantly from its initial flight path which was evident from the large spread in the exit holes on the back plate. The bullet instability was amplified by the oblique web and in some cases the bullet made a 90° turn inside the aluminum panel and came to a complete stop in the outer oblique web. Generally, the jacket was stripped off by the rear plate.



Figure 6: Cross section of an AA6005-T6 panel that was struck without sand. Left: $v_i = 618.9 \text{ m/s}$ and $v_r = 386.3 \text{ m/s}$. Right: $v_i = 534.9 \text{ m/s}$ and $v_r = 292.6 \text{ m/s}$.

2.4 Results from the tests on sand-filled aluminum panels

The residual velocities v_r from the tests on the sand-filled panels plotted against their respective initial velocities v_i are shown in Figure 7. The figure reveals that there is no one-to-one relation between v_i and v_r , i.e., the tests are not easily repeatable and the scatter is large. However, it is clear that filling the panels with sand of any kind increased the panels' resistance to perforation as expected. To compare the results to the empty panels we define a combined critical velocity v_{crit} for all the sand-filled panels. If the bullet's initial velocity exceeds v_{crit} , perforation can be expected. This is a conservative estimate, but $v_{crit} = 646.0$ m/s is a 43.5% increase from the capacity of the empty panels and it clearly illustrates that the capacity can be substantially increased by filling the panels with sand. No clear and significant change in the ballistic limit velocity was found between the three different sand types used in this study.

A panel sliced in half is shown in Figure 8. Contrary to what happened inside the empty panels, the bullet's jacket was normally stripped off between the front plate and the oblique web when the panels were filled with sand. Figure 7 clearly displays that results from perforation of the sand-filled panels are more dispersed than results from perforation of empty aluminum panels in Figure 5. Definite conclusions about the perforation resistance of the three sand types are difficult to draw and have not been emphasized in the ensuing numerical work.

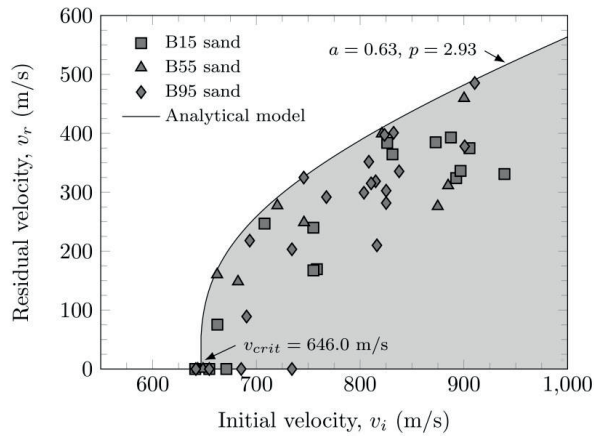


Figure 7: Results from ballistic tests of the AA6005-T6 aluminum alloy panels filled with the three different sand types. Each test is identified by a mark, while the gray area represents the unsafe domain where perforation can be expected.

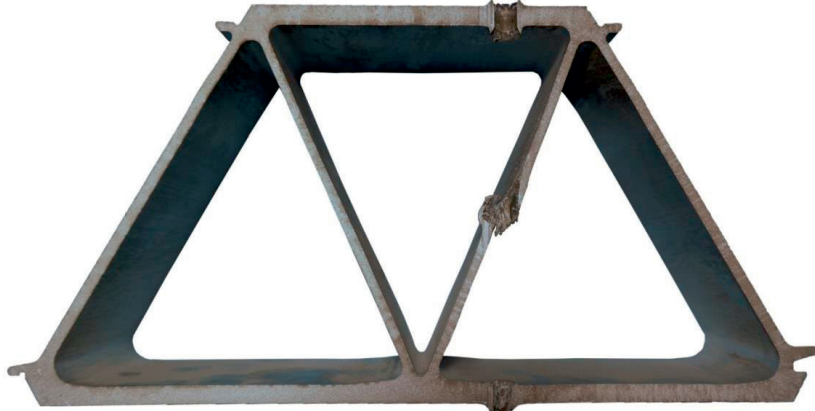


Figure 8: Cross section of an AA6005-T6 panel that was struck when filled with B95 sand: $v_i = 910.5 \text{ m/s}$ and $v_r = 485.4 \text{ m/s}$.

The large scatter in the test data was checked for B95 sand in two test series with an impact velocity of $820 \pm 20 \text{ m/s}$: (1) Five shots fired into five separate brand new panels with previously unused sand, and (2) four shots fired into the same panel without changing the sand between the shots. The mean value and the scatter was similar in both test series, indicating that the employed experimental procedure was adequately accurate.

3. NUMERICAL STUDY

3.1 Aluminum panels and 7.62 AP-bullets

A comprehensive study on the material behavior of aluminum alloy AA6005-T6 extruded panels was presented by Børvik et al. [3]. Quasi-static tension tests, pre-notched tension tests, and tension tests at elevated strain rates and temperatures were conducted to calibrate modified versions [24] of the Johnson-Cook (JC) flow stress model and the JC failure model. In the current paper we have used the original model proposed by Johnson and Cook [25] that reads

$$\sigma_{eq} = (A + Bp^n) \left(1 + c \ln \left(\frac{\dot{p}}{\dot{p}_0} \right) \right) \left(1 - \left(\frac{T - T_r}{T_m - T_r} \right)^m \right). \quad (2)$$

A , B and n are hardening parameters, p is the equivalent plastic strain, \dot{p} is the plastic strain rate, \dot{p}_0 is a reference strain rate, T is the current temperature, T_r is the ambient/room temperature, T_m is the melting temperature, while c and m are parameters controlling the

strain rate sensitivity and temperature dependency, respectively. The original JC failure criterion [26] is used to model failure of the aluminum panels in this study; the damage parameter D is dependent on the incremental plastic strain Δp as

$$D = \sum \frac{\Delta p}{p_f} \quad (3)$$

and the current plastic failure strain reads

$$p_f = (D_1 + D_2 \exp(D_3 \sigma^*)) \left(1 + D_4 \ln\left(\frac{\dot{p}}{\dot{p}_0}\right) \right) \left(1 + D_5 \left(\frac{T - T_r}{T_m - T_r} \right) \right). \quad (4)$$

D_1 , D_2 , D_3 , D_4 and D_5 are model parameters, $\sigma^* = \sigma_H / \sigma_{eq}$ is the stress triaxiality ratio and $\sigma_H = (\sigma_1 + \sigma_2 + \sigma_3)/3$ where $\sigma_1 \geq \sigma_2 \geq \sigma_3$ are the ordered principal stresses. All the material and failure parameters for the panels can be found in Table 2. Note that c and D_4 were recalibrated from the values presented in Ref. [3] since the rate-sensitivity terms in the original and modified versions of the JC constitutive models and failure criteria are slightly different. The reason for using the original JC model, and not the modified JC model, is that the modified JC failure model is not implemented in the standard version of IMPETUS Afea Solver.

Table 2: Model constants for the aluminum alloy AA6005-T6 panel [3].

A (MPa)	B (MPa)	n	D_1	D_2	D_3	D_4 ²	D_5	m
270.0	134.0	0.514	0.06	0.497	-1.551	0.0329	6.80	0.703
E (MPa)	ν	ρ (kg/m ³)	c ³	\dot{p}_0 (s ⁻¹)	C_p (J/kg K)	α (K ⁻¹)	T_r (K)	T_m (K)
70,000	0.3	2700.0	0.0086	1×10^{-3}	910.0	2.3×10^{-5}	293	893

² Modified from the original value of 0.0286 due to the change from a power term to a logarithmic term

³ Modified from the original value of 0.0082 due to the change from a power term to a logarithmic term.

Table 3: Model constants for the bullet materials [27].

	A (MPa)	B (MPa)	n	W_{cr} (MPa)	\dot{p}_0 (s ⁻¹)	c ⁴	m
Lead tip	24.0	300.0	1.0	175.0	5×10^{-4}	0.2293	1.0
Brass jacket	206.0	505.0	0.42	914.0	5×10^{-4}	0.0108	1.68
	E (MPa)	ν	ρ (kg/m ³)	C_p (J/kg K)	α (K ⁻¹)	T_r (K)	T_m (K)
Lead tip	10,000	0.42	10,660	124	2.9×10^{-5}	293.0	760.0
Brass jacket	115,000	0.31	8520	385	1.9×10^{-5}	293.0	1189.0

The 7.62 mm AP bullet has been used in several previous studies by the authors, e.g., [11][27][28]. The hardened steel core was considered as a rigid body with density $\rho = 7850 \text{ kg/m}^3$, while the brass jacket and lead tip were modeled using the original JC constitutive equation presented in Eq. (2). Failure of these parts was controlled by the one-parameter failure criterion proposed by Cockcroft and Latham (CL) [29]

$$D = \frac{1}{W_{cr}} \int_0^p \langle \sigma_1 \rangle dp = \frac{1}{W_{cr}} \int_0^p \left\langle \sigma^* + \frac{3 + \mu_\sigma}{3\sqrt{3 + \mu_\sigma^2}} \right\rangle \sigma_{eq} dp, \quad \langle \sigma_1 \rangle = \max(0, \sigma_1), \quad (5)$$

where W_{cr} is the failure parameter and σ_1 is the major principal stress. As shown in Eq. (5), the major principal stress can be expressed as a function of the stress triaxiality ratio σ^* and the Lode parameter μ_σ defined here as

$$\mu_\sigma = \frac{2\sigma_2 - \sigma_1 - \sigma_3}{\sigma_3 - \sigma_1}. \quad (6)$$

The failure parameter W_{cr} represents an amplified plastic work to failure and can be found from a uniaxial tension test by integrating σ_1 over the entire plastic strain path to specimen failure. Material and failure parameters for the bullet materials can be found in Table 3.

3.2 The discrete particle method

Sand is modeled with the discrete particle method described in more detail by Børvik et al. [7]. The method employs a robust penalty-based contact formulation where elasticity, friction and damping may all be accounted for. The rheological model, which is similar to a model proposed by Deshpande et al. [30], is shown in Figure 9 and it includes a tangential and

⁴ Modified from 0.1 to 0.2293 and 0.01 to 0.0108 respectively due to the change from a power term to a logarithmic term.

a normal spring both with stiffness k_s , a normal dashpot with damping coefficient c_s , and lastly a frictional element with a Coulomb friction coefficient μ_s that controls the tangential elastic spring force. In addition to this, a particle-structure friction coefficient, μ_{ps} controls the friction between particles and finite elements. Recently, a similar, but augmented, model was employed by Oñate et al. [14] to represent cohesive materials.

The discrete particles are included in the various numerical models by distributing unit cells with 1000 particles of equal size and with periodic particle stacking. Just like the JC flow stress model presented in Section 3.1 the discrete particle method is phenomenological. No attempt is made to describe all the underlying physical processes related to the deformation of the sand; they are instead incorporated in the simulations by adapting parameters to experimental calibration tests as will be done in the following. Important phenomena like particle fracture and particle rotation are not modeled explicitly, but accounted for in the calibration of the model through the inter-particle stiffness k_s and the friction μ_s . The inter-particle damping c_s was neglected in this study because friction seems to be the dominating energy dissipating mechanism in dry sand; this was discussed in further detail by Børvik et al. [7].

3.3 Calibration of the discrete particle model

Traditional methods of characterizing granular materials undergoing high strain rate loading are complex and require advanced test facilities. Four common testing methods were identified by Omidvar et al. [20]: uniaxial compression tests, Split Hopkinson Pressure Bar tests, triaxial compression tests and plane wave shock tests. In the current paper we used a simplified method for characterization of the sand which is explained below. The calibration test is similar enough to the component test to capture the most important phenomena without invalidating the prediction of the component behavior by being too similar.

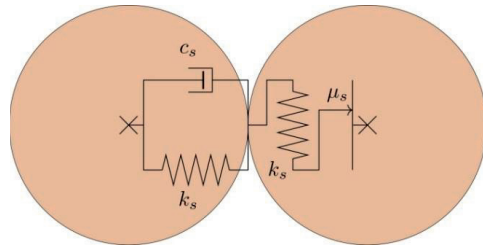


Figure 9: Rheological model for the discrete particles

Table 4: Results from the calibration tests on 50 mm thick sand slabs struck with 10 mm rigid steel balls.

	v_i (m/s)	v_r (m/s)
Test 1	277.6	57.9
Test 2	277.9	59.1
Test 3	279.1	65.0
Average	278.2	60.7

Calibration of the discrete particles and their constants was done by performing some simple perforation tests of sand slabs contained in a specially designed steel container. The box was 50 mm thick in the impact direction and had inner dimensions of 250 mm \times 200 mm in the directions transverse to the flight path. The transverse dimensions of the box were chosen to minimize the effects of the boundaries. Holes with diameter 25 mm were drilled in the front and back walls of the box to create a free passage for the projectile. These holes were covered with 0.1 mm thick domestic aluminum foil before filling the box with sand. Rigid steel balls of diameter 10 mm and with a Rockwell C hardness of 60 were fired from a compressed gas-gun of which more information can be found in Ref. [3]. The initial and residual velocities, v_i and v_r respectively, of the steel balls were measured by a high-speed camera of the same type as described in Section 2.1, now at a resolution of 1280 \times 208 pixels and with a frame rate of 60,000 fps.

The B95 sand with a median grain size of 0.95 mm was used in the calibration tests. Three tests were performed to investigate the repeatability of the measurements. Initial velocities of around 275 m/s were chosen to ensure a significant reduction in the velocity through the tests. Figure 10 shows a timelapse from calibration test 3. Table 4 shows the results and almost no spread in terms of residual velocity was seen. An average initial velocity $\bar{v}_i = 278.2$ m/s and an average residual velocity $\bar{v}_r = 60.7$ m/s were found and are used in the subsequent calibration. It should be mentioned that these tests are simpler and cheaper than the material tests listed by Omidvar et al. [20], but they provide less information about the general behavior of sand.

Figure 11 shows the sand box model that was made in the IMPETUS Afea Solver to study the influence of the particle size, inter-particle friction and stiffness, and the particle–structure friction. The default parameters for the generic dry sand that are available in IMPETUS Afea Solver [6][7] are listed in Table 5; these were used in the investigation of particle size. The effect of particle–structure friction was neglected. In Ref. [11] it was found that particles somewhat larger than the median grain size of the sand would produce good results while

limiting the computational time. Simulations with 50,000 to 8,000,000 particles were run with an otherwise identical model. The average particle diameter then varied from 1.93 mm to 0.415 mm and the solid volume fraction was constant at 0.6. Figure 12 shows the residual velocity plotted as a function of the number of particles. It is clear that the resistance against perforation decreases by increasing the number of particles. A total of 830,000 discrete particles were chosen for subsequent calibration, i.e., a particle diameter of approximately 1.5 mm will be used in the rest of this paper.

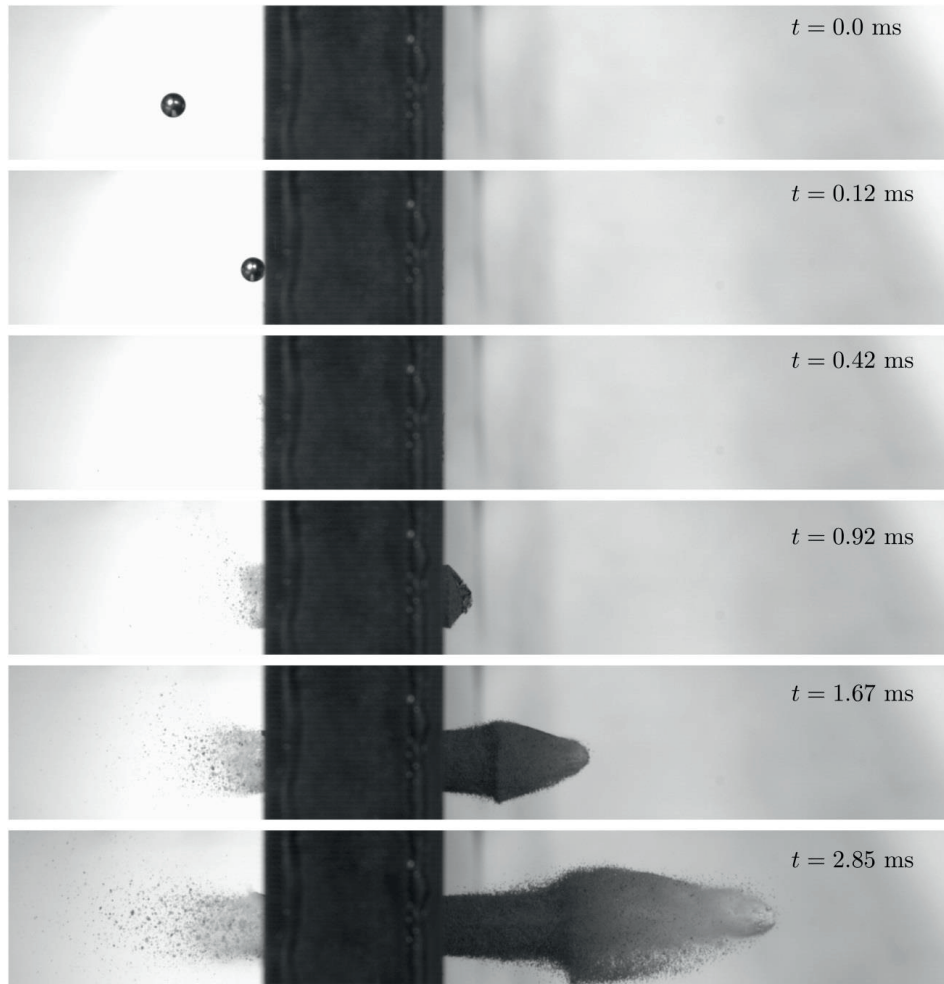


Figure 10: Timelapse from calibration test 3, $v_i = 279.1 \text{ m/s}$ and $v_r = 65.0 \text{ m/s}$.

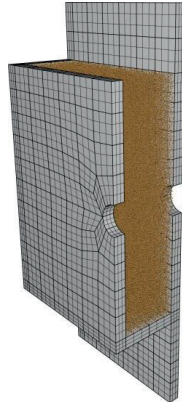


Figure 11: Simulation model of the steel box used in the calibration analyses. Only half the model is shown to improve visualization.

Individual effects of inter-particle friction μ_s and the particle–structure friction μ_{ps} were also investigated and the results are shown in Figure 13. We find that by increasing either of the friction parameters we increase the resistance against perforation. The residual velocity is more sensitive to the inter-particle friction than to the particle–structure friction. The inter-particle stiffness was also varied, but the effect was small compared to the friction and we decided to keep the default stiffness value $k_s = 4.0 \times 10^8$ N/m.

Based on the preceding discussion it appears that several parameter combinations can give the same residual velocities. We have chosen a combination of inter-particle friction $\mu_s = 0.225$ and particle–structure friction $\mu_{ps} = 0.2$. By considering three different impact positions (± 1 mm) we get results within 7% of the experimental average. The numerical average, however, is identical to the experimental average. Table 5 summarizes the calibrated constants for the discrete particle model. A numerical simulation of the calibration model is shown in Figure 14, and comparing this figure to Figure 10 reveals that the numerical behavior is close to the experiment both quantitatively and qualitatively.

Table 5: The model constants for the discrete particle model

	ρ_s (kg/m ³)	k_s (N/m)	μ_s	μ_{ps}	c_s
Generic dry sand	1620.0	4.0×10^8	0.1	0.0	0.0
Calibrated values used in this paper	1731.0	4.0×10^8	0.225	0.2	0.0

The discrete particle method applied in this work has so far only been validated for high impact velocities between 250 m/s and 1000 m/s. The calibration tests reported above have been done within the velocity-domain where the method is valid, but at a lower velocity than in the component tests. For low velocities, say 10 m/s, other mechanisms dominate the energy dissipation process. This requires a different friction description which is outside the scope of this research.

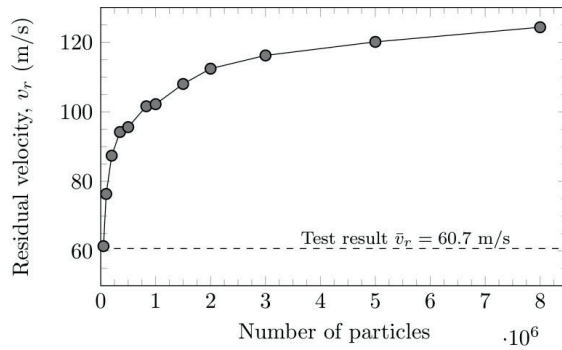


Figure 12: Residual velocity as a function of the number of particles in the calibration model.
Note that the x-axis goes from 0 to 8,000,000 particles.

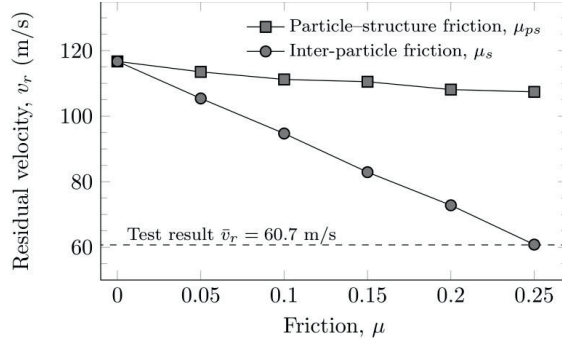


Figure 13: Effects of the inter-particle friction and particle–structure friction in the discrete particle model. The particle diameter is $d = 1.5$ mm (830,000 particles in the calibration model). Note that when μ_{ps} changes μ_p is kept constant, and vice versa.

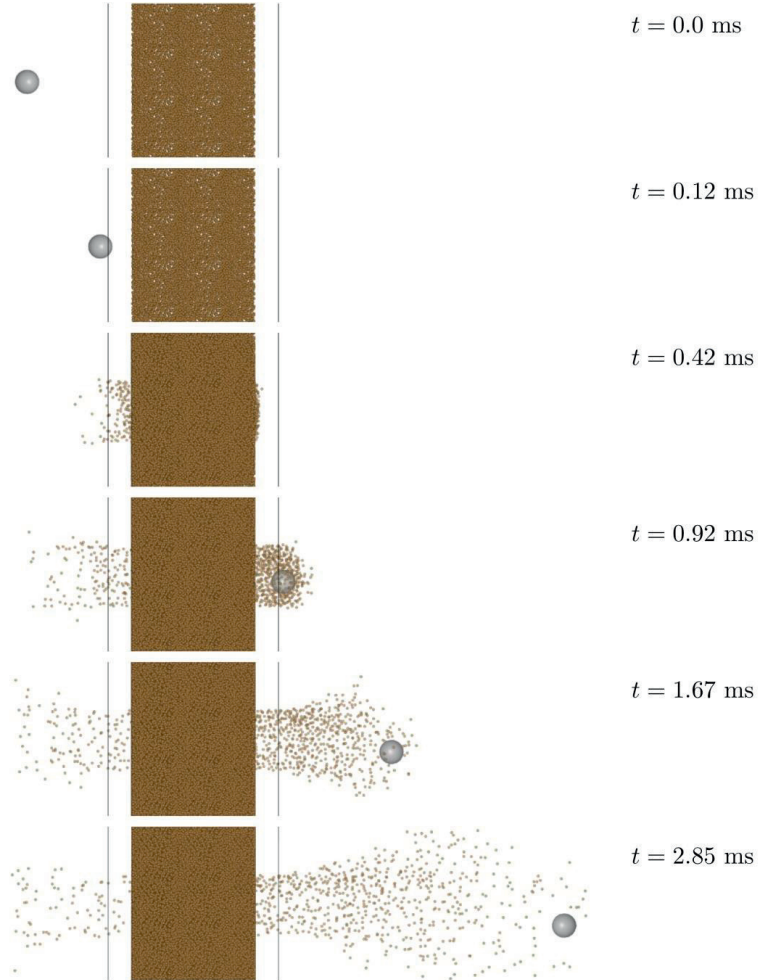


Figure 14: Timelapse from the calibration simulation, $v_i = 279.1 \text{ m/s}$ and $v_r = 62.8 \text{ m/s}$.

3.4 Numerical models

A numerical model of the AA6005-T6 aluminum panel was made based on the geometry in Figure 2. The mesh is shown in Figure 15. Some simplifications were made in the finite element discretization: we included only 200 mm of the panel in the extrusion direction and the geometry near the panel's corners was simplified. These alterations are not expected to affect the results. In the impact region fully integrated 3rd-order 64-node hexahedral elements of approximate size $1 \text{ mm} \times 1 \text{ mm} \times 1 \text{ mm}$ were chosen while in the peripheral parts of the panel the mesh was coarser and the elements were linear 8-node hexahedrons. No significant change in the residual velocity was seen with a finer discretization. The bullet was discretized with only the 3rd-order 64-node hexahedral elements. Such higher-order elements are

available in the IMPETUS Afea Solver and they have been applied previously in other perforation studies [27][28]. A more thorough description of the higher order elements can be found in Holmen et al. [31]. The calibration of the discrete particle method in Section 3.3 was based on a grain diameter of 1.5 mm. To obtain the same diameter in the simulations of the component tests 1,460,000 particles were used.

The material parameters determined in Section 3.1-3.3, and listed in Table 2, Table 3 and Table 5, were used in most of the simulations. Elements in the bullet are removed from the analysis when 16 out of their 64 integration points reach $D=1$ as defined in Eq. (5) or when the stable time step drops below 5 ns. For the elements in the aluminum panel the deviatoric resistance in an integration point is removed when $D=1$ as defined in Eq. (3), but the element is not removed from the analysis until its stable time step reaches a value of 3 ns. Friction between the bullet and the panel exists and it might be of significance, but it is disregarded in these simulations. By omitting frictional effects, the velocity at which the bullet strikes the sand will be higher. This will most likely give conservative results, i.e., higher residual velocities.

Impact velocities for the empty aluminum panels were chosen in regular intervals between 400 m/s and 900 m/s to be able to predict the ballistic limit curve and the ballistic limit velocity v_{bl} . For the sand-filled panels the impact velocity was chosen between 550 m/s and 900 m/s because of the increased resistance from the sand. Sensitivity studies regarding the bullet's impact point and pitch angle were also conducted. In this study we adopt the definitions from Goldsmith [32] where the pitch α is the angle between the bullet's centerline and the velocity vector as shown in Figure 16.

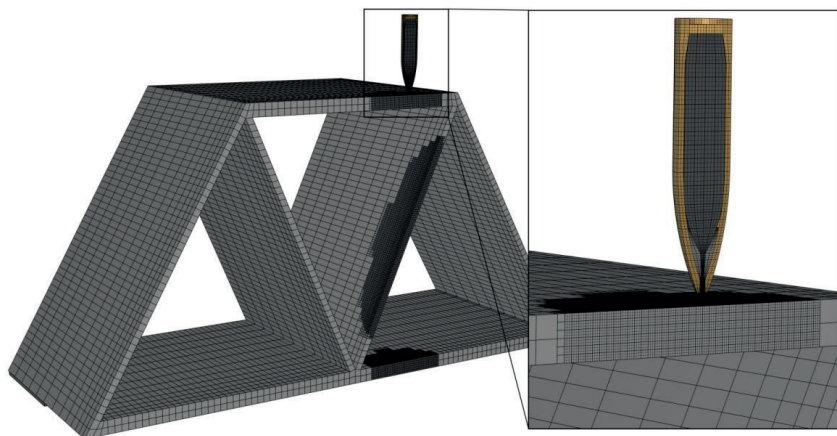


Figure 15: Finite element mesh used for the AA6005-T6 aluminum panels.

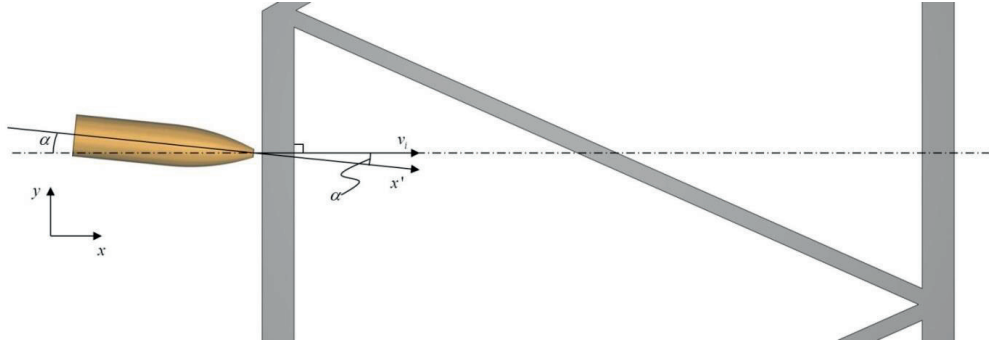


Figure 16: Definition of the positive pitch angle α , where v_i is the initial velocity and x' is in the direction of the centerline of the bullet.

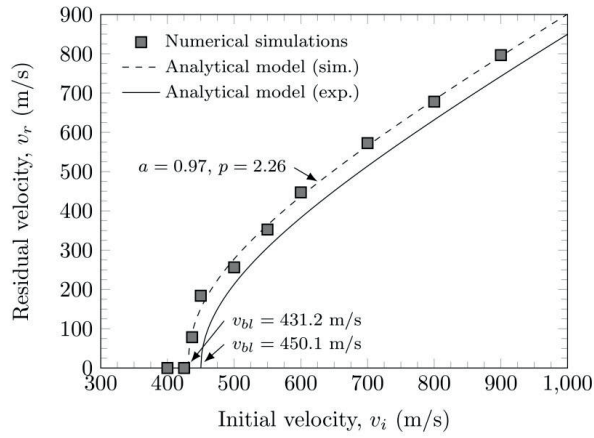


Figure 17: Numerical results from the simulations of the empty aluminum profiles compared to the experimentally fitted analytical model.

3.5 Numerical results

Figure 17 shows the simulation results for the empty aluminum panels compared to the ballistic tests reported in Section 2.3. For the simulations with no initial pitch angle, i.e., normal impact, the residual velocities were slightly overestimated, meaning that the ballistic limit velocity was underestimated. The difference from the experiments is, however, only 4.2 %. For initial velocities close to the ballistic limit velocity a positive pitch angle gives slightly lower residual velocities. Conversely, a negative pitch angle gives slightly higher residual velocities. A typical timelapse of the perforation process is shown in Figure 18. We see that the lead cap was completely eroded before perforation of the oblique web and that the brass jacket was nearly stripped off the rigid core after complete perforation of the panel. For this particular velocity we also see that the bullet turned towards the oblique web during perforation which was also seen in some of the experimental tests, see Figure 6. For lower

impact velocities the bullet turned in the opposite direction during perforation displayed for $v_i = 500 \text{ m/s}$ in Figure 19, where we also see that below the ballistic limit velocity the bullet turned completely and in some cases it did not even reach the rear plate, just as in the experimental tests.

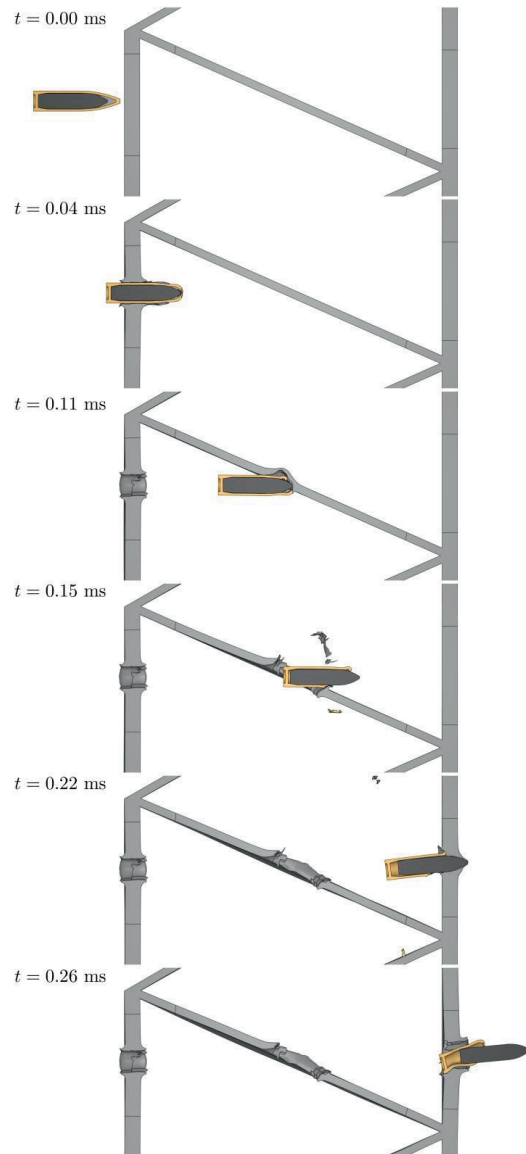


Figure 18: Timelapse of the perforation process of an empty aluminum panel with $v_i = 700 \text{ m/s}$ and $v_r = 572.5 \text{ m/s}$. The panel is cut in half to better illustrate the deformation process.

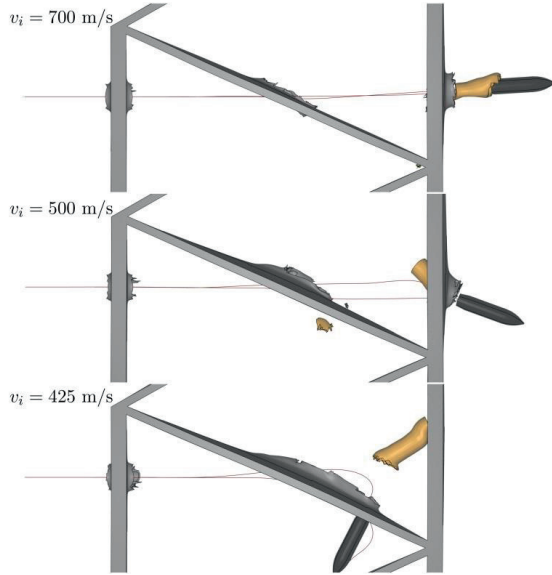


Figure 19: Pictures from the end of a selection of simulations. The lines are the trace of the front-center and rear-center nodes of the rigid core.

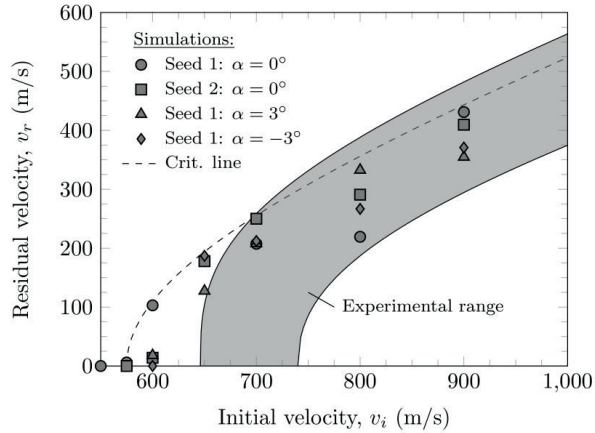


Figure 20: Numerical results from the simulations of the sand-filled aluminum panels.

In Figure 20 the results from the numerical simulations of the sand-filled aluminum panels are compared to the results from the ballistic tests reported in Section 2.4. Various impact points and pitch angles have been considered. The critical velocity was found to be 575.0 m/s. This is an 11% underestimation of the experimental value, meaning that the results are on the conservative side which is preferred from a design point of view. For higher impact velocities the results are within the experimental scatter. In the experiments the brass jacket was stripped off between the front plate and the oblique web in most of the tests. In the simulations with

high initial velocities the jacket was stripped off by the oblique web, while at lower velocities it was stripped off between the oblique web and the rear plate. Figure 21 shows a typical timelapse of the perforation process after normal impact. The direction in which the bullet turns during perforation seems somewhat arbitrary in these simulations and they, to some extent, capture the effect of random particle stacking from the experiments. Figure 22 shows a picture from a simulation where the bullet's impact point was moved 0.5 mm; this is denoted *seed 2* in Figure 20. The initial velocity was identical as in Figure 21 (700 m/s); however, the bullet turned in the opposite direction after perforation for *seed 2*. Also note that the residual velocities for the two striking points are fairly different.

Lastly, a direct qualitative comparison between an experiment and a numerical simulation is given in Figure 23. The experiment was performed with B95 sand and the sand has been suppressed from the simulation to improve visualization. These pictures show that the failure mechanisms from the experiment can be reproduced by the simulation and it further suggests that the proposed method is successful at predicting experimental observations.

4. DISCUSSION

Experimental observations from the current study confirm the conclusions made by Børvik et al. [1][2] that filling panels with granular materials significantly increases the perforation capacity. Ref. [1][2] also found that if the grain size is significantly smaller than the projectile, the capacity of the component is lower than if the grain size is larger than the projectile. In the current study it was hard to see any conclusive evidence of which sand-type gave the highest capacity which might not be surprising since the bullet is an order of magnitude larger than all the median grains investigated here.

Perforation of sand-filled aluminum profiles, or penetration of granular materials of any kind, is not easy to model, i.e., a certain initial velocity does not necessarily give the same residual velocity in consecutive experiments due to the influence of individual grains, variations in density, etc. Figure 20 shows that this behavior was to some extent captured in the simulations since moving the impact point 0.5 mm or tilting the bullet by an angle of 3° in some cases changed the residual velocity considerably. It is also clear from the calibration simulations that the particle size affected the residual velocity of the rigid steel balls and consequently the resisting force from the discrete particles on the penetrator; larger particles give larger forces.

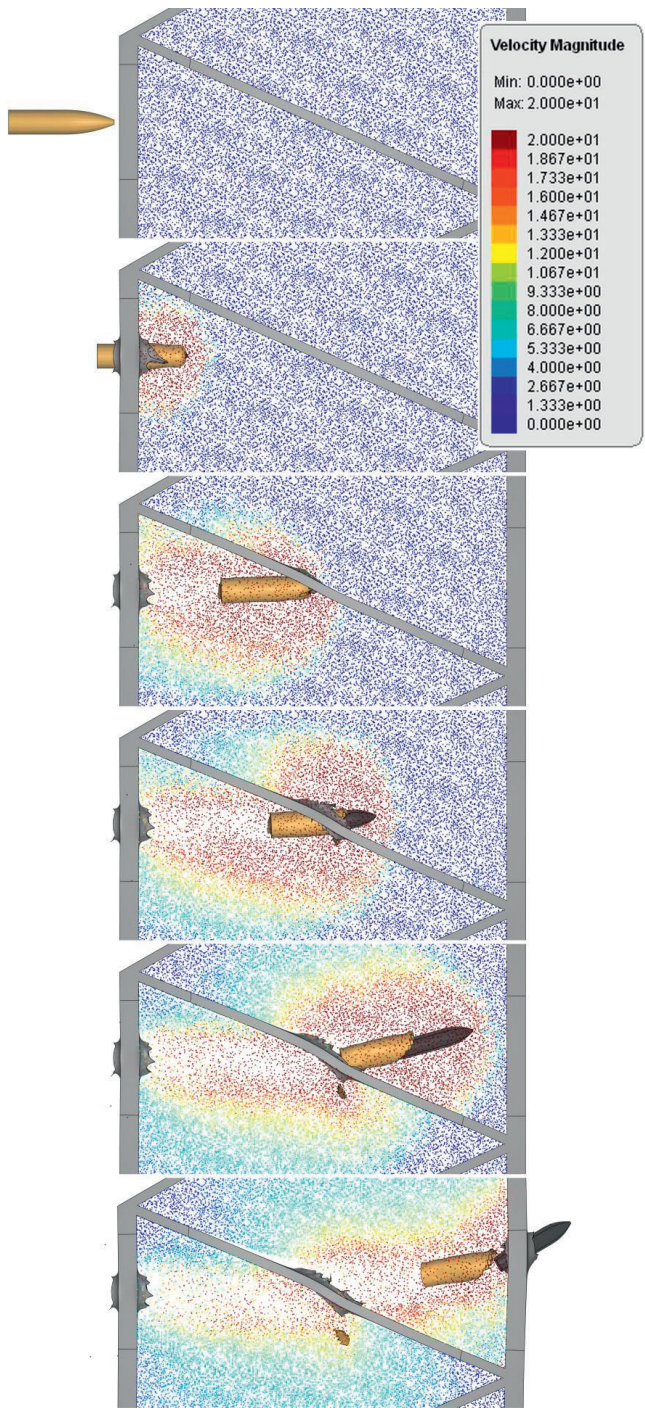


Figure 21: Timelapse of the perforation process and the velocity magnitude of the particles for a sand-filled aluminum panel with $v_i = 700 \text{ m/s}$ and $v_r = 207.4 \text{ m/s}$.

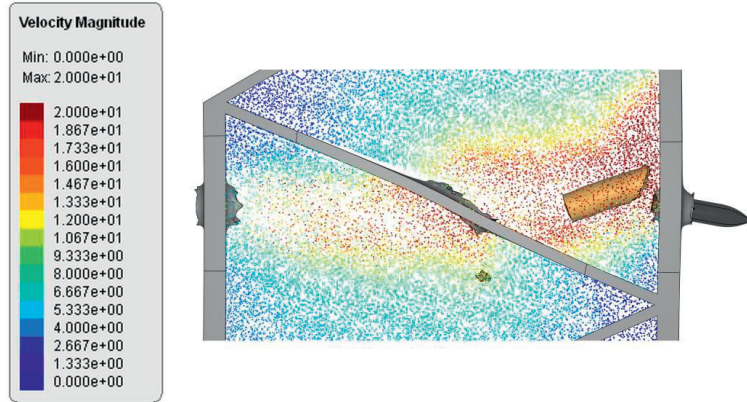


Figure 22: Picture at time 0.35 ms , i.e., the same point in time as the last frame in Figure 21 with the same initial velocity, but different striking point, $v_i = 700 \text{ m/s}$ and $v_r = 250.0 \text{ m/s}$.



Figure 23: Pictures of an experiment and a simulation of a sand-filled panel to show the qualitative similarities. Left: experiment ($v_i = 910.5 \text{ m/s}$ and $v_r = 485.4 \text{ m/s}$). Right: simulation ($v_i = 900.0 \text{ m/s}$ and $v_r = 431.0 \text{ m/s}$).

The explicit non-linear finite element method using Lagrangian meshes is prevalent when analyzing the response of structures subjected to ballistic impact. Although a Lagrangian mesh provides convenient treatment of complicated boundary conditions and history-dependent variables, difficulties arise when the deformations become too extreme resulting in small time steps and possibly inverted elements. When modeling granular materials, the individual grains shuffle around and switch places and this makes a physical description of sand subjected to penetration or perforation challenging with a standard Lagrangian mesh. Seeing that the behavior of sand is not directly dependent upon history variables, a coupled approach like the one presented here is well-suited to represent this in explicit simulations where the sand is modeled with discrete particles and structural components are modeled with a conventional finite element mesh.

5. CONCLUDING REMARKS

This study first presented experiments on the perforation resistance of empty and sand-filled aluminum alloy AA6005-T6 panels impacted by 7.62 mm AP-bullets. A ballistic limit velocity of 450.1 m/s was found for the empty panels. Subsequent tests were done where sand with median grain size 0.15 mm, 0.55 mm or 0.95 mm, respectively, was filled in the panel's cavities prior to testing. The added resistance from the sand resulted in a 43.5 % increase in the capacity regardless of the type of sand used as filling material.

Numerical simulations were carried out using a coupled discrete particle–finite element approach. Finite elements were used to represent the aluminum panels while discrete particles were used to represent the sand.

The following observations were made: Simulations of the empty aluminum panels predicted the perforation process and the capacity of the panels within 5 % of the experimental values confirming that the behavior of the aluminum panels was adequately captured. The critical perforation capacity of the sand-filled panels was predicted within 11 % of the critical velocity from the experiments when normal impact and only one impact point was considered, a reasonable result when we recognize the complexity of the problem. Numerical simulations of protective structures consisting of a combination of granular and solid materials are challenging and require robust and advanced numerical algorithms. In this study we have shown that coupled discrete particle–finite element methods can improve the engineering design process and serve as a useful tool for research purposes.

ACKNOWLEDGMENT

The financial support for this work comes from the Structural Impact Laboratory (SIMLab) at the Norwegian University of Science and Technology, The Research Council of Norway, and from the Norwegian Defense Estates Agency (NDEA). The authors would also like to express their gratitude to MSc-students Fredrik R. Bjerke and Lars M. Hansen for their help with the experimental work.

REFERENCES

- [1] Børvik T, Hanssen AG, Dey S, Langberg H, Langseth M. On the ballistic and blast load response of a 20 ft ISO container protected with aluminium panels filled with a local mass - Phase I: Design of protective system. *Engineering Structures* 2008; 30; 1605-1620.
- [2] Børvik T, Burbach A, Langberg H, Langseth M. On the ballistic and blast load response of a 20 ft ISO container protected with aluminium panels filled with a local mass – Phase II: Validation of protective system. *Engineering Structures* 2008; 30; 1621-1631.
- [3] Børvik T, Clausen AH, Eriksson M, Berstad T, Hopperstad OS, Langseth M. Experimental and numerical study on the perforation of AA6005-T6 panels. *International Journal of Impact Engineering* 2005; 32; 35-64.
- [4] Olovsson L. *Corpuscular Method for Airbag Deployment Simulations in LS-DYNA*. IMPETUS Afea AB, Huddinge (ISBN 978-82-997587-0-3).
- [5] Olovsson L, Hanssen AG, Børvik T, Langseth M. A particle-based approach to close-range blast loading. *European Journal of Mechanics A/Solids* 2010; 29; 1-6.
- [6] IMPETUS Afea AS. IMPETUS Afea Solver: <http://www.impetus-afea.com> [cited: 2015-03-01].
- [7] Børvik T, Olovsson L, Hanssen AG, Dharmasena KP, Hansson E, Wadley HNG. A discrete particle approach to simulate the combined effect of blast and sand impact loading of steel plates. *Journal of the Mechanics and Physics of Solids* 2011; 59; 950-958
- [8] Wadley HNG, Børvik T, Olovsson L, Wetzel JJ, Dharmasena KP, Hopperstad OS, Deshpande VS, Hutchinson JW. Deformation and fracture of impulsively loaded sandwich panels. *Journal of the Mechanics and Physics of Solids* 2013; 61; 674-699.
- [9] Holloman RL, Deshpande V, Wadley HNG. Impulse transfer during sand impact with a solid block. *International Journal of Impact Engineering* 2015; 76; 98-117.

- [10] Holloman RL, Deshpande V, Wadley HNG. Impulse transfer during sand impact with a cellular structure. International Journal of Impact Engineering 2015; 82; 36-58.
- [11] Børvik T, Dey S, Olovsson L. Penetration of granular materials by small-arms bullets. International Journal of Impact Engineering 2015; 75; 123-139.
- [12] Cundall PA, Strack ODL. A discrete numerical model for granular assemblies. Géotechnique 1979; 1; 47-65
- [13] Oñate E, Rojek J. Combination of discrete element and finite element methods for dynamic analysis of geomechanics problems. Computer Methods in Applied Mechanics and Engineering 2004; 193; 3087-3128.
- [14] Oñate E, Zárate F, Miquel J, Santasusana M, Celigueta MA, Arrufat F, Gandikota R, Valiullin K, Ring L. A local constitutive model for the discrete element method. Application to geomaterials and concrete. Computational Particle Mechanics 2015; 2; 139-160.
- [15] Cil MB, Alshibli KA. 3D assessment of fracture of sand particles using discrete element method. Géotechnique Letters 2012; 2; 161-166.
- [16] Cundall PA. A discontinuous future for numerical modelling in geomechanics? In: Proceedings of the Institution of Civil Engineers. Geotechnical Engineering 149. Issue 1. 2001, p. 41-47.
- [17] Braslau D. Partitioning of energy in hypervelocity impact against loose sand target. Journal of Geophysical Research 1970; 75; 3987-3999.
- [18] Parab ND, Claus B, Hudspeth MC, Black JT, Mondal A, Sun J, Fezzaa K, Xiao X, Luo SN, Chen W. Experimental assessment of fracture of individual sand particles at different loading rates. International Journal of Impact Engineering 2014; 68; 8-14.
- [19] Omidvar M, Malioche JD, Bless S, Iskander M. Phenomenology of rapid penetration into granular soils. International Journal of Impact Engineering 2015; 85; 146-160.
- [20] Omidvar M, Iskander M, Bless S. Stress-strain behavior of sand at high strain rates. International Journal of Impact Engineering 2012; 49; 192-213.
- [21] Omidvar M, Iskander M, Bless S. Response of granular media to rapid penetration. International Journal of Impact Engineering 2014; 66; 60-82.
- [22] Recht RF, Ipson TW. Ballistic perforation dynamics. Journal of Applied Mechanics 1963; 30; 384-390.
- [23] Zukas JA (Editor), 1982. *Impact Dynamics*, John Wiley & Son, New York.

- [24] Børvik T, Hopperstad OS, Berstad T, Langseth M. A computational model of viscoplasticity and ductile damage for impact and penetration. European Journal of Mechanics – A/Solids 2001; 5; 685-712.
- [25] Johnson GR, Cook WH. A constitutive model and data for metals subjected to large strains, high strain rates and high temperatures. In: Proceedings of the 7th International Symposium on Ballistics. 1983, p. 541-547.
- [26] Johnson GR, Cook WH. Fracture characteristics of three metals subjected to various strains, strain rates, temperatures and pressures. International Journal of Engineering Fracture Mechanics 1985; 21; 31-48.
- [27] Børvik T, Olovsson L, Dey S, Langseth M. Normal and oblique impact of small arms bullets on AA6082-T4 aluminium protective plates. International Journal of Impact Engineering 2011; 38; 577-589.
- [28] Holmen JK, Johnsen J, Jupp S, Hopperstad OS, Børvik T. Effects of heat treatment on the ballistic properties of AA6070 aluminium alloy. International Journal of Impact Engineering 2013; 57; 119-133.
- [29] Cockcroft MG, Latham DJ. Ductility and the workability of metals. Journal of the Institute of Metals 1968; 96; 33-39.
- [30] Deshpande VS, McMeeking RM, Wadley HNG, Evans AG. Constitutive model for predicting dynamic interactions between soil ejecta and structural panels. Journal of the Mechanics and Physics of Solids 2009; 57; 1139-1164.
- [31] Holmen JK, Johnsen J, Hopperstad OS, Børvik T. Influence of fragmentation upon the capacity of aluminum alloy plates subjected to ballistic impact. European Journal of Mechanics – A/Solids 2016; 55; 221-233.
- [32] Goldsmith W. Non-ideal projectile impact on targets. International Journal of Impact Engineering 1999; 22; 95-395.

Jens Kristian Holmen, Lars Olovsson, Tore Børvik

Discrete modeling of low velocity penetration in sand

Submitted for possible journal publication.

Part 6

Discrete modeling of low-velocity penetration in sand

Jens Kristian Holmen^{a,b,*}, Lars Olovsson^c, Tore Børvik^{a,b}

^a*Structural Impact Laboratory (SIMLab), Department of Structural Engineering, Norwegian University of Science and Technology (NTNU), NO-7491 Trondheim, Norway*

^b*Centre for Advanced Structural Analysis (CASA), NTNU, NO-7491 Trondheim, Norway*

^c*IMPETUS Afea AB, Sördalavägen 22, 14160, Huddinge, Sweden*

ABSTRACT

A discrete particle method was in this paper evaluated and used in numerical simulations of low-velocity penetration of sand. Hemispherical, blunt and ogival-nosed impactors were tested at striking velocities below 5 m/s. The tests were done in a dropped-object-rig where the resisting force from the sand was measured continuously during the experiments, providing ample comparison for the simulations. The shape of the force-penetration depth curves was different for the various impactors, but the ultimate penetration depths were similar in all tests with the same impact velocity. 3D simulations with the discrete particle method were in general able to describe the behavior of the sand, but the peak force was underestimated and consequently the ultimate penetration depth was slightly overestimated. The results presented in this study supplements previous evaluations of the discrete particle method that were done at high impact velocities and show that the method can be used to describe the overall response of sand subjected to low-velocity impact.

Keywords: Experiment; Discrete particle method; Low-velocity penetration; Impact; Granular material

* Corresponding author: + 47 930 45 837 (Jens Kristian Holmen)
Email address: jens.k.holmen@ntnu.no (Jens Kristian Holmen)
URL: www.ntnu.edu/casa (CASA)

1. INTRODUCTION

From meteor cratering to pile driving; penetration of granular materials takes place in many situations at different scales and velocities, but it is challenging to model due to its discrete nature. Discrete modeling of granular matter was pioneered by Cundall and Strack [1], and methods that treat each grain of sand or piece of rock as a separate entity have prevailed ever since. A goal of the discrete modeling approach is to identify the distribution between the energy dissipating mechanisms of inter-particle friction, particle-intruder friction, and collisional energy dissipation [2][3][4]. Specifically, the effect of frictional drag on the penetration has attracted interest [2][5][6][7]. Grain fracture also dissipates energy in granular materials subjected to high loading rates; especially during high-velocity impact [8][9][10][11]. Sophisticated experimental techniques like digital projectile tracking [2], photoelasticity [5] and grain-scale particle tracking [6] have been developed and are being used to study, *in situ*, the behavior of granular materials. These studies are mainly done by physicists and they deal with, partially, idealized materials to explore the underlying physics of the problem. Thus, their results can be exploited in a variety of applications at several scales. Recent work also utilizes transparent soils to determine in detail the particle-structure interactions during low velocity penetration [12].

In the current study we adopt an engineering approach of solving the penetration problem, meaning that the motion of individual sand grains is not measured in the experimental part of the paper. Instead we evaluate the macroscopic response of the sand and compare it to numerical simulations. The results from this work can be applied for instance in onshore and offshore pile driving, in foundation design and for other cases of low-velocity impact into granular materials. Both the finite element method [13][14][15] and discrete numerical methods [16][17] have been used for such purposes in the past.

The discrete particle method (DPM) used in this paper has been implemented in the commercial explicit nonlinear finite element code IMPETUS Afea Solver [18]. The method was originally developed by Olovsson [19] and used to handle the gas-fabric contact issues in airbag-deployment simulations; it is based on a Lagrangian formulation and uses spherical particles that transfer forces through contact and collisions. The DPM has later been developed for several applications, including blast loading [20], combined blast loading and sand impact [21][22][23][24], and high-velocity penetration and perforation of sand [25][26][27]. The main advantages of the DPM are computational efficiency and a simple

contact formulation. It does, however, neglect physical phenomena like particle crushing and rotation. Until now, its features have only been explored for high pressures and high impact velocities, but we show in this work that the method seems to be able to describe the overall behavior of low-velocity penetration problems of sand. We show in this work that the method can now simulate both low and high-velocity impact of sand.

2. EXPERIMENTAL WORK

2.1 Material description

Sand from AB Baskarpsand in Sweden was used in this study. The median grain diameter was 0.95 mm, the moisture content was less than 0.30 % and the compacted density was 1731 kg/m³. Figure 1 shows the grain size distribution. The sand consisted of 77.1 % quartz (SiO_2), 12.5 % alumina (Al_2O_3) and minor fractions of other elements.

2.2 Test setup and procedure

Figure 2 presents the experimental setup of the impact test. The test machine is an Instron CEAST 9350 dropped-object-rig capable of imparting a maximum kinetic energy of 1800 J. We used impactors with three different nose shapes: a hemispherical-nosed impactor with total mass of 5.0445 kg, a blunt-nosed impactor with total mass of 5.1045 kg, and an ogival-nosed impactor with a total mass of 5.0695 kg. They all have a diameter of 20 mm, and were equipped with a calibrated load cell located approximately 55 mm from the tip. This load cell measured the force with a temporal resolution of 100 kHz. All tests had a measurement duration of 0.1 s giving a total of 10,000 data points for each test. The exact striking velocity was measured by a photocell just before impact.

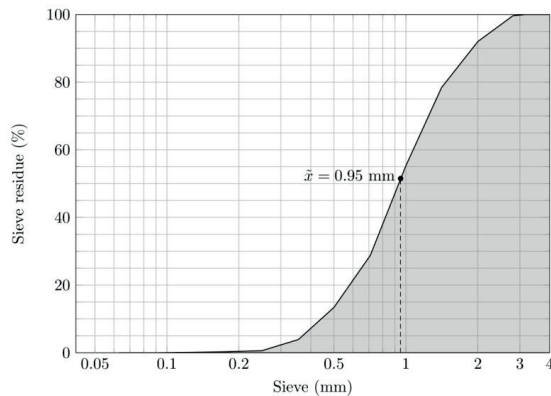


Figure 1: Grading curve for the sand, the median grain diameter $\tilde{x} = 0.95$ mm is indicated in the figure.

Five impact tests were conducted for all nose shapes with an approximate striking velocity of 2.5 m/s. Additional five impact tests were done with the hemispherical-nosed impactor at an approximate striking velocity of 5.0 m/s, giving a total of 20 impact tests. The following numerical integration scheme was performed to determine the velocities and displacements from the force measurements:

$$v_{n+1} = v_n - \left(\frac{F_{n+1} + F_n}{2m} - g \right) \Delta t, \quad u_{n+1} = u_n + \left(\frac{v_{n+1} + v_n}{2} \right) \Delta t \quad (1)$$

where v is the velocity, u is the displacement, F is the resisting force from the sand on the impactor, m is the total impacting mass, $g = 9.81 \text{ m/s}^2$ is the gravitational acceleration, and Δt is the sampling time of 0.01 ms. Subscripts $n+1$ and n denote current and previous values of the variables, respectively. Since the load cell is not located at the tip of the impactor we have to account for the mass below the strain gage to find the resisting force from the sand on the impactor. By using dynamic equilibrium, we obtain the equation for the resisting force as a function of the measured force P as

$$F = P \left(1 + \frac{m_1}{m_2} \right) \quad (2)$$

where m_1 is the mass below the load cell and m_2 is the mass above the load cell ($m = m_1 + m_2$). With the experimental setup used in this work the ratio is $m_1/m_2 \approx 0.02$, and consequently the resisting force is slightly higher than the measured force.

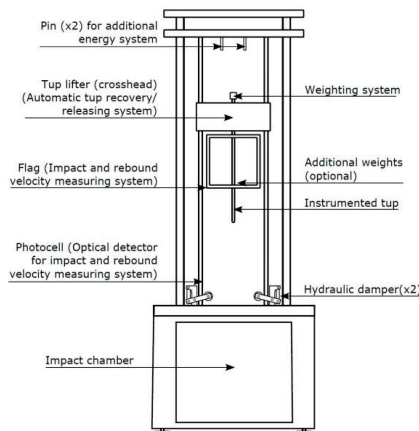


Figure 2: Schematic drawing of the Instron CEAST 9350 dropped-objects rig [28].



Figure 3: The aluminum tube used to contain the sand in the tests

Sand was filled into a cylindrical aluminum container with an inner diameter of 123 mm and a height of 350 mm as shown in Figure 3. The side of the container was gently tapped with a rubber hammer to compact the sand before each test and we were careful to use the same amount of sand every time. All the sand was changed between consecutive tests. We could obtain a maximum penetration depth of 140 mm with the current experimental setup which limited the potential striking velocities. The striker came to a complete stop only due to the resisting force of the sand in all the successful tests.

2.3 Experimental results

All the experimental force-penetration depth curves are shown in Figure 4. We identify some experimental scatter, particularly for the hemispherical-nosed impactor, but the overall shape of the curves is similar for replicate tests. Focusing on the tests with an approximate striking velocity of 2.5 m/s and the hemispherical-nose (Figure 4a), we see that the force abruptly increases at initial impact to around 50 N where the force remains constant for around 20 mm. At this penetration depth the slope of the curves changes and the force climbs toward its peak that occurs at penetration depths between 70 mm and 80 mm. Halfway to the peak force the slope suddenly increases. The peak is followed by a steep drop in the force. Further penetration results in a second rise in the force before the ultimate penetration depth is reached. In general, the results from the tests with a striking velocity of approximately 5.0 m/s look the same (Figure 4b), but the forces are higher and the displacements are larger.

The tests with the blunt-nosed impactor (Figure 4c) displayed only slight scatter between themselves, but they look different from the hemispherical tests. At initial impact the force rises rapidly to its maximum because of the impactor's flat tip. This takes place at penetration depths less than 4 mm. A subsequent drop that almost completely unloads the load cell occurs immediately after. Then a plateau with slight slope from a depth of 20 mm to 80 mm precedes a local force maximum just before the ultimate penetration depth.

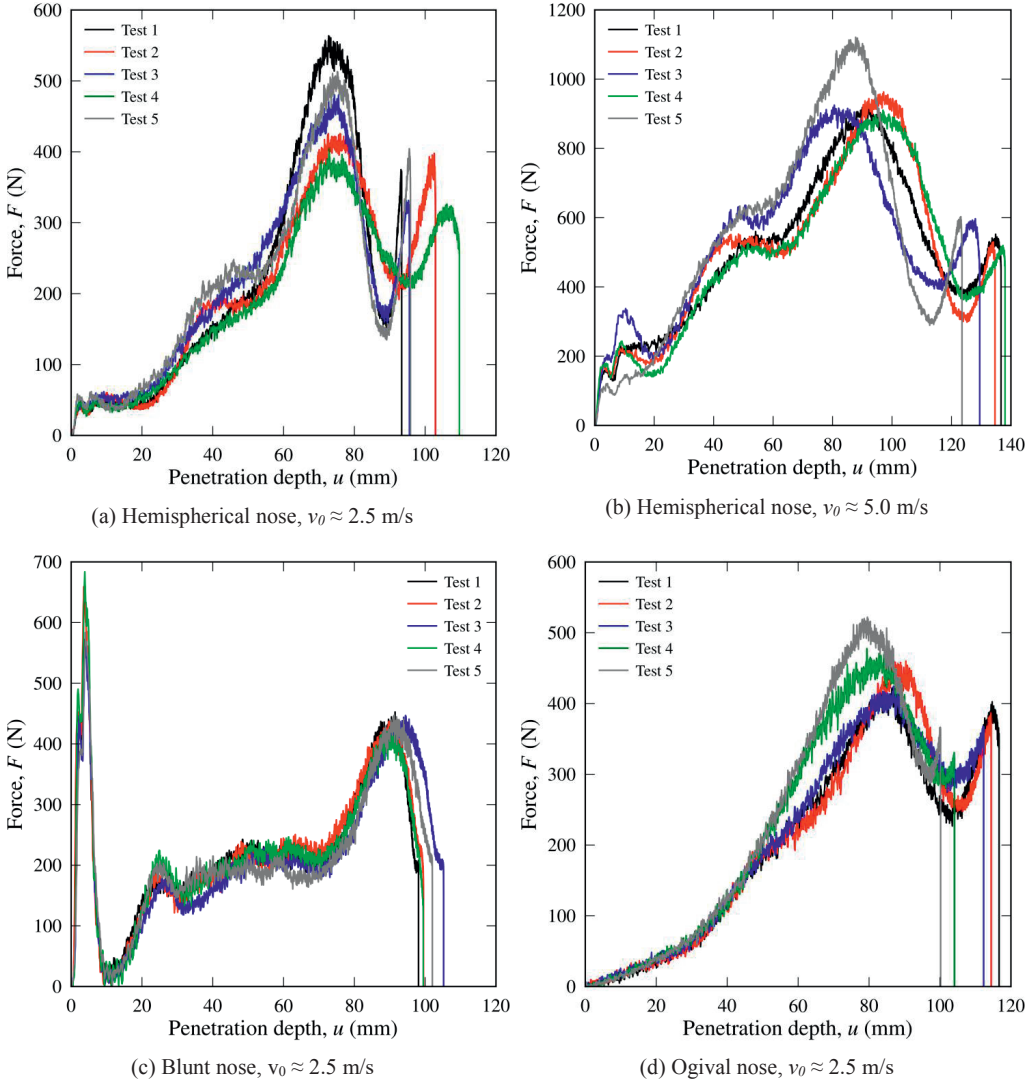


Figure 4: Force-penetration depth curves for the various setups. The curves are stopped at max displacement.

Figure 4d shows the results from the ogival-nosed impactors. Here the initial impact point was difficult to identify because the ogival shape gave a gradual transition from an unloaded state to a loaded state. At a penetration depth of about 35 mm the initially gentle slope exhibits a distinct kink and in some of the tests this steeper slope lasts until the maximum force is reached at penetration depths around 80 mm. Similar to the hemispherical-nosed impactor the force drops before it increases again right before the ultimate penetration depth. The force in three of the tests rose slower to the, and this peak force occurred at penetration

depths between 90 mm and 100 mm. They also had a larger ultimate penetration depth. We believe that these differences can be attributed to the packing of the sand in front of the nose of the impactor.

Table 1 summarizes the experimental results and Figure 5 compares typical force-penetration depth curves for the three nose shapes. The divergent is clearly the blunt-nosed impactor for which the force-penetration depth curve has a distinctly different shape than the two other nose-shapes. However, both the average penetration depth and the average work is almost the same for all nose shapes with the same approximate striking velocity. For the tests with $v_0 \approx 2.5$ m/s, the blunt-nosed impactor experienced the highest peak force from the sand (601 N). This took place immediately after impact. Respective peak forces for the hemispherical and ogival-nosed impactors are 473 N and 453 N; they occur later in the penetration process. We did not see any signs of crushed sand in the tests.

Table 1: Number of experimental tests conducted in this study supplemented by some average test data

Nose shape	Number of tests	Avg. striking velocity (m/s)	Avg. maximum penetration depth (mm)	Average max force (N)	Average work (Nm)
Hemispheric	5	2.49	100	473	20.6
	5	4.96	134	958	68.6
Blunt	5	2.59	103	601	22.3
Ogival	5	2.63	111	453	23.1

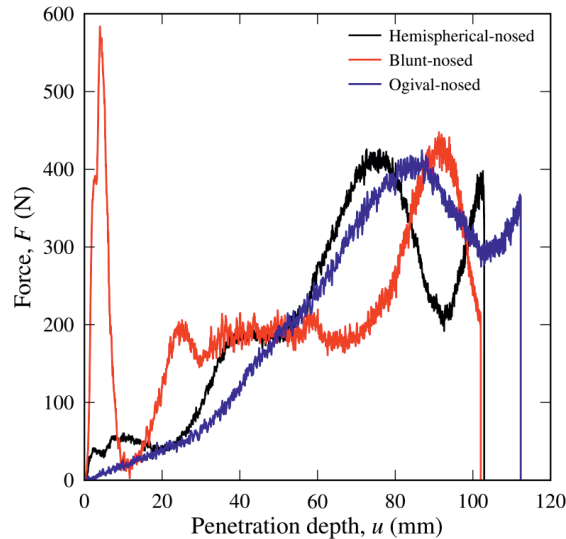


Figure 5: Comparison of representative force-displacement curves for the three different nose-shapes with $v_0 \approx 2.5$ m/s.

3. NUMERICAL WORK

3.1 The discrete particle method

The discrete particle method (DPM) uses rigid spherical particles that transfer forces through contact and elastic collisions based on a Lagrangian formulation [21][22]. Continuum models require constitutive equations for the bulk sand, and, from an impact mechanics perspective, finite elements with element erosion make for instance loose sand ejecta difficult to capture. Coupled Eulerian-Lagrangian approaches' potential to describe loose sand ejecta and particle-particle contact is limited too [29]. They can also suffer from numerical advection errors and contact problems. Two advantages of discrete particle methods are that they need few input parameters, and that relatively simple assumptions on the particle level are sufficient to capture complicated behavior of the bulk material. Further, for this DPM the robust treatment of the interactions between the particles themselves and between the particles and the structure allows for a simple and physically clear treatment of for instance the interaction between a deformable structure and sand. Since particle rotations are neglected in the numerical integration scheme, this can all be done while still keeping the computational time at a reasonable level [21].

In this study we use the following parts of the rheological model (Figure 6): a normal and a tangential spring with equal stiffness k_s and a frictional element μ_s that scales the tangential inter-particle elastic spring force. Further, friction between the discrete particles and finite elements is controlled by the frictional coefficient μ_{ps} . The rheological model also includes a damping coefficient c_s (usually used for wet sand) and a cut-off value η , or shear cap, which limits the tangential forces between particles (for high velocity impacts). The damping coefficient c_s was not used in this study and the shear cap for the tangential forces η does not affect the results in low-velocity penetration.

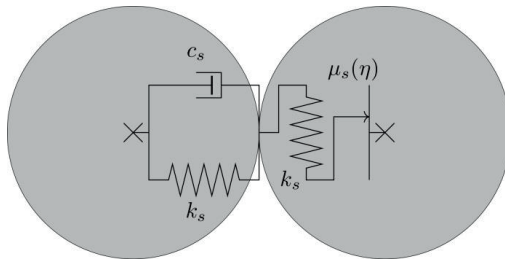


Figure 6: Rheological model for the discrete particles.

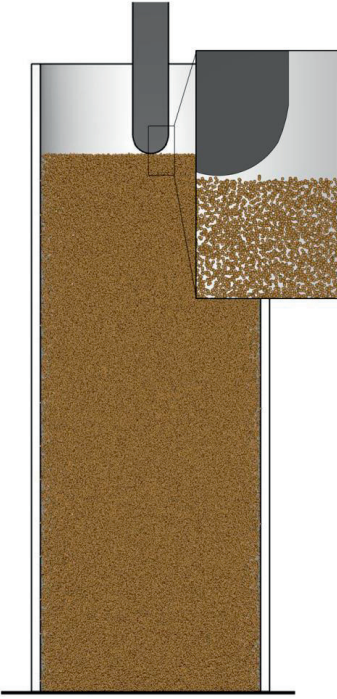


Figure 7: Numerical model of the hemispherical-nosed impactor (the model is sliced in half to improve visualization)

We did not see any indication of fracture of the sand grains in the experiments, but when the impact velocity is high, grain fracture can contribute significantly to the energy dissipation. The DPM does not explicitly account for grain fracture, but its effect can be implicitly accounted for in the particle-particle friction μ_s . More advanced simulations of this can for instance be found in Lammi and Vogler [9].

3.2 Numerical models

The numerical simulations were conducted with the IMPETUS Afea Solver [18]. It is a multi-purpose explicit finite element solver that includes the discrete particle model (DPM). Figure 7 shows a numerical model in the initial configuration before impact; the sand is represented by particles, and the aluminum tube and the impactor are modeled with finite elements. Previous work shows that a particle diameter marginally larger than the median grain diameter in the real sand gives good results [25]. In this work we use a median particle diameter of 1.09 mm, giving 3,200,000 particles in the model. Table 2 lists the parameters that were used in the simulations. We used the compacted sand density ρ_s that was measured in the laboratory and the elastic spring stiffness k_s from a thorough calibration procedure

presented elsewhere [21]. The damping coefficient c_s was neglected because friction seems to be the dominating energy dissipating mechanism in dry sand [3], which is also in accordance with prior studies using this DPM [21][22][25][26]. This leaves the friction parameters μ_s and μ_{ps} that were determined by trial-and-error. The simulations indicated that they needed to be significantly higher than what has been used for high velocity impacts in the past [25]. This is the reason why the shear cap η was implemented in the model as will be explained in Section 4.3. The model's sensitivity to some of the parameters is presented in Section 3.3.

An impact simulation consists of two steps: First, we need to compact the sand in an initial analysis. Here a gravitational field is imposed on the model and the sand is given an initial velocity in the same direction as the gravitational acceleration. Second, the positions of the sand particles at the end of the compaction simulation are imported into the main model in which the impactor strikes the sand target. Since neither the impactor nor the aluminum tube showed any signs of deformation in the experiments, we modeled them as rigid bodies. The impactor was prevented from moving in any direction except the impact direction, in the same way as in the tests. The same pre-compaction of the sand was used in all the impact simulations, and only the shape, weight, and striking velocity of the impactor were varied.

3.3 Sensitivity studies

Results from discrete particle simulations are obviously sensitive to the input parameters. Here, we show how the inter-particle friction μ_s , impactor-particle friction μ_{ps} , and the elastic-spring stiffness k_s change the simulation results. We also know that the particle size influences the behavior of the granular assembly: large particles mean high resisting forces. The sensitivity simulations were done with 500,000 particles; this dramatically reduces the computational time compared to using 3,200,000 particles. In fact, the computational time is reduced from 110 hours to 12 hours. It means, however, that the ultimate penetration depths are underestimated in the sensitivity simulations.

Table 2: The model constants used in the discrete particle model

ρ_s (kg/m ³)	k_s (N/m)	μ_s	μ_{ps}	c_s	η
1731.0	4.0×10^8	0.5	1.0	0.0	0.0005

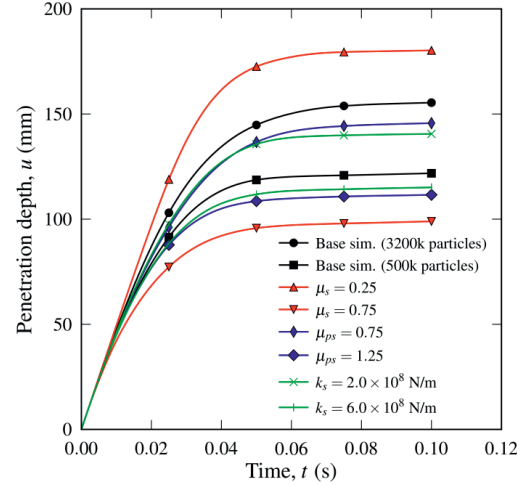


Figure 8: Sensitivity study for the DPM. The simulations were run with 500,000 particles, $\mu_s = 0.5$, $\mu_{ps} = 1.0$ and $k_s = 4.0 \times 10^8$ unless otherwise stated in the legend.

In order to save additional computational time, the hemispherical-nosed impactor impacting at 4.96 m/s was chosen for the sensitivity study. Figure 8 shows the penetration depth-time curves from a series of simulations. It appears that both inter-particle friction, impactor-particle friction and the elastic spring stiffness influences the penetration depth, as expected. Inter-particle friction seems to affect the results more than the two other parameters for this impact configuration. We see that the number of particles also affects the ultimate penetration depth. However, keeping the particle size close to the real grain size makes sense and it also limits the number of adjustable parameters.

3.4 Numerical results

We used 3,200,000 particles and the parameters from Table 2 in the simulations presented in the following.

Figure 9a and Figure 9b compare the force-penetration depth curves from the numerical simulations to the experiments with the hemispherical-nosed impactor. On average, the force level is captured both for $v_0 \approx 2.5$ m/s and $v_0 \approx 5.0$ m/s, but the simulation overpredicts the resisting force upon impact and underpredicts the force near the ultimate penetration depth. The force from the simulation with the blunt-nosed impactor replicates the experimental data (Figure 9c). The simulation captures the initial force peak immediately after impact, the lower sustained force during most of the penetration, and the increase in force toward the end of the penetration process. Figure 9d shows that the force-penetration depth curve from the

numerical simulation of ogival-nosed impact adheres well to the experimental curves, but the predicted peak force is too low.

Table 3 presents some data from the simulations and experiments. The peak force was underestimated by around 15 % in all simulations which explains why the final penetration depths were all overestimated. The results confirm that the dissipated energy is about the same in corresponding experiments and simulations.

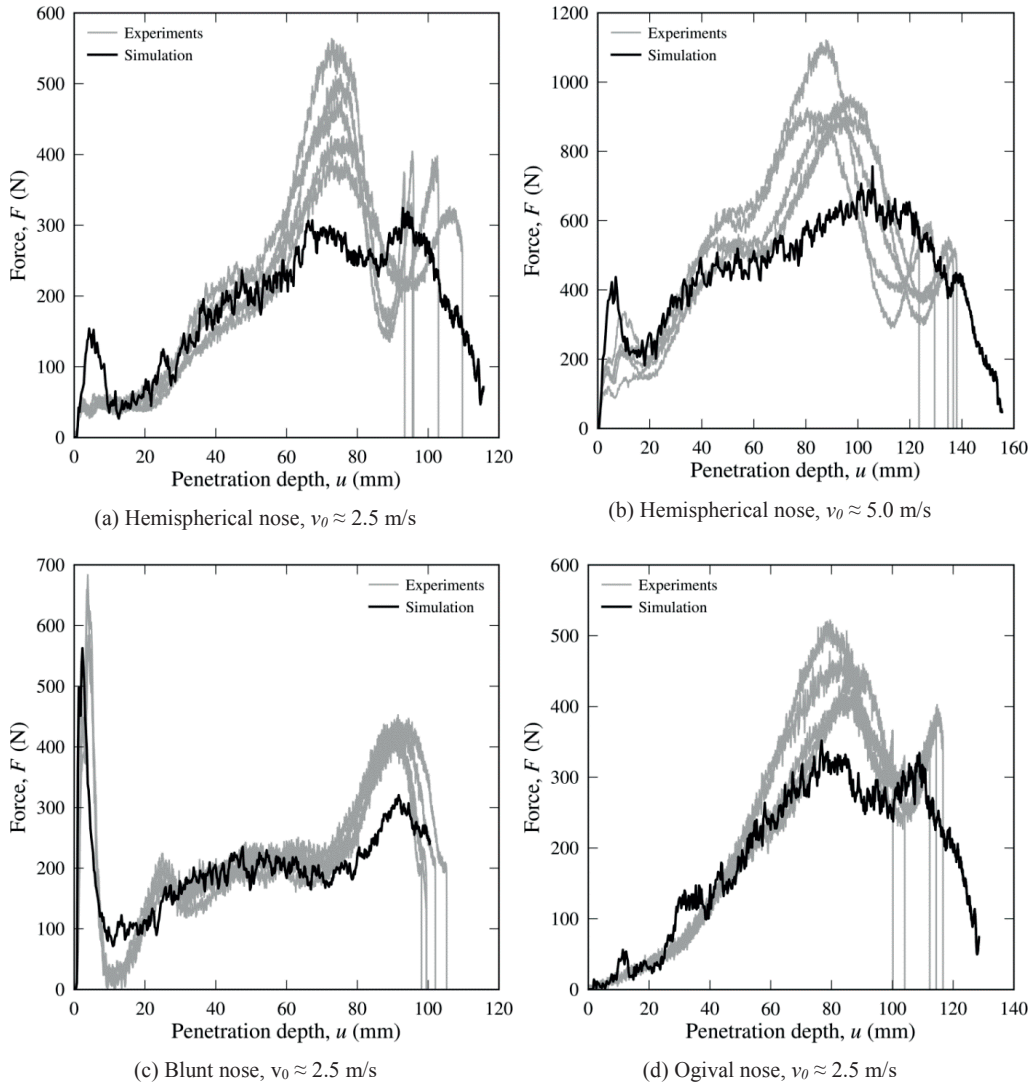


Figure 9: Simulated penetration resistance-penetration depth curves for the various impactors compared to the respective experiments.

Table 3: Results from the numerical simulations compared to the average test data from the experiments

Nose shape	Striking velocity (m/s)	Penetration depth			Maximum force			Energy dissipation		
		Exp. (mm)	Sim. (mm)	Dev. (%)	Exp. (N)	Sim. (N)	Dev. (%)	Exp. (Nm)	Sim. (Nm)	Dev. (%)
Hemispheric	2.49	100	115	15.0	473	324	-31.5	20.6	21.4	3.9
	4.96	134	155	13.5	958	757	-20.9	68.6	69.8	1.7
Blunt	2.59	103	116	12.6	601	563	-6.3	22.3	22.5	0.9
Ogival	2.63	111	129	16.2	453	352	-22.3	23.1	23.9	3.5

4. DISCUSSION

4.1 Experimental phenomena

Figure 5 illustrates that the sand responds in different ways to penetration by the three different nose shapes. The blunt-nosed impactor experiences large resisting forces during initial penetration because its flat shape does not push the sand away in the lateral direction in the same way as a pointed projectile. When the nose has an ogival shape the resisting force from the sand gradually increases as the impactor penetrates; no abrupt rise in the force was seen for this nose shape. Hemispherical-nosed impactors experience a jump in the force at initial impact, but it stabilizes after about 5 mm of penetration.

Both the hemispherical and ogival-nosed tests exhibit a rather smooth increase in the resisting force toward the peak value. The blunt-nosed tests on the other hand were nearly completely unloaded immediately after the initial force peak before a steep increase in the force took place. Then the force level stabilized until the last local force maximum. We observe a sudden rise in the penetration resistance close to the terminal displacement for all tests regardless of nose shape. This phenomenon has previously been seen for soils subjected to both low velocity and high velocity impact [1]; a possible explanation for this force peak is the transition from inertial resistance to frictional resistance in the sand [30].

Comparing the tests with $v_0 \approx 2.5$ m/s to those with $v_0 \approx 5.0$ m/s for the hemispherical-nosed impactor reveal, as already mentioned, that the overall shape of the force-penetration depth curves remains the same. By doubling the striking velocity, we double the peak force, however the ultimate penetration depth increases with only 34 %. Not enough tests were done to draw any further conclusions; this is outside the scope of this study and left for future work.

4.2 On the numerical simulation results

Previous studies report that impactor-grain frictional effects do not affect the force from the sand on the penetrator if the penetrator is a rather short projectile [7][31]. Here, we see,

numerically, that the impactor-grain friction is important and that the stopping force increases significantly when the impactor-grain friction (μ_{ps}) increases. This is probably because we used a heavy and long rod-like impactor in this study that has a relatively large area on which frictional forces can act.

Figure 10 to Figure 13 show some pictures from simulations and their positions on the corresponding force-penetration depth curves. We see more sand ejecta and larger crater formation when the striking velocity is high (compare Figure 10 to Figure 11). The amount of ejecta and cratering is also nose-shape dependent: both are more pronounced for the blunt (Figure 12) than for the ogival-nosed impactor (Figure 13). We also see from these figures that the peak force for the blunt-nosed impactor happens before any lateral displacement of sand has taken place, meaning that the peak force is probably independent of impactor-grain friction for this nose-shape. Further, the extent of lateral displacement of particles is approximately the same for the all nose shapes. An interesting observation is also that the friction causes the impactor to drag the adjacent particles along with it during the penetration so that the upper layer of the sand has no lateral displacement toward the end of the simulation.

The simulations capture, with reasonable accuracy, the rise and fall in penetration resistance close to the ultimate penetration depth, particularly for the blunt and ogival-nosed impactors. Although the behavior of the sand was not perfectly reproduced, the average dissipated energy was accurately predicted.

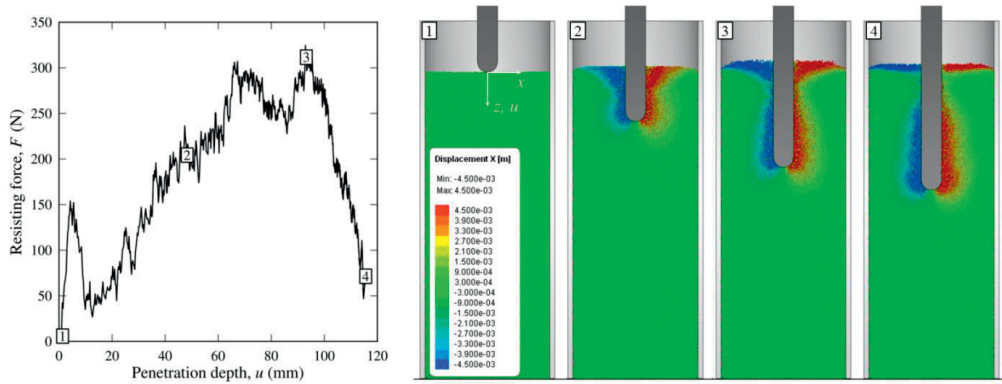


Figure 10: Force-penetration depth synchronized against lateral displacement of the grains for the hemispherical-nosed impactor at $v_0 \approx 2.5$ m/s.

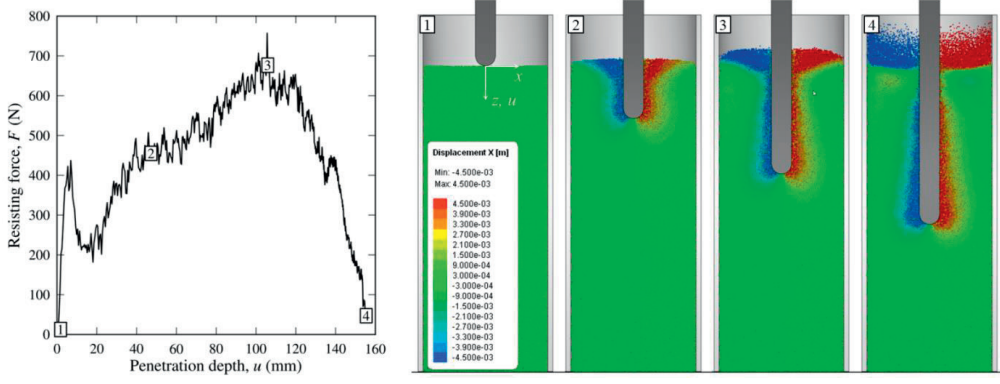


Figure 11: Force-penetration depth synchronized against lateral displacement of the grains for the hemispherical-nosed impactor at $v_0 \approx 5.0$ m/s.

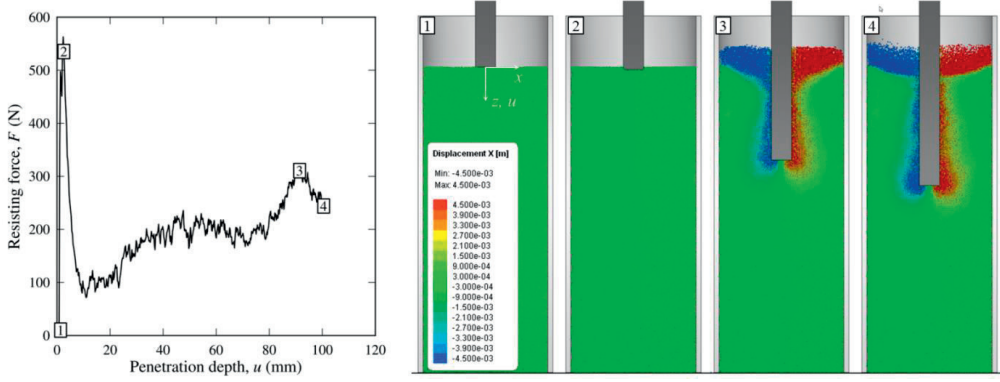


Figure 12: Force-penetration depth synchronized against lateral displacements of the grains for the blunt-nose impactor at $v_0 \approx 2.5$ m/s.

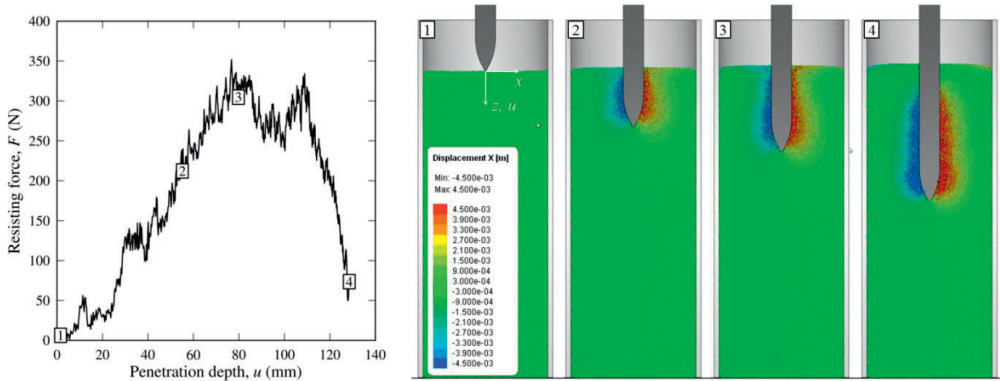


Figure 13: Force-penetration depth synchronized against lateral displacements of the grains for the ogival-nosed impactor at $v_0 \approx 2.5$ m/s.

4.3 Low versus high velocity penetration

To show that the DPM can give reasonable predictions at both low and high pressures the same set of parameters that was used in Section 3.2 for striking velocities of less than 5 m/s was used to simulate perforation tests of identical sand with striking velocities between 150 m/s and 360 m/s. The tangential force cut-off, or shear cap (η), now becomes important. This parameter does not influence the results at low velocities, but we will show that it at high velocities is crucial in order to obtain good results.

A steel sphere with a diameter of 10 mm was fired by a gas-gun toward a 50 mm thick sand slab contained in a purpose-made steel box. Holes were drilled in the box and they were covered by domestic aluminum foil to allow for perforation by the steel sphere. We optically measured the striking and the residual velocities with a high-speed camera; further details regarding the same type of experiments are given in Ref. [26]. Figure 14 shows the model of the sand slab that was made in IMPETUS Afea Solver and also the residual velocity as a function of striking velocity compared to the tests. The predicted residual velocities for striking velocities from 100 m/s to 400 m/s are close to the experiments, especially for $\eta = 0.0005$, which shows that the DPM gives reasonable results also for higher velocities. We also see that the value of η affects the results, high η gives higher perforation resistance.

Figure 15 illustrates the behavior of the numerical model compared to an experiment.

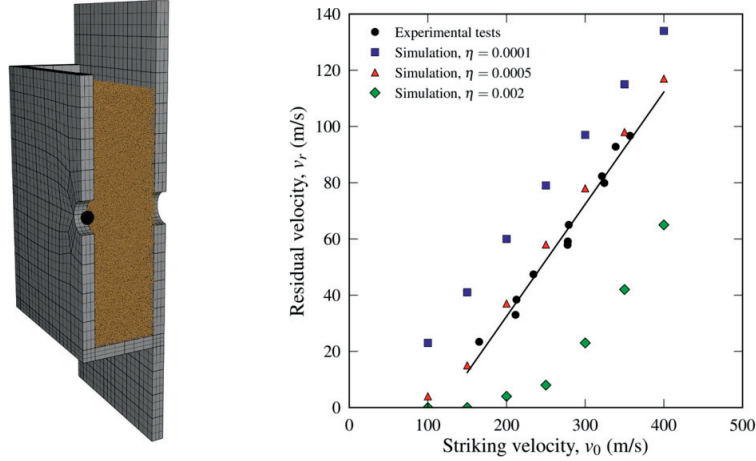


Figure 14: Geometry and results from simulations with the DPM for perforation tests at high velocities.



Figure 15: Visual comparison of an experiment ($v_0 = 279.1 \text{ m/s}$, $v_r = 65.0 \text{ m/s}$) and a simulation ($v_0 = 278.2 \text{ m/s}$, $v_r = 69.2 \text{ m/s}$) of high velocity impact.

5. CONCLUSION

The experimental tests in this paper showed that the shape of the force-penetration depth curves changes dramatically with changing impactor geometry. Blunt-nosed impactors have a force peak almost instantaneously after penetration before nearly complete unloading takes place. Hemispherical and ogival-nosed impactors display a gradual increase to the peak force that comes toward the end of the penetration process. For the tests with matching impact velocities the ultimate penetration depths were almost the same regardless of nose-shape. Further, the behavior of the sand, particularly for the ogival-nosed impactor, seems to be determined by the degree of compaction; however, no systematic study of this was done in this paper.

Numerical simulations with the discrete particle method (DPM) were in general able to predict the behavior of the sand during penetration although the peak forces were underestimated by about 15 % and the penetration depths were slightly overestimated. The results presented in this work suggests that this DPM can be used in simulations of low-velocity penetration. And although the model has been explored for use in a range of applications, e.g., low and high-velocity penetration and perforation, blast loading, drilling and mine blasts of buried charges, it needs further development and validation.

ACKNOWLEDGMENT

This research was supported financially by the Norwegian Defence Estates Agency (NDEA).

REFERENCES

- [1] Cundall, P.A., Strack, O.D.L., 1979. A discrete numerical model for granular assemblies. *Géotechnique* 29, 47-65.
- [2] Uehara, J.S., Ambroso, M.A., Ojha, R.P., Durian, D.J., 2003. Low-speed impact craters in loose granular media. *Physical Review Letters* 90, 194301 – 1-4.
- [3] Tsimring, L.S., Volfson, D., 2005. Modeling of impact cratering in granular media. Garca-Rojo, R., Herrmann, H.J., McNamara, S. (Eds.), In: *Powders and Grains*, vol. 2. A.A. Balkema, Rotterdam pp. 1215-1223.
- [4] Seguin, A., Bertho, Y., Gondret, P., Crassous, J., 2009. Sphere penetration by impact in a granular medium: A collisional process. *Europhysics Letters* 88, 44002 – 1-6.
- [5] Clark, A.H., Kondic, L., Behringer, R.P., 2012. Particle scale dynamics in granular impact. *Physical Review Letters* 109, 238302 – 1-5.
- [6] Nordstrom, K.N., Lim, E., Harrington, M., Losert, W., 2014. Granular dynamics during impact. *Physical Review Letters* 112, 228002 – 1-5.
- [7] Iskander, M., Bless, S., Omidvar, M., 2015. *Rapid Penetration into Granular Media*, Elsevier Inc., Amsterdam, Netherlands.
- [8] Braslau, D., 1970. Partitioning of energy in hypervelocity impact against loose sand target. *Journal of Geophysical Research* 75, 3987-3999.
- [9] Lammi, C.J., Vogler, T.J., 2012. Mesoscale simulations of granular materials with peridynamics. Elert, M.L., Buttler, W.T., Borg, J.P., Jordan, J., Vogler, T.J. (eds.), In: *Shock compression and condensed matter 2011: proceedings of the conference of the American Physical Society topical group on shock compression of condensed matter*. AIP Publishing pp. 1467-1470.
- [10] Borg, J.P., Vogler, T.J., 2013. Rapid compaction of granular material: characterizing two- and three-dimensional mesoscale simulations. *Shock Waves* 23, 153-176.
- [11] Parab, N.D., Claus, B., Hudspeth, M.C., Black, J.T., Mondal, A., Sun, J., Fezzaa, K., Xiao, X., Luo, S.N., Chen, W., 2014. Experimental assessment of fracture of individual sand particles at different loading rates. *International Journal of Impact Engineering* 68, 8-14.
- [12] Omidvar, M., Iskander, M., Bless, S., 2016. Soil-projectile interactions during low velocity penetration. *International Journal of Impact Engineering* 93, 211-221.
- [13] Mabsout, M.E., Tassoulas, J.L., 1994. A finite element model for the simulation of pile driving. *International Journal for Numerical Methods in Engineering* 37, 257-278.

- [14] Paik, K., Salgado, R., Lee, J., Kim, B., 2003. Behavior of open- and closed-ended piles driven into sands. *Journal of Geotechnical and Geoenvironmental Engineering* 129, 296-306.
- [15] Ko, J., Jeong, S., Lee, J.K., 2016. Large deformation FE analysis of driven steel pipe piles with soil plugging. *Computers and Geotechnics* 71, 82-97.
- [16] Tran, Q.A., Chevalier, B., Breul, P., 2016. Discrete modeling of penetration tests in constant velocity and impact conditions. *Computers and Geotechnics* 71, 12-18.
- [17] Lobo-Guerrero, S., Vallejo, L.E., 2005. DEM analysis of crushing around driven piles in granular materials. *Géotechnique* 55, 617-623.
- [18] IMPETUS Afea Solver. <http://www.impetus-afea.com> [cited: 2015-12-01].
- [19] Olovsson, L., 2007. Corpuscular Method for Airbag Deployment Simulations in LS-DYNA. IMPETUS Afea AB, Huddinge (ISBN 978-82-997587-0-3).
- [20] Olovsson, L., Hanssen, A.G., Børvik, T., Langseth, M., 2010. A particle-based approach to close-range blast loading. *European Journal of Mechanics – A/Solids* 29, 1-6.
- [21] Børvik, T., Olovsson, L., Hanssen, A.G., Dharmasena, K.P., Hansson, E., Wadley, H.N.G., 2011. A discrete particle approach to simulate the combined effect of blast and sand impact loading of steel plates. *Journal of the Mechanics and Physics of Solids* 59, 950-958.
- [22] Wadley, H.N.G., Børvik, T., Olovsson, L., Wetzel, J.J., Dharmasena, K.P., Hopperstad, O.S., Deshpande, V.S., Hutchinson, J.W., 2013. Deformation and fracture of impulsively loaded sandwich panels. *Journal of the Mechanics and Physics of Solids* 61, 674-699.
- [23] Holloman, R.L., Deshpande, V., Wadley, H.N.G., 2015. Impulse transfer during sand impact with a solid block. *International Journal of Impact Engineering* 76, 98-117.
- [24] Holloman, R.L., Deshpande, V., Wadley, H.N.G., 2015. Impulse transfer during sand impact with a cellular structure. *International Journal of Impact Engineering* 82, 36-58.
- [25] Børvik, T., Dey, S., Olovsson, L., 2015. Penetration of granular materials by small-arms bullets. *International Journal of Impact Engineering* 75, 123-139.
- [26] Holmen, J.K., Hopperstad, O.S., Børvik, T., 2016. Experiments and simulations of empty and sand-filled aluminum alloy panels subjected to ballistic impact. Submitted for possible journal publication.
- [27] Moxnes, J.F., Frøyland, Ø., Skriudalen, S., Prytz, A.K., Teland, J.A., Friis, E., Ødegårdstuen, G., 2016. On the study of ricochet and penetration in sand, water and gelatin by spheres, 7.62 mm, and 25 mm projectiles. *Defence Technology* 12, 159-170.

- [28] Bjerke, F.R., Hansen, L.M., 2015. Experimental and Numerical Study on the Perforation of Empty and Sand-filled Aluminium Panels. Master's thesis, Norwegian University of Science and Technology.
- [29] Deshpande, V.S., McMeeking, R.M., Wadley, H.N.G., Evans, A.G., 2009. Constitutive model for predicting dynamic interactions between soil ejecta and structural panels. *Journal of the Mechanics and the Physics of Solids* 57, 1139-1164.
- [30] Goldman, D.I., Umbanhowar, P., 2008. Scaling and dynamics of sphere and disk impact into granular media. *Physical Review E* 77, 021308-1 – 021308-14.
- [31] Kondic, L., Fang, X., Losert, W., O'Hern, C.S., Behringer, R.P., 2012. Microstructure evolution during impact on granular matter. *Physical Review E* 85, 011305-1 – 011305-17.

**DEPARTMENT OF STRUCTURAL ENGINEERING
NORWEGIAN UNIVERSITY OF SCIENCE AND TECHNOLOGY**

N-7491 TRONDHEIM, NORWAY
Telephone: +47 73 59 47 00 Telefax: +47 73 59 47 01

"Reliability Analysis of Structural Systems using Nonlinear Finite Element Methods",
C. A. Holm, 1990:23, ISBN 82-7119-178-0.

"Uniform Stratified Flow Interaction with a Submerged Horizontal Cylinder",
Ø. Arntsen, 1990:32, ISBN 82-7119-188-8.

"Large Displacement Analysis of Flexible and Rigid Systems Considering
Displacement-Dependent Loads and Nonlinear Constraints",
K. M. Mathisen, 1990:33, ISBN 82-7119-189-6.

"Solid Mechanics and Material Models including Large Deformations",
E. Levold, 1990:56, ISBN 82-7119-214-0, ISSN 0802-3271.

"Inelastic Deformation Capacity of Flexurally-Loaded Aluminium Alloy Structures",
T. Welo, 1990:62, ISBN 82-7119-220-5, ISSN 0802-3271.

"Visualization of Results from Mechanical Engineering Analysis",
K. Aamnes, 1990:63, ISBN 82-7119-221-3, ISSN 0802-3271.

"Object-Oriented Product Modeling for Structural Design",
S. I. Dale, 1991:6, ISBN 82-7119-258-2, ISSN 0802-3271.

"Parallel Techniques for Solving Finite Element Problems on Transputer Networks",
T. H. Hansen, 1991:19, ISBN 82-7119-273-6, ISSN 0802-3271.

"Statistical Description and Estimation of Ocean Drift Ice Environments",
R. Korsnes, 1991:24, ISBN 82-7119-278-7, ISSN 0802-3271.

"Properties of concrete related to fatigue damage: with emphasis on high strength
concrete",
G. Petkovic, 1991:35, ISBN 82-7119-290-6, ISSN 0802-3271.

"Turbidity Current Modelling",
B. Brørs, 1991:38, ISBN 82-7119-293-0, ISSN 0802-3271.

"Zero-Slump Concrete: Rheology, Degree of Compaction and Strength. Effects of
Fillers as Part Cement-Replacement",
C. Sørensen, 1992:8, ISBN 82-7119-357-0, ISSN 0802-3271.

"Nonlinear Analysis of Reinforced Concrete Structures Exposed to Transient Loading",
K. V. Høiseth, 1992:15, ISBN 82-7119-364-3, ISSN 0802-3271.

"Finite Element Formulations and Solution Algorithms for Buckling and Collapse
Analysis of Thin Shells",
R. O. Bjørum, 1992:30, ISBN 82-7119-380-5, ISSN 0802-3271.

"Response Statistics of Nonlinear Dynamic Systems",
J. M. Johnsen, 1992:42, ISBN 82-7119-393-7, ISSN 0802-3271.

"Digital Models in Engineering. A Study on why and how engineers build and operate
digital models for decision support",
J. Høyte, 1992:75, ISBN 82-7119-429-1, ISSN 0802-3271.

"Sparse Solution of Finite Element Equations",
A. C. Damhaug, 1992:76, ISBN 82-7119-430-5, ISSN 0802-3271.

"Some Aspects of Floating Ice Related to Sea Surface Operations in the Barents Sea",
S. Løset, 1992:95, ISBN 82-7119-452-6, ISSN 0802-3271.

"Modelling of Cyclic Plasticity with Application to Steel and Aluminium Structures",
O. S. Hopperstad, 1993:7, ISBN 82-7119-461-5, ISSN 0802-3271.

"The Free Formulation: Linear Theory and Extensions with Applications to Tetrahedral
Elements
with Rotational Freedoms",
G. Skeie, 1993:17, ISBN 82-7119-472-0, ISSN 0802-3271.

"Høyfast betongs motstand mot piggdekslitasje. Analyse av resultater fra prøving i
Veisliter'n",
T. Tveter, 1993:62, ISBN 82-7119-522-0, ISSN 0802-3271.

"A Nonlinear Finite Element Based on Free Formulation Theory for Analysis of
Sandwich Structures",
O. Aamlid, 1993:72, ISBN 82-7119-534-4, ISSN 0802-3271.

"The Effect of Curing Temperature and Silica Fume on Chloride Migration and Pore
Structure of High Strength Concrete",
C. J. Hauck, 1993:90, ISBN 82-7119-553-0, ISSN 0802-3271.

"Failure of Concrete under Compressive Strain Gradients",
G. Markeset, 1993:110, ISBN 82-7119-575-1, ISSN 0802-3271.

"An experimental study of internal tidal amphidromes in Vestfjorden",
J. H. Nilsen, 1994:39, ISBN 82-7119-640-5, ISSN 0802-3271.

"Structural analysis of oil wells with emphasis on conductor design",
H. Larsen, 1994:46, ISBN 82-7119-648-0, ISSN 0802-3271.

"Adaptive methods for non-linear finite element analysis of shell structures",
K. M. Oksstad, 1994:66, ISBN 82-7119-670-7, ISSN 0802-3271.

"On constitutive modelling in nonlinear analysis of concrete structures",
O. Fyrilev, 1994:115, ISBN 82-7119-725-8, ISSN 0802-3271.

"Fluctuating wind load and response of a line-like engineering structure with emphasis
on motion-induced wind forces",
J. Bogunovic Jakobsen, 1995:62, ISBN 82-7119-809-2, ISSN 0802-3271.

"An experimental study of beam-columns subjected to combined torsion, bending and
axial actions",
A. Aalberg, 1995:66, ISBN 82-7119-813-0, ISSN 0802-3271.

"Scaling and cracking in unsealed freeze/thaw testing of Portland cement and silica
fume concretes",
S. Jacobsen, 1995:101, ISBN 82-7119-851-3, ISSN 0802-3271.

"Damping of water waves by submerged vegetation. A case study of laminaria
hyperborea",
A. M. Dubi, 1995:108, ISBN 82-7119-859-9, ISSN 0802-3271.

"The dynamics of a slope current in the Barents Sea",
Sheng Li, 1995:109, ISBN 82-7119-860-2, ISSN 0802-3271.

"Modellering av delmaterialenes betydning for betongens konsistens",
Ernst Mørtsell, 1996:12, ISBN 82-7119-894-7, ISSN 0802-3271.

"Bending of thin-walled aluminium extrusions",
Birgit Søvik Opheim, 1996:60, ISBN 82-7119-947-1, ISSN 0802-3271.

"Material modelling of aluminium for crashworthiness analysis",
Torodd Berstad, 1996:89, ISBN 82-7119-980-3, ISSN 0802-3271.

"Estimation of structural parameters from response measurements on submerged
floating tunnels",
Rolf Magne Larssen, 1996:119, ISBN 82-471-0014-2, ISSN 0802-3271.

"Numerical modelling of plain and reinforced concrete by damage mechanics",
Mario A. Polanco-Loria, 1997:20, ISBN 82-471-0049-5, ISSN 0802-3271.

"Nonlinear random vibrations - numerical analysis by path integration methods",
Vibeke Moe, 1997:26, ISBN 82-471-0056-8, ISSN 0802-3271.

“Numerical prediction of vortex-induced vibration by the finite element method”,
Joar Martin Dalheim, 1997:63, ISBN 82-471-0096-7, ISSN 0802-3271.

“Time domain calculations of buffeting response for wind sensitive structures”,
Ketil Aas-Jakobsen, 1997:148, ISBN 82-471-0189-0, ISSN 0802-3271.

“A numerical study of flow about fixed and flexibly mounted circular cylinders”,
Trond Stokka Meling, 1998:48, ISBN 82-471-0244-7, ISSN 0802-3271.

“Estimation of chloride penetration into concrete bridges in coastal areas”,
Per Egil Steen, 1998:89, ISBN 82-471-0290-0, ISSN 0802-3271.

“Stress-resultant material models for reinforced concrete plates and shells”,
Jan Arve Øverli, 1998:95, ISBN 82-471-0297-8, ISSN 0802-3271.

“Chloride binding in concrete. Effect of surrounding environment and concrete
composition”,
Claus Kenneth Larsen, 1998:101, ISBN 82-471-0337-0, ISSN 0802-3271.

“Rotational capacity of aluminium alloy beams”,
Lars A. Moen, 1999:1, ISBN 82-471-0365-6, ISSN 0802-3271.

“Stretch Bending of Aluminium Extrusions”,
Arild H. Clausen, 1999:29, ISBN 82-471-0396-6, ISSN 0802-3271.

“Aluminium and Steel Beams under Concentrated Loading”,
Tore Tryland, 1999:30, ISBN 82-471-0397-4, ISSN 0802-3271.

“Engineering Models of Elastoplasticity and Fracture for Aluminium Alloys”,
Odd-Geir Lademo, 1999:39, ISBN 82-471-0406-7, ISSN 0802-3271.

“Kapasitet og duktilitet av dybelforbindelser i trekonstruksjoner”,
Jan Siem, 1999:46, ISBN 82-471-0414-8, ISSN 0802-3271.

“Etablering av distribuert ingeniørarbeid; Teknologiske og organisatoriske erfaringer fra
en norsk ingeniørbedrift”,
Lars Line, 1999:52, ISBN 82-471-0420-2, ISSN 0802-3271.

“Estimation of Earthquake-Induced Response”,
Símon Ólafsson, 1999:73, ISBN 82-471-0443-1, ISSN 0802-3271.

“Coastal Concrete Bridges: Moisture State, Chloride Permeability and Aging Effects”
Ragnhild Holen Relling, 1999:74, ISBN 82-471-0445-8, ISSN 0802-3271.

“Capacity Assessment of Titanium Pipes Subjected to Bending and External Pressure”,
Arve Bjørset, 1999:100, ISBN 82-471-0473-3, ISSN 0802-3271.

“Validation of Numerical Collapse Behaviour of Thin-Walled Corrugated Panels”,
Håvar Ilstad, 1999:101, ISBN 82-471-0474-1, ISSN 0802-3271.

“Strength and Ductility of Welded Structures in Aluminium Alloys”,
Miroslaw Matusiak, 1999:113, ISBN 82-471-0487-3, ISSN 0802-3271.

“Thermal Dilation and Autogenous Deformation as Driving Forces to Self-Induced
Stresses in High Performance Concrete”,
Øyvind Bjøntegaard, 1999:121, ISBN 82-7984-002-8, ISSN 0802-3271.

“Some Aspects of Ski Base Sliding Friction and Ski Base Structure”,
Dag Anders Moldestad, 1999:137, ISBN 82-7984-019-2, ISSN 0802-3271.

”Electrode reactions and corrosion resistance for steel in mortar and concrete”,
Roy Antonsen, 2000:10, ISBN 82-7984-030-3, ISSN 0802-3271.

”Hydro-Physical Conditions in Kelp Forests and the Effect on Wave Damping and
Dune Erosion. A case study on Laminaria Hyperborea”,
Stig Magnar Løvås, 2000:28, ISBN 82-7984-050-8, ISSN 0802-3271.

”Random Vibration and the Path Integral Method”,
Christian Skaug, 2000:39, ISBN 82-7984-061-3, ISSN 0802-3271.

”Buckling and geometrical nonlinear beam-type analyses of timber structures”,
Trond Even Eggen, 2000:56, ISBN 82-7984-081-8, ISSN 0802-3271.

”Structural Crashworthiness of Aluminium Foam-Based Components”,
Arve Grønsund Hanssen, 2000:76, ISBN 82-7984-102-4, ISSN 0809-103X.

“Measurements and simulations of the consolidation in first-year sea ice ridges, and
some aspects of mechanical behaviour”,
Knut V. Høyland, 2000:94, ISBN 82-7984-121-0, ISSN 0809-103X.

”Kinematics in Regular and Irregular Waves based on a Lagrangian Formulation”,
Svein Helge Gjøsund, 2000:86, ISBN 82-7984-112-1, ISSN 0809-103X.

”Self-Induced Cracking Problems in Hardening Concrete Structures”,
Daniela Bosnjak, 2000:121, ISBN 82-7984-151-2, ISSN 0809-103X.

”Ballistic Penetration and Perforation of Steel Plates”,
Tore Børvik, 2000:124, ISBN 82-7984-154-7, ISSN 0809-103X.

”Freeze-Thaw resistance of Concrete. Effect of: Curing Conditions, Moisture Exchange
and Materials”,
Terje Finnerup Rønning, 2001:14, ISBN 82-7984-165-2, ISSN 0809-103X

"Structural behaviour of post tensioned concrete structures. Flat slab. Slabs on ground",
Steinar Trygstad, 2001:52, ISBN 82-471-5314-9, ISSN 0809-103X.

"Slipforming of Vertical Concrete Structures. Friction between concrete and slipform panel",
Kjell Tore Fosså, 2001:61, ISBN 82-471-5325-4, ISSN 0809-103X.

"Some numerical methods for the simulation of laminar and turbulent incompressible flows",
Jens Holmen, 2002:6, ISBN 82-471-5396-3, ISSN 0809-103X.

"Improved Fatigue Performance of Threaded Drillstring Connections by Cold Rolling",
Steinar Kristoffersen, 2002:11, ISBN: 82-421-5402-1, ISSN 0809-103X.

"Deformations in Concrete Cantilever Bridges: Observations and Theoretical Modelling",
Peter F. Takács, 2002:23, ISBN 82-471-5415-3, ISSN 0809-103X.

"Stiffened aluminium plates subjected to impact loading",
Hilde Giæver Hildrum, 2002:69, ISBN 82-471-5467-6, ISSN 0809-103X.

"Full- and model scale study of wind effects on a medium-rise building in a built up area",
Jónas Thór Snæbjörnsson, 2002:95, ISBN 82-471-5495-1, ISSN 0809-103X.

"Evaluation of Concepts for Loading of Hydrocarbons in Ice-infested water",
Arnor Jensen, 2002:114, ISBN 82-417-5506-0, ISSN 0809-103X.

"Numerical and Physical Modelling of Oil Spreading in Broken Ice",
Janne K. Økland Gjøsteen, 2002:130, ISBN 82-471-5523-0, ISSN 0809-103X.

"Diagnosis and protection of corroding steel in concrete",
Franz Pruckner, 20002:140, ISBN 82-471-5555-4, ISSN 0809-103X.

"Tensile and Compressive Creep of Young Concrete: Testing and Modelling",
Dawood Atrushi, 2003:17, ISBN 82-471-5565-6, ISSN 0809-103X.

"Rheology of Particle Suspensions. Fresh Concrete, Mortar and Cement Paste with Various Types of Lignosulfonates",
Jon Elvar Wallevik, 2003:18, ISBN 82-471-5566-4, ISSN 0809-103X.

"Oblique Loading of Aluminium Crash Components",
Aase Reyes, 2003:15, ISBN 82-471-5562-1, ISSN 0809-103X.

"Utilization of Ethiopian Natural Pozzolans",
Surafel Ketema Desta, 2003:26, ISSN 82-471-5574-5, ISSN:0809-103X.

“Behaviour and strength prediction of reinforced concrete structures with discontinuity regions”, Helge Brå, 2004:11, ISBN 82-471-6222-9, ISSN 1503-8181.

“High-strength steel plates subjected to projectile impact. An experimental and numerical study”, Sumita Dey, 2004:38, ISBN 82-471-6282-2 (printed version), ISBN 82-471-6281-4 (electronic version), ISSN 1503-8181.

“Alkali-reactive and inert fillers in concrete. Rheology of fresh mixtures and expansive reactions.”

Bård M. Pedersen, 2004:92, ISBN 82-471-6401-9 (printed version), ISBN 82-471-6400-0 (electronic version), ISSN 1503-8181.

“On the Shear Capacity of Steel Girders with Large Web Openings”.

Nils Christian Hagen, 2005:9 ISBN 82-471-6878-2 (printed version), ISBN 82-471-6877-4 (electronic version), ISSN 1503-8181.

”Behaviour of aluminium extrusions subjected to axial loading”.

Østen Jensen, 2005:7, ISBN 82-471-6873-1 (printed version), ISBN 82-471-6872-3 (electronic version), ISSN 1503-8181.

”Thermal Aspects of corrosion of Steel in Concrete”.

Jan-Magnus Østvik, 2005:5, ISBN 82-471-6869-3 (printed version), ISBN 82-471-6868 (electronic version), ISSN 1503-8181.

”Mechanical and adaptive behaviour of bone in relation to hip replacement.” A study of bone remodelling and bone grafting.

Sébastien Muller, 2005:34, ISBN 82-471-6933-9 (printed version), ISBN 82-471-6932-0 (electronic version), ISSN 1503-8181.

“Analysis of geometrical nonlinearities with applications to timber structures”.

Lars Wollebæk, 2005:74, ISBN 82-471-7050-5 (printed version), ISBN 82-471-7019-1 (electronic version), ISSN 1503-8181.

“Pedestrian induced lateral vibrations of slender footbridges”,

Anders Rönnquist, 2005:102, ISBN 82-471-7082-5 (printed version), ISBN 82-471-7081-7 (electronic version), ISSN 1503-8181.

“Initial Strength Development of Fly Ash and Limestone Blended Cements at Various Temperatures Predicted by Ultrasonic Pulse Velocity”,

Tom Ivar Fredvik, 2005:112, ISBN 82-471-7105-8 (printed version), ISBN 82-471-7103-1 (electronic version), ISSN 1503-8181.

“Behaviour and modelling of thin-walled cast components”,

Cato Dørum, 2005:128, ISBN 82-471-7140-6 (printed version), ISBN 82-471-7139-2 (electronic version), ISSN 1503-8181.

“Behaviour and modelling of selfpiercing riveted connections”,
Raffaele Porcaro, 2005:165, ISBN 82-471-7219-4 (printed version), ISBN 82-471-7218-6 (electronic version), ISSN 1503-8181.

”Behaviour and Modelling og Aluminium Plates subjected to Compressive Load”,
Lars Rønning, 2005:154, ISBN 82-471-7169-1 (printed version), ISBN 82-471-7195-3 (electronic version), ISSN 1503-8181.

”Bumper beam-longitudinal system subjected to offset impact loading”,
Satyanarayana Kokkula, 2005:193, ISBN 82-471-7280-1 (printed version), ISBN 82-471-7279-8 (electronic version), ISSN 1503-8181.

”Control of Chloride Penetration into Concrete Structures at Early Age”,
Guofei Liu, 2006:46, ISBN 82-471-7838-9 (printed version), ISBN 82-471-7837-0 (electronic version), ISSN 1503-8181.

”Modelling of Welded Thin-Walled Aluminium Structures”,
Ting Wang, 2006:78, ISBN 82-471-7907-5 (printed version), ISBN 82-471-7906-7 (electronic version), ISSN 1503-8181.

”Time-variant reliability of dynamic systems by importance sampling and probabilistic analysis of ice loads”,
Anna Ivanova Olsen, 2006:139, ISBN 82-471-8041-3 (printed version), ISBN 82-471-8040-5 (electronic version), ISSN 1503-8181.

”Fatigue life prediction of an aluminium alloy automotive component using finite element analysis of surface topography”.
Sigmund Kyrre Ås, 2006:25, ISBN 82-471-7791-9 (printed version), ISBN 82-471-7791-9 (electronic version), ISSN 1503-8181.

”Constitutive models of elastoplasticity and fracture for aluminium alloys under strain path change”,
Dasharatha Achani, 2006:76, ISBN 82-471-7903-2 (printed version), ISBN 82-471-7902-4 (electronic version), ISSN 1503-8181.

”Simulations of 2D dynamic brittle fracture by the Element-free Galerkin method and linear fracture mechanics”,
Tommy Karlsson, 2006:125, ISBN 82-471-8011-1 (printed version), ISBN 82-471-8010-3 (electronic version), ISSN 1503-8181.

”Penetration and Perforation of Granite Targets by Hard Projectiles”,
Chong Chiang Seah, 2006:188, ISBN 82-471-8150-9 (printed version), ISBN 82-471-8149-5 (electronic version), ISSN 1503-8181.

“Deformations, strain capacity and cracking of concrete in plastic and early hardening phases”,

Tor Arne Hammer, 2007:234, ISBN 978-82-471-5191-4 (printed version), ISBN 978-82-471-5207-2 (electronic version), ISSN 1503-8181.

“Crashworthiness of dual-phase high-strength steel: Material and Component behaviour”, Venkatapathi Tarigopula, 2007:230, ISBN 82-471-5076-4 (printed version), ISBN 82-471-5093-1 (electronic version), ISSN 1503-8181.

“Fibre reinforcement in load carrying concrete structures”,

Åse Lyslo Døssland, 2008:50, ISBN 978-82-471-6910-0 (printed version), ISBN 978-82-471-6924-7 (electronic version), ISSN 1503-8181.

“Low-velocity penetration of aluminium plates”,

Frode Grytten, 2008:46, ISBN 978-82-471-6826-4 (printed version), ISBN 978-82-6843-1 (electronic version), ISSN 1503-8181.

“Robustness studies of structures subjected to large deformations”,

Ørjan Fyllingen, 2008:24, ISBN 978-82-471-6339-9 (printed version), ISBN 978-82-471-6342-9 (electronic version), ISSN 1503-8181.

“Constitutive modelling of morsellised bone”,

Knut Birger Lunde, 2008:92, ISBN 978-82-471-7829-4 (printed version), ISBN 978-82-471-7832-4 (electronic version), ISSN 1503-8181.

“Experimental Investigations of Wind Loading on a Suspension Bridge Girder”,

Bjørn Isaksen, 2008:131, ISBN 978-82-471-8656-5 (printed version), ISBN 978-82-471-8673-2 (electronic version), ISSN 1503-8181.

“Cracking Risk of Concrete Structures in The Hardening Phase”,

Guomin Ji, 2008:198, ISBN 978-82-471-1079-9 (printed version), ISBN 978-82-471-1080-5 (electronic version), ISSN 1503-8181.

“Modelling and numerical analysis of the porcine and human mitral apparatus”,

Victorien Emile Prot, 2008:249, ISBN 978-82-471-1192-5 (printed version), ISBN 978-82-471-1193-2 (electronic version), ISSN 1503-8181.

“Strength analysis of net structures”,

Heidi Moe, 2009:48, ISBN 978-82-471-1468-1 (printed version), ISBN 978-82-471-1469-8 (electronic version), ISSN 1503-8181.

“Numerical analysis of ductile fracture in surface cracked shells”,

Espen Berg, 2009:80, ISBN 978-82-471-1537-4 (printed version), ISBN 978-82-471-1538-1 (electronic version), ISSN 1503-8181.

“Subject specific finite element analysis of bone – for evaluation of the healing of a leg lengthening and evaluation of femoral stem design”,
Sune Hansborg Pettersen, 2009:99, ISBN 978-82-471-1579-4 (printed version), ISBN 978-82-471-1580-0 (electronic version), ISSN 1503-8181.

“Evaluation of fracture parameters for notched multi-layered structures”,
Lingyun Shang, 2009:137, ISBN 978-82-471-1662-3 (printed version), ISBN 978-82-471-1663-0 (electronic version), ISSN 1503-8181.

“Modelling of Dynamic Material Behaviour and Fracture of Aluminium Alloys for Structural Applications”
Yan Chen, 2009:69, ISBN 978-82-471-1515-2 (printed version), ISBN 978-82 471-1516-9 (electronic version), ISSN 1503-8181.

“Nanomechanics of polymer and composite particles”
Jianying He 2009:213, ISBN 978-82-471-1828-3 (printed version), ISBN 978-82-471-1829-0 (electronic version), ISSN 1503-8181.

“Mechanical properties of clear wood from Norway spruce”
Kristian Berbom Dahl 2009:250, ISBN 978-82-471-1911-2 (printed version) ISBN 978-82-471-1912-9 (electronic version), ISSN 1503-8181.

“Modeling of the degradation of TiB₂ mechanical properties by residual stresses and liquid Al penetration along grain boundaries”
Micol Pezzotta 2009:254, ISBN 978-82-471-1923-5 (printed version) ISBN 978-82-471-1924-2 (electronic version) ISSN 1503-8181.

“Effect of welding residual stress on fracture”
Xiabo Ren 2010:77, ISBN 978-82-471-2115-3 (printed version) ISBN 978-82-471-2116-0 (electronic version), ISSN 1503-8181.

“Pan-based carbon fiber as anode material in cathodic protection system for concrete structures”
Mahdi Chini 2010:122, ISBN 978-82-471-2210-5 (printed version) ISBN 978-82-471-2213-6 (electronic version), ISSN 1503-8181.

“Structural Behaviour of deteriorated and retrofitted concrete structures”
Irina Vasililjeva Sæther 2010:171, ISBN 978-82-471-2315-7 (printed version) ISBN 978-82-471-2316-4 (electronic version) ISSN 1503-8181.

“Prediction of local snow loads on roofs”
Vivian Meløysund 2010:247, ISBN 978-82-471-2490-1 (printed version) ISBN 978-82-471-2491-8 (electronic version) ISSN 1503-8181.

“Behaviour and modelling of polymers for crash applications”
Virgile Delhaye 2010:251, ISBN 978-82-471-2501-4 (printed version) ISBN 978-82-471-2502-1 (electronic version) ISSN 1503-8181.

“Blended cement with reducted CO₂ emission – Utilizing the Fly Ash-Limestone Synergy”,
Klaartje De Weerdt 2011:32, ISBN 978-82-471-2584-7 (printed version) ISBN 978-82-471-2584-4 (electronic version) ISSN 1503-8181.

“Chloride induced reinforcement corrosion in concrete” Concept of critical chloride content – methods and mechanisms.
Ueli Angst 2011:113, ISBN 978-82-471-2769-9 (printed version) ISBN 978-82-471-2763-6 (electronic version) ISSN 1503-8181.

“A thermo-electric-Mechanical study of the carbon anode and contact interface for Energy savings in the production of aluminium”.
Dag Herman Andersen 2011:157, ISBN 978-82-471-2859-6 (printed version) ISBN 978-82-471-2860-2 (electronic version) ISSN 1503-8181.

“Structural Capacity of Anchorage Ties in Masonry Veneer Walls Subjected to Earthquake”. The implications of Eurocode 8 and Eurocode 6 on a typical Norwegian veneer wall.
Ahmed Mohamed Yousry Hamed 2011:181, ISBN 978-82-471-2911-1 (printed version)
ISBN 978-82-471-2912-8 (electronic ver.) ISSN 1503-8181.

“Work-hardening behaviour in age-hardenable Al-Zn-Mg(-Cu) alloys”.
Ida Westermann , 2011:247, ISBN 978-82-471-3056-8 (printed ver.) ISBN 978-82-471-3057-5 (electronic ver.) ISSN 1503-8181.

“Behaviour and modelling of selfpiercing riveted connections using aluminium rivets”.
Nguyen-Hieu Hoang, 2011:266, ISBN 978-82-471-3097-1 (printed ver.) ISBN 978-82-471-3099-5 (electronic ver.) ISSN 1503-8181.

“Fibre reinforced concrete”.
Sindre Sandbakk, 2011:297, ISBN 978-82-471-3167-1 (printed ver.) ISBN 978-82-471-3168-8 (electronic ver) ISSN 1503:8181.

“Dynamic behaviour of cablesupported bridges subjected to strong natural wind”.
Ole Andre Øiseth, 2011:315, ISBN 978-82-471-3209-8 (printed ver.) ISBN 978-82-471-3210-4 (electronic ver.) ISSN 1503-8181.

“Constitutive modeling of solargrade silicon materials”
Julien Cochard, 2011:307, ISBN 978-82-471-3189-3 (printed ver). ISBN 978-82-471-3190-9 (electronic ver.) ISSN 1503-8181.

“Constitutive behavior and fracture of shape memory alloys”
Jim Stian Olsen, 2012:57, ISBN 978-82-471-3382-8 (printed ver.) ISBN 978-82-471-3383-5 (electronic ver.) ISSN 1503-8181.

“Field measurements in mechanical testing using close-range photogrammetry and digital image analysis”

Egil Fagerholt, 2012:95, ISBN 978-82-471-3466-5 (printed ver.) ISBN 978-82-471-3467-2 (electronic ver.) ISSN 1503-8181.

“Towards a better understanding of the ultimate behaviour of lightweight aggregate concrete in compression and bending”,

Håvard Nedrelid, 2012:123, ISBN 978-82-471-3527-3 (printed ver.) ISBN 978-82-471-3528-0 (electronic ver.) ISSN 1503-8181.

“Numerical simulations of blood flow in the left side of the heart”

Sigrid Kaarstad Dahl, 2012:135, ISBN 978-82-471-3553-2 (printed ver.) ISBN 978-82-471-3555-6 (electronic ver.) ISSN 1503-8181.

“Moisture induced stresses in glulam”

Vanessa Angst-Nicollier, 2012:139, ISBN 978-82-471-3562-4 (printed ver.) ISBN 978-82-471-3563-1 (electronic ver.) ISSN 1503-8181.

“Biomechanical aspects of distraction osteogenesis”

Valentina La Russa, 2012:250, ISBN 978-82-471-3807-6 (printed ver.) ISBN 978-82-471-3808-3 (electronic ver.) ISSN 1503-8181.

“Ductile fracture in dual-phase steel. Theoretical, experimental and numerical study”

Gaute Gruben, 2012:257, ISBN 978-82-471-3822-9 (printed ver.) ISBN 978-82-3823-6 (electronic ver.) ISSN 1503-8181.

“Damping in Timber Structures”

Nathalie Labonnote, 2012:263, ISBN 978-82-471-3836-6 (printed ver.) ISBN 978-82-471-3837-3 (electronic ver.) ISSN 1503-8181.

“Biomechanical modeling of fetal veins: The umbilical vein and ductus venosus bifurcation”

Paul Roger Leinan, 2012:299, ISBN 978-82-471-3915-8 (printed ver.) ISBN 978-82-471-3916-5 (electronic ver.) ISSN 1503-8181.

“Large-Deformation behaviour of thermoplastics at various stress states”

Anne Serine Ognedal, 2012:298, ISBN 978-82-471-3913-4 (printed ver.) ISBN 978-82-471-3914-1 (electronic ver.) ISSN 1503-8181.

“Hardening accelerator for fly ash blended cement”

Kien Dinh Hoang, 2012:366, ISBN 978-82-471-4063-5 (printed ver.) ISBN 978-82-471-4064-2 (electronic ver.) ISSN 1503-8181.

“From molecular structure to mechanical properties”

Jianyang Wu, 2013:186, ISBN 978-82-471-4485-5 (printed ver.) ISBN 978-82-471-4486-2 (electronic ver.) ISSN 1503-8181.

“Experimental and numerical study of hybrid concrete structures”
Linn Grepstad Nes, 2013:259, ISBN 978-82-471-4644-6 (printed ver.) ISBN 978-82-471-4645-3 (electronic ver.) ISSN 1503-8181.

“Mechanics of ultra-thin multi crystalline silicon wafers”
Saber Saffar, 2013:199, ISBN 978-82-471-4511-1 (printed ver.) ISBN 978-82-471-4513-5 (electronic ver). ISSN 1503-8181.

“Through process modelling of welded aluminium structures”
Anizahyati Alisibramulisi, 2013:325, ISBN 978-82-471-4788-7 (printed ver.) ISBN 978-82-471-4789-4 (electronic ver.) ISSN 1503-8181.

“Combined blast and fragment loading on steel plates”
Knut Gaarder Rakvåg, 2013:361, ISBN 978-82-471-4872-3 (printed ver.) ISBN 978-82-4873-0 (electronic ver.). ISSN 1503-8181.

“Characterization and modelling of the anisotropic behaviour of high-strength aluminium alloy”
Marion Fourmeau, 2014:37, ISBN 978-82-326-0008-3 (printed ver.) ISBN 978-82-326-0009-0 (electronic ver.) ISSN 1503-8181.

“Behaviour of threaded steel fasteners at elevated deformation rates”
Henning Fransplass, 2014:65, ISBN 978-82-326-0054-0 (printed ver.) ISBN 978-82-326-0055-7 (electronic ver.) ISSN 1503-8181.

“Sedimentation and Bleeding”
Ya Peng, 2014:89, ISBN 978-82-326-0102-8 (printed ver.) ISBN 978-82-326-0103-5 (electric ver.) ISSN 1503-8181.

“Impact against X65 offshore pipelines”
Martin Kristoffersen, 2014:362, ISBN 978-82-326-0636-8 (printed ver.) ISBN 978-82-326-0637-5 (electronic ver.) ISSN 1503-8181.

“Formability of aluminium alloy subjected to prestrain by rolling”
Dmitry Vysochinskiy, 2014:363,, ISBN 978-82-326-0638-2 (printed ver.) ISBN 978-82-326-0639-9 (electronic ver.) ISSN 1503-8181.

“Experimental and numerical study of Yielding, Work-Hardening and anisotropy in textured AA6xxx alloys using crystal plasticity models”
Mikhail Khadyko, 2015:28, ISBN 978-82-326-0724-2 (printed ver.) ISBN 978-82-326-0725-9 (electronic ver.) ISSN 1503-8181.

“Behaviour and Modelling of AA6xxx Aluminium Alloys Under a Wide Range of Temperatures and Strain Rates”
Vincent Vilamosa, 2015:63, ISBN 978-82-326-0786-0 (printed ver.) ISBN 978-82-326-0787-7 (electronic ver.) ISSN 1503-8181.

“A Probabilistic Approach in Failure Modelling of Aluminium High Pressure Die-Castings”
Octavian Knoll, 2015:137, ISBN 978-82-326-0930-7 (printed ver.) ISBN 978-82-326-0931-4 (electronic ver.) ISSN 1503-8181.

“Ice Abrasion on Marine Concrete Structures”
Egil Møen, 2015:189, ISBN 978-82-326-1034-1 (printed ver.) ISBN 978-82-326-1035-8 (electronic ver.) ISSN 1503-8181.

“Fibre Orientation in Steel-Fibre-Reinforced Concrete”
Giedrius Zirgulis, 2015:229, ISBN 978-82-326-1114-0 (printed ver.) ISBN 978-82-326-1115-7 (electronic ver.) ISSN 1503-8181.

“Effect of spatial variation and possible interference of localised corrosion on the residual capacity of a reinforced concrete beam”
Mohammad Mahdi Kioumarsi, 2015:282, ISBN 978-82-326-1220-8 (printed ver.) ISBN 978-82-1221-5 (electronic ver.) ISSN 1503-8181.

“The role of concrete resistivity in chloride-induced macro-cell corrosion”
Karla Horbostel, 2015:324, ISBN 978-82-326-1304-5 (printed ver.) ISBN 978-82-326-1305-2 (electronic ver.) ISSN 1503-8181.

“Flowable fibre-reinforced concrete for structural applications”
Elena Vidal Sarmiento, 2015-335, ISBN 978-82-326-1324-3 (printed ver.) ISBN 978-82-326-1325-0 (electronic ver.) ISSN 1503-8181.

“Development of crushed sand for concrete production with microproportioning”
Rolands Cepuritis, 2016:19, ISBN 978-82-326-1382-3 (printed ver.) ISBN 978-82-326-1383-0 (electronic ver.) ISSN 1503-8181.

“Withdrawal properties of threaded rods embedded in glued-laminated timer elements”
Haris Stamatopoulos, 2016:48, ISBN 978-82-326-1436-3 (printed ver.) ISBN 978-82-326-1437-0 (electronic ver.) ISSN 1503-8181.

“An Experimental and numerical study of thermoplastics at large deformation”
Marius Andersen, 2016:191, ISBN 978-82-326-1720-3 (printed ver) ISBN 978-82-326-1721-0 (electronic ver.) ISSN 1503-8181.